

*H. Woodard*

AFFDL-TR-73-146-VOL. I

(AD A 001580)

# METHODS FOR PREDICTING THE AERODYNAMIC AND STABILITY AND CONTROL CHARACTERISTICS OF STOL AIRCRAFT

VOLUME I ★ BASIC THEORETICAL METHODS

M. I. Goldhammer  
M. L. Lopez  
C. C. Shen

Douglas Aircraft Company  
McDonnell Douglas Corporation

TECHNICAL REPORT AFFDL-TR-73-146

December 1973

Approved for public release; distribution unlimited

Air Force Flight Dynamics Laboratory  
Air Force Systems Command  
Wright-Patterson Air Force Base, Ohio 45433

*contrails.iit.edu***NOTICE**

When Government drawings, specifications, or other data are used for any purpose other than in connection with a definitely related Government procurement operation, the United States Government thereby incurs no responsibility nor any obligation whatsoever; and the fact that the government may have formulated, furnished, or in any way supplied the said drawings, specifications, or other data, is not to be regarded by implication or otherwise as in any manner licensing the holder or any other person or corporation, or conveying any rights or permission to manufacture, use, or sell any patented invention that may in any way be related thereto.

**Copies of this report should not be returned unless return is required by security considerations, contractual obligations, or notice on a specific document.**

AIR FORCE/56780/25 November 1974 — 250

**AFFDL-TR-73-146-VOL. I**

# **METHODS FOR PREDICTING THE AERODYNAMIC AND STABILITY AND CONTROL CHARACTERISTICS OF STOL AIRCRAFT**

**VOLUME I ★ BASIC THEORETICAL METHODS**

**M. I. Goldhammer  
M. L. Lopez  
C. C. Shen**

**Douglas Aircraft Company  
McDonnell Douglas Corporation**

---

**Approved for public release; distribution unlimited**





## FOREWORD

This report summarizes work accomplished by the Douglas Aircraft Company, McDonnell Douglas Corporation, Long Beach, California for the Air Force Flight Dynamics Laboratory, AFSC, Wright-Patterson Air Force Base, Ohio, under USAF Contract F33615-71-C-1861 (Project 643A). This document, presented in three volumes, constitutes the final report under the contract.

This work was accomplished during the period 1 July 1971 to 30 November 1973, and this report was released by the authors in December 1973. The Air Force Project Engineer was Mr. Henry W. Woolard of the Control Criteria Branch, Flight Control Division, AFFDL. His assistance in monitoring the work and providing necessary data is greatly appreciated.


Several analytical methods presented in this report are based on the results of research sponsored by the McDonnell Douglas Independent Research and Development Program (IRAD), the Office of Naval Research, Contract N00014-71-C-0250, and the Air Force Flight Dynamics Laboratory, Contract F33615-69-C-1602.

The authors gratefully acknowledge the contributions to the work presented in this volume made by Mr. N. D. Halsey (ground effect and momentum induced drag method), Messrs. D. M. Friedman and A. L. Stelmak (vectored jet flow field computer program), and Messrs. N. F. Wasson and W. V. Whitman (EVD and STAMP computer programs). The assistance and cooperation of Dr. P. T. Wooler of the Aircraft Division of Northrop Corporation during the development of the vectored-jet flow

field computer program, which is based on his research in this field, is appreciated. A number of other people contributed to the various phases of the work reported herein for which the authors are grateful.

This report contains no classified information.

This technical report has been reviewed and is approved.



C. B. Westbrook  
Chief, Control Criteria Branch  
Flight Control Division  
Air Force Flight Dynamics Laboratory

## ABSTRACT

This is the first of three volumes of a report that describes methods for predicting the aerodynamic and stability and control characteristics of STOL aircraft which utilize either the internally ducted jet flap, externally blown jet flap, or a mechanical flap with vectored thrust system. It is the intention that this methodology will provide design personnel with a capability to predict static and dynamic longitudinal and lateral-directional stability and control derivatives and coefficients during takeoff, approach, and landing phases of flight both in and out of ground effect.

For the three selected powered high lift systems, a common theoretical basis for the formulation of analytical engineering methods is presented. The theoretical methods developed and described herein include the following:

- The Elementary Vortex Distribution (EVD) Jet-Wing Lifting Surface Theory
- The Ground Effect Method (an extension of the EVD method)
- The Jet-Wing Flow Field Method
- The Vectored Jet Flow Field Method
- The Modified Slender Body Fuselage Method
- The Empennage Method

An extensive comparison of results obtained with these methods and those obtained with other theories and with experimental data is included. The computer program required for the solution of each method is described in Volume II. Engineering methods for applying these theoretical methods to practical STOL aircraft configurations are presented in Volume III.

## CONTENTS

1.0	Introduction . . . . .	1
2.0	Internally Ducted and Externally Blown Jet Flaps. . . . .	7
2.1	Background . . . . .	10
2.1.1	The Basic Jet-Flap High Lift Concept. . . . .	10
2.1.2	Applications of the Jet-Flap Principle. . . . .	12
2.1.3	Theoretical Treatments of the Jet Flap. . . . .	13
2.2	The Elementary Vortex Distribution Jet-Wing Lifting Surface Theory . . . . .	20
2.2.1	Theoretical Interpretation of the Jet- Wing Problem . . . . .	21
2.2.1.1	Statement of the Problem . . . . .	21
2.2.1.2	Basic Assumptions. . . . .	22
2.2.1.3	Formulation of the Theoretical Model . . . . .	23
2.2.1.4	Fundamental Cases. . . . .	31
2.2.1.5	Ground Effect. . . . .	33
2.2.2	Numerical Solution. . . . .	40
2.2.2.1	Description of the Elementary Vortex Distribution Method . . . . .	42
2.2.2.2	The Downwash Influence Coefficients. . . . .	44
2.2.2.3	Modification of the Downwash Influ- ence Coefficients for Ground Effect. . . . .	46
2.2.2.4	Boundary Conditions. . . . .	47
2.2.2.5	Determination of Aerodynamic Loading or Local Vortex Intensity. . . . .	50
2.2.3	Aerodynamic Characteristics . . . . .	54
2.2.3.1	Sectional Aerodynamic Characteristics. . . . .	54
2.2.3.1.1	Lift . . . . .	54
2.2.3.1.2	Pitching Moment . . . . .	54
2.2.3.1.3	Thrust and Induced Drag . . . . .	56
2.2.3.1.4	Sectional Aerodynamic Char- acteristics - Their Depen- dence on Angle of Attack . . . . .	58



2.2.3.2	Total Aerodynamic Forces and Moments . . .	62
2.2.3.2.1	Lift . . . . .	63
2.2.3.2.2	Pitching Moment . . . . .	63
2.2.3.2.3	Thrust and Induced Drag . . . . .	65
2.2.3.2.4	Side Force . . . . .	66
2.2.3.2.5	Rolling Moment . . . . .	66
2.2.3.2.6	Yawing Moment . . . . .	67
2.2.3.2.7	Alternative Approach to the Estimation of Induced Drag - Momentum Analysis . . . . .	68
2.2.4	Dynamic Stability Derivatives . . . . .	74
2.2.4.1	General Remarks . . . . .	74
2.2.4.2	Pitching Jet-Wing . . . . .	77
2.2.4.3	Rolling Jet-Wing . . . . .	80
2.2.4.4	Yawing Jet-Wing . . . . .	83
2.2.4.5	Sideslipping Jet-Wing . . . . .	86
2.2.5	Comments on Convergence and Accuracy - Spacing Study . . . . .	88
2.2.6	Method Validation . . . . .	91
2.2.6.1	Some Comparisons with the Results of Other Theories . . . . .	91
2.2.6.2	Comparisons with Experiment . . . . .	94
2.2.6.2.1	Rectangular Wings . . . . .	94
2.2.6.2.2	Swept Wings . . . . .	95
2.2.6.2.3	Dynamic Stability Derivatives . . . . .	96
2.2.6.3	Ground Effect . . . . .	97
2.2.7	Summary and Concluding Remarks . . . . .	103
2.3	Jet-Wing Flow Field Method . . . . .	106
2.3.1	Background . . . . .	106
2.3.2	Theoretical Analysis of the Jet-Wing Flow Field Problem . . . . .	107
2.3.3	Method Validation . . . . .	111
2.3.4	Summary and Concluding Remarks . . . . .	114

3.0	Mechanical Flap Systems with Vectored Thrust . . . . .	116
3.1	Jet Flow Field Method . . . . .	119
3.1.1	Jet Envelope . . . . .	119
3.1.2	Jet Induced Velocity . . . . .	126
3.1.3	Summary and Concluding Remarks . . . . .	131
3.2	Aerodynamic/Propulsion Interferences . . . . .	133
4.0	Methods for the Analysis of the Aerodynamics of Aircraft Components . . . . .	135
4.1	Fuselage Analysis . . . . .	136
4.1.1	Slender Body Theory . . . . .	136
4.1.2	Modification of Slender Body Theory for Non-Axisymmetric Bodies in Non-Uniform Flows . . . . .	142
4.1.3	Jet-Wing Interference . . . . .	145
4.1.4	Aerodynamic Characteristics . . . . .	146
4.1.4.1	Pitching Moment . . . . .	147
4.1.4.2	Yawing Moment . . . . .	147
4.1.5	Dynamic Stability Derivatives. . . . .	148
4.1.5.1	Pitching Fuselage . . . . .	148
4.1.5.2	Yawing Fuselage . . . . .	149
4.1.6	Method Validation . . . . .	149
4.1.7	Summary and Concluding Remarks . . . . .	152
4.2	Empennage Analysis . . . . .	154
4.2.1	Lifting Surface Theory for Multiplanar Systems . . . . .	155
4.2.2	Jet-Wing Interference . . . . .	158
4.2.3	Aerodynamic Characteristics . . . . .	158
4.2.3.1	Tail Lift . . . . .	158
4.2.3.2	Tail Side Force . . . . .	159
4.2.3.3	Tail Induced Drag . . . . .	160
4.2.3.4	Tail Pitching Moment . . . . .	161
4.2.3.5	Tail Rolling Moment . . . . .	161
4.2.3.6	Tail Yawing Moment . . . . .	162
4.2.4	Dynamic Stability Derivatives . . . . .	162
4.2.4.1	Pitching Tail . . . . .	163
4.2.4.2	Rolling Tail . . . . .	163
4.2.4.3	Yawing Tail . . . . .	165
4.2.5	Summary and Concluding Remarks . . . . .	165

5.0	References . . . . .	167
Appendix I	. . . . .	173
I.1	Downwash Influence Coefficients . . . . .	173
I.1.1	Regular EVD . . . . .	174
I.1.2	Leading Edge EVD . . . . .	176
I.1.3	Hinge EVD . . . . .	178
I.1.4	Infinity (Far-Jet) EVD . . . . .	182
I.1.5	Ground Effect Influence Coefficients . . . . .	184
I.2	Integration Coefficients . . . . .	187
I.3	Leading Edge Suction . . . . .	190
I.4	Numerical Technique for Evaluating Induced Downwash at Infinity . . . . .	192
I.5	Ground Effect - Thin Airfoil Theory . . . . .	197
Appendix II	. . . . .	203
	Normal-wash Influence Coefficients for an Arbitrarily Oriented Discrete Horseshoe Vortex	
Appendix III	. . . . .	206
	Neumann Solution for the Potential Flow About an Arbitrary Two-Dimensional Body	
Appendix IV	. . . . .	211
	General Remarks - Half Span Wind Tunnel Testing	
Illustrations	. . . . .	214

## LIST OF ILLUSTRATIONS

<u>No.</u>		<u>Page</u>
2.1	Various Jet-Flap Schemes . . . . .	214
2.2	Theoretical Model of a Basic Jet-Wing System . . . . .	215
2.3	Jet-Wing Fundamental Cases . . . . .	216
2.4	(a) Illustration of the EVD Jet-Wing Method . . . . .	217
	(b) Illustration of the EVD Jet-Wing Ground Effect Method . . . . .	218
2.5	Comparison Between Downwash Induced by a Triangular EVD and by a Discrete Horseshoe Vortex of the Same Total Strength . . . . .	219
2.6	Illustration of the Jet-Wing Momentum Analysis . . . . .	220
2.7	(a) Jet-Wing in Sideslip . . . . .	221
	(b) Stability Axes for Jet-Wing . . . . .	221
2.8	Effect of the EVD Element Spacing on the Aero- dynamic Characteristics of a Rectangular Wing of Aspect Ratio 4.5 . . . . .	222
2.9	Effect of the EVD Element Spacing on the Aero- dynamic Characteristics of a Rectangular Jet-Wing of Aspect Ratio 4.5 With Uniform Full-Span Blowing (Angle of Attack Case). . . . .	223
2.10	Effect of the EVD Element Spacing on the Aero- dynamic Characteristics of a Rectangular Jet-Wing of Aspect Ratio 4.5 With Uniform Full-Span Blowing (Jet Deflection Case) . . . . .	224
2.11	Lift Curve Slope of Elliptical Wings - Comparison of Results from Various Theoretical Methods . . . . .	225
2.12	Aerodynamic Center of Elliptical Wings - Comparison of Results from Various Theoretical Methods. . . . .	225
2.13	Comparison of the Spanwise Variation of Theoretical Sectional Lift Curve Slope for Elliptical Wings. . . . .	226
2.14	Comparison of the Spanwise Variation of Theoretical Sectional Center of Pressure for Elliptical Wings. . . . .	226
2.15	Comparison of the Theoretical Chordwise Loading Distributions for Elliptical Wings . . . . .	227
2.16	The Effect of Jet Momentum on the Lift of an Elliptical Jet-Wing of Aspect Ratio 6.8 - Com- parison of Theoretical Results . . . . .	228
2.17	The Effect of Jet Momentum on the Induced Drag of an Elliptical Jet-Wing . . . . .	229



<u>No.</u>	<u>Page</u>
2.18 Comparison of the EVD Theoretical Aerodynamic Characteristics for a Large Aspect Ratio Wing (AR = 100) with 2-D Analytical Results ( $\alpha = 1.0$ rad., $\delta_j = 0$ ) . . . . .	230
2.19 Comparison of the EVD Theoretical Aerodynamic Characteristics for a Large Aspect Ratio Wing (AR = 100) with 2-D Analytical Results ( $\alpha = 0$ , $\delta_j = 1.0$ rad.) . . . . .	231
2.20 The Lift Curve Slope of Rectangular Wings ( $C_j = 0$ ) - Comparison of the EVD Method with Other Theories and Experiment . . . . .	232
2.21 Lift of Rectangular Wings with Uniform Full-Span Blowing - Comparison Between Theory and Experiment. $\partial C_{L_T} / \partial \alpha$ versus AR . . . . .	233
2.22 Lift of Rectangular Wings with Uniform Full-Span Blowing - Comparison Between Theory and Experiment. $\partial C_{L_T} / \partial \delta_j$ versus AR . . . . .	233
2.23 Spanwise Variation of Sectional Lift Curve Slope of a Rectangular Wing (AR = 4.5) with Uniform Full-Span Blowing - Comparison Between Theory and Experiment. . . . .	234
2.24 Spanwise Variation of Sectional Lift of a Rectangular Wing (AR = 4.5) with a Uniform Full-Span Jet Deflected at $30^\circ$ - Comparison Between Theory and Experiment. . . . .	234
2.25 Comparison of the EVD Theory with Experimental Results for Chordwise Loading of a Rectangular Wing with Uniform Full-Span Blowing. . . . .	235
2.26 Theoretical and Experimental Lift, Pitching Moment, and Drag Characteristics of a Tapered Swept Wing ( $C_j = 0$ ) . . . . .	236
2.27 Spanwise Variation of Lift, Center of Pressure, and Induced Drag - Comparison of Theory and Experiment for a Tapered Swept Wing ( $C_j = 0$ ) . . . . .	237
2.28 Comparison of EVD Theory with Experimental Results - Chordwise Loading on a Tapered Swept Wing ( $C_j = 0$ ) . . . . .	238
2.29 Comparison of Theory and Experiment - Spanwise Circulation Lift Distribution of a $45^\circ$ Swept Wing with Uniform Full-Span Blowing . . . . .	239
2.30 Comparison of Theory and Experiment - Spanwise Circulation Lift Distribution of a $45^\circ$ Swept Wing with Partial Span Blowing . . . . .	239

<u>No.</u>	<u>Page</u>
2.31 Measured and Calculated Stability Derivatives due to Pitching, Rolling, and Yawing for a Rectangular Wing of Aspect Ratio 5.16 ( $C_J = 0$ ) . . . . .	240
2.32 Measured and Calculated Stability Derivatives due to Pitching, Rolling, and Yawing for a 45° Swept, Constant-Chord Wing - AR = 2.61 ( $C_J = 0$ ) . . . . .	241
2.33 Lift on a Two-Dimensional Hinged Flat-Plate Airfoil In Ground Effect - Comparison Between Linear and Non-linear Theory . . . . .	242
2.34 Lift on a Two-Dimensional Hinged Flat-Plate Airfoil In Ground Effect Calculated By Linear Theory - Ratio of Lift In Ground Effect to Lift in Free Air . . . . .	243
2.35 Lift on a Two-Dimensional Flat-Plate Airfoil with Jet Flap in Ground Effect - Comparison Between Linear and Non-Linear Theory . . . . .	244
2.36 Lift on a Two-Dimensional Hinged Flat-Plate Airfoil with Jet Flap in Ground Effect - Comparison Between Linear and Non-Linear Theory . . . . .	244
2.37 Pressure Distribution on a Two-Dimensional Hinged Flat-Plate Airfoil with Jet Flap in Ground Effect - Comparison Between Linear and Non-Linear Theory . . . . .	245
2.38 Effect of Ground Proximity on the Lift Curve Slope of a Rectangular Wing - Comparison Between Theory and Experiment . . . . .	246
2.39 Effect of Ground Proximity on the Lift of a Rectangular Jet-Wing - Comparison Between Theory and Experiment . . . . .	247
2.40 Lanchester's Representation of Vortex Roll Up . . . . .	248
2.41 Typical Rolled Up Wake For a Wing with a Simple Spanwise Loading Distribution - Comparison Between Theory (reference 51) and Experiment. . . . .	249
2.42 Typical Rolled Up Wake for a Wing with a Part- span Flap - Theoretical Prediction (2nd Iteration) of the Method of Reference 51. . . . .	250
2.43 Variation of Wing Induced Downwash in the Plane of Symmetry Behind the USA 45 Wing - Comparison Between Theory and Experiment . . . . .	251
2.44 Variation of Jet-Wing Induced Downwash with Position - Comparison Between Theory and Experiment . . . . .	252

<u>No.</u>	<u>Page</u>
2.45	Variation of Jet-Wing Induced Downwash with Jet Momentum - Comparison Between Theory and Experiment . . . . . 255
3.1	Illustration of a Vectored-Jet in a Cross Flow - Geometry and Mathematical Model . . . . . 256
3.2	Comparison of Predicted and Experimental Jet Parameters . . . . . 257
3.3	Typical Wing/Vectored Jet Aerodynamic Interferences . . . . . 258
4.1	Illustration of the Fuselage Method . . . . . 260
4.2	Division of the Fuselage Into Streamwise Segments for the Modified Slender Body Solution . . . . . 261
4.3	Division of Fuselage Cross-Sections Into Circumferential Segments for the Modified Slender Body Solution . . . . . 262
4.4	Representation of the Fuselage By a Lattice of Quadrilateral Elements for the Modified Slender Body Solution . . . . . 263
4.5	Definition of the Normal Vector on the Fuselage Surface . . . . . 264
4.6	Pressure Distribution on Spheroids of Several Thickness Ratios at Zero Angle of Attack - Comparison Between Exact Theory and the Present Slender Body Method . . . . . 265
4.7	Pressure Distribution on Spheroids of Several Thickness Ratios at 20° Angle of Attack - Comparison Between Exact Theory and the Present Slender Body Method . . . . . 266
4.8	Pitching Moment on Spheroids of Several Thickness Ratios - Comparison Between Exact Theory and the Present Slender Body Method . . . . . 267
4.9	Pressure Distribution on a Tri-Axial Ellipsoid at Zero Angle of Attack - Comparison Between Exact Theory and the Present Slender Body Method . . . . . 268
4.10	Pressure Distribution on a Tri-Axial Ellipsoid at 20° Angle of Attack - Comparison Between Exact Theory and the Present Slender Body Method . . . . . 269
4.11	Illustration of a Typical STOL Empennage Arrangement . . . . . 270

<u>No.</u>		<u>Page</u>
I.1	Illustration of EVD Types . . . . .	271
I.2	Illustration of the Derivation of Integration Coefficients . . . . .	272
II.1	Illustration of the Biot-Savart Law for a Discrete Vortex Filament . . . . .	273
II.2	Illustration of the Evaluation of the Biot- Savart Law for a Discrete Horseshoe Vortex . . . . .	273
III.1	Illustration of the Application of the Neumann Solution to a Fuselage Cross-Section . . . . .	274
III.2	Illustration of the Calculation of the Velocity Induced by a Source Line Element . . . . .	275



## NOMENCLATURE

AR	Aspect ratio
A	Fourier series coefficients
$A_{ij}$	Normal wash influence coefficient for discrete horseshoe vortex
$A_{ij}$	Normal wash influence coefficient for source line element
$A_j$	Local jet cross-sectional area
$a, a_{ij}$	Downwash influence coefficient
$\bar{a}, \bar{a}_{ij}$	Downwash influence coefficient for image jet-wing
b	Wing span
$b_H$	Horizontal tail span
$b_V$	Vertical tail span
$b, b_{ij}$	Downwash influence coefficient due to singular part of Hinge EVD
$\bar{b}, \bar{b}_{ij}$	Downwash influence coefficient due to singular part of Hinge EVD for image jet-wing
C	Local jet circumference
$C_D$	Jet cross-flow drag coefficient
$C_{D_i}$	Total induced drag coefficient ( $D_i/qS$ )
$C_{D_J}$	Portion of total induced drag coefficient contributed by jet reaction only
$C_{D_T}$	Portion of total induced drag coefficient contributed by circulation (pressure) only
$C_J$	Total jet momentum coefficient ( $\bar{J}/qS$ )
$C_L$	Total lift coefficient ( $L/qS$ )
$C_{L_J}$	Portion of total lift coefficient contributed by jet reaction only
$C_{L_q}$	Lift-coefficient derivative due to pitching ( $\partial C_L / \partial (\frac{q\tilde{c}}{2U})$ )
$C_{L_\alpha}$	Lift-curve slope ( $\partial C_L / \partial \alpha$ )

## NOMENCLATURE

$C_{L_P}$	Portion of total lift coefficient contributed by circulation (pressure) only
$C_l$	Total rolling-moment coefficient ( $L/qSb$ )
$C_{l_J}$	Portion of total rolling-moment coefficient contributed by jet reaction only
$C_{l_p}$	Rolling-moment-coefficient derivative due to roll $\left(\partial C_l / \partial \left(\frac{pb}{2U}\right)\right)$
$C_{l_r}$	Rolling-moment-coefficient derivative due to yaw $\left(\partial C_l / \partial \left(\frac{rb}{2U}\right)\right)$
$C_{l_P}$	Portion of total rolling-moment coefficient contributed by circulation (pressure) only
$C_m$	Total pitching-moment coefficient about wing apex point ( $M/qS\bar{c}$ ), nose up positive
$C_{m_J}$	Portion of total pitching-moment coefficient contributed by vertical component of jet reaction only
$(C_m)_{m.c.}$	Total pitching-moment coefficient about moment center
$C_{m_q}$	Pitching-moment-coefficient derivative due to pitching $\left(\partial C_m / \partial \left(\frac{q\bar{c}}{2U}\right)\right)$
$C_{m_T}$	Portion of total pitching-moment coefficient contributed by horizontal component of jet reaction only
$C_{m_P}$	Portion of total pitching-moment coefficient contributed by circulation lift (pressure) only
$C_n$	Total yawing-moment coefficient ( $N/qSb$ )
$C_{n_J}$	Jet-reaction (horizontal component) contribution to total yawing-moment coefficient
$C_{n_p}$	Yawing-moment coefficient derivative due to roll $\left(\partial C_n / \partial \left(\frac{pb}{2U}\right)\right)$
$C_{n_r}$	Yawing-moment coefficient due to yaw $\left(\partial C_n / \partial \left(\frac{rb}{2U}\right)\right)$
$C_{n_P}$	Portion of total yawing-moment coefficient contributed by circulation (pressure) thrust ( $c_{t_P}$ ) and leading-edge suction ( $c_s$ )
$C_s$	Total suction coefficient
$C_T$	Total thrust coefficient ( $T/qS$ )
$C_{T_J}$	Portion of total thrust coefficient contributed by jet reaction only

## NOMENCLATURE

$C_{T_R}$	Portion of total thrust coefficient contribution by circulation lift (pressure) only
$C_Y$	Total side-force coefficient
$c$	Chord length of a wing section
$\bar{c}$	Mean aerodynamic chord (MAC) of wing $\frac{1}{S} \int_{-b/2}^{b/2} c^2 dy$
$\bar{\bar{c}}$	Geometrical mean chord of wing $\frac{1}{b} \int_{-b/2}^{b/2} c dy$
$\tilde{c}$	Wing reference chord
$c_{d_i}$	Sectional induced drag coefficient ( $d_i/qc$ )
$c_f$	Flap chord
$c_{ij}$	Influence coefficient for the perturbation velocity in the freestream direction
$c_l$	Sectional lift coefficient ( $L/qc$ )
$c_{l_R}$	Portion of sectional lift coefficient contributed by circulation (pressure) only
$c_{l_\mu}$	Portion of sectional lift coefficient contributed by jet reaction only
$c_m$	Sectional pitching-moment coefficient about wing apex point ( $m/qc$ ), nose up positive
$(c_m)_{m.c}$	Sectional pitching-moment coefficient about moment center
$c_{m_t}$	Portion of sectional pitching-moment coefficient contributed by horizontal component of jet reaction only
$c_{m_R}$	Portion of sectional pitching-moment coefficient contributed by circulation lift (pressure) only
$c_{m_\mu}$	Portion of sectional pitching-moment coefficient contributed by vertical component of jet reaction only

## NOMENCLATURE

$c_p$	Pressure coefficient $(p - p_\infty)/q$
$\Delta c_p$	Difference in pressure coefficient (loading coefficient) between the lower and upper surfaces
$c_r$	Root chord of wing
$c_s$	Sectional leading-edge suction coefficient
$c_t$	1. Sectional thrust coefficient $(t/qc)$ 2. Tip chord of wing
$c_{t_T}$	Portion of sectional thrust coefficient contributed by circulation (pressure) only
$c_{t_\mu}$	Portion of sectional thrust coefficient contributed by jet reaction only
$c_\mu$	Sectional jet momentum coefficient $(J/qc)$
$D_i$	Total induced drag
$d$	Distance from the wing trailing edge to the vortex point of the infinity EVD in a jet-wing section
$d_i$	Sectional induced drag
$d_j$	1. Jet thickness 2. Local jet diameter 3. Major axis of ellipse
$d_{j_0}$	Jet exit diameter
$E$	1. Flap-chord ratio $(c_f/c)$ 2. Jet entrainment
$E_1, E_2, E_3$	Jet entrainment empirical parameters
$e$	Induced span-efficiency factor - or ratio of the induced drag used on the assumption of an elliptical loading distribution to the actual induced drag
$F$	Surface of body in slender-body solution
$F_p$	Pressure force on jet boundary
$H$	Horizontal tail (subscript)



## NOMENCLATURE

h	<ol style="list-style-type: none"> <li>1. Height of wing above the ground</li> <li>2. Perpendicular distance from discrete horseshoe vortex to control point</li> </ol>
$h_{\ell}$	Vertical displacement of the wing leading edge above the wing apex point
$h_t$	Initial $h_{\ell}$ due to wing twist and dihedral
$\bar{J}$	Total jet momentum
J	Sectional jet momentum
$k_i$	Jet entrainment empirical parameter
L	<ol style="list-style-type: none"> <li>1. Total lift</li> <li>2. Total rolling moment</li> </ol>
K	Number of fundamental cases
$\ell$	Sectional lift
M	<ol style="list-style-type: none"> <li>1. Total pitching moment</li> <li>2. Number of spanwise divisions used in the EVD method</li> </ol>
m	<ol style="list-style-type: none"> <li>1. Sectional pitching moment</li> <li>2. Jet to freestream velocity ratio (<math>V_{J_0}/U</math>)</li> </ol>
N	<ol style="list-style-type: none"> <li>1. Total yawing moment</li> <li>2. Total number of EVD elements</li> </ol>
$N_J$	Number of chordwise division of a jet section used in the EVD method
$N_W$	Number of chordwise divisions of a wing section used in the EVD method
$\vec{n}$	Normal vector to the body surface
p	<ol style="list-style-type: none"> <li>1. Static pressure</li> <li>2. Rate of roll</li> </ol>
$p_{\infty}$	Free stream static pressure
$Q_i$	Velocity induced by a discrete vortex filament
q	<ol style="list-style-type: none"> <li>1. Dynamic pressure <math>\left(\frac{1}{2} \rho U^2\right)</math></li> <li>2. Rate of pitching</li> <li>3. Strength of source distribution used in fuselage axial flow solution</li> </ol>

## NOMENCLATURE

$\vec{q}$	Total velocity ( $U + u, v, w$ )
$\vec{q}'$	Perturbation velocity ( $u, v, \bar{w}$ )
R	1. Longitudinal radius of curvature of jet sheet 2. Radius of curvature of jet centerline
r	Rate of yaw
$r, \theta, x$	Cylindrical coordinates defined in Section 4.1
S	1. Wing planform reference area 2. Body cross-sectional area 3. Distance along jet centerline
T	Total thrust
t	Sectional Thrust
$U, U_\infty$	Free-stream velocity
$u, v, \bar{w}$	Perturbation velocity components in the $x, y, z$ directions, respectively
$u', v', w'$	Perturbation velocities in the $x, y, z$ directions, respectively, induced by the image jet-wing
$u_x, u_r, u_\theta$	Perturbation velocities in the $x, r, \theta$ directions, respectively
V	Vertical tail (subscript)
$V_J$	1. Jet velocity 2. Non-dimensional jet velocity $V_J/V_{J_0}$
$V_{J_0}$	Initial jet velocity
$V_1, V_2$	Total velocity above and below the jet sheet, respectively
$V_T$	Tangential velocity
w	1. Downwash ( $w = -\bar{w}$ ) 2. Complex velocity
$x_{a.c.}$	x-coordinate of the aerodynamic center of the wing
$x_{C.L.}$	x-coordinate of the center of lift of the wing
$x_{c.g.}$	x-coordinate of the center of gravity of the wing
$x_{c.p.}$	x-coordinate of the center of pressure of the wing

## NOMENCLATURE

$x_{m.c.}$	x-coordinate of reference moment center
$x, y$	Local rectilinear coordinates defined in Appendix A.1 in the calculation of downwash influence coefficients
$x, y, z$	Cartesian coordinates as defined in the text for the jet-wing problem (x parallel to free-stream velocity and measured from the wing apex point)
$x_l$	x-coordinate of a wing leading-edge point
$x_t$	x-coordinate of a wing trailing-edge point
$\bar{x}$	Fraction of chord measured from the leading edge of a wing section $(x - x_l)/c$
$\bar{x}_{c.l.}$	Sectional center-of-lift location in terms of fraction of chord
$\bar{x}_{c.p.}$	Sectional center-of-pressure location in terms of fraction of chord
$Y$	Total side force
$y_u$	Ordinate of the upper surface of an airfoil
$y_L$	Ordinate of the lower surface of an airfoil
$y_m$	Ordinate of the airfoil mean line
$y_t$	Ordinate of the airfoil thickness distribution
$\Delta z$	Vertical displacement of the wing trailing edge below the corresponding leading edge at a wing section
$\bar{z}$	Jet deflection below the wing trailing edge
$\tilde{z}$	z-coordinate of the jet sheet
$\alpha$	Angle of attack of a wing
$\alpha_{i_\infty}$	Downwash angle or jet angle with respect to freestream at infinity downstream
$\alpha_t$	Twist angle of a wing section
$\beta$	1. Deflection angle ( $\delta_f, \delta_j,$ or $\delta_s$ ) 2. Sideslip angle 3. Angle of normal to fuselage section boundary
$\Pi$	Complex potential

## NOMENCLATURE

$\rho, \rho_\infty$	Density of freestream flow
$\rho_J$	Jet flow density
$\sigma$	Source strength used in Neumann solution
$\phi$	Perturbation velocity potential
$\Phi$	Total velocity potential
$\psi$	Slope of fuselage meridian
$\omega$	Complex velocity
$\Gamma$	Total circulation around a jet-wing section
$\Gamma$	1. Strength of a discrete horseshoe vortex 2. Dihedral angle
$\gamma$	Infinitesimal horseshoe vortex intensity (per unit area)
$\gamma^*$	EVD vortex intensity
$\bar{\gamma}$	Leading-edge EVD mean vortex intensity
$\Delta$	Half of spanwise width of an EVD base
$\delta, \delta_1, \delta_2$	Chordwise interval lengths of an EVD base
$\delta_f$	Ideal flap-deflection angle
$\delta_J$	Jet-deflection angle with respect to wing trailing-edge slope
$\delta_\ell$	Chordwise interval length of a leading-edge EVD
$\delta_S$	Leading-edge-flap deflection angle
$\epsilon$	Local incidence angle of wing
$\epsilon_C$	Camber angle
$\epsilon_\infty$	Incidence angle of the vortex wake in the Trefftz plane
$\theta$	Jet deflection angle with respect to freestream
$\theta_J$	Jet efflux angle relative to the freestream
$\theta_S$	Deflection angle of the leading-edge flap with respect to main chord in a wing section

## NOMENCLATURE

$\Lambda_\ell$	Local wing leading-edge sweepback angle $\tan^{-1}\left(\frac{dx_\ell(y)}{dy}\right)$
$\Lambda_{c/4}$	Wing quarter-chord-line sweepback angle
$\lambda$	Wing taper ratio ( $c_t/c_r$ )
$\mu$	Doublet strength used in fuselage cross-flow solution
$\nu$	Jet-strength quantity defined by $2/(c c_\mu)$
$\xi, \eta, \zeta$	Cartesian coordinates (dummies of $x, y, z$ )



## 1.0 INTRODUCTION

The increasing emphasis on the development of powered high lift systems for STOL aircraft applications as well as the broad range of aerodynamic parameters associated with them have intensified the need for methods that would enable both the performance and stability and control characteristics of a given configuration to be predicted. Several problems unique to each system have, unfortunately, hampered the development of suitable and accurate aerodynamic methods. These problems are, to a large extent, either the result of the synthesis of the propulsive system of an aircraft with its airframe, leading to a significant and often desirable aerodynamic-propulsion interaction, or the employment of pure jet-lift in conjunction with mechanical high lift systems in a role in which any jet/airframe aerodynamic interferences may not at first seem important.

In view of the complexity of the aerodynamic phenomena associated with powered high lift systems, it is often argued that the aerodynamic characteristics of a specific STOL aircraft configuration should be obtained simply by resorting to wind tunnel testing. This approach is sometimes justified on the ground that a theoretical solution of a specific aerodynamic problem is not considered tractable. On the other hand, although it is unlikely that one could ever dispense completely with wind tunnel testing, there is a need for a more rational basis for the evaluation, design, and development of STOL aircraft. This rational basis must include the aerodynamic methodology mentioned earlier.

Several of the powered lift systems in which interest has been expressed in recent years involve, in part, the utilization of the jet-flap principle to generate the required lift for takeoff and landing. To achieve this lift, the jet flap in its basic form requires the complete integration of the propulsive system and airframe with the entire propulsive jet being ejected in the form of a thin, full-span sheet from the trailing edge of the wing. This might well be considered as the most effective approach to achieving the required STOL performance, if it were not for the lack of a practical solution for the structural, powerplant, acoustic, and aerodynamic problems that have been encountered. There are, however, several alternative systems which overcome

several of these problems while still relying to a degree on the underlying principle of the basic jet flap. The externally blown jet flap, upper surface blown flap, and the augmentor or ejector jet flap would fall in this category. As might be expected, each one of these concepts exhibit a strong aerodynamic-propulsion interaction. This, in turn, requires that any analytical approach to the estimation of the aerodynamic characteristics of configurations employing high lift systems which utilize the jet-flap principle would have to consider the jet and wing as an integrated system.

It has been suggested earlier that an alternative approach to the development of the high lift required for STOL operations is the employment of mechanical flap systems with the vectoring of the propulsive thrust. In this way, the integration of the propulsive system and the airframe is not essential. This does not imply, however, that an aerodynamic-propulsion interaction is avoided. In fact, there is now sufficient experimental evidence to suggest that important interferences between the vectored jets and the airframe can exist. These aerodynamic interferences can be either favorable or unfavorable depending on, for example, the location and orientation of the vectored jets relative to the wing. Thus, an ability to predict these interferences is required.

In recent years, our understanding of the aerodynamics of many of the powered lift systems, mentioned earlier, has been broadened as a result of experimental studies conducted both in this country and abroad. In addition, noticeable progress in the development of methods suitable to the prediction of their aerodynamic characteristics has been made. Some of this methodology has been developed by the Douglas Aircraft Company under the sponsorship of the Air Force Flight Dynamics Laboratory (e.g., the investigation reported on herein). It must be understood, however, that despite the progress made to date there remains room for further development.

The primary goal of the present study has been the development of a unified set of analytical methods which would provide the capability to calculate the stability and control characteristics of an arbitrary STOL aircraft configuration that might employ the internally ducted jet flap, externally blown jet flap, or a mechanical high lift system with vectored thrust. This report, in which



the results of this and related studies are presented, has, for convenience, been divided into three volumes:

- Volume I - Basic Theoretical Methods
- Volume II - STOL Aerodynamic Methods Computer Program
- Volume III - Engineering Methods

Volume I presents the complete theoretical development of the relevant analytical methods. In addition, it presents comparisons of these methods with other analytical solutions and with experimental data.

Volume II provides complete details for the use of the STOL Aerodynamic Methods Program (STAMP), including a brief review of the theoretical methods, fundamentals of program use including element spacing guidelines, instructions for input to the program and for interpretation of the output, and a complete description of the program. The STAMP computer package has been developed for use on both a CDC 6000 series and the IBM 360/370 series computers. It is written in the Fortran IV language.

Volume III of the report, Engineering Methods, provides additional analytical and semi-empirical methods to supplement and modify the results obtained from the theoretical methods and their associated computer programs (Volumes I and II). The methods presented include several which are based on methods contained in the USAF Stability and Control Datcom (reference 68) as well as other related sources. Contained also in Volume III is the information necessary for the effective implementation of STAMP as a preliminary design and data analysis tool. Finally, comprehensive methods validation studies are presented for each of the three STOL powered lift systems being considered: the internally ducted jet, externally blown jet flap, and mechanical flap system with vectored thrust.

As a more detailed introduction to this volume (i.e., Volume I), the reader's attention is drawn to the fact that several analytical methods, each of which has the capability to evaluate the aerodynamic characteristics of a particular STOL aircraft component, and several interference methods to account for the influence of one component on another, are described herein.

These methods include:

- The Elementary Vortex Distribution (EVD) Jet-Wing Lifting Surface Theory
- The Ground Effect Method (an extension of the EVD method)
- The Jet-Wing Flow Field Method
- The Vectored Jet Flow Field Method
- The Modified Slender Body Fuselage Method
- The Empennage Method

In general, these methods are distinguished from previous analytical aerodynamic analysis techniques by their ability to predict the aerodynamic characteristics, not only of conventional or STOL aircraft, but also of STOL aircraft under conditions in which aerodynamic/propulsive interactions or interferences might be important.

An essential ingredient in the evaluation of the aerodynamic characteristics of jet-flap concepts is a recently developed lifting surface theory for jet-wings which is based on the finite element scheme - the method of Elementary Vortex Distribution or the EVD method. This method utilizes a set of independent but overlapped elementary horseshoe vortex distributions to represent the wing and jet sheet on which are satisfied a set of mixed-type boundary conditions. The solution includes chordwise and spanwise loading distributions, from which sectional and total aerodynamic quantities (e.g., lift, pitching moment, induced drag) are derived. The present method, which is applicable to jet-wings of arbitrary planform, camber, twist, partial-span flaps, and arbitrary trailing-edge jet-momentum distribution, reduces to a conventional lifting surface theory when the jet momentum is zero.

Stability and control coefficients and derivatives associated with a limited range of motions of the wing can all be evaluated with the EVD method. In addition to static longitudinal and lateral characteristics, dynamic derivatives associated with pitching, rolling, yawing, and sideslipping can also be evaluated on the basis of quasi-steady assumptions. Proximity to the ground can be considered with a mathematical model consisting of the

basic EVD jet-wing and its image. The resulting vortex distribution in ground effect is, of course, a linear function of, for example, angle of attack. A second-order correction to the aerodynamic loading has, however, been applied. Although this provides better agreement with exact theories and experimental data, it is not completely satisfactory. It is concluded that scope exists for the improvement of the ground effect method and suggestions to this effect are mentioned.

The capability to consider mechanical flap systems with vectored thrust is partly the result of the work of P. T. Wooler (reference 55 and 56), who has developed a method for calculating some of the aerodynamic features of a circular jet issuing into a uniform freestream. The approach utilizes a sink-doublet model to describe the flow external to the jet. The equations of continuity and momentum for the inner flow of the jet are developed in terms of an unknown rate of entrainment and arbitrary cross-sectional jet shape or envelope. These equations are solved not only for the singularity strength but also the trajectory of the jet. To solve these equations, it is still necessary, however, to postulate the cross-sectional shape of the jet and to establish the coefficients in the empirical equations for jet entrainment and the so-called cross-flow drag force. The latter is assumed to act perpendicular to the local jet centerline direction and, along with the freestream momentum entrainment contribution, is assumed to supply the necessary force to produce a centripetal acceleration of the local jet mass, thus causing the jet to bend. In general, the necessary coefficients are chosen to give a good correlation with available test data for jet trajectories.

Although there are a number of simplifying assumptions involved in the Wooler approach, good agreement has nevertheless been obtained from the results of this simple method and the experimental data for single jets emerging from infinite flat plates and from wings. For the type of STOL aircraft under consideration the efflux of the vectored jet system is unlikely to be in close proximity to any aircraft component. Hence, the jet trajectory, for example, can be assumed to be independent of the wing and the associated aerodynamic interference effects can be interpreted in terms of superimposed jet induced downwash fields which are akin to camber and angle of attack changes. Thus the

aerodynamic interferences can be evaluated, in the case of the wing, with the use of the aforementioned EVD lifting surface theory.

In addition to the aerodynamic characteristics of a jet-wing or the aerodynamic/propulsion interferences associated with the wing/vectored jet combinations, it is also necessary to consider the contributions of other aircraft components to the overall aerodynamics of a STOL aircraft. The capability to undertake this task is provided through a series of so-called interference techniques. The techniques depend to a large extent on the evaluation of the flow fields induced either by a jet-wing or vectored jet system. With the flow fields known, the aerodynamic characteristics of the fuselage and empennage can be readily determined providing the mutual interaction between these component and the jet-wing-wake are neglected. Fortunately, satisfactory results can be obtained on the basis of this assumption. Methods for predicting the contributions of the empennage and fuselage to overall stability and control characteristics based on this procedure are, therefore, presented herein.

## 2.0 INTERNALLY DUCTED AND EXTERNALLY BLOWN JET FLAPS

Since the aerodynamic characteristics of externally blown jet flaps tend to be closely associated with those of pure jet-flap high lift systems (e.g., internally ducted jet flap), jet flap or jet-wing theory, together with the development of theoretical methods to calculate flow fields and the contributions of other aircraft components (i.e., fuselage and empennage) to aircraft stability and control characteristics are subjects of direct interest and will be considered in later sections. Some elaboration of the approach used to evaluate the aerodynamic characteristics of externally blown jet flaps and internally ducted jet flaps, which are discussed in detail in Volume III, is desirable before discussing the theoretical methods that have been formulated as a framework to the development of prediction techniques.

To introduce the basic aerodynamic concepts of externally blown jet flaps, it is helpful to consider first the behavior and influence of a single jet directed towards a slotted flap system. Typically, the jet efflux distorts rapidly into a flat jet sheet as the flap deflects the jet flow and guides it over and/or under the flap. From the trailing edge of the flap, this jet sheet is deflected downstream by the freestream flow. Flow visualization studies indicate that the downstream deviation of the jet sheet is analogous to that of basic jet-flap schemes. Furthermore, experimental studies associated with the development of a transport aircraft incorporating the externally blown jet flap also indicate that most of the aerodynamic problems of consequence are similar to those encountered with internally ducted jet-flap systems. For example, both the downwash,  $\epsilon$ , and its rate of change with angle of attack,  $\frac{d\epsilon}{d\alpha}$ , increase steadily with the so-called jet momentum coefficient,  $C_J$ , affecting even high horizontal tail locations. The trimming power of a conventional horizontal tail has been found to be inadequate due to the large pitching moments involved. There is also experimental evidence of large rolling moments due to sideslip generated at high flap and/or jet deflections and high thrust levels. This effect can be alleviated by the addition of dihedral and sweepback, but the reduction from sweepback has been found not to rise steadily with increasing lift as would be deduced from conventional arguments. Sweepback has also been found to cause substantial increases in yawing moment and side force derivatives due to sideslip as a result of sidewash variations

over the fuselage and vertical tail.

The effects of ground proximity on all concepts which utilize the jet flap principle result in significant reductions in lift curve slope and stalling incidence if the jet momentum or jet angle relative to the wing is sufficiently large to cause jet impingement on the ground. The influence of the ground does, of course, lead to a constraint on the jet path which, in turn, has been shown to drastically reduce the downwash aft of the wing even at high horizontal tail positions.

It has been suggested that the jet-flap effect is likely to be responsible for the major part of the aerodynamic/propulsive interaction associated with the externally blown jet flap, at least insofar as the overall aerodynamic characteristics of the wing and the contributions to them of the fuselage and empennage are concerned. If this were so, this jet flap-theory could provide the theoretical framework for the development of suitable analytical engineering methods. There are, of necessity, some assumptions in existing jet-flap theories which could be strongly criticized. Fortunately, the assumptions that the momentum flux along the jet is constant and that the jet is locally inclined at only small angles to the undisturbed freestream flow, have been supported by its successful application to the analysis of basic jet-flap schemes. The application of jet flap theoretical methods to externally blown jet flaps would, however, involve a number of additional assumptions which, though possible as a means of making the problem tractable, would have to be justified on fundamental grounds. For example, there would be little justification for neglecting the presence of the jet beneath the wing or its entrainment properties. In addition, the application of jet-flap theory would require the postulation of a physically acceptable momentum distribution at the trailing edge. A clarification of the fundamental mechanism by which the jet is turned and spread would be valuable for this purpose. Despite all these misgivings, comparisons (reference 1) with experimental results so far suggest that jet-flap theory provides a realistic and useful working basis for the prediction of externally blown jet-flap aerodynamic characteristics.

Thus, the analogy between the externally blown jet flap and internally ducted jet flaps has been introduced. Also, jet-flap theory would appear to

have some practical value in the development of techniques to predict the aerodynamic performance and stability and control characteristics of both concepts and justify further refinement and extension.

## 2.1 BACKGROUND

### 2.1.1 The Basic Jet Flap High Lift Concept

In recent years, both commercial and military planners have shown an increasing interest in the potential advantages inherent in aircraft which possess a short field operational capability. Such aircraft would have to be economical, safe, have an acceptable noise level, and, in the case of a commercial aircraft, achieve public acceptance comparable to or better than conventional aircraft. For a short takeoff and landing (i.e., STOL) performance to be possible, one obvious necessity is a means for the generation and control of very high lift coefficients. Although a large number of STOL high lift concepts, each one possessing certain intrinsic merits, have been conceived during the past several decades, three main trends can hitherto be seen. In one, a small fraction of the energy available from the propulsive system is used to provide boundary layer control so that the ultimate theoretical performance of an ideal wing can be almost, but not quite, realized. In the other two, there has been a growing tendency towards the synthesis of the propulsive system with the airframe. Of these, the development of gas turbines has reached a state where their employment for the generation of pure jet lift seems attractive. Thus, several STOL high-lift concepts have emerged which depend upon nothing more than the use, for example, of light-weight lift engines or the mechanical vectoring of the propulsive engine momentum. In other words, it is the underlying intention that the generation of the additional lift required for STOL operation be achieved independently of the wing. In the other, a significant increase in aerodynamic lift over and above the lift component of the jet reaction is realized with the complete integration of the propulsive and lifting systems. One such example is the pure jet flap.

The term jet flap has been used to indicate that the entire propulsive jet is directed to leave the trailing edge of an airfoil or wing as a thin sheet at an angle of inclination to the mainstream. Because of the jet, an asymmetrical flow pattern is generated which provides additional circulation. This contributes appreciably to the total lift which includes the direct lift associated with the vertical component of the jet momentum. The propulsive



thrust lies between the corresponding horizontal component and the full jet momentum. Although novel, the underlying physical principle of the jet flap is by no means new, for the increase in circulation lift can be attributed to the effects of boundary layer control and to what is sometimes termed supercirculation or circulation control. The latter is commonly found as a side effect in experimental investigations on boundary layer control by blowing over the upper surface of conventional trailing edge flaps. Since boundary layer control in its original and concise conception was thought of as a means of raising the lift coefficient of a wing to the theoretical predicted value, circulation control, on which the jet flap principle is based, is regarded to start where boundary layer control ends. The relative magnitude of the contribution resulting from either one is largely dependent on the magnitude of the jet momentum.

As mentioned above, the discovery of supercirculation was a byproduct of boundary layer control studies. Although Shubauer<sup>3</sup>, Hagedorn and Ruden<sup>4</sup> were responsible during the 1930's for some of the first experimental results on supercirculation, it was not until 1952, according to Davidson<sup>5</sup> and Stratford<sup>6</sup>, that the significance of supercirculation and its practical application in the form of the pure jet flap was truly recognized. In France, the discovery of supercirculation was made independently. The first relevant French publication was by Poisson-Quinton<sup>7</sup> in 1948 while, in late 1954, Jousserandot<sup>8</sup> described the results of extensive experiments in which the active principle of the jet flap was all but isolated. More detailed experimental investigations of the jet-flap mechanism were conducted by Dimmock<sup>9</sup>, Williams and Alexander<sup>10</sup>, and Lowry and Vogler<sup>11</sup> during the early 1950's. Experimental studies that followed were either directed towards providing data for preliminary design activities or to assist in the development and validation of analytical methods. Notable among these are the wind tunnel tests by Gainer<sup>12</sup> on a semi-span rectangular jet-wing model of aspect ratio 8.3, the tests of Williams and Alexander<sup>13</sup> on a similar model of aspect ratio 6, the six-component tests of a complete jet-flap model with variation of aspect ratio, dihedral, and sweepback by Butler et al<sup>14</sup>, and the experimental investigation conducted by Das<sup>15</sup> of jet wings of rectangular and swept planforms. Much of British research on jet flaps during this period led to the design, manufacture, and testing of what is now known as the BAC H-126

jet flap research aircraft which was built to flight test the jet-flap principle (reference 69).

### 2.1.2 Applications of the Jet Flap Principle

It is unlikely that the pure jet-flap principle will ever be adopted for STOL aircraft unless it is possible to control the jet deflection during flight and provide an alternative means of generating lift in the event of a failure of the jet blowing system. Several concepts (figure 2.1) have, therefore, been conceived in an attempt to provide, in part, a practical solution to these problems. For example, the gas can be ducted through the wing to a slot at the knee of a flap which is used for varying the jet angle, or the gas can be ducted to the trailing edge where a jet control flap or plug will accomplish the same task. In general, the jet flap/mechanical flap combination or jet augmented flap is aerodynamically superior to pure jet-flap systems, providing that the tangential blowing at the knee of the flap ensures a proper flow over the flap at any desired deflection. It should be realized, however, that several additional factors have to be considered before any of these jet-flap schemes, often referred to as "internal flow" systems, can be regarded as ultimate solutions to problems associated with the adoption of the jet-flap principle. It has been shown, for example, that the aerodynamic performance advantages attributed to the utilization of a number of basic jet-flap concepts may be appreciably reduced in practice when consideration is given to structural, power-plant, and aerodynamic stability and control problems.

It must be realized that the unquestioned adoption of the jet-flap principle for STOL high lift concepts must be met with some reservation unless a practical solution to a number of technical problems is available. Several alternative and technically feasible concepts that provide an attractive solution to such problems have been conceived in recent years. For example, the underslung podded engines of a jet aircraft can be arranged such that the jet efflux is directed toward a slotted flap system which in turn deflects the jet flow and guides it over and/or under the flap to form a flattened jet sheet at the trailing edge. Alternatively, either circular or fishtail nacelles could be mounted above the wing for blowing over a mechanical

flap system. Such "external flow" systems (figure 2.1 ) have the advantage that the reduction in propulsive efficiency resulting from duct losses and the increased aircraft structural weight associated with internally ducted systems can be eliminated. This is not without sacrificing, however, the advantages of cross ducting, which, in the event of an engine failure, can be used to reduce control requirements. Although duct losses can have a significant effect on the installed thrust required for a specified STOL mission, several jet-flap "internal flow" concepts which utilize the jet-efflux to give augmentation of wing lift and jet thrust, thus compensating for any reduction in overall performance due to such losses, have been proposed. Aerodynamically, there is no doubt that ejector or augmentor jet flaps will realize a high lift efficiency if there is the slightest augmentation in jet momentum, since this will result in increased supercirculation and reaction lift. What should not be overlooked, however, is an increase in "ram" drag resulting from the ejector secondary or entrained flow from the freestream, although this might be partly compensated for by the reenergizing of the wing boundary layer.

### 2.1.3 Theoretical Treatments of the Jet Flap

As might be expected, the pioneering experimental work on jet flaps stimulated a number of theoretical investigations into idealized jet-wing systems. Quite early, a simple but rigorous analysis by Maskell and Gates<sup>16</sup> established the properties of the thin two-dimensional jet in inviscid flow and the overall momentum relations satisfied by the two-dimensional jet-flap system. The first analytical treatments of the two-dimensional jet-flap airfoil were based on semi-empirical arguments and an analogy between the jet and a conventional mechanical flap. Subsequent mathematical treatments, in which the jet sheet is assumed infinitely thin but possesses finite momentum flux independent of the region under consideration, have been largely based on the usual approximations associated with small perturbation theory. Spence<sup>17,18</sup>, for example, has obtained a solution by adopting the classical approximations of linearized thin airfoil theory. The effect of the jet on the outer flow is assumed analogous to that which would cause a surface of discontinuity of pressures emanating from the trailing edge and forming an extension of the airfoil to downstream infinity. Both the airfoil and jet can, therefore, be considered as a sheet of vorticity.

The vorticity along the airfoil and the jet must, however, be such as to make them streamlines (i.e., "kinematic" boundary condition). On the jet sheet, a "dynamic" boundary condition which expresses its state of equilibrium, namely, that the pressure difference across the jet is proportional to its local curvature and momentum, must be introduced. These boundary conditions produce integro-differential equations in two variables, the vorticity along the airfoil and the slope of the jet. The solution of these equations becomes tractable if the jet is shallow, in which case by introducing the approximations of small perturbations inherent in the airfoil theory, both the kinematic and dynamic boundary condition can be reduced to a simpler linearized form and transferred to a semi-infinite line parallel to the undisturbed flow and passing through the trailing edge. For the purpose of evaluation of the perturbation velocity it is further assumed that the vortex distribution representing the jet and airfoil are aligned in the undisturbed-stream direction. This, in part, leads to a single integro-differential equation for the slope of the jet. On the basis of these considerations, Spence obtains the solution of this simple mixed-boundary-value problem by finally considering the vortex distribution representing the airfoil and jet to be expressed as a Fourier series, together with functions possessing the correct (i.e., logarithmic) singular behavior at, for example, the trailing edge. The problem is finally reduced to a system of linear equations which can be solved without difficulty by a computer. The overall lift and pitching moment in the most general case can be deduced by a linear combination of three fundamental solutions. The lift, for example, can be determined by the relation:

$$c_l = \frac{\partial c_l}{\partial \alpha} \alpha + \frac{\partial c_l}{\partial \delta_f} \delta_f + \frac{\partial c_l}{\partial \delta_j} \delta_j$$

where the derivatives  $\frac{\partial c_l}{\partial \alpha}$ ,  $\frac{\partial c_l}{\partial \delta_f}$ , and  $\frac{\partial c_l}{\partial \delta_j}$  are, respectively, the fundamental solutions for a flat plate at an angle of attack  $\alpha$ , a flap set at an angle  $\delta_f$ , both with simple blowing from the trailing edge of the flap, and the jet forming an angle  $\delta_j$  relative to the flap. Useful interpolation formulas derived by Spence for some of these derivatives are summarized below:

$$\frac{\partial c_\ell}{\partial \alpha} = 2\pi(1 + 0.151 c_\mu^{1/2} + 0.219 c_\mu) \quad (2.1)$$

$$\frac{\partial c_\ell}{\partial \delta_J} = 2 (\pi c_\mu)^{1/2} (1 + 0.151 c_\mu^{1/2} + 0.139 c_\mu)^{1/2} \quad (2.2)$$

where  $c_\mu$  is the jet momentum coefficient. From a global and local balance of forces on the airfoil, taking into account leading edge suction, it can be shown (reference 17) that the derivatives given by equations (2.1) and (2.2) are related, that is:

$$\left(\frac{\partial c_\ell}{\partial \delta_J}\right)^2 = 2c_\mu \left(\frac{\partial c_\ell}{\partial \alpha} - \frac{c_\mu}{2}\right) \quad (2.3)$$

Spence's theoretical method is limited to the calculation of the pressure distribution, jet shape, and overall aerodynamic forces and moments of thin jet-flapped airfoils only. A separate method has been developed by Küchemann<sup>19</sup> for evaluating the pressure distribution taking into account thickness and camber effects, but this method requires the overall lift and thrust to be specified. An extension of this method to the problem of finite-aspect ratio jet-wings also is presented in reference 19. This has provided what may be considered as the first method for calculating the pressure distribution of three-dimensional jet-wings.

Spence's two-dimensional formulation has been extended to include three-dimensional effects by Maskell and Spence<sup>20</sup>. They considered a thin jet-wing of finite aspect ratio in an inviscid stream. The transverse transport of momentum within the jet was neglected which is tantamount to assuming that no significant rolling-up of the jet sheet takes place. This simplification is found particularly useful since it implies that the streamlines of the jet flow stay permanently in their plane of emission, and as a consequence, the boundary conditions for each streamwise section are identical to the two-dimensional ones. In principle, equations (16), (17), and (18) of reference 20 are sufficient to render  $\gamma(x,y)$ , the distribution of elementary horseshoe vortices, determinate. Unfortunately, the double integral equation (i.e., equation (18)) for the upwash  $\bar{w}_1(x,y,z=0)$  induced by the bound and trailing vorticity is intractable. Maskell and Spence, therefore, take the limit of equation (18) as  $x$  tends to infinity for the special case for which camber

and twist are zero. Furthermore, they prescribe an elliptic spanwise distribution of both wing chord and jet momentum with constant jet angle over the span. They define  $\bar{w}_i(x)$  as the upwash due to the trailing vorticity and denote its value in the limit as  $x$  tends to infinity by  $\bar{w}_{i\infty} = -U\alpha_{i\infty}$  which is independent of  $y$  because of the special spanwise loading considered. Maskell and Spence also derive (see Section (2.2.4)) exact expressions for the total lift and induced drag in terms of  $\bar{w}_i$  which is found by making an arbitrary assumption as to how  $\bar{w}_i(x)$  varies between  $\bar{w}_i$ , its value at the wing, and  $\bar{w}_{i\infty}$ . Since  $\bar{w}_{i\infty}$  is taken to be independent of  $x$  it is, in effect, assumed that the trailing vorticity system induces a change of incidence but not camber. Maskell and Spence make two alternative assumptions for the variation of  $\bar{w}_i(x)$  and refer to them as the first and second interpolations. The first interpolation is so chosen as to make use of the known two-dimensional jet-flap solution thus enabling the total lift to be expressed by the following relation:

$$C_L = \frac{c_{\ell} (AR + \frac{2}{\pi} C_J)}{AR + \frac{2}{\pi} \frac{\partial c_{\ell}}{\partial \alpha} - 2(1 + \sigma)} \quad (2.4)$$

where  $\sigma$  is a factor relating the induced downwash,  $\alpha_i$ , at the wing to  $\alpha_{i\infty}$  far downstream,  $\sigma = 1 - \frac{1}{2} \frac{\alpha_i}{\alpha_{i\infty}}$ . It will be noted that the first interpolation gives the conventional result (i.e.,  $C_L = \frac{2\pi AR \alpha}{AR + 2}$ ) in the limit  $C_J=0$ , if  $\sigma = 0$  and  $\partial c_{\ell} / \partial \alpha = 2\pi$ . This agreement with Prandtl's theory occurs because the bound vorticity due to the induced incidence is assumed to be on the wing only. In effect, this is equivalent to disregarding the fundamental principle of the jet flap; that the jet can support a pressure difference. The second interpolation is based on the assumption that  $\bar{w}_i(x)$  is linearly related to the total upwash. Maskell and Spence argue that, for small  $C_J$ , the total lift is still given by equation (2.4) and use the second interpolation to evaluate  $\sigma$ . After making further approximations, it appears that  $\sigma$  depends solely upon the parameters  $(C_J/\pi AR)$  and  $\alpha_{i\infty}/(\delta_J + \alpha) = \lambda$ , say, and can be expressed as follows:

$$\sigma = \frac{(1 - \lambda) \left( \frac{C_J}{\pi AR} \right)}{\lambda (1 - \lambda) \left( \frac{C_J}{\pi AR} \right)} \quad (2.5)$$

where

$$\lambda = \frac{2 c_{\ell} / (\delta_J + \alpha)}{AR + 2 \frac{\partial c_{\ell}}{\partial \alpha} - 2\pi(1 + \sigma)}$$

For most practical purposes it is permissible to treat  $\sigma$  as a constant equal to zero when the aspect ratio is greater than 4. These assumptions nonetheless can be strictly valid only in the limit  $C_J$  equal to zero. With this approximation, the derivatives  $\frac{\partial C_L}{\partial \delta_J}$  and  $\frac{\partial C_L}{\partial \alpha}$  for the finite wing are obtained by multiplying the corresponding two-dimensional values discussed earlier by the factor:

$$F(AR, C_J) = \frac{AR + \frac{2}{\pi} C_J}{AR + 2 + 0.604 C_J^{1/2} + 0.876 C_J} \quad (2.6)$$

For the elliptic wing, Maskell<sup>20</sup> by a general momentum analysis, was also able to establish that the induced drag coefficient  $C_{D_i}$ , or more specifically the deficiency  $(C_J - C_T)$  of the net thrust  $C_T$ , is simply given by:

$$C_{D_i} = \frac{C_L^2}{\pi AR + 2 C_J} \quad (2.7)$$

Based on Multhopp's<sup>21</sup> lifting surface theory, Das<sup>15</sup> has developed a method for predicting the spanwise and chordwise loading distribution of jet-flapped wings. Multhopp and hence Das employ the so-called influence function technique which requires the chordwise vortex distribution to be expressed by a linear superposition of a set of fundamental distributions with unknown coefficients. The unknown coefficients are normally determined through the application, at selected points, of the known boundary conditions. Although the calculation of the influence functions, that is, the downwash due to each fundamental vortex distribution, demands considerable effort, they can

be determined in advance once and for all. Accordingly, Das assumed the vortex distribution along the wing chord to be represented by the first three terms in Birnbaum's expression for the chordwise vortex or loading distribution of a two-dimensional thin airfoil, and the vortex distribution along the jet to be represented by the first three terms of Spence's jet-flap solution. From there on, an approximate procedure is introduced, in which jet-flap characteristics derived by Spence are used to reduce the independent unknown coefficients to three. As a result, the method requires only three points along a chordwise section to satisfy the boundary conditions, these being at the 1/4 chord, 3/4 chord, and infinity downstream. The particular method employed by Multhopp in the spanwise integration of the downwash integral dictates, for a given number of spanwise stations, the spanwise location of the pivotal points at which the boundary conditions are to be satisfied. Inasmuch as there is no limitation to the number of spanwise stations selected, Das' method is claimed to be applicable to a jet-wing system of arbitrary planform geometry and spanwise distribution of jet momentum and jet deflection. Obviously this is not entirely true. The selection of spanwise stations and the assumed spanwise variation of bound vorticity might not, for example, be satisfactory for the solution of some partial span blowing problems. In addition, since only three chordwise pivotal points are selected, it is unlikely that the effects of camber or flaps can be predicted with sufficient accuracy.

The rheoelectric analogy technique has also been successfully applied to the three dimensional jet-flap problem by Malavard<sup>22</sup>. Based on the same linear approximations adopted by Das, the problem is reduced to one of finding a harmonic function for the perturbation velocity potential set up by the presence of the wing and jet sheet. The perturbation velocity may then be found from the velocity potential. This velocity potential is measured by Malavard as an electric potential in the electrolytic tank. Although this approach can produce both spanwise and chordwise loading distributions, it does require the facilities of an electrolytic tank.

In recent years, several new theoretical developments have emerged. Erickson and Kaskel<sup>23</sup> have developed a method for low aspect ratio rectangular jet-wings with full span blowing. A uniformly valid asymptotic solution has



been constructed by Tokuda<sup>24</sup> for high aspect ratio wings using the method of asymptotic expansions. A useful method has been developed by Lopez<sup>1</sup> for moderate to large aspect ratio wings with arbitrary jet momentum distributions. Other methods for high aspect ratio jet-flapped wings have been developed by Lissaman<sup>70</sup> and by Kerney<sup>71</sup>.

Despite the linearized nature of the theoretical methods described above, the lift predictions agree quite well with experimental results for full-span trailing-edge blowing. As mentioned earlier, some difficulties still arise in applying them to the case of part-span blowing over flaps. Primarily because of losses due to viscous effects, these methods have also been found to markedly overestimate thrust.

To date, there have been several experimental and theoretical studies conducted to investigate the effects of ground proximity on jet-flapped wings. Insofar as theoretical methods are concerned, however, only a simple mathematical representation of the two-dimensional jet-flap airfoil has been formulated<sup>25</sup>. The flow behavior with jet-flap wings of finite aspect-ratio has proved substantially different from that observed in early small scale two-dimensional tests, primarily because of so-called spanwise venting. There is, as yet, no realistic two or three-dimensional theoretical treatment for jet-wings under conditions of jet impingement on the ground. The prediction of certain jet-flap aircraft stability derivatives has, to date, been made by simple modifications to the method of Maskell and Spence. Taylor<sup>26</sup> has undertaken a theoretical investigation of the longitudinal stability and control derivatives and response characteristics of jet-flap aircraft, and Thomas and Rose<sup>27</sup> have developed methods for predicting rotary lateral stability derivatives. All these studies were restricted to wings with an elliptical distribution of both lift and jet momentum.

## 2.2 THE ELEMENTARY VORTEX DISTRIBUTION JET-WING LIFTING SURFACE THEORY

In the preceding section, the concept of the jet flap or jet-wing has been introduced. It is understood that the presence of a jet sheet behind the trailing edge of a wing could greatly influence the flow external to the jet, thus producing induced pressure forces on the wing in both the thrust and lift direction. In addition to the magnitude and spanwise distribution of jet momentum at the trailing edge, the location or shape of the jet determines the magnitude of these changes. The shape of the jet is, however, influenced by the configuration and attitude of the wing relative to the free-stream. There is also experimental evidence that this interaction between the jet and the lifting system is sufficiently significant that any analysis of the jet-wing problem inherently requires that the wing and jet be treated as an integrated system.

Several applications of the jet-flap principle have also been discussed in the previous section. Since all these schemes exhibit a jet sheet at the trailing edge, which characteristically has the same effect of inducing supercirculation (pressure lift), the authors are of the opinion that jet-flap theory could provide the theoretical framework for the development of suitable analytical methods for predicting their aerodynamic characteristics. In other words, all these jet-flap schemes could be considered to be equivalent to a basic jet-wing system with a thin jet sheet of known strength emerging from the trailing edge. Local aerodynamic disturbances or effects associated with some of these schemes would have, however, to be considered separately.

Although the "general" aerodynamics of basic jet-flapped wings is now reasonably well established, there is clearly scope for further theoretical developments aimed at specific problems. The jet-wing lifting surface theory described in this report has, therefore, been developed to meet the need for an analytical method sufficiently versatile enough that the aerodynamic performance and stability and control characteristics of complicated jet-wing systems can, with confidence, be predicted.

## 2.2.1 Theoretical Interpretation of the Jet-Wing Problem

Thus far, theoretical treatments of jet-flap aerodynamic problems have been based on the method of small perturbations. The method presented in this report employs this approximation. The approach adopts a theoretical model similar to that suggested by Maskell and Spence<sup>20</sup>. In the following paragraphs an interpretation and generalization of their approach is, therefore, made.

### 2.2.1.1 Statement of the Problem

The basic jet-wing system considered in the present analysis is illustrated in figure (2.2) , in which the essentials involved in the mathematical formulation are displayed. As depicted in this figure, the jet-wing system is placed in an inviscid, irrotational, and incompressible flow of velocity  $U$  and density  $\rho$ . It is assumed that the jet emerges from the trailing edge and forms an extremely thin and curved jet sheet which extends to downstream infinity. Unlike the two-dimensional jet flap, the jet sheet will never completely turn to the free-stream direction.

A right-hand rectilinear coordinate system will be used in the analysis. Its origin has been chosen to coincide with the apex of the wing. The  $x$ -axis is parallel to the free-stream direction and positive downstream. The wing is defined by the geometric characteristics of its projection on the horizontal plane  $xOy$ . The wing has a span  $b$ , an area  $S$ , a mean aerodynamic chord (MAC)  $\bar{c}$ , and an aspect ratio  $AR$ . In general at any spanwise station, the wing section leading-edge and trailing-edge  $x$ -coordinates and chord are denoted by  $x_l(y)$ ,  $x_t(y)$ , and  $c(y)$ , respectively. The local incidence or slope of the wing is denoted by  $\epsilon_c(x,y)$ , twist,  $\alpha_t(y)$ , trailing edge flap deflection,  $\delta_f(y)$ , leading edge flap deflection,  $\delta_s(y)$ , etc.

The conditions of jet emission are selected so that at each point along the trailing edge of the wing the  $y$ -component of jet momentum is assumed to be negligibly small compared to the  $x$ - and  $z$ -components. In the plane  $y=\text{constant}$ , the direction of the jet is defined by the angle  $\theta(y)$  formed by  $V_j(y)$ , the

resultant mean velocity vector in this plane, and the free-stream direction. The angle which  $V_j(y)$  forms with the tangent to the camber line at the trailing edge is designated by  $\delta_j(y)$ . Hence,  $\theta(y) = \delta_j(y) + \epsilon_t(y)$  where  $\epsilon_t(y)$  is the local slope of the wing at the trailing edge (i.e.,  $x_t(y)$ ). Since the jet parameter which governs the aerodynamic characteristics of any jet-wing system has been found to be the jet momentum rather than the velocity, it will become convenient to introduce non-dimensional coefficients for the jet momentum. Thus, a sectional jet momentum coefficient is defined as:

$$c_{\mu}(y) = \frac{J(y)}{q c(y)} \quad (2.8)$$

where  $q$  denotes the free-stream dynamic pressure, that is  $1/2 \rho U^2$ , and  $J(y)$  is the sectional jet momentum flow; that is,

$$J(y) = \rho_j(y) V_j^2(y) d_j(y) \quad (2.9)$$

in which  $\rho_j(y)$  and  $d_j(y)$  are respectively the density and thickness of the jet. Integrating the total spanwise distribution of  $J(y)$  yields the total momentum of the jet,

$$\bar{J} = \int_{-b/2}^{b/2} J(y) dy \quad (2.10)$$

and hence the total jet momentum coefficient is defined as:

$$C_J = \frac{\bar{J}}{qS} = \frac{1}{S} \int_{-b/2}^{b/2} c(y) c_{\mu}(y) dy \quad (2.11)$$

### 2.2.1.2 Basic Assumptions

In establishing a theoretical model (see Section 2.2.1.3) for the analysis of the flow around the jet-wing system several assumptions, briefly discussed below, will be adopted.

By adopting the classical approximations normally associated with linearized lifting surface theories it is possible to assume that the effect of wing thickness is negligible and that the local incidence of the wing which

is associated with its mean camber, twist, dihedral, etc., is small. It will not be essential, however, to assume that the variation of local incidence is continuous. For example, a sudden jump in incidence that would result from the deflection of an ideal leading or trailing edge flap will be permissible.

The jet, as mentioned earlier, is assumed to emerge from the trailing edge as a thin jet sheet which extends downstream to infinity. The flows both within and outside the jet are considered to be incompressible, inviscid, and irrotational. Entrainment into and the transverse transport of momentum within the jet will be neglected. The latter is tantamount to assuming that no significant rolling-up of the jet sheet takes place. This simplification is found particularly useful since it implies that the streamlines of the jet flow stay permanently within the plane of emission, that is, the plane  $y=\text{constant}$ . Although it might be argued that either near the edges of the jet close to the wing or further downstream the rolling-up might become significant, it is likely that the contribution to the total downwash will be small. When the jet is thin and the mean jet velocity is substantially greater than the external flow velocity at the boundaries of the jet, then the jet momentum  $J(y)$  may be considered constant along the jet if the thickness also remains constant. In fact, it is assumed that the jet is represented by an infinitely thin sheet while within any plane  $y=\text{constant}$  the jet momentum is finite. Furthermore, the jet deflection angle  $\theta(y)$  will also be assumed to be small. As will be discussed in more detail in the following paragraphs, it is thus possible to replace the surface constituted by the jet sheet by its projection on the plane  $xOy$ .

### 2.2.1.3 Formulation of the Theoretical Model

Based on the above assumptions, the jet-wing problem may be treated as a potential flow problem for which the small perturbation concept also applies. In other words, the problem is to look for a perturbation potential  $\phi$  such that  $\phi$  satisfies the Laplace equation

$$\nabla^2 \phi = 0 \quad (2.12)$$

and that the velocity field

$$\vec{q} = (U + u, v, \bar{w}) = U \vec{e}_x + \nabla\phi \quad (2.13)$$

derived therefrom satisfies the boundary conditions on the wing as well as on the jet. In the above,  $\vec{e}_x$  indicates a unit vector in the x-direction; and  $u$ ,  $v$ , and  $\bar{w}$  are respectively the perturbation velocities in the  $x$ ,  $y$ , and  $z$  directions.

The boundary condition on the wing portion of the jet-wing is simply the streamline criterion that the flow be tangential to the body surface. This can be simply expressed as

$$\frac{w}{U + u} = \tan \epsilon \quad (\text{on the wing}) \quad (2.14)$$

where  $w$  now represents the downwash in contrast to  $\bar{w}$  for the upwash ( $w = -\bar{w}$ ).

To construct the boundary condition on the jet, an alternative approach is necessary. Considering the potential flow inside the jet in addition to that outside and on requiring the pressure to be continuous across the jet boundaries, Spence<sup>17</sup> has derived a relationship for the pressure or velocity jump across a two-dimensional jet. Maskell and Spence<sup>20</sup> subsequently extended this to a three-dimensional jet sheet. In view of the assumption neglecting the transverse flow, each streamwise section of the jet may be considered isolated from its adjacent sections. In other words, the two-dimensional relationship for the jet boundary condition still applies. Instead of going through a review of Spence's derivation, the same condition will be derived by a simple physical argument.

Consider an element of the jet, depicted in figure (2.2) which subtends an angle  $d\psi$  at its center of curvature and has a mean radius of curvature  $R$ . Since viscous forces resulting in entrainment have been neglected, the deflection of the jet can only be due to the centripetal action of a pressure force on the jet boundary. It can, therefore, be readily shown that,

$$p_2 - p_1 = \frac{J}{R} \quad (\text{on the jet}) \quad (2.15)$$

where  $p_1$  and  $p_2$  are the pressures on the upper and lower surfaces of the jet element.

In view of the irrotational character of the flow outside the jet, it can be easily shown using Bernoulli's equation that,

$$\Delta p = \frac{1}{2} \rho (V_1^2 - V_2^2) \quad (2.16)$$

where

$$\Delta p = p_2 - p_1$$

in which  $V_1$  and  $V_2$  are the total velocities parallel to the upper and lower surfaces of the jet. Hence, one can derive from equations (2.15) and (2.16) an expression for the external velocity jump across the jet boundaries, namely:

$$V_1^2 - V_2^2 = \frac{2J}{\rho R} \quad (2.17)$$

To complete the boundary conditions, a Kutta condition, namely that the pressure jump  $\Delta p$  across the boundary vanishes, must be satisfied at the trailing edge on those portions of the wing where there is no jet emission and downstream at infinity on the jet. To summarize,

$$\Delta p = 0 \left\{ \begin{array}{l} x \rightarrow \infty \text{ when } c_{\mu}(y) \neq 0 \\ x = x_t^-(y), \text{ when } c_{\mu}(y) = 0 \end{array} \right\} \quad (2.18)$$

where  $x_t^-(y)$  is used to indicate the  $x$  coordinate immediately before the trailing edge. The initial direction of the jet flow at the wing trailing edge is determined a priori, that is,

$$\frac{w}{U + u} = \tan \theta, (x = x_t^+(y), \text{ when } c_\mu(y) \neq 0) \quad (2.19)$$

where  $x_t^+(y)$  is used to indicate the  $x$  coordinate immediately after the trailing edge.

Equations (2.14), (2.17), (2.18), and (2.19) thus comprise a complete description of the boundary conditions. They appear to be generally true, irrespective of whether or not the wing incidence and the jet deflection are small, so long as both the wing and jet are thin and the transverse flow can be neglected.

Now, in principle, the jet-wing problem is governed by the Laplace equation together with the boundary conditions. It is still not known, however, where exactly the jet boundary condition (equation (2.17)) should be applied, because the location of the jet sheet cannot be determined beforehand. This so-called free-boundary problem, plus the nonlinearity involved in all the boundary conditions, presents a formidable task for the aerodynamicist.

### Linearization

In order to reduce the complexity of the problem, further simplification of the above equations is necessary. The simplification is achieved through the linearization of the boundary conditions. To do so, first of all, the perturbation velocities are assumed to be small. This is an acceptable condition since this inherently requires that all the incidences and deflections are assumed to be small. Secondly, the boundary conditions are assumed to be satisfied not on the actual boundaries but on their projections in the plane parallel to the free-stream, or more precisely, the  $z = 0$  plane. The latter assumption eliminates the difficulty associated with the uncertainty of the free jet boundary; it is expected to be approximately valid as long as the jet path stays shallow.



In view of the approximations adopted above, the wing boundary condition (i.e., equation (2.14)) can be expressed as,

$$\frac{w}{U} \approx \epsilon, \quad (z = 0, \text{ wing boundary}) \quad (2.20)$$

since the perturbation velocity  $u$  is neglected with respect to  $U$ , and  $\tan \epsilon$  is approximated by  $\epsilon$ .

Since it has been assumed that the curvatures  $\frac{1}{R(x,y)}$  and the slopes  $\frac{\partial \tilde{z}}{\partial x}(x,y)$  of the jet sheet are small, it can be shown that for any point on the jet,

$$\frac{1}{R} = \frac{\frac{\partial^2 \tilde{z}}{\partial x^2}}{\left[ 1 + \left( \frac{\partial \tilde{z}}{\partial x} \right)^2 \right]^{3/2}} \approx \frac{\partial^2 \tilde{z}}{\partial x^2} \quad (2.21)$$

and since the jet is also a streamline,

$$\frac{\partial \tilde{z}}{\partial x} \approx -\frac{w}{U} \quad (2.22)$$

where  $z = z(x,y)$  describes the actual location of the jet sheet. Furthermore, since it can be shown that  $V_1^2 - V_2^2 = 2U(u_1 - u_2)$ , in its linearized form, the jet boundary condition can be expressed as:

$$u_1 - u_2 \approx -\frac{J}{\rho U^2} \frac{\partial w}{\partial x} = -\frac{c(y)c_\mu(y)}{2} \frac{\partial w}{\partial x}, \quad (z = 0, \text{ jet portion}) \quad (2.23)$$

The remaining boundary conditions are easily reduced to

$$u_1 - u_2 \approx 0, \quad \left\{ \begin{array}{l} x \rightarrow \infty, \text{ when } c_\mu(y) \neq 0 \\ x = x_t^-(y), \text{ when } c_\mu(y) = 0 \end{array} \right\} \quad (2.24)$$

and

$$\frac{w}{U} \approx \theta, \quad \left( x = x_t^+(y), \text{ when } c_\mu(y) \neq 0 \right) \quad (2.25)$$

## Vortex Model

Since the primary objective of the jet-wing lifting surface theory, like that of any conventional lifting surface theory, is to derive the forces and moments acting on the wing rather than the potential or the velocity field throughout the entire surrounding space, it is only necessary to establish aerodynamic properties on the boundary. A successful means of fulfilling this requirement has been provided previously in several conventional lifting-surface theories. In these models, elementary horseshoe vortices are assumed to originate everywhere from the wing and extend downstream to infinity. They are bounded in the wing but are free to move behind the wing. In the jet-wing case, it has been suggested in the general formulation that the jet sheet may be replaced by a rigid membrane, in other words, an extension of the wing. Based on this analogy, it is most appropriate to assume that the horseshoe vortices also originate everywhere from the jet sheet. With the wing and jet both represented by a vortex sheet, the jet-wing problem simply becomes that of determining the vorticity distribution over these boundaries, or rather, their projections in the  $z = 0$  plane. The theoretical treatment of the horseshoe vortex scheme may be found in many treatises, such as Ashley and Landahl<sup>28</sup>. Only the most pertinent results or equations are to be adopted for application to the present jet-wing theory. If the horseshoe vortices of intensity  $\gamma(x,y)$  are distributed over the wing and jet boundaries in the  $z = 0$  plane, then the downwash  $w$  in the same plane induced by these vortices is given by the following equation

$$w(x,y) = -\frac{1}{4\pi} \int_{-b/2}^{b/2} \frac{d\eta}{(y-\eta)^2} \int_{x_l}^{x_t \text{ or } \infty} \gamma(\xi,\eta) \left(1 + \frac{x-\xi}{r}\right) d\xi \quad (2.26)$$

where

$$r = \sqrt{(x-\xi)^2 + (y-\eta)^2}$$

The upper limit in the  $\xi$ -integral is either  $x_t$  or  $\infty$  depending on whether or not  $c_u(\eta) = 0$ . The cross sign on the  $\eta$ -integral indicates that the Mangler Principle<sup>28</sup> value is to be taken; namely,

$$\int_a^b \frac{F(\eta) d\eta}{(y-\eta)^2} = \lim_{\epsilon \rightarrow 0} \left[ \int_a^{y-\epsilon} \frac{F(\eta) d\eta}{(y-\eta)^2} + \int_{y+\epsilon}^b \frac{F(\eta) d\eta}{(y-\eta)^2} - \frac{2F(y)}{\epsilon} \right] \quad (2.27)$$

Now the bound vorticity distribution will obviously give rise to a velocity jump across the vortex sheet; that is,

$$u_1 - u_2 = \gamma \quad (2.28)$$

The substitution of this relation into equation (2.23) reduces the jet boundary condition to the following

$$\frac{\partial w(x,y)}{\partial x} = - \frac{2}{c(y)c_\mu(y)} \gamma(x,y) \quad (2.29)$$

and the Kutta condition, equation (2.24), becomes

$$\gamma(x,y) = 0, \left\{ \begin{array}{l} x \rightarrow \infty, \text{ when } c_\mu(y) \neq 0 \\ x = x_t^-(y), \text{ when } c_\mu(y) = 0 \end{array} \right\} \quad (2.30)$$

The other two conditions, equations (2.20) and (2.25) remain unchanged.

Accordingly, the jet-wing problem involves the solution of the vortex intensity  $\gamma(x,y)$  on both the wing and the jet sheet subject to the boundary conditions, (2.20), (2.25), (2.29), and (2.30), in which the downwash  $w(x,y)$  is expressed in equation (2.26).

The aerodynamic loading on the wing,  $\Delta p = p_2 - p_1$ , is found to be directly proportional to  $\gamma$ ; namely,

$$\Delta p = \rho U \gamma \quad (2.31)$$

Incidentally, this relation follows the application of the Bernoulli equation and the velocity jump vorticity relation, equation (2.28). Linearization of

the Bernoulli equation is not required, for the second order quantity ( $u^2+v^2+w^2$ ) disappears in the equation for  $\Delta p$  on account of the flow symmetry inherently associated with the assumed vortex model. When the loading distribution is known, all the force and moment characteristics can be readily calculated through the chordwise and spanwise integration of the loading.

In conclusion, it is noted that although the boundary conditions are greatly simplified, they are still of a mixed type. In other words,  $w$  is specified in one region and  $\frac{dw}{dx}$  in the other. As is well known, mixed type boundary-value problems are difficult to solve.

The variables in the above formulation are now normalized as follows: the lengths,  $x, y, \xi, \eta, r, x_l, x_t$  and  $c$  by  $b/2$ , the downwash  $w$  by  $U$ , and the vortex intensity  $\gamma$  also by  $U$ . The ground height  $h$  is also normalized by  $b/2$ . For convenience, all the normalized variables are to retain their original symbols.

Written in terms of these dimensionless variables, the normalized equations pertinent to the solving of the jet-wing problem are summarized below:

$$w(x,y) = \varepsilon(x,y), \quad (z = 0, \text{ wing portion}) \quad (2.32)$$

$$\frac{\partial w}{\partial x}(x,y) = - \frac{2}{c(y) c_{\mu}(y)} \gamma(x,y), \quad (z = 0, \text{ jet portion}) \quad (2.33)$$

$$w(x,y) = \theta(y), \quad (x = x_t^+(y), \text{ when } c_{\mu}(y) \neq 0) \quad (2.34)$$

$$\gamma(x,y) = 0, \quad \left\{ \begin{array}{l} x \rightarrow \infty, \text{ when } c_{\mu}(y) \neq 0 \\ x = x_t^-(y), \text{ when } c_{\mu}(y) = 0 \end{array} \right\} \quad (2.35)$$

in which the downwash  $w$  is expressed by

$$w(x,y) = -\frac{1}{4\pi} \int_{-b/2}^{b/2} \frac{d\eta}{(y-\eta)^2} \int_{x_l}^{x_t \text{ or } \infty} \gamma(\xi, \eta) \left(1 + \frac{x-\xi}{r}\right) d\xi \quad (2.36)$$

The loading coefficient  $\Delta c_p$ , defined as  $\Delta p / \frac{1}{2} \rho U^2$ , assumes the following form:

$$\Delta c_p = 2\gamma \quad (2.37)$$

The above normalized equations (2.32) through (2.35) will be adopted as the basis for the subsequent solution of the jet-wing problem.

#### 2.2.1.4 Fundamental Cases

An examination of equations (2.32) through (2.35) will reveal that these equations are linear in  $\epsilon$ ,  $\theta$ ,  $w$ , and  $\gamma$ .

If, for a particular solution of the jet-wing problem  $\epsilon$  and  $\theta$  can, for example, be written as the linear summations,

$$\epsilon = \sum_{m=1}^K a_m \epsilon_m \quad (2.38)$$

and

$$\theta = \sum_{m=1}^K a_m \theta_m \quad (2.39)$$

where  $\epsilon_m$  and  $\theta_m$  will be designated as the geometric data for the  $m^{\text{th}}$  fundamental case, then the solution  $\gamma$  for the particular case is also a linear summation which can be expressed as follows:

$$\gamma = \sum_{m=1}^K a_m \gamma_m \quad (2.40)$$

In equation (2.40),  $\epsilon_m$  must satisfy the same set of equations as the total does, or more precisely,

$$w_m = \epsilon_m, \quad (z = 0, \text{ wing portion}) \quad (2.41)$$

$$\frac{\partial w_m}{\partial x} = -\frac{2}{c c_\mu} \gamma_m, \quad (z = 0, \text{ jet portion}) \quad (2.42)$$

$$w_m = \theta_m, \quad (x = x_t^+(y), \text{ when } c_\mu(y) \neq 0) \quad (2.43)$$

$$\gamma_m = 0, \quad \left\{ \begin{array}{l} x \rightarrow \infty, \text{ when } c_\mu(y) \neq 0 \\ x = x_t^-(y), \text{ when } c_\mu(y) = 0 \end{array} \right\} \quad (2.44)$$

Thus,  $\gamma_m$  is a solution of the  $m^{\text{th}}$  fundamental case.

Fundamental cases commonly encountered include, for example, camber and twist of the wing, angle of attack, deflection of a trailing edge or leading edge flap, and jet deflection. These are illustrated in figure (2.3). For simplicity, only the sectional characteristics of each is illustrated. The spanwise variation is not shown. In practice, solutions for a particular jet-wing problem might involve the combination of any number of fundamental cases. Since each fundamental case can be solved independently, maximum computing efficiency can, as indicated above, be realized by the linear superposition of the required fundamental case solutions. It must be noted, however, that inherent in the formulation of the theoretical model is a restriction that prevents a change in the magnitude and distribution of  $c_\mu$  or wing planform geometry from being regarded as a fundamental case. In other words, the linear superposition of fundamental case solutions is only valid for those problems having the same wing planform geometry and trailing edge  $c_\mu$  distribution.

### 2.2.1.5 Ground Effect

For conditions where the jet sheet does not impinge on the ground, the significant effect of ground proximity is to change the aerodynamic characteristics of the jet-wing and also to constrain the jet path and downwash field, which can lead to significant changes in the empennage contributions to stability and control characteristics. These effects should be amenable to treatment by potential flow methods similar to those currently being discussed. However, as the jet path comes in close proximity to the ground or should the jet actually impinge on the ground, then the flow behavior will be significantly altered with noticeable changes in the viscous-inviscid interaction.

As mentioned earlier, the theoretical treatment of the aerodynamics of jet-wings in ground effect has received little attention in recent years. Ground effects on two-dimensional jet-flap airfoils have, of course, been examined. The flow behavior for finite aspect ratio wings has, however, proved substantially different from that observed in two-dimensional experiments, primarily because of the spanwise venting which can occur. More extensive theoretical studies of jet-wings in ground proximity are needed.

The authors have, as part of the present program, given serious consideration to what would be regarded as a realistic theoretical treatment of the three-dimensional jet-wing ground effect problem in which the close proximity or impingement of the jet on the ground would be, to some extent, considered. In order to establish the behavior of the aerodynamics, an iterative approach would have to be adopted. The location of the jet sheet for the solution of the first step in the iterative scheme could be obtained from the present jet-wing lifting surface theory, modified to include the influence of the ground in a linearized sense. Use of the linearized approach as a first step of the iterative scheme is dictated by the fact that the jet shape is a function of the loading distribution both on the jet and the wing and, therefore, is unknown a priori. The next step in such a solution would be to determine from the jet shape if there is ground impingement of the jet. Although once impingement has occurred viscous effects might become important, it should be reasonable to assume that no further vortex shedding occurs downstream of the impingement point. The jet shape and ground impingement specified,

it would then be necessary to again solve the jet-wing problem at each angle of attack using a fully non-planar non-linear lifting surface theory. The new loading could then be used to recalculate the jet shape and ground impingement point, and the process could then be repeated.

Although a non-linear iterative technique as described above should provide a realistic theoretical model of a jet-wing in ground effect, owing to its complexity, it is desirable to investigate simplifications of such an approach in order to evaluate their usefulness in establishing engineering methods for preliminary design purposes. The simplification that has been adopted to date is to use only the first step of the full solution. In other words, the ground effect problem will be treated here within the framework of the linearized jet-wing lifting surface theory. The usefulness of such an approach might well be questioned. For wing-ground heights typical of STOL transport aircraft, however, the segment of the jet closest to the wing where most of the jet turning (and hence loading) takes place might be sufficiently displaced from the ground for the linearization assumptions to apply. The validity of the assumptions will be assessed later when a comparison with experiment can be made. What must not be overlooked, however, is that the method described herein can at a later date be utilized as part of the more rigorous procedure outlined earlier.

In view of the above, the basic assumptions adopted in Section 2.2.1.2 for the jet-wing in free air will again be used in the solution of the ground effect problem. That is, it is assumed that the effect of wing thickness is negligible and the local incidences of the wing are small. Also, the flows, both within and outside the jet sheet, are assumed to be incompressible, inviscid, and irrotational. Rolling up of the wake and jet sheet is neglected. Based on these assumptions, the jet-wing in ground effect problem may be treated as a potential flow problem. Thus, the governing equation is Laplace's equation (2.12), subject to the boundary conditions (equations (2.14), (2.17), (2.18), and (2.19)). As mentioned previously, the jet-wing problem is a free boundary problem with non-linear boundary conditions. In free air, the problem has been simplified through a linearization of the boundary conditions and through the assumption that, because of the small incidences and deflections, it is satisfactory to satisfy the boundary conditions not on the actual



boundaries but on their projections on the  $z = 0$  plane. The validity of these last two assumptions must be re-examined for the ground effect problem.

Before linearization of the boundary conditions can be further pursued, the basic mathematical model to be employed in this analysis must be discussed. Since the ground must be a streamline of the flow (i.e., the ground is impermeable), it is logical to place an image jet-wing below the ground such that the ground becomes a plane of symmetry between the "real" jet-wing and its mirror image [figure (2.4b)]. Although such a scheme returns the problem to having a fully infinite regime of flow as in the free air case rather than semi-infinite, the regime is now multiply connected rather than simply connected. Because of its multiply connected nature, the assumptions adopted in the formulation of the jet-wing lifting surface theory, in particular the simplification of the boundary conditions, must be reassessed.

In ground effect the wing moves, in part, in a velocity field induced by the image of the jet-wing system. Now the complex problem of finding the aerodynamic characteristics of the wing out of ground effect was simplified by making two important approximations. The first was that in calculating the velocity field induced by the jet it was permissible to ignore the entrainment into and the thickness of the jet. The second assumption was that the approximations of linear perturbation theory could be introduced. These two assumptions, when valid in ground effect, imply that the loading induced on the wing due to the ground and hence its image can be calculated to first order by considering only the downwash  $w'$  induced by the image jet-wing bound and trailing vorticity. This can be shown as follows:

Consider the kinematic boundary condition expressed by equation (2.14). In the case of ground effect equation (2.14) becomes

$$\tan \epsilon = \frac{w + w'}{U + u + u'} \quad (2.45)$$

where  $w'$  and  $u'$  are the perturbation or disturbance velocities induced by the image. Now for high aspect ratio wings and providing the height: chord ratio is not too small and  $\epsilon$  not too large, it follows that the value of  $w'$  or  $u'$  will be of the  $O(\epsilon)$  or higher. Adopting, therefore, the

linearization employed in the derivation of equation (2.20), equation (2.45) can be replaced by

$$\frac{w'}{U} + \frac{w}{U} = \left( \epsilon + \frac{\epsilon^3}{3} + \dots \right) \left( 1 + \frac{u}{U} + \frac{u'}{U} \right) \approx \epsilon \quad (2.46)$$

which is in agreement with equation (2.20) providing  $\epsilon$  is taken to be equal to the total downwash.

Turning now to the dynamic boundary condition, an important consequence of the assumption that the jet has zero thickness is that equation (2.17) is exact and uniformly valid for all heights of the wing relative to the ground. No attempt will be made here to show that this is the case, but the reader can consult a paper by Maskell and Gates (reference 16) which gives results from which it can be shown that

$$v_1^2 - v_2^2 = \frac{2J}{\rho R} \left\{ 1 + \frac{1}{2} d_J \left( \frac{u}{v_J} \right) \left( \frac{\rho}{\rho_J} \right) \left[ \left( \frac{v_1}{U} \right)^2 + \left( \frac{v_2}{U} \right)^2 - 2 \right] \right\} \left\{ 1 + \left( \frac{d_J}{R} \right)^2 \right\}^{-1} \quad (2.47)$$

where  $d_J$  is the jet thickness. This yields for  $d_J = 0$  the relation given in section 2.2.1.3

$$v_1^2 - v_2^2 = \frac{2J}{\rho R} \quad , \quad d_J = 0 \quad (2.48)$$

The linearization of the dynamic boundary condition is quite straightforward. Combining equation (2.45) and (2.48) gives

$$\frac{\gamma}{U} = \frac{c_{\mu} c}{2R} \frac{\cos \epsilon}{1 + \frac{u}{U} + \frac{u'}{U}} \quad (2.49)$$

where  $\gamma$ , as before, is the vorticity distribution which gives rise to a jump in velocity (i.e.,  $v_1 - v_2$ ) across the jet sheet. Substituting for  $R$  [i.e., equation (2.21)] it follows that

$$\frac{\gamma}{U} = \frac{c_{\mu} c}{4 \left( \frac{w}{U} + \frac{w'}{U} \right)} \sin 2\epsilon \frac{d\epsilon}{dn}$$

which for small first-order quantities,  $O(\epsilon)$  say, can be written

$$\frac{\gamma}{U} = \frac{c_{\mu} c}{2} \left[ \frac{d(w/U + w'/U)}{dx} + O(\epsilon^2) \right]$$

$$\approx \frac{c_{\mu} c}{2} \frac{d(w/U + w'/U)}{dx} \quad (2.50)$$

This means that both the dynamic and kinematic boundary conditions derived for the wing out of ground effect apply equally well in ground effect, providing  $w$  is now the total downwash.

At this point it is pertinent to inquire if the linear perturbation theory is valid over the range of ground heights of interest. A point to notice is that in the linearization of the ground effect problem, it was necessary to neglect terms of  $O(\epsilon^2)$  while out of ground the error would, in general, be of higher order. It is possible to conclude, therefore, that the accuracy of the linear perturbation theory may be low and that an approximate correction, at least to the lift if not the aerodynamic loading, is worth seeking.

In thin-wing theory the induced velocities are assumed small in comparison with the main-stream velocity for deriving the boundary conditions (2.46) and (2.50). In particular, it was found necessary and correct in a first-order theory to neglect, in calculating the aerodynamic loading, the "u" perturbation velocity. In other words, the exact expression for  $\Delta c_p$  as given by Bernoulli's equation, namely:

$$\Delta c_p = 2 \frac{\gamma}{U} \left( 1 + \frac{u}{U} + \frac{u'}{U} \right)$$

is, neglecting second- and higher-order terms, given by equation (2.37). To the same order of approximation when integrating aerodynamic loading to obtain total lift or pitching moment, it was found useful to assume that  $\Delta c_p$  could be evaluated using the following expression

$$\Delta c_p = 2 \frac{\gamma}{U} \left( 1 + \frac{u'}{U} \right) \quad (2.51)$$

In justifying the second-order correction  $2(\gamma/U)(u'/U)$  in equation (2.51) to the first-order theory value of  $\Delta c_p$  (i.e.,  $2\gamma/U$ ), it was found profitable to have a look at the classical theory of an airfoil without a jet flap (i.e., the special case  $c_\mu = 0$ ). The most important example of the linear perturbation theory, given in Appendix I.5, is the case of the flat-plate airfoil at a height  $h$  from the ground. Because the freestream perturbation velocity associated with the image is neglected (i.e.,  $\Delta c_p = 2\gamma/U$ ), the lift coefficient,  $c_l$ , becomes, neglecting powers of  $(c/4h)^2$  greater than the first,

$$c_{l, \text{1st order theory}} = 2\pi\alpha \left[ 1 + \frac{1}{4} \left( \frac{c}{2h} \right)^2 \right] \quad (2.52)$$

Now this is the lift coefficient that would be obtained with the present method as  $AR \rightarrow \infty$  for an airfoil of chord  $c$  and an angle of attack  $\alpha$ . Several authors have, however, developed approximate theories for the flat plate in which higher-order terms in  $(c/4h)^2$  have been considered without restriction on the incidence  $\alpha$ . The reader can consult, for example, L.C. Woods', "The Theory of Subsonic Plane Flow,"<sup>40</sup> in which the following expression for  $c_l$  is given:

$$c_l = 2\pi \sin \alpha \left[ 1 - \left( \frac{c}{2h} \right) \sin \alpha + \frac{1}{4} \left( \frac{c}{2h} \right)^2 (1 + 3 \sin^2 \alpha) + \dots \right] \quad (2.53)$$

which for  $h \rightarrow \infty$  gives the well-known exact formula for  $c_l$ .

It follows from an examination of the last two equations that the error in predicting the change in lift in ground effect could be large if  $\alpha$  is of  $O(c/2h)$ . Consider now the magnitude of  $u'/U$  which according to Appendix A.5 becomes

$$\frac{u'}{U} = -\frac{1}{4\pi} \left( \frac{c}{2h} \right) c_{l, \text{1st order theory}} \quad (2.54)$$

Hence, if the expression for  $\Delta c_p$  given in equation (2.51) is employed, one finds

$$c_{\ell} = 2\pi\alpha \left[ 1 - \frac{\alpha}{2} \left( \frac{c}{2h} \right) + \frac{1}{4} \left( \frac{c}{2h} \right)^2 + o \left( \frac{c}{2h} \right)^3 \right] \quad (2.55)$$

in which the restriction is that terms of  $O(c/2h)^3$  and higher are neglected and that  $\alpha$ , as usual, be small. From a close examination of equations (2.52), (2.53) and (2.55), one can conclude that the error in predicting the change in lift in ground effect has been reduced by approximately fifty percent for small  $\alpha$ .

The discrepancy between equations (2.53) and (2.55) is simply associated with the steps taken in the linearization of the kinematic boundary conditions in which the second-order terms (i.e., of  $O(\epsilon^2)$ ) have been neglected. It is unlikely, therefore, that any further improvement can be made to the first-order theory without considering the second step in the iterative method of solving the "exact" ground effect problem. The iterative method the authors have in mind is that described earlier in this section. An additional and important result that can also be deduced from equations (2.53) and (2.55) is that the correction made earlier to the first-order theory (i.e., the  $u'/U$  term) can be of comparable order of magnitude as the image induced downwash  $w'/U$ .

Having established a useful approximate theory for the flat plate in ground effect, it is pertinent to inquire if it is uniformly valid for the arbitrary thin airfoil in which  $c_{\mu} \geq 0$ . Clearly it cannot hold for all conditions. Nor will any attempt be made here to justify, in a rigorous sense, its application to the general problem. An important consequence of the assumption that  $\Delta c_p$  is given by equation (2.51), has been, however, a consistently better agreement in the general case between the results obtained from the present ground effect method and exact jet flap airfoil theory. This is a point which will be demonstrated later (section 2.2.6.3) for conditions in which  $c_{\mu}$  is greater than or equal to zero.

### 2.2.2 Numerical Solution

Most STOL jet-wing high lift systems are likely, in practice, to require the use of part-span mechanical flaps with or without chord extension, partial span blowing, etc. Since it is essential to be able to evaluate the aerodynamic characteristics of these configurations, the authors are of the opinion that a solution to the jet-wing problem, as formulated in the previous section, requires a numerical approach based on a finite-element method.

Consider the general application of a finite-element method to the numerical solution of the jet-wing problem. The boundary region, or the vortex sheet, must be divided into a finite number of small elements, each containing an unknown vortex distribution. Presumably when these vortex distributions are calculated, their sum represents the total vortex distribution in the boundary region. The problem would involve finding the individual distributions in each element through the application of the jet-wing boundary conditions; i.e., equations (2.32) through (2.35). In particular, a finite element method would require that the boundary conditions be satisfied at one point (control point) on each element. In the following paragraph a detailed description of the present method will be presented.

The downwash  $w$  contained in equations (2.32) through (2.36) is required to be written in terms of the summation of downwash induced by every element. Let the  $j^{\text{th}}$  element be denoted by  $\Delta S_j$ , then according to equation (2.36) the downwash  $w_i$  at the  $i^{\text{th}}$  control point  $(x_i, y_i)$  may be expressed as follows:

$$w_i = \sum_{j=1}^N \Delta w_{ij} \quad (2.56)$$

where

$$\Delta w_{ij} = -\frac{1}{4\pi} \iint_{\Delta S_j} \frac{\gamma_j(\xi, \eta)}{(y_i - \eta)^2} \left( 1 + \frac{x_i - \xi}{r_i} \right) d\xi d\eta \quad (2.57)$$

with

$$r_i = \sqrt{(x_i - \xi)^2 + (y_i - \eta)^2}$$

where  $w_{ij}$  is the downwash at the  $i^{\text{th}}$  control point induced by the vortex distribution at the  $j^{\text{th}}$  element. The notation  $N$  denotes the total number of elements involved.

Next, it is necessary to find a simple model to represent the vortex distribution  $\gamma_j(\xi, \eta)$  in the element. It is highly desirable that this elementary vortex distribution can be expressed by a general function times an unknown factor  $\gamma_j$  so that its induced downwash,  $\Delta w_{ij}$ , according to equation (2.57), is also proportional to the same factor. In other words, if

$$\gamma_j(\xi, \eta) = \gamma_j g_j(\xi, \eta) \quad (2.58)$$

then

$$\Delta w_{ij} = a_{ij} \gamma_j \quad (2.59)$$

where

$$a_{ij} = -\frac{1}{4\pi} \iint_{\Delta S_j} \frac{g_j(\xi, \eta)}{(y_i - \eta)^2} \left(1 + \frac{x_i - \xi}{r_i}\right) d\xi d\eta \quad (2.60)$$

The term  $a_{ij}$  is normally referred to as the downwash influence coefficient, that is, the downwash induced by an elementary vortex distribution of unit magnitude. The advantage of this formulation is that only one unknown (a linear factor) is associated with an element. Thus, a set of linear equations can be easily constructed, with the same number of equations as unknowns. The problem remains to define a model of the elementary vortex distribution.

In the solution of conventional wing problems, promising results have been obtained in recent years with the "vortex lattice" and "box" methods (references 29 and 30). The semi-infinite area of discontinuity and mixed

boundary conditions which arise in the jet-wing case were partly responsible, however, for the development and selection of the method described in the following section. In the meantime, it should be noted that the specific model of the elementary vortex distribution attempts to satisfy two criteria essential to the evaluation of the correct downwash distribution throughout the entire region. First, the vortex must be assumed to be distributive and secondly, continuous (i.e., the elementary vortex distribution in an element must join adjacent ones continuously).

#### 2.2.2.1 Description of the Elementary Vortex Distribution Method

In the following, the flow around the wing and the jet sheet will be determined by first considering that the wing and jet boundary regions ( $z = 0$ ) are divided into chordwise strips parallel to the free-stream, with each strip then subdivided, as illustrated in figure (2.4), into rectangular elements. Although this simplifies the task of deriving the downwash influence coefficients, obviously, in the case of a swept wing, these elements do not exactly reproduce the leading or trailing edge of the wing. If, however, a sufficient number of elements are used, the solution of rectangular elements does not impose a serious restriction, a fact that is substantiated by the comparison of calculated results with those available from conventional wing lifting surface theories.

A vortex model consisting, except for singularities, of a continuous vortex distribution in the chordwise direction, representing the correct distribution as closely as possible while not sacrificing simplicity, will now be adopted. Along each strip, this model will primarily consist of rectangular elements represented by a linear vortex distribution. At the leading edge, the flap hinge and the trailing edge with a deflected jet, where the real vortex distribution approaches infinity, the model adopts the appropriate singularity for the leading edge, and the logarithmic singularity for both the hinge and the trailing edge with a deflected jet. The leading edge and flap hinge singularities are well-known since they are present in most conventional lifting surface theories. The trailing edge singularity with a jet is derived from Spence's theoretical analysis of the two-dimensional jet-flap problem. Finally, the vortex model also adopts a vortex distribution



for the last element on the far downstream end of the jet that prescribes the appropriate decay property ( $\gamma$  goes to zero as  $x$  approaches infinity). The last element is assumed to be infinitely long, thus eliminating the need to truncate the jet sheet.

The adopted vortex model and its real counterpart are illustrated in figure (2.4) where it is apparent that all the linear distributions are actually equivalent to a set of overlapping triangular distributions, with each of them straddling on two successive elements. In fact, the vortex model that has been adopted is now represented equivalently by a set of composite elementary vortex distributions (abbreviated as EVD's) consisting of the following four types:

- i. Regular EVD: Triangular in shape and distributed over two successive elements.
- ii. Leading Edge EVD: Distributed over the leading edge element. It is square root singular when approaching the leading edge and becomes zero at the other end of the element.
- iii. Hinge EVD: Consisting of two parts. One is the Regular EVD, the other is the additional hinge distribution having a logarithmic singularity at the hinge with its strength directly proportional to the deflection angle of the flap or the jet (e.g.,  $\delta_s$ ,  $\delta_f$ , or  $\delta_j$ ). It is distributed over the two elements adjacent to the flap hinge line or to the trailing edge with a deflected jet.
- iv. Infinity (Far-Jet) EVD: Distributed over the last two elements of the jet at the downstream end. The front half is linear, while the other half gradually decays to zero (proportional to  $x^{-2}$ ) on approaching infinity.

The four types of the EVD's are designated specifically in figure (2.4). The derivation and precise mathematical definition of each of these EVD's is

given in detail in Appendix I.1.

It is understood that, associated with each elementary vortex distribution, there are trailing vortex lines emanating from the streamwise edges of each element since it is assumed that the spanwise bound vortex distribution within an element is constant. This implies that a discontinuity exists in the vortex distribution across the streamwise edges of an element, in contrast to the requirement of continuity. Nevertheless, this compromise was considered desirable in order to maintain simplicity. In view of the discontinuity, the control point is chosen on the streamwise center line of an element; otherwise it can be anywhere on this center line. The center line criterion appears, at first, to be a logical choice, which is later substantiated by the solution.

In summary, the wing surface and jet sheet have been replaced by their projection on the plane  $xOy$  and are considered to be equivalent to a sheet of vorticity. The jet-wing boundary has been divided into a set of rectangular elements, and the vortex distribution has been represented by a set of EVD's overlapping each other. The EVD permits a chordwise variation of vorticity but it remains constant along the spanwise direction. Each EVD can be represented by only one unknown, which is the vortex intensity value at the apex of the vortex distribution in the case of the Regular EVD or the Infinity EVD. In the case of Hinge EVD, the unknown is the apex value of the regular part of the distribution. The additional part is predetermined and proportional to  $\beta$ . Finally, in the case of the Leading-Edge EVD, the mean vortex value over the element is taken as the unknown. The boundary conditions are required to be satisfied at one control point for every element. Since there are as many EVD's as there are elements, the same number of equations can be set up to solve for an equal number of unknowns. Since the present method for the jet-wing problem uses the EVD model, it will be referred to as the EVD method, an abbreviation for the method of Elementary Vortex Distribution.

#### 2.2.2.2 The Downwash Influence Coefficients

The calculation of the downwash influence coefficient associated with each EVD will now be considered. Irrespective of the type of EVD, in

general, the local vortex strength,  $\gamma_j^*(\xi, \eta)$ , of each one can be expressed by

$$\gamma_j^*(\xi, \eta) = \gamma_j g_j(\xi) + \beta_j h_j(\xi), \quad (-\Delta < \eta < \Delta) \quad (2.61)$$

where  $\Delta$  is the element semispan,  $\gamma_j$  is the unknown, and  $\beta_j$  is the deflection angle (in radians), both associated with the  $j^{\text{th}}$  EVD. The  $\beta$ - term automatically vanishes when  $\beta_j = 0$ , that is, when the  $j^{\text{th}}$  EVD is not a hinge EVD. The  $\beta_j$  term is either the peak value or the average value of the vortex strength of each vortex distribution.

With  $\gamma_j^*$  defined above, the downwash  $\Delta w_{ij}$  at a control point  $(x_i, y_i)$  due to the  $j^{\text{th}}$  EVD can be calculated according to equation (2.57), yielding the following expression:

$$\Delta w_{ij} = a_{ij} \gamma_j + b_{ij} \beta_j \quad (2.62)$$

which contains two downwash influence coefficients,  $a_{ij}$  and  $b_{ij}$ . These downwash influence coefficients are given by:

$$a_{ij} = -\frac{1}{4\pi} \iint_{\Delta A_j} \frac{g_j(\xi)}{(y_i - \eta)^2} \left( 1 + \frac{x_i - \xi}{r_i} \right) d\xi d\eta \quad (2.63)$$

and

$$b_{ij} = -\frac{1}{4\pi} \iint_{\Delta A_j} \frac{h_j(\xi)}{(y_i - \eta)^2} \left( 1 + \frac{x_i - \xi}{r_i} \right) d\xi d\eta \quad (2.64)$$

where the integration is performed over the base of the  $j^{\text{th}}$  EVD, denoted by  $\Delta A_j$ .

The preceding downwash expression appears to be more complicated than equation (2.59), but the  $\beta$  term is no more than a known constant, contributed by the additional hinge distribution only. The analytical formulas for the downwash influence coefficients associated with each type of EVD are derived in Appendix I.1 by using the corresponding vortex distribution in evaluating the integrals given by equations (2.63) and (2.64). It is

particularly noteworthy that all the EVD's possess the unique property that the vortex intensity is either zero or approaching an integrable singularity at either chordwise end. As a result, the downwash calculated from an EVD is, except for singularities, continuous along a chordwise section and thus, complicated numerical computations are eliminated.

Retaining the expression (equation (2.62)) for  $\Delta w_{ij}$ , the total downwash  $w_i$  at a control point,  $(x_i, y_i)$ , due to all the EVD's (Note: The total number of EVD's is denoted by  $N$ ), according to equation (2.56), can be written as:

$$w_i = \sum_{j=1}^N a_{ij} \gamma_j + \sum_{j=1}^N b_{ij} \beta_j \quad (2.65)$$

where, again, the second term on the right hand side is known.

### 2.2.2.3 Modification of the Downwash Influence Coefficients for Ground Effect

As discussed in Section 2.2.1.5, the ground effect problem is solved by placing a mirror image of the jet-wing below the ground such that the ground becomes a streamline of the flow. It is necessary to calculate an additional set of downwash influence coefficients which relate the downwash induced by each element of the jet-wing by each element of the image jet-wing. Therefore, equation (2.62) can be reformulated and expressed as

$$\Delta w_{ij} = (a_{ij} + \bar{a}_{ij})\gamma_j + (b_{ij} + \bar{b}_{ij})\beta_j \quad (2.66)$$

where  $\bar{a}_{ij}$  and  $\bar{b}_{ij}$  are the two downwash influence coefficients for the image jet-wing which correspond directly with equations (2.63) and (2.64), respectively. Similarly, the total downwash  $w_i$  at a control point  $(x_i, y_i)$  due to all the elements on the real jet-wing and its mirror image becomes

$$w_i = \sum_{j=1}^N (a_{ij} + \bar{a}_{ij})\gamma_j + \sum_{j=1}^N (b_{ij} + \bar{b}_{ij})\beta_j \quad (2.67)$$

The downwash influence coefficients associated with the image jet-wing can be approximated by expressions simpler than those given in Appendix I.1.1 through I.1.4 because the image jet-wing is sufficiently removed from the real jet-wing and, therefore, the details of the loading distribution on the image are mathematically unimportant. Hence, it is not necessary to represent the infinitesimal horseshoe vortex distribution of the image by the continuous vortex distributions used in the EVD theory. Instead, the image jet-wing has been replaced by a lattice of discrete horseshoe vortices, one per rectangular element equal in strength to the corresponding EVD. Figure (2.5) compares the downwash distribution induced by a triangular shaped elementary vortex distribution with that of a concentrated horseshoe vortex of the same total vortex strength and shows that the downwash induced by the two distributions differs only in a region the size of the vortex element. Hence, the approximation employed herein should be valid except when the wing-ground height approaches the size of the vortex elements. For each horseshoe vortex on the image jet-wing, the bound segment of the vortex is placed at points on the image corresponding to vortex points on the real jet-wing, which are the leading edge points of each element. Unlike standard vortex lattice theory, where the bound vortex must be located at the 1/4-chord position and the downwash point at the 3/4-chord position, there is no stringent collocation requirement here since the downwash points are on the real jet-wing and hence are in the far field relative to the singularities of the vortex lattice. The additional hinge contribution is not used for the ground effect solution because of the vortex lattice representation of the image jet-wing. The analytical formulas for the image jet-wing downwash influence coefficients are derived in Appendix I.1.5. In addition, a freestream perturbation influence coefficient  $c_{ij}$  is derived in Appendix I.1.5. This coefficient is discussed in Section 2.2.3.1.4.

#### 2.2.2.4 Boundary Conditions

The EVD method requires that the boundary conditions be satisfied at one control point on each element. The boundary conditions denoted by equations (2.32) and (2.33) can, for the  $i^{\text{th}}$  control point  $(x_i, y_i)$ , be expressed by:

$$w_i = \epsilon_i, \quad (\text{when the } i^{\text{th}} \text{ control point is on the wing)} \quad (2.68)$$

$$\left(\frac{dw}{dx}\right)_i = -\frac{2}{c(y_i)c_\mu(y)} \gamma_i, \quad (\text{when the } i^{\text{th}} \text{ control point is on the jet sheet)} \quad (2.69)$$

On substituting the downwash expression, equation (2.65), into the wing boundary condition, equation (2.68), and then transferring the known constant term to the right-hand side of the equation, a linear algebraic equation in  $\gamma_i$  is obtained.

$$\sum_{j=1}^N a_{ij} \gamma_j = \epsilon_i - \sum_{j=1}^N b_{ij} \beta_j, \quad (i, \text{ on the wing}) \quad (2.70)$$

Although the EVD model is designed to reproduce the downwash  $w$  accurately, it does not suffice to guarantee that the derivative  $\frac{dw}{dx}$  will be as accurate. Hence, in order to make the jet boundary condition more suitable for numerical computation, equation (2.69) is integrated over a small distance along the jet, say from one control point  $x_{i-1}$  to the following one  $x_i$ , to give

$$w_i - w_{i-1} = -\frac{2}{c(y)c_\mu(y_i)} \int_{x_{i-1}}^{x_i} \gamma(\xi, y_i) d\xi, \quad (i, \text{ on the jet sheet}) \quad (2.71)$$

which no longer contains the derivative. The integral on the right hand side of the equation represents the total vorticity contained in the interval of integration. Although the solution of this integral in terms of the unknown  $\gamma_j$ 's is derived in Appendix I.2, in general, it may be expressed follows:

$$\int_{x_{i-1}}^{x_i} \gamma(\xi, y_i) d\xi = \sum_{j=1}^N e_{ij} \gamma_j + \sum_{j=1}^N f_{ij} \beta_j \quad (2.72)$$

As before, the  $\beta$  term is known. Most of the integration coefficients  $e_{ij}$  and  $f_{ij}$  are found to be zero, except for those  $j$ 's adjacent to  $i$ .

By substituting the downwash equation (2.65) and the integration

equation (2.72) into equation (2.71), a linear equation for the dynamic boundary condition on the jet can also be introduced.

$$\sum_{j=1}^N (a_{ij} - a_{i-1,j} + v(y_i) e_{ij}) \gamma_j = - \sum_{j=1}^N (b_{ij} - b_{i-1,j} + v(y_i) f_{ij}) \beta_j, \quad (i, \text{ on the jet sheet}) \quad (2.73)$$

where  $v(y_i)$  is defined as

$$v(y_i) = \frac{2}{c(y_i) c_\mu(y_i)} \quad (2.74)$$

Special consideration should be given to the leading jet element at a chordwise section, where the integration of equation (2.69) is supposed to start from the trailing edge  $(x_t, y_i)$  rather than  $x_{i-1}$ , because the equation does not apply ahead of the trailing edge. Consequently,  $w_{i-1}$  is replaced by the initial jet angle,  $\theta(y_i)$ , and the jet boundary condition corresponding to equation (2.73) becomes

$$\sum_{j=1}^N (a_{ij} + v(y_i) e_{ij}) \gamma_j = \theta(y_i) - \sum_{j=1}^N (b_{ij} + v(y_i) f_{ij}) \beta_j, \quad (i \text{ is the leading control point on the jet}) \quad (2.75)$$

In view of this special consideration, the other boundary condition given by equation (2.34) has automatically been satisfied.

Equation (2.73) or (2.75) does not, of course, stipulate that the jet boundary condition is satisfied precisely at the control point, nor at any other specific point on an element. It is apparent that  $w_i - w_{i-1}$  is directly proportional to the mean value of the derivative  $\frac{dw}{dx}$  over the interval from  $x_{i-1}$  to  $x_i$ , and also that the  $\gamma$  integral is proportional to the mean value in the same interval. If the exact solution had been known for both  $w$  and  $\gamma$ , a point could be found within the interval, where both the local values  $\frac{dw}{dx}$  and  $\gamma$  take the corresponding mean values of the interval. So, effectively speaking, equation (2.73) or (2.75) requires the jet boundary condition to be satisfied at a point somewhere in between the two consecutive

control points. It should also be noted that the Kutta condition prescribed by equation (2.35) has been built-in inherently within the EVD model. On the infinity or far-jet elements, the Infinity EVD is assumed. Since  $\gamma$  vanishes as  $x$  tends towards infinity for this EVD, the Kutta condition at the blown sections is fulfilled. On the trailing-edge elements where there is no jet emission, the Regular "triangular" EVD is used. This guarantees that the value will be zero at the trailing edge. Thus, the Kutta condition at the unblown section is also satisfied.

In conclusion, equations (2.70), (2.73), and (2.75) now contain all the necessary information or conditions for solving the jet-wing problem. These form a system of  $N$  linear algebraic equations to be solved for  $N$  unknown  $\gamma$  values, which are mostly the local vortex intensity values.

So far the location of the control point relative to an element has not been specified except for the restriction that it lie on the streamwise center line. In principle, any point on the center line should serve the purpose. Those integration coefficients  $e_{ij}$  and  $f_{ij}$  given in Appendix I.2, however, are derived specifically at the midpoint of the center line.

#### 2.2.2.5 Determination of Aerodynamic Loading or Local Vortex Intensity

In summarizing, the linear equations, (i.e., equation (2.70), (2.73), and (2.75)) may be combined in simple form:

$$\sum_{j=1}^N A_{ij} \gamma_j = B_i, \quad (i = 1, 2, \dots, N) \quad (2.76)$$

where the coefficient matrix  $A_{ij}$  is given by

$$A_{ij} = \begin{cases} a_{ij}, & (i, \text{ on the wing}) \\ a_{ij} + v(y_i) e_{ij}, & (i, \text{ the leading point on the jet}) \\ a_{ij} - a_{i-1,j} + v(y_i) e_{ij}, & (i, \text{ other points on the jet}) \end{cases} \quad (2.77)$$



and the coefficient matrix  $B_i$  is

$$B_i = \begin{cases} \epsilon_i - \sum_{j=1}^N b_{ij} \beta_j, & (i, \text{ on the wing}) \\ \theta(y_i) - \sum_{j=1}^N [b_{ij} + v(y_i)f_{ij}] \beta_j, & (i, \text{ the leading points on the jet}) \\ -\sum_{j=1}^N [b_{ij} - b_{i-1,j} + v(y_i)f_{ij}] \beta_j, & (i, \text{ other points on the jet}) \end{cases} \quad (2.78)$$

The downwash influence coefficients  $a_{ij}$  and  $b_{ij}$  required in the above equations may be calculated according to the formulas given in Appendix I.1, while the integration coefficients  $e_{ij}$  and  $f_{ij}$  required are those given in Appendix I.2 if the mid-points of the elements are selected as the control points. For the ground effect solution, the coefficient matrix  $A_{ij}$  becomes

$$A_{ij} = \begin{cases} a_{ij} + \bar{a}_{ij}, & (i, \text{ on the wing}) \\ a_{ij} + \bar{a}_{ij} + v(y_i)e_{ij}, & (i, \text{ the leading point on the jet}) \\ (a_{ij} + \bar{a}_{ij}) - (a_{i-1,j} + \bar{a}_{i-1,j}) + v(y_i)e_{ij}, & (i, \text{ other points on the jet}) \end{cases} \quad (2.79)$$

while the column matrix  $B_i$  remains the same as the free air case, equation (2.78). The ground effect downwash influence coefficients  $\bar{a}_{ij}$  may be calculated according to the formulas derived in Appendix I.1.5.

The linear system of equation (2.76) can be readily solved (reference 2) for the unknown  $\gamma_j$ 's with the aid of the digital computer. Most of the  $\gamma$  - values of the solution represent the peak value of an elementary vortex distribution. Since the peak value is also the local vortex intensity of the resultant vorticity distribution, the vortex intensity is then known discretely at a large number of points throughout the jet-wing system. All these points are located at the chordwise ends of rectangular elements. In Section 2.2.1.4

the concept of fundamental cases was introduced. These fundamental cases can be considered as additional columns on the right hand side of the matrix equation (2.76) and so solved simultaneously. This feature has been found to be particularly useful in increasing computer operation efficiency.

As a result of having adopted the classical approximations of linearized theory, it has been shown in equation (2.37) that the loading or pressure jump coefficient  $\Delta c_p$  across either the wing or the jet sheet is proportional to  $\gamma$ . Hence, the loading coefficient at a point  $(x_i, y_i)$  is

$$\Delta c_{p_i} = 2 \gamma_i(x_i, y_i) \quad (2.80)$$

In ground effect it has been shown in equation (2.51) that the pressure jump coefficient  $\Delta c_p$  is proportional to both  $\gamma$ , the local vortex intensity, and  $u'$ , the perturbation flow induced in the freestream direction by the image wing on the real wing. Hence, the loading coefficient at a point  $(x_i, y_i)$  in ground proximity is

$$\Delta c_{p_i} = 2 \left[ 1 + u'_i(x_i, y_i) \right] \gamma_i(x_i, y_i) \quad (2.81)$$

To obtain, in general, a continuous chordwise loading distribution  $\Delta c_p(x)$  in any chordwise section, it is necessary to use a curve fitting procedure that passes an approximate curve through all the known points. The ordinary curve fitting method, which considers bounded functions only, is not satisfactory, because the actual loading according to the jet-wing lifting surface theory becomes singular in certain places. These singular loadings have been incorporated in the EVD model; that is, the square root singularity for the Leading Edge EVD and the logarithmic singularity for the Hinge EVD. A very accurate representation of the chordwise loading distribution can be obtained by incorporating the expressions for the singular EVD's which are given in Appendix I.1 into the curve fitting procedure. In other words, the loading in the singular region is represented separately by the corresponding singular EVD plus the relevant part of the Regular EVD, while throughout the remaining region, where discrete values of the loading exist, a regular curve fitting is applied.

The chordwise loading distribution  $\Delta c_p$  on the wing obtained in this section can be integrated to provide both sectional and total aerodynamic characteristics. In addition to the pressure contribution, there is always a reaction contribution associated with the jet. Both will be discussed in detail in the following section.

### 2.2.3 Aerodynamic Characteristics

In this section, the detailed formulas for the aerodynamic (including propulsive and stability and control) characteristics are defined. They are expressed and subsequently used in their non-dimensional form only.

#### 2.2.3.1 Sectional Aerodynamic Characteristics

##### 2.2.3.1.1 Lift

The sectional or local wing lift coefficient  $c_{l\Gamma}$  resulting from the circulation around a wing section can be obtained from an integration of the chordwise loading distribution  $\Delta c_p$  obtained in the preceding section. The sectional wing total lift coefficient at any spanwise station  $y$  which also includes a component of the reaction force  $c_{l\mu}$ , can be expressed by

$$c_{l\Gamma}(y) = \frac{l(y)}{qc(y)} = c_{l\Gamma}(y) + c_{l\mu}(y) \quad (2.82)$$

where

$$c_{l\Gamma}(y) = \frac{1}{c(y)} \int_{x_{l\Gamma}(y)}^{x_t(y)} \Delta c_p(x,y) dx = \int_0^1 \Delta c_p(\bar{x},y) d\bar{x} \quad (2.83)$$

and

$$c_{l\mu}(y) = c_{\mu}(y)\theta(y) \quad (2.84)$$

In equation (2.83) it will be noted that for convenience an auxiliary non-dimensional coordinate  $\bar{x} = \frac{x - x_{l\Gamma}(y)}{c(y)}$  has been introduced.

##### 2.2.3.1.2 Pitching Moment

To obtain the pitching moment, a moment center must first be selected. In the theoretical analysis of the aerodynamic characteristics of conventional wings, it has been clearly established that the effect of the

induced drag on the pitching moment can normally be neglected. It has, therefore, been the general practice to consider only the horizontal position of the moment center. In the case of the jet-wing, both the horizontal and the vertical component of the resultant jet reaction can lead to a first-order contribution to pitching moment. In the derivation of the relevant equation for sectional pitching moment it will, therefore, be assumed that the moment center is fixed at the leading edge of each wing section. Accordingly, the total sectional pitching moment coefficient,  $c_m$ , can be written as:

$$c_m(y) = \frac{m(y)}{qc^2(y)} = c_{m_p}(y) + c_{m_\mu}(y) + c_{m_t}(y) \quad (2.85)$$

where

$$c_{m_p}(y) = -\frac{1}{c^2(y)} \int_{x_\ell(y)}^{x_t(y)} \Delta c_p(x,y)[x - x_\ell(y)]dx = -\int_0^1 \Delta c_p(\bar{x},y)\bar{x}d\bar{x} \quad (2.86)$$

$$c_{m_\mu}(y) = -c_\mu(y)\theta(y) \quad (2.87)$$

and

$$c_{m_t}(y) = c_\mu(y) \frac{\Delta z(y)}{c(y)} \quad (2.88)$$

In the above expressions,  $c_{m_p}$ ,  $c_{m_\mu}$ , and  $c_{m_t}$  designate the pitching moment (positive nose up) contributed by the pressure and the vertical and horizontal components of the jet reaction, respectively. The term  $\Delta z$  is used to denote the vertical displacement of the trailing edge relative to the leading edge of a wing section.

Suppose that the local angle of attack at a section, that is, the wing angle of attack  $\alpha$  plus the twist  $\alpha_t(y)$ , is measured from the chord line joining the leading and trailing edges, then  $\Delta z(y)$  may be expressed as

$$\frac{\Delta z(y)}{c(y)} = \alpha + \alpha_t(y) - \theta_s(y) + \sum_{i=1}^K \beta_i(y) \frac{c_{f_i}(y)}{c(y)} \quad (2.89)$$

It will be noted that this expression for  $\Delta z$  takes into account several ideal leading and trailing edge flap deflections, each with a deflection angle  $\beta_i$  and flap length  $cf_i$  measured from the hinge to the trailing edge. The angle  $\theta_s$  denotes the resultant inclination with respect to the free-stream due to the deflection, if any, of all leading edge flaps.

In view of the above, expressions for the center of lift, naturally including the aerodynamic center, can be readily established. Introducing  $\bar{x}_{c.p.}$  as the center of pressure lift and  $\bar{x}_{c.l.}$  as the center of total lift in the plane  $xOy$ , by definition

$$\bar{x}_{c.p.}(y) = -\frac{c_{m_\Gamma}(y)}{c_{l_\Gamma}(y)} \quad (2.90)$$

and

$$\bar{x}_{c.l.}(y) = -\frac{c_{m_\Gamma}(y) + c_{m_\mu}(y)}{c_l(y)} \quad (2.91)$$

where it will be noted that  $c_{m_t}$  is not required in the above calculation, even though it contributes to the total sectional pitching moment.

### 2.2.3.1.3 Thrust and Induced Drag

In contrast to the two-dimensional jet-flap case, complete thrust recovery is not, in view of the induced drag, obtained with a finite wing. It is to be understood that the chordwise loading distribution, leading edge suction, and the thrust component of the jet reaction will all contribute to the local thrust. In other words, the sectional thrust coefficient,  $c_t$ , can be given by:

$$c_t(y) = \frac{t(y)}{qc(y)} = c_{t_\Gamma}(y) + c_s(y) + c_{t_\mu}(y) \quad (2.92)$$

where  $c_{t_\Gamma}$ ,  $c_s$ , and  $c_{t_\mu}$  are, respectively, the contribution associated with pressure lift, leading edge suction, and jet reaction and are given by:

$$c_{t_{\Gamma}}(y) = -\frac{1}{c(y)} \int_{x_{\ell}(y)}^{x_t(y)} \Delta c_p(x,y) \epsilon(x,y) dx = -\int_0^1 \Delta c_p(\bar{x},y) \epsilon(\bar{x},y) d\bar{x}$$

$$\approx -\int_0^1 \gamma(\bar{x},y) \epsilon(\bar{x},y) d\bar{x} \quad (2.93)$$

$$c_s(y) = \frac{2\pi}{9} \frac{\delta_{\ell}(y)}{c(y)} \bar{\gamma}_{\ell}^2(y) \quad (2.94)$$

$$c_{t_{\mu}}(y) = c_{\mu}(y) \left(1 - \frac{\theta^2(y)}{2}\right) \quad (2.95)$$

It has been shown earlier, that in proximity to the ground there is some justification for the introduction of a correction to the lift and possibly the pitching moment given by the first-order theory. The correction was shown to be equivalent to evaluating  $\Delta c_p$  by the following expression

$$\Delta c_p = 2\gamma(x,y)[1 + u'(x,y)]$$

where  $u'$  in the "u" perturbation velocity induced by the image. In evaluating  $c_{t_{\Gamma}}$ , it will be noticed that the term  $2\gamma(\bar{x},y)u'(\bar{x},y)$  has been omitted. This approximation is not likely to cause a serious error in the drag. Alternatively, it can be argued that there is no justification for including the second-order term in  $\Delta c_p$  in the evaluation of  $c_{t_{\Gamma}}$  without considering higher-order terms in the determination of the leading-edge suction and its contribution to drag.

The derivation of the expression for leading-edge suction,  $c_s$ , is not, necessarily, self-apparent. A detailed discussion of the derivation of equation (2.94) is, therefore, contained in Appendix I.1.3. It should be noted here that  $\delta_{\ell}$  denotes the chordwise length of the leading-edge element, and  $\bar{\gamma}_{\ell}$  is the mean of the " $\gamma$ " distribution associated with the leading-edge EVD. It will be recalled that  $\bar{\gamma}_{\ell}$  was chosen as the unknown in the solution of the jet-wing problem and, thus, is obtained directly as one of the  $\gamma_j$ -solutions.

It has already been mentioned that, in general,  $c_t$  will be less than the section jet momentum coefficient  $c_\mu$ . The sectional induced drag coefficient is, therefore, defined as

$$c_{d_i}(y) = c_\mu(y) - c_t(y) \quad (2.96)$$

which, by introducing equations (2.92) and (2.95), can be expressed by:

$$c_{d_i}(y) = -c_{t_r}(y) - c_s(y) + c_\mu(y) \frac{\theta^2(y)}{2} \quad (2.97)$$

These three contributions to the sectional induced drag are second-order quantities and are nonlinear with respect, for example, to the angles  $\alpha$ ,  $\delta_f$ ,  $\delta_j$ .

#### 2.2.3.1.4 Sectional Aerodynamic Characteristics – Their Dependence on Angle of Attack

Although the strength of the vorticity obtained for each fundamental case in the solution of the jet-wing problem is linear with respect, for example, to the angles  $\alpha$ ,  $\delta_j$ , and  $\delta_f$ , in ground effect the aerodynamic loading parameter  $\Delta c_p$  is not. Hence, both the sectional lift and pitching moment, as well as the induced drag, will be nonlinear with respect to these angles.

Now in the equation for  $\Delta c_p$ , namely:

$$\Delta c_p(x,y) = 2[1 + u'(x,y)]\gamma(x,y) \quad (2.98)$$

the term  $u'(x,y)$  (i.e., the perturbation velocity induced in the  $xy$ -plane by the image of the jet-wing) is calculated from

$$u'_i(x,y) = \sum_{j=1}^N c_{ij} \gamma_j \quad (2.99)$$



The perturbation freestream velocity influence coefficient  $c_{ij}$  is derived in Appendix 1.1.5. Therefore, the term  $u'(x,y)\gamma(x,y)$  in equation (2.98) is nonlinear (i.e., quadratic) in  $\gamma$ . Accordingly, the fundamental case concept discussed in Section 2.2.1.4 applies only to the vorticity distribution and not to  $\Delta c_p$  and hence lift and pitching moment in ground effect. It should be noted that whether in or out of ground effect the induced drag coefficient,  $c_{di}$ , is second order and thus nonlinear in  $\gamma$ .

It has been found useful to consider composite case loading characteristics (for either free air or ground effect) in such a way that angle of attack,  $\alpha$ , becomes the independent variable. Hence,  $\Delta c_p$  for an arbitrary composite case composed of an angle of attack fundamental case and  $K$  other fundamental cases, each modulated by a factor  $a_m$ , is

$$\begin{aligned}
 \Delta c_p(x,y) &= 2 \left[ 1 + u'_\alpha(x,y) + \sum_{m=1}^K a_m u'_m(x,y) \right] \left[ \gamma_\alpha(x,y) + \sum_{m=1}^K a_m \gamma_m(x,y) \right] \\
 &= 2 \left[ 1 + \sum_{m=1}^K a_m u'_m(x,y) \sum_{m=1}^K a_m \gamma_m(x,y) \right] \\
 &\quad + 2 \left\{ u'_\alpha(x,y) \sum_{m=1}^K a_m \gamma_m(x,y) + \left[ 1 + \sum_{m=1}^K a_m u'_m(x,y) \right] \gamma_\alpha(x,y) \right\} \alpha \\
 &\quad + 2 \left[ u'_\alpha(x,y) \gamma_\alpha(x,y) \right] \alpha^2 \tag{2.100} \\
 &= \Delta c_{p_0}(x,y) + \Delta c_{p_\alpha}(x,y) \alpha + \Delta c_{p_\alpha^2}(x,y) \alpha^2
 \end{aligned}$$

The  $\Delta c_{p_\alpha^2}$  term is, of course, zero in the free-air case. It should be noted that  $u'_\alpha(x,y)$  and  $\gamma_\alpha(x,y)$  are obtained from a solution of the fundamental matrix equation (2.76) for a flat-plate wing at an angle of attack of unity (i.e., the so-called alpha case).

Having defined the ground effect pressure coefficient,  $\Delta c_p(x,y)$ , the sectional aerodynamic coefficients, with the exception of the induced drag, can be determined by suitable integration of  $\Delta c_p(x,y)$  in a manner similar to that of Sections 2.2.3.1.1 and 2.2.3.1.2. In the paragraphs that follow,

all three sectional aerodynamic characteristics will be expressed in coefficient form as a quadratic in terms of angle of attack.

Lift – The sectional lift coefficient  $c_{l_l}$  is composed of a circulation component  $c_{l_{\Gamma}}$  obtained by an integration of the chordwise loading distribution  $\Delta c_p(x,y)$  obtained in the above, and a reaction component  $c_{l_{\mu}}$ , and can be expressed by

$$c_{l_{\Gamma}}(y) = c_{l_{\Gamma_0}}(y) + c_{l_{\Gamma_{\alpha}}}(y)\alpha + c_{l_{\Gamma_{\alpha^2}}}(y)\alpha^2 \quad (2.101)$$

$$c_{l_{\mu}}(y) = c_{l_{\mu_0}}(y) + c_{l_{\mu_{\alpha}}}(y)\alpha \quad (2.102)$$

where

$$c_{l_{\Gamma_0}}(y) = \int_0^1 \Delta c_{p_0}(\bar{x},y) d\bar{x}; \quad c_{l_{\Gamma_{\alpha}}}(y) = \int_0^1 \Delta c_{p_{\alpha}}(\bar{x},y) d\bar{x};$$

$$c_{l_{\Gamma_{\alpha^2}}}(y) = \int_0^1 \Delta c_{p_{\alpha^2}}(\bar{x},y) d\bar{x} = 0, \quad (h = \infty)$$

$$c_{l_{\mu_{\alpha}}}(y) = c_{\mu}(y); \quad c_{l_{\mu_0}}(y) = c_{\mu}(y) \sum_{m=1}^K a_m \theta_m(y)$$

Pitching Moment – In direct correspondence with the discussion of Section 2.1.4.1.2 and equations (2.85) through (2.89), the sectional pitching moment coefficient  $c_{m_m}$  is composed of circulation, reaction lift, and reaction thrust coefficients, expressed as

$$c_{m_{\Gamma}}(y) = c_{m_{\Gamma_0}}(y) + c_{m_{\Gamma_{\alpha}}}(y)\alpha + c_{m_{\Gamma_{\alpha^2}}}(y)\alpha^2 \quad (2.103)$$

$$c_{m_{\mu}}(y) = c_{m_{\mu_0}}(y) + c_{m_{\mu_{\alpha}}}(y)\alpha \quad (2.104)$$

$$c_{m_t}(y) = c_{\mu}(y) \frac{\Delta z(y)}{c(y)} \quad (2.105)$$

where

$$\begin{aligned}
 c_{m_{\Gamma_0}}(y) &= - \int_0^1 \Delta c_{p_0}(\bar{x}, y) \bar{x} d\bar{x}; & c_{m_{\Gamma_\alpha}}(y) &= - \int_0^1 \Delta c_{p_\alpha}(\bar{x}, y) \bar{x} d\bar{x}; \\
 c_{m_{\Gamma_\alpha^2}}(y) &= - \int_0^1 \Delta c_{p_\alpha^2}(\bar{x}, y) \bar{x} d\bar{x} & &= 0, \quad (h = \infty) \\
 c_{m_{\mu_0}}(y) &= c_\mu(y); & c_{m_{\mu_\alpha}}(y) &= c_\mu(y) \sum_{m=1}^K a_{m\theta_m}(y)
 \end{aligned}$$

and  $\Delta z(y)/c(y)$  is defined by equation (2.89).

Thrust and Induced Drag – As discussed in Section 2.1.4.1.3, the sectional thrust coefficient is composed of circulation, leading-edge suction, and jet-reaction components, equation (2.93). As explained earlier, each one of these terms is nonlinear with respect to angle of attack. In or out of ground effect, therefore, equation (2.93) can be written as

$$c_{t_\Gamma}(y) = c_{t_{\Gamma_0}}(y) + c_{t_{\Gamma_\alpha}}(y)\alpha + c_{t_{\Gamma_\alpha^2}}(y)\alpha^2 \quad (2.106)$$

where

$$\begin{aligned}
 c_{t_{\Gamma_0}}(y) &= -2 \int_0^1 \gamma_0(\bar{x}, y) \epsilon(\bar{x}, y) d\bar{x} \\
 c_{t_{\Gamma_\alpha}}(y) &= -2 \int_0^1 \gamma_0(\bar{x}, y) + [\gamma_\alpha(\bar{x}, y) \epsilon(\bar{x}, y)] d\bar{x} \\
 c_{t_{\Gamma_\alpha^2}}(y) &= -2 \int_0^1 \gamma_\alpha(\bar{x}, y) d\bar{x}
 \end{aligned}$$

in which  $\gamma$  is expressed by:

$$\gamma = \gamma_0 + \gamma_\alpha$$

The leading-edge suction (i.e., equation (2.94)) can also be expressed by

$$c_s(y) = c_{s_0}(y) + c_{s_\alpha}(y)\alpha + c_{s_\alpha^2}(y)\alpha^2 \quad (2.107)$$

where

$$c_{s_0}(y) = \frac{2\pi}{9} \frac{\delta_\ell(y)}{c(y)} \bar{\gamma}_{\ell_0}^2(y)$$

$$c_{s_\alpha}(y) = \frac{4\pi}{9} \frac{\delta_\ell(y)}{c(y)} \bar{\gamma}_{\ell_0}(y) \bar{\gamma}_{\ell_\alpha}(y)$$

$$c_{s_\alpha^2}(y) = \frac{2\pi}{9} \frac{\delta_\ell(y)}{c(y)} \bar{\gamma}_{\ell_\alpha}^2(y)$$

Finally, the jet-reaction contribution to total thrust (i.e., equation (2.95)) is

$$c_{t_\mu}(y) = c_{t_{\mu_0}}(y) + c_{t_{\mu_\alpha}}(y)\alpha + c_{t_{\mu_\alpha^2}}(y)\alpha^2 \quad (2.108)$$

where

$$c_{t_{\mu_0}}(y) = c_\mu(y) \left\{ 1 - \frac{1}{2} \left[ \sum_{m=2}^K \theta_m(y) \right]^2 \right\}$$

$$c_{t_{\mu_\alpha}}(y) = c_\mu(y) \sum_{m=2}^K \theta_m(y)$$

$$c_{t_{\mu_\alpha^2}}(y) = \frac{1}{2} c_\mu(y)$$

Note that the first fundamental case (i.e.,  $m = 1$ ) is assumed to be the "alpha" case.

### 2.2.3.2 Total Aerodynamic Forces and Moments

In the derivation of total aerodynamic forces and moments it has been assumed (see Section 2.2.1.3) that all geometric parameters have been normalized by  $b/2$  and that, for convenience, all normalized variables retain their original symbols. The equations derived in the following sections apply both in and out of ground effect.

### 2.2.3.2.1 Lift

The total lift coefficient  $C_L$  follows directly from a spanwise integration of the sectional quantities and can be expressed by:

$$C_L = \frac{L}{qS} = C_{L_T} + C_{L_J} \quad (2.109)$$

where

$$C_{L_T} = \frac{1}{S} \int_{-1}^{+1} c(y) c_{\ell_T}(y) dy \quad (2.110)$$

and

$$C_{L_J} = \frac{1}{S} \int_{-1}^{+1} c(y) c_{\ell_u}(y) dy \quad (2.111)$$

The first integral (i.e., equation (2.110)) corresponds to the pressure lift and the second integral the lift-reaction contribution due to the rate of change of momentum in the jet. Although various numerical methods may be used in the evaluation of these integrals, it has been established that a simple step-function procedure (i.e., assuming a constant integrand within the spanwise integral) is adequate for this purpose. Finally, it should be noted that the lift curve slope corresponds to the lift coefficient for the angle-of-attack case with a unit angle of attack.

### 2.2.3.2.2 Pitching Moment

To obtain the pitching moment coefficients, a moment center must first be selected. Let it be located at the wing apex ( $x = 0, y = 0$ ). Recall that for each wing section the sectional moment is calculated about the sectional leading edge which does not necessarily coincide with  $x = 0$  because of the wing sweep. Therefore, the pitching moments  $C_{m_T}$ ,  $C_{m_J}$ , and  $C_{m_T}$  (nose up positive) due to the pressure loading, and the vertical and horizontal components of the jet reaction, respectively, are given as follows:

$$C_{m_T} = \frac{1}{Sc} \int_{-1}^{+1} \left[ c^2(y) c_{m_T}(y) - c(y) c_{\ell_T}(y) x_{\ell}(y) \right] dy \quad (2.112)$$

$$C_{m_J} = \frac{1}{S\tilde{c}} \int_{-1}^{+1} [c^2(y)c_{m_\mu}(y) - c(y)c_{\ell_\mu}(y)x_\ell(y)] dy \quad (2.113)$$

and

$$C_{m_T} = \frac{1}{S\tilde{c}} \int_{-1}^{+1} [c^2(y)c_{m_t}(y) - c(y)c_\mu(y)h_\ell(y)] dy \quad (2.114)$$

where  $\tilde{c}$  denotes the reference chord, usually the MAC. Also, in the above,  $h_\ell$  is the vertical displacement (normal to the free-stream) of the wing leading edge above the wing apex. At any section,

$$h_\ell(y) = h_t(y) - x_\ell(y)\alpha - c(y)\theta_s(y) + \sum_{i=1}^{K_S} c_{f_i}(y)\delta_{s_i}(y) \quad (2.115)$$

where the summation is over the leading edge flap angles only. The initial displacement due to twist, etc., is represented by  $h_t(y)$ .

The total pitching moment coefficient is simply the sum,

$$C_m = \frac{M}{qS\tilde{c}} = C_{m_\Gamma} + C_{m_J} + C_{m_T} \quad (2.116)$$

The moment center need not, of course, be at the apex, but calculating the pitching moment about any other moment center becomes only a matter of coordinate transformation after the pitching moment about the apex is known.

The center of pressure may be expressed by

$$\frac{x_{C.p.}}{\tilde{c}} = -\frac{C_{m_\Gamma}}{C_{L_\Gamma}} \quad (2.117)$$

and the center of total lift is given by

$$\frac{x_{C.L.}}{\tilde{c}} = -\frac{C_{m_\Gamma} + C_{m_J}}{C_L} \quad (2.118)$$

Both are measured from the apex of the wing.

### 2.2.3.2.3 Thrust and Induced Drag

By integrating their counterparts in a section, the thrust coefficients due to the pressure, leading-edge suction, and jet reaction, respectively, are obtained as follows:

$$C_{T_P} = \frac{1}{S} \int_{-1}^{+1} c(y)c_{t_P}(y)dy \quad (2.119)$$

$$C_S = \frac{1}{S} \int_{-1}^{+1} c(y)c_s(y)dy \quad (2.120)$$

and

$$\begin{aligned} C_{T_J} &= \frac{1}{S} \int_{-1}^{+1} c(y)c_{t_\mu}(y)dy \\ &= C_J - \frac{1}{S} \int_{-1}^{+1} c(y)c_\mu(y) \frac{\theta^2(y)}{2} dy \end{aligned} \quad (2.121)$$

The total thrust coefficient therefore becomes

$$C_T = \frac{T}{qS} = C_{T_P} + C_S + C_{T_J} \quad (2.122)$$

The induced drag coefficient, as in the sectional calculation, is defined as the difference between the ideal value of the thrust  $C_J$  and the actual thrust  $C_T$ ; that is,

$$C_{D_i} = C_J - C_T \quad (2.123)$$

This is not to imply, however, that there is complete thrust recovery. The deficiency in thrust recovery is considered to be part of the induced drag. On substituting for  $C_T$  equation (2.122) can be expressed by

$$C_{D_i} = -C_{T_r} - C_S + \frac{1}{S} \int_{-1}^{+1} c(y)c_{\mu}(y) \frac{\theta^2(y)}{2} \quad (2.124)$$

Note that  $C_{D_i}$  is a second-order quantity and varies nonlinearly, for example, with angle of attack  $\alpha$ .

#### 2.2.3.2.4 Side Force

In view of the assumptions adopted regarding the conditions of jet emission, the total side force coefficient  $C_Y$ , can be expressed by:

$$C_Y = \frac{1}{S} \int_{-1}^{+1} c(y)c_s(y) \frac{dx_{\ell}(y)}{dy} dy \quad (2.125)$$

where  $\tan^{-1}(dx_{\ell}(y)/dy)$  is, of course, the local leading-edge sweepback angle  $\Lambda_{\ell}(y)$ . It will be noted that in deriving equation (2.125), it has been assumed that the resultant leading-edge suction force acts normal to the leading edge (see Appendix I.3).

#### 2.2.3.2.5 Rolling Moment

The rolling moment coefficient  $C_{l_1}$ , about the x-axis (right wing down positive) is calculated in two components, that due to the pressure lift

$$C_{l_{1r}} = -\frac{1}{Sb} \int_{-1}^{+1} c(y)c_{\ell r}(y)ydy \quad (2.126)$$

and that due to the vertical component of jet reaction

$$C_{l_{1j}} = -\frac{1}{Sb} \int_{-1}^{+1} c(y)c_{\ell \mu}(y)ydy \quad (2.127)$$

This total rolling moment coefficient is given by



$$C_l = \frac{L}{qSb} = C_{l_T} + C_{l_J} \quad (2.128)$$

where  $L$  is used to denote the rolling moment (instead of the lift). The reference-span width  $b$  must be equal to two to be consistent with the present normalized variable system.

### 2.2.3.2.6 Yawing Moment

In the derivation of the relevant equation for total yawing moment coefficient (right wing backward positive) it will be assumed that the reference moment center is at the wing apex. The yawing moment comprises two terms; one is associated with the chordwise loading and leading-edge suction and is given by the expression

$$C_{n_T} = -\frac{1}{Sb} \int_{-1}^{+1} c(y)c_{t_T}(y)ydy - \frac{1}{Sb} \int_{-1}^{+1} c(y)c_s(y) \left[ x_\ell(y) \frac{dx_\ell(y)}{dy} + y \right] dy \quad (2.129)$$

The other term represents the yawing moment contribution due to any asymmetrical distribution of the horizontal component of the jet reaction. The jet deflection angle  $\theta(y)$  being small by hypothesis, a yawing moment coefficient denoted by  $C_{n_J}$  can be expressed by

$$C_{n_J} = -\frac{1}{Sb} \int_{-1}^{+1} c(y)c_\mu(y)ydy + \frac{1}{Sb} \int_{-1}^{+1} c(y)c_\mu(y) \frac{\theta^2(y)}{2} ydy \quad (2.130)$$

where the first part is due to the ideal thrust.

Finally, the expression for total yawing moment is

$$C_n = \frac{N}{qSb} = C_{n_J} + C_{n_T} \quad (2.131)$$

where, again,  $b$  must be equal to 2.

### 2.2.3.2.7 Alternative Approach to the Estimation of Induced Drag – Momentum Analysis

It has already been established<sup>16</sup> that in the two dimensional case the jet must ultimately become parallel to the undisturbed stream, otherwise the entire flow field would eventually deviate from the horizontal and possess an infinite vertical momentum. It has also been stated that by considering the horizontal flux of momentum across a plane far downstream the thrust experienced by a two dimensional jet-flap airfoil is independent of the jet deflection angle and equal to the total momentum flux of the jet. In the three dimensional case, however, the jet remains deflected, and the thrust  $T$  is less than the total jet momentum flux  $\mathcal{J}$ . The difference between the two has been defined as the induced drag. In Section (2.2.3.2), a relationship for induced drag in terms of an integration of the detailed forces acting on the wing was established. An alternative approach for the evaluation of total induced drag based on a far-field momentum analysis will be briefly described below. It should be noted that all variables are considered dimensional, in contrast to the preceding parts of Section (2.2.3) and that the jet-wing will initially be considered to be out of ground effect (i.e.,  $h = \infty$ ).

Consider a control volume, figure (2.6), surrounding the jet-wing system whose surfaces are either parallel or perpendicular to the free-stream flow. The total force which the fluid in the control volume exerts on the wing is given by the momentum equation. This is expressed as

$$\vec{F} = - \iint_{\Sigma} p \vec{n} dS - \iint_{\Sigma} \rho \vec{q} (\vec{q} \cdot \vec{n}) dS \quad (2.132)$$

where the integration is over the surface which bounds the control volume. Far from the wing, this surface is denoted by  $\Sigma$  and has a unit normal vector  $\vec{n}$  taken positive out from the control volume.  $p$ ,  $\rho$ , and  $\vec{q}$  are the fluid pressure, density, and velocity, respectively.

By adopting small perturbation concepts, both  $\vec{q}$  and  $p$  can, for any point on the control surface, be expressed by

$$\vec{q} = U \vec{e}_x + \vec{q}'(u, v, \bar{w}) \quad (2.133)$$

and

$$p = p_{\infty} + \frac{1}{2} \rho (U^2 - \vec{q}^2) = p_{\infty} - \rho (Uu + \frac{1}{2} \vec{q}'^2) \quad (2.134)$$

Hence, equation (2.132) can be rewritten as

$$\vec{F} = \rho \iint_{\Sigma} \left\{ \left( Uu + \frac{1}{2} \vec{q}'^2 \right) \vec{n} - \left[ (U\vec{e}_x + \vec{q}') \cdot \vec{n} \right] (U\vec{e}_x + \vec{q}') \right\} ds \quad (2.135)$$

Now, let the control volume expand. In the limit, as the control surfaces approach infinity, all perturbation velocities at any point on a control surface will vanish except those associated with the downstream control surface. This surface, which is normal to the undisturbed stream is commonly referred to as the Trefftz plane. In fact, the perturbation flow ( $v$  and  $\bar{w}$  only) becomes two dimensional in this plane. The momentum integral, equation (2.135), now reduces to a Trefftz plane integral only, that is

$$F = \rho \iint_{\text{T.P.}} \left[ \frac{1}{2} (v^2 + \bar{w}^2) \vec{e}_x - U\vec{q}' \right] dy dz - \int_{\substack{-b/2 \\ \text{T.P.}}}^{b/2} J(y) dy + QU\vec{e}_x \quad (2.136)$$

The second term in equation (2.136) represents the momentum flux of the jet which in the Trefftz plane is assumed to leave the control volume through a slit  $-b/2 \leq y \leq b/2$ ,  $z = 0$ , at a small angle  $\alpha_{i\infty}(y)$  with respect to the free-stream direction or  $x$  axis. The last term is the ram-drag of the propulsive system where  $Q$  is that part of the mass flow not emitted by a source within the wing. On writing out the lift and thrust components explicitly,

$$L = -\rho U \iint_{\text{T.P.}} \bar{w} dy dz + \int_{-b/2}^{b/2} J(y) \alpha_{i\infty}(y) dy \quad (2.137)$$

$$T = -\rho \iint_{\text{T.P.}} \frac{1}{2} (v^2 + \bar{w}^2) dy dz + \int_{-b/2}^{b/2} J(y) \left( 1 - \frac{\alpha_{i\infty}^2}{2} \right) dy - QU \quad (2.138)$$

Since  $Q$  has been assumed to be zero (i.e., source type flow), the induced drag which has been defined as the difference between the ideal thrust  $\bar{J}$  and the real thrust  $T$ , is then

$$D_i = \bar{J} - T = \rho \iint_{T.P.} \frac{1}{2} (v^2 + \bar{w}^2) dydz + \frac{1}{2} \int_{-b/2}^{b/2} J(y) \alpha_i^2 dy \quad (2.139)$$

Consider the Trefftz plane integrals contained in the above equations. The first integral is

$$\iint_{T.P.} \bar{w} dydz = \int_{-\infty}^{\infty} \int_{-\infty}^{\infty} \frac{\partial \phi}{\partial z} dz dy = \int_{-b/2}^{b/2} [\phi_-(y) - \phi_+(y)] dy \quad (2.140)$$

where  $\bar{w}$  has been written in terms of the velocity potential  $\phi$ , and  $\phi_-$  and  $\phi_+$  are the  $\phi$  values on the lower and upper surfaces, respectively, of the jet sheet or the trailing-vortex sheet. Now, the circulation  $\Gamma$  around the wing and jet in a plane  $y = \text{const.}$  can be expressed by

$$\Gamma(y) = \oint \vec{q} \cdot d\vec{s} = \phi_+ - \phi_- \quad (2.141)$$

Hence,

$$\iint_{T.P.} \bar{w} dydz = - \int_{-b/2}^{b/2} \Gamma(y) dy \quad (2.142)$$

Incidentally, the total circulation  $\Gamma$  according to the jet-wing lifting surface theory is also given by

$$\Gamma(y) = \int_{x_l}^{\infty} \gamma(x) dx \quad (2.143)$$

For the second integral, an application of Green's Theorem yields

$$\begin{aligned} \iint_{T.P.} (v^2 + \bar{w}^2) dydz &= \iint_{T.P.} (\nabla\phi)^2 dydz \\ &= \int_{-b/2}^{b/2} -\phi_+ \frac{\partial\phi_+}{\partial z} dy + \int_{-b/2}^{b/2} \phi_- \frac{\partial\phi_-}{\partial z} dy = \int_{-b/2}^{b/2} U\alpha_{i_\infty}(y)\Gamma(y)dy \end{aligned} \quad (2.144)$$

In equation (2.144)  $U\alpha_{i_\infty}$  has been substituted for  $w = \partial\phi_+/\partial z = \partial\phi_-/\partial z$ .

In view of the above

$$L = \int_{-b/2}^{b/2} [\rho U\Gamma(y) + J(y)\alpha_{i_\infty}(y)] dy \quad (2.145)$$

$$D_i = \frac{1}{2} \int_{-b/2}^{b/2} [\rho U\Gamma(y) + J(y)\alpha_{i_\infty}(y)] \alpha_{i_\infty}(y) dy \quad (2.146)$$

The integrand in the lift expression, equation (2.145), can be identified as the spanwise lift distribution. Now it can be shown from an integration of the jet boundary condition (i.e., equation (2.33)), that

$$J(y)\theta(y) = J(y)\alpha_{i_\infty}(y) + \rho U \int_{x_t}^{\infty} \gamma(x,y) dx \quad (2.147)$$

Then, by definition, the sectional lift is given by:

$$l(y) = \rho U \int_{x_\ell}^{x_t} \gamma(x,y) dx + J(y)\theta(y) \quad (2.148)$$

It follows directly from equations (2.147) and (2.148) that the sectional lift can also be expressed by:

$$\ell(y) = \rho U \Gamma(y) + J(y) \alpha_{i\infty}(y) \quad (2.149)$$

Since similar expressions (i.e., equations (2.148) and (2.149)) for the induced drag cannot be derived, the integrand in equation (2.146) must not be interpreted as the spanwise induced drag distribution.

Written in nondimensional forms, the lift and drag equations become

$$C_L = \frac{1}{S} \int_{-1}^{+1} c(y) c_\ell(y) dy \quad (2.150)$$

and

$$C_{D_i} = \frac{1}{2S} \int_{-1}^{+1} c(y) c_\ell(y) \alpha_{i\infty}(y) dy \quad (2.151)$$

This completes for a jet-wing out of ground effect the derivation of an alternative expression for induced drag. A similar expression for a jet-wing in ground proximity can also be developed. Although the theory will be left to the reader to develop, two points should be noted. First, the total lift, jet-wing plus image, will be zero. Second, the final expression for the induced drag coefficient (i.e.,  $C_{D_i}$ ) must not, of course, include the correction to the spanwise lift distribution for the "u" perturbation velocity induced by the image. In other words, the induced drag must be evaluated by making use of equation (2.146) with  $\alpha_{i\infty}$  being now the total downwash angle.

Whether in or out of ground effect the downwash angle  $\alpha_{i\infty}(y)$  may be evaluated according to the following formula:

$$\alpha_{i\infty}(y) = \frac{1}{2\pi U} \int_{-1}^{+1} \frac{d\Gamma(\eta)/d\eta}{y-\eta} d\eta - \frac{1}{2\pi U} \int_{-1}^{+1} \frac{(y-\eta) d\Gamma(\eta)/d\eta}{(2h)^2 + (y-\eta)^2} d\eta \quad (2.152)$$

where  $b/2$  is assumed equal to 1.

The first integral follows either from a reduction of the general downwash equation (2.26), or by imagining a two-dimensional vortex distribution of intensity  $d\Gamma(y)/d\eta$  along the slit (jet and trailing vortex sheet) in the Trefftz plane. The second integral represents the downwash induced by the wake of the image jet-wing.

Since  $\Gamma(y)$  is known from the jet-wing EVD solution, the downwash angle  $\alpha_{i\infty}(y)$  can now be evaluated numerically (see Appendix I.4). With  $\alpha_{i\infty}(y)$  so determined and the lift distribution also known, the induced drag can easily be determined. Incidentally, this drag value provides a check on the drag value calculated directly by the pressure integration method outlined in Section (2.2.3.1.3).

## 2.2.4 Dynamic Stability Derivatives

### 2.2.4.1 General Remarks

In general, the aerodynamic forces and moments acting on an aircraft at any instant depend strictly on the whole history of the motion. That this must be so follows essentially from the fact that the aircraft sheds eddies or vortices in the air as it moves through it, and these vortices, which have a considerable degree of permanence, continue to influence the flow in the neighborhood of the aircraft. The evaluation of the forces and moments acting on an aircraft at any one instant is, in general, extremely difficult. There are, however, important cases where the influence of past motions is negligible and others in which such influence is calculated with comparative ease because the past motion conforms to some simple type. In a general way it can be said that past history is only of great importance when there are sudden and violent changes of motion or configuration, for then the induced velocities in the vicinity of the aircraft are, therefore, large. In fact, in most investigations concerning aircraft stability and control, it is important to know simply the change in a force or moment brought about by a small change in a component of velocity or acceleration. The method of representing these changes in the aerodynamic forces and moments is essentially that introduced by Bryan. It is in this method that the concept of an aerodynamic derivative is introduced. It is important to note, however, that derivatives exist and are constant (i.e., independent of time) only in the following circumstances:

- (a) Where all the velocities of deviation are extremely small in relation to the displacements of deviation, and the acceleration is very small in relation to the velocities. The derivatives for this case can be evaluated on the basis of purely quasi-steady consideration.
- (b) Where all the aerodynamic perturbations are proportional to the exponential function of time  $e^{\lambda t}$ , where  $\lambda$  is a real, pure imaginary or complex constant, and the motion of deviation has existed for an infinite time. The derivatives then are functions of  $\lambda$ .

It is fortunate that the kinds of motion which occur in investigations



of aircraft stability are associated with the two types of disturbances mentioned above since the use of constant derivatives in the derivation and solution of the equations of motion becomes justified. It must be admitted, however, that the influence of the frequency parameter associated with aerodynamic perturbations has hitherto been neglected in most investigations of the stability of an aircraft, although it has been taken into account in flutter analysis. There can be no doubt that it is incorrect to use the same derivatives for long-period and short-period motions; for instance, the derivatives appropriate to the phugoid oscillation will not strictly be applicable to the rapid longitudinal oscillation.

In the preceding sections a method for the determination of the static longitudinal and lateral stability and control coefficients and derivatives of an arbitrary jet-wing was considered. It has also been argued that the evaluation of dynamic derivatives based on the assumption of quasi-steady flow conditions should suffice for most stability calculations. In other words, the theory of steady motion, in this case the EVD Jet-Wing Lifting Surface Theory, together with the correct boundary conditions for unsteady flow might be sufficiently accurate to permit the prediction of stability derivatives due to pitching, rolling, yawing, and sideslipping. This is, of course, the so-called quasi-static method. The following remarks may be sufficient to explain the procedure which it is usual to consider and which has here been adopted as the quasi-static approach to the evaluation of the dynamic derivatives of a jet-wing.

Consider a flat wing which rotates about an axis  $\ell$  in its own plane and at the same time is displaced with constant linear velocity in a direction parallel to  $\ell$ . Let  $\ell$  be the  $x$ -axis of a system of coordinates which moves with the jet-wing, such that the positive direction of the  $x$ -axis is opposed to the direction of motion of the wing; and the  $y$ - and  $z$ -axes are in the plane of the wing and normal to it.

Let  $p$  be the angular velocity of the wing, and let  $\phi$  be the velocity potential of the motion referred to a system of coordinates which is at rest relative to the medium at infinity, but which coincides instantaneously with

the system of coordinates defined above. Then it is not difficult to see directly that the boundary condition at the wing is

$$-w = \frac{\partial \phi}{\partial z} = \rho y.$$

The above equation can also be derived formally from the general boundary condition for unsteady flow.

The product  $\rho b$  will now be considered small compared with the forward velocity  $U$ , where  $b$  is the span of the wing. As the wing advances, a sheet of trailing vortices is formed in its wake. At the same time, the jet sheet is itself displaced. An additional distribution of vorticity, in this case bound and trailing, can be associated with this action. The velocity distribution induced at the wing by the vorticity associated both with the jet sheet and wake is determined by the law of Biot-Savart. It can be readily shown that according to that law the effect of vortex elements which are sufficiently far downstream (say more than three space lengths) is unimportant. On the other hand, if the angular velocity  $\rho$  is sufficiently small, as assumed above, and if the jet emerges from the wing at a small angle relative to the direction of motion of the wing, an assumption made earlier in the development of the EVD method, then the remaining portion of the vortex system, just downstream of the wing, is approximately plane. So far as the calculation of the flow around the wing is concerned, it therefore will be assumed that the vortex system associated with the jet sheet and wing wake is situated in the  $x, y$ -plane. Thus, the entire problem is reduced to one of steady flow in three dimensions, and this simplified problem can be solved by the EVD Jet-Wing Lifting Surface Theory. It also appears that the wing boundary condition can now be interpreted as that due to a linearly varying twist in the spanwise direction for an equivalent steady case.

There are of necessity some assumptions adopted in the quasi-static approach to the evaluation of jet-wing dynamic derivatives which could be criticized. The authors recognize that further work on the calculation of dynamic derivatives will be necessary. For example, experimental measurements of such derivatives under oscillatory condition should be conducted in

order to ascertain whether periodic variations in the jet bound vorticity and the wing and jet trailing vorticity can introduce phase lags of practical importance. In other words, the authors are of the opinion that further analytical studies leading to either an improvement in the present method or the development of methods for predicting derivatives associated with experimental deviations, for example, should await experimental confirmation of the present method.

The procedure or so-called quasi-static method that will be adopted in determining the dynamic derivatives associated with the motion of a jet-wing in steady pitch, roll, yaw, or sideslip has been introduced. It has been explained that the simplifying assumptions reduce the problem to one in which the determination of aerodynamic loads and stability derivatives simply requires the use of the EVD method, together with the corresponding boundary conditions for unsteady flow. These boundary conditions as well as some of the details associated with evaluating the derivatives once having determined the aerodynamic loads are discussed below.

#### 2.2.4.2 Pitching Jet-Wing

The motion of a wing in steady pitch can be considered as the motion of a wing along a circular path. The boundary condition associated with the curvature of the flight path is equivalent to a chordwise variation in the slope of the camber line or, within the framework of the assumptions adopted earlier, equivalent to a chordwise variation in induced downwash.

Let c.g.  $(x_{c.g.}, 0, 0)$  be the origin of a stability axes system (figure 2.7). For a wing undergoing a motion of steady pitch or roll, or yaw, the  $x_s$  axis will be taken to be parallel to the original  $x_s$  axis. If  $q$  is the rate of pitch about the  $y_s$  axis, then the induced downwash,  $\frac{\Delta W}{U}$ , can be expressed by

$$\frac{\Delta W}{U} = \left( \frac{q\tilde{c}}{2U} \right) \frac{b}{\tilde{c}} \left( \frac{x}{b/2} - \frac{x_{c.g.}}{b/2} \right) \quad (2.153)$$

Consider next the boundary conditions pertinent to the solution of the jet-wing problem. (i.e., equations (2.32), (2.33), (2.34), and (2.35)). Bearing

in mind that a quasi-static procedure has been adopted, these boundary conditions must be replaced by

$$w(x,y) = \left(\frac{q\tilde{c}}{2U}\right)\left(\frac{2}{\tilde{c}}\right)(x-x_{c.g}) + \epsilon(x,y), \quad (z=0, \text{ wing portion}) \quad (2.154)$$

$$\frac{\partial w(x,y)}{\partial x} = -\frac{2}{c(y)c_{\mu}(y)} \gamma(x,y), \quad (z=0, \text{ jet portion}) \quad (2.155)$$

$$w(x,y) = \left(\frac{q\tilde{c}}{2U}\right) \frac{2}{\tilde{c}} (x_t(y) - x_{c.g}) + \theta(y), \quad (x = x_t^+(y), \text{ when } c_{\mu}(y) \neq 0) \quad (2.156)$$

$$\gamma(x,y) = 0, \quad \begin{cases} x \rightarrow \infty, \text{ when } c_{\mu}(y) \neq 0 \\ x = x_t^-(y), \text{ when } c_{\mu}(y) = 0 \end{cases} \quad (2.157)$$

where  $x$  and  $y$  are retained as nondimensional variables (i.e., nondimensionalized by  $b/2$ ) and  $w$  is the total downwash (i.e., it includes the downwash induced by the jet-wing image (see Section 2.2.1.5))

For a given jet-wing geometry and height from the ground, equations (2.154) through (2.157) are linear in  $\left(\frac{q\tilde{c}}{2U}\right)$ . Hence, a solution for the vorticity distribution due to pitching can be readily obtained by considering one additional fundamental case in the solution of equation (2.76).

Having determined  $\gamma$  one can now calculate the loading or pressure jump coefficient  $\Delta c_p$  at any point by means of equation (2.81). In other words,

$$\Delta c_p(x,y) = 2 \left[ 1 + u'(x,y) \right] \gamma(x,y) \quad (2.158)$$

where  $u'$  is the perturbation velocity induced in the freestream direction by the jet-wing image. If  $u'$  and  $\gamma$  are written as

$$\begin{aligned}
u'(x,y) &= u'_0(x,y) + \hat{q} \frac{\partial u'(x,y)}{\partial \hat{q}} \\
\gamma(x,y) &= \gamma_0(x,y) + \hat{q} \frac{\partial \gamma(x,y)}{\partial \hat{q}}
\end{aligned}
\tag{2.159}$$

where  $q = \frac{\rho \tilde{c}}{2U}$  then equation (2.158) becomes

$$\begin{aligned}
\Delta C_p(x,y) &= 2 \left( 1 + u'_0(x,y) + \hat{q} \frac{\partial u'(x,y)}{\partial \hat{q}} \right) \\
&\quad \left( \gamma_0(x,y) + \hat{q} \frac{\partial \gamma(x,y)}{\partial \hat{q}} \right)
\end{aligned}
\tag{2.160}$$

This yields

$$C_{Lq} = \frac{\partial C_L}{\partial \hat{q}} = \frac{1}{S} \iint_S \frac{\partial \Delta C_p(x,y)}{\partial \hat{q}} dx dy
\tag{2.161}$$

for the lift pitching derivative which may also be written in the form

$$C_{Lq} = \left\{ \begin{array}{ll} C_{Lq_0} + \hat{q} C_{Lq_1}, & (h < \infty) \\ C_{Lq_0}, & (h = \infty) \end{array} \right\}
\tag{2.162}$$

where

$$\begin{aligned}
C_{Lq_0} &= \frac{1}{S} \iint_S \left[ \left( 1 + u'_0(x,y) \right) \frac{\partial \gamma(x,y)}{\partial \hat{q}} \right. \\
&\quad \left. + \gamma_0(x,y) \frac{\partial u'(x,y)}{\partial \hat{q}} \right] dx dy
\end{aligned}$$

and

$$C_{Lq_1} = \frac{2}{S} \iint_S \frac{\partial u'(x,y)}{\partial \hat{q}} \frac{\partial \gamma(x,y)}{\partial \hat{q}} dx dy$$

Similarly, for the pitching moment derivative about the  $y_s$  axis

$$C_{m_q} = \frac{\partial C_m}{\partial \dot{q}} = \left\{ \begin{array}{l} C_{m_{q_0}} + \hat{q} C_{m_{q_1}}, \quad (h < \infty) \\ C_{m_{q_0}}, \quad (h = \infty) \end{array} \right\} \quad (2.163)$$

where

$$C_{m_{q_0}} = \frac{1}{cS} \iint_S \left[ \left( 1 + u'_0(x,y) \right) \frac{\partial \gamma(x,y)}{\partial \dot{q}} + \gamma_0(x,y) \frac{\partial u'(x,y)}{\partial \dot{q}} \right] x dx dy$$

$$C_{m_{q_1}} = \frac{2}{cS} \iint_S \frac{\partial u'(x,y)}{\partial \dot{q}} \cdot \frac{\partial \gamma(x,y)}{\partial \dot{q}} dx dy$$

#### 2.2.4.3 Rolling Jet-Wing

The rolling jet-wing was introduced in Section (2.2.4.1). It was shown, as an example of the application of the quasi-static method, that the unsteady boundary condition was equivalent in the steady theory to a spanwise variation of wing twist. With reference to figure (2.7b), if  $p$  is denoted as the rate of roll about the  $x_s$  axis, then the local angle of attack or induced downwash can be expressed by

$$\frac{\Delta w}{U} = \left( \frac{pb}{2U} \right) \frac{y}{b/2} \quad (2.164)$$

It follows that the jet-wing boundary conditions can be written as

$$w(x,y) = \left( \frac{pb}{2U} \right) y + \epsilon(x,y), \quad (z = 0, \text{ wing portion}) \quad (2.165)$$

$$\frac{\partial w(x,y)}{\partial x} = - \frac{2}{c(y)c_u(y)} \gamma(x,y), \quad (z = 0, \text{ jet portion}) \quad (2.166)$$

$$w(x,y) = \left( \frac{pb}{2U} \right) y + \theta(y), \quad (x = x_t^+(y), \text{ when } c_u(y) \neq 0) \quad (2.167)$$

$$\gamma(x,y) = 0, \quad \left\{ \begin{array}{l} x \rightarrow \infty, \text{ when } c_u(y) \neq 0 \\ x = x_t^-(y), \text{ when } c_u(y) = 0 \end{array} \right\} \quad (2.168)$$

The aerodynamic derivatives for a steady roll motion can be expressed in a similar form to those derived for the pitch motion. Three derivatives will be considered. The first, the rolling moment derivative can be written as

$$C_{lp} = \frac{\partial C_l}{\partial \hat{\beta}} = \left\{ \begin{array}{l} C_{lp} + \hat{\beta} C_{lp_1}, \quad (h < \infty) \\ C_{lp_0}, \quad (h = \infty) \end{array} \right\} \quad (2.169)$$

where

$$C_{lp_0} = \frac{1}{Sb} \iint_S \left[ (1 + u'_0(x,y)) \frac{\partial \gamma(x,y)}{\partial \hat{\beta}} + \gamma_0(x,y) \frac{\partial u'(x,y)}{\partial \hat{\beta}} \right] y dx dy$$

and

$$C_{lp_1} = \frac{2}{Sb} \iint_S \frac{\partial u'(x,y)}{\partial \hat{\beta}} \cdot \frac{\partial \gamma(x,y)}{\partial \hat{\beta}} y dx dy$$

Note that  $\hat{\beta}$  has been substituted for  $\left(\frac{pb}{2U}\right)$ .

The second derivative is the yawing moment due to rate of roll. In deriving the following expression, the reader should refer to Sections (2.2.3.1.3) and (2.2.3.2.6).

$$C_{np} = \frac{\partial C_n}{\partial \hat{\beta}} = C_{np_0} + \hat{\beta} C_{np_1}, \quad (h \leq \infty) \quad (2.170)$$

where

$$C_{np_0} = - \frac{4\pi}{9Sb} \int_{-1}^{+1} \delta_\ell(y) \bar{\gamma}_{\ell_0}(y) \frac{\partial \gamma_\ell(y)}{\partial \hat{\beta}} \left( x_\ell(y) \frac{dx_\ell(y)}{dy} + y \right) dy$$

$$+ \frac{1}{Sb} \iint_S \frac{\partial \gamma(x,y)}{\partial \hat{\beta}} \epsilon(x,y) y \, dx dy$$

and

$$C_{np_1} = \frac{8\pi}{9Sb} \int_{-1}^{+1} \left( \frac{\partial \gamma_\ell(y)}{\partial \hat{\beta}} \right)^2 \left[ x_\ell(y) \frac{dx_\ell(y)}{dy} + y \right] dy$$

It again will be noted here that  $\delta_\ell$  denotes the chordwise length of the leading-edge element,  $\bar{\gamma}_\ell = \gamma_{\ell_0} + \frac{\partial \gamma_\ell}{\partial \hat{\beta}} \hat{\beta}$  is the mean of the "y" distribution associated with the Leading-Edge EVD, and  $\tan^{-1} \left( \frac{dx_\ell}{dy} \right)$  is the local leading edge sweepback angle.

The third and final derivative is the side force due to rate of roll. Although small in magnitude and normally neglected in stability analysis, the equation for deriving it is, for completeness, given here.

$$C_{Yp} = \frac{\partial C_Y}{\partial \hat{\beta}} = C_{Yp_0} + \hat{\beta} C_{Yp_1}, \quad (h \leq \infty) \quad (2.171)$$

where

$$C_{Yp_0} = \frac{4\pi}{9S} \int_{-1}^{+1} \delta_\ell(y) \bar{\gamma}_{\ell_0}(y) \frac{\partial \gamma_\ell(y)}{\partial \hat{\beta}} \frac{dx_\ell(y)}{dy} dy$$

and

$$C_{Yp_1} = \frac{8\pi}{9S} \int_{-1}^{+1} \left( \frac{\partial \bar{\gamma}_\ell(y)}{\partial \hat{\beta}} \right)^2 \frac{dx_\ell(y)}{dy} dy$$



#### 2.2.4.4 Yawing Jet-Wing

The analysis of the yawing jet-wing is more complex since the magnitude and direction of the onset flow relative to the wing are functions of both the spanwise and chordwise position on the wing. The components parallel and normal to the plane of symmetry are

$$\frac{\Delta u}{U} = \left( \frac{rb}{2U} \right) \frac{y}{b/2} \quad (2.172)$$

and

$$\frac{\Delta v}{U} = - \left( \frac{rb}{2U} \right) \frac{x-x_{c.g}}{b/2} \quad (2.173)$$

where  $r$  is the rate of yaw about the  $z_s$  axis. Within the framework of the EVD lifting surface theory, accepting the hypothesis of small perturbations, it seems quite legitimate to neglect the velocity normal to the wing plane of symmetry. This simplification is found particularly useful since the wing can be regarded as having an effective camber,  $\epsilon_{\text{eff}}(x,y) = \epsilon(x,y)(1 - \frac{\Delta u}{U})$  as well as an effective jet deflection angle  $\theta_{\text{eff}}(x,y) = \theta(x,y)(1 - \frac{\Delta u}{U})$ .

Before proceeding further, it is pertinent to ask whether it is correct to consider the effects of a rate of yaw as an equivalent change in camber and should not some correction be made to the dynamic boundary condition. It is not, of course, possible to strictly justify these assumptions. For example,  $\frac{\Delta u}{U}$  is of order  $\epsilon$  and in a first order theory should be neglected. It has, however, been the accepted practice to adopt such approximation in evaluating, for example, the rolling moment derivative due to rate of yaw and although agreement with experimental data does leave something to be desired, the accuracy in predicting such derivatives has normally been regarded as acceptable for the purpose of stability analysis. The only explanation that, at this time, can be offered for neglecting a correction to the dynamic boundary condition is computational expediency. By the way, it can be shown that this correction would be equivalent to utilizing an effective distribution of momentum at the trailing edge (i.e.,  $C_{\mu\text{eff}} = (1 + \frac{\Delta u}{U}) C_{\mu}$ ).

Based on the above assumptions, for any point on the wing and jet the complete set of boundary conditions becomes

$$w(x,y) = -\left(\frac{rb}{2U}\right) y \epsilon(x,y) + \epsilon(x,y), \quad (z = 0, \text{ wing portion}) \quad (2.174)$$

$$\frac{\partial w(x,y)}{\partial x} = -\frac{2}{c(y) c_u(y)} \gamma(x,y), \quad (z = 0, \text{ jet portion}) \quad (2.175)$$

$$w(x,y) = -\left(\frac{rb}{2U}\right) y \theta(y) + \theta(y), (x = x_t^+(y), \text{ when } c_\mu(y) \neq 0) \quad (2.176)$$

$$\gamma(x,y) = 0, \left\{ \begin{array}{l} x \rightarrow \infty, \text{ when } c_\mu(y) \neq 0 \\ x = x_t^+(y), \text{ when } c_\mu(y) = 0 \end{array} \right\} \quad (2.177)$$

where again  $x$  and  $y$  have been retained as nondimensional variables. An examination of these boundary conditions will reveal that to evaluate the effects of yawing on  $\gamma$  will require the solution of an additional series of fundamental cases. These additional fundamental cases, just as in the original jet-wing problem, (see Section 2.2.1.4) can be expressed as follows

$$-\left(\frac{rb}{2U}\right) y \epsilon(x,y) = -\sum_{m=K+1}^{2K} \left(\frac{rb}{2U}\right) y a_{m-K} \epsilon_{m-K}(x,y) \quad (2.178)$$

and

$$-\left(\frac{rb}{2U}\right) y \theta(y) = -\sum_{m=K+1}^{2K} \left(\frac{rb}{2U}\right) y a_{m-K} \epsilon_{m-K}(y) \quad (2.179)$$

where the  $m^{\text{th}}$  cases are regarded as the additional fundamental cases.

There are three derivatives associated with the yawing jet-wing. Although only the rolling moment derivative is considered of any significance in stability analysis, equations are also given below for the yawing moment and side force derivatives.

First consider the rolling moment derivative due to rate of yaw,  $C_{l_r}$ ,

which can be written as

$$C_{l_r} = \frac{\partial C_l}{\partial \hat{r}} = \begin{cases} C_{l_{r_0}} + \hat{r} C_{l_{r_1}}, & (h < \infty) \\ C_{l_{r_0}}, & (h = \infty) \end{cases} \quad (2.180)$$

where

$$C_{l_{r_0}} = - \frac{1}{Sb} \int_S \left[ \left( 1 + u'_0(x,y) \right) \frac{\partial \gamma(x,y)}{\partial \hat{r}} + \gamma_0(x,y) \frac{\partial u'_0(x,y)}{\partial \hat{r}} \right] y \, dx \, dy$$

and

$$C_{l_{r_1}} = \frac{2}{Sb} \iint_S \frac{\partial u'_0(x,y)}{\partial \hat{r}} \frac{\partial \gamma(x,y)}{\partial \hat{r}} y \, dx \, dy$$

Note, that  $\hat{r}$  has been substituted for  $\left( \frac{rb}{2U} \right)$ .

Next, consider the yawing moment derivative due to rate of yaw,  $C_{n_r}$ , which, as in the case of the derivatives treated before, can be written as

$$C_{n_r} = \frac{\partial C_n}{\partial \hat{r}} = C_{n_{r_0}} + C_{n_{r_1}} \quad (h \leq \infty) \quad (2.181)$$

where

$$C_{n_{r_0}} = \frac{4\pi}{9Sb} \int_{-1}^{+1} \delta_\ell(y) \bar{\gamma}_{\ell_0}(y) \left( \frac{\partial \gamma_\ell(y)}{\partial \hat{r}} \right)^2 \left( \frac{dx_\ell}{dy} \right) dy + \frac{1}{Sb} \iint_S \frac{\partial \gamma(x,y)}{\partial \hat{r}} \epsilon(x,y) y \, dx \, dy$$

and

$$C_{n_{r_1}} = \frac{8\pi}{9Sb} \int_{-1}^{+1} \left( \frac{\partial \gamma_{\ell}(y)}{\partial \hat{r}} \right)^2 \left( x_{\ell}(y) \frac{dx_{\ell}(y)}{dy} + y \right) dy$$

Finally, the side force due to rate of yaw can be written as

$$C_{Y_r} = \frac{\partial C_Y}{\partial \hat{r}} = C_{Y_{r_0}} + \hat{r} C_{Y_{r_1}}, \quad (h \leq \infty) \quad (2.182)$$

where

$$C_{Y_{r_0}} = \frac{4\pi}{9S} \int_{-1}^{+1} \delta_{\ell}(y) \gamma_{\ell_0}(y) \frac{\partial \gamma_{\ell}(y)}{\partial r} \frac{dx_{\ell}(y)}{dy} dy$$

and

$$C_{Y_{r_1}} = \frac{8\pi}{9S} \int_{-1}^{+1} \left( \frac{\partial \gamma_{\ell}(y)}{\partial \hat{r}} \right)^2 \frac{dx_{\ell}(y)}{dy} dy$$

This completes the derivation of the rotary dynamic derivatives of a jet-wing. It will be noted that the expression for some derivatives includes a term which is a function of their respective angular velocities. In the solution of the classical equations of motion, these terms are rightfully neglected. They are, however, retained here partly for consistency and also to provide a basis for a preliminary evaluation of the significance of these terms under conditions heretofore unexplored.

#### 2.2.4.5 Sideslipping Jet-Wing

One of the most important lateral stability derivatives is the rolling moment derivative due to sideslip  $C_{l_{\beta}}$ . The chief contribution to  $C_{l_{\beta}}$  is from the wing and the wing-fuselage interference effects. The wing contribution to this and other derivatives due to sideslip considered here is influenced by wing dihedral as well as sweepback.

Consider first a wing without dihedral (figure (2.7a)). The resultant velocity of the free stream relative to the wing, when the wing is moving forward with velocity  $U \cos \beta$  (where  $\beta$  is the angle of sideslip) and sideslipping with velocity  $U \sin \beta$ , which in most circumstances is small compared with

$U \cos \beta$ , is  $U$ . It can be readily deduced from figure (2.7a) that the aerodynamic characteristics due to sideslip are simply found by considering the three dimensional problem of a jet-wing which is non-symmetric about the  $Ox$  axis, which is parallel to  $U$ . Two items must be considered in using this procedure. First, one must utilize an effective distribution of trailing edge momentum such that  $c_{\mu\text{eff}}(y) = c_{\mu}(y) \cos \beta$  and second, the stability derivatives, which are normally converted to a stability axes system, will be a nonlinear function of  $\beta$ .

Suppose now that the wing has a dihedral angle  $\Gamma(y)$ . The velocity  $v$  of sideslip can be resolved into a component  $v \cos \Gamma(y)$  in the plane of the wing and a component  $v \sin \Gamma(y)$  perpendicular to it. To a first approximation the component  $v \cos \Gamma(y)$  will be neglected. However, the component  $v \sin \Gamma(y)$  is equivalent to an effective change in wing twist and resultant jet deflection which can be expressed as follows:

$$\begin{aligned} \Delta\epsilon(x) &= \frac{v}{U} \sin \Gamma(y) \\ &\approx \beta \Gamma(y) \end{aligned} \tag{2.183}$$

$$\Delta\theta(y) \approx \beta \Gamma(y) \tag{2.184}$$

Hence, the problem of determining the effect of dihedral simply involves the solution of the EVD method for one additional fundamental case. The derivatives, for example,  $C_{l\beta}$ , can be obtained directly from the basic equation given in Section (2.2.3).

### 2.2.5 COMMENTS ON CONVERGENCE AND ACCURACY - SPACING STUDY

The accuracy of the EVD method is inherently dependent on the number and location, and hence, spacing of the EVD elements. One criterion which establishes the validity of the EVD method is the convergence of the solution to the jet-wing problem as the number of elements is increased.

To begin the discussion of the validity of the present method, the results of a "spacing" study are presented below.

Three numbers of spanwise divisions have been considered, namely, 7, 13, and 20, in conjunction with three sets of chordwise divisions, 6-4, 11-8, and 18-10 (Note that the first number indicates the divisions on the wing and the second those on the jet).

Calculations of the aerodynamic characteristics of an untwisted and uncambered rectangular jet-wing of aspect ratio 4.5 have been made with each of the above combinations of spanwise and chordwise divisions with the exception of that combination which involves the greatest number of EVD elements. Three jet-wing operating modes were considered, namely:

1. An unblown wing at a given angle of attack  $\alpha$
2. A wing at an angle  $\alpha$  and with a uniform jet ( $c_{\mu} = 1$ ) emitted so that  $\delta_J = 0$  and  $\theta = \alpha$
3. A wing at zero angle of attack and with a uniform jet ( $c_{\mu} = 1$ ) emitted so that  $\delta_J = \text{constant}$  and  $\theta = \delta_J$

A summary of the aerodynamic characteristics appropriate to each operating mode or jet-wing configuration is presented in figures (2.8) through (2.10). The total lift, the center of lift, and the total induced drag are given in terms of a percentage error relative to some nominal value of these quantities. Since there exists no exact analytical solution of the jet-wing problem, the 13 x 11-8 combination was selected for this purpose. Let the subscript "o" denote the aerodynamic quantities associated with the above spacing, then  $\Delta C_L'$ ,  $\frac{\Delta X_{C.L.}}{\bar{c}}$ , and  $\Delta C_{D_j}'$  are defined as

$$\Delta C_L' = \frac{C_L - (C_L)_0}{(C_L)_0}$$

$$\frac{\Delta X_{C.L.}}{\tilde{c}} = \left[ \frac{X_{C.L.}}{\tilde{c}} - \left( \frac{X_{C.L.}}{\tilde{c}} \right)_0 \right] / \left( \frac{X_{C.L.}}{\tilde{c}} \right)_0$$

$$\Delta C_{D_i}' = \frac{C_{D_i} - (C_{D_i})_0}{(C_{D_i})_0}$$

Incidentally,  $\Delta C_{D_i}'$  is shown for both the pressure integral method and the momentum method, and  $(C_{D_i})_0$  is based on the momentum method. The induced spanwise-efficiency factor  $e$ , which is also given, is defined as

$$e = \left( \frac{1}{\pi AR + 2 C_J} \right) / \left( \frac{C_{D_i}}{C_L^2} \right)$$

It will be observed that the EVD method, in general, exhibits good convergence characteristics in all three cases. For a fixed arrangement of spanwise divisions, the convergence with increasing chordwise divisions is apparent, while for a fixed arrangement of chordwise divisions, the results also converge with increasing spanwise divisions. By increasing the spanwise divisions, however, the differences between the results of two sets of chordwise divisions are not decreased.

It is important to note that the number of spanwise divisions has a greater influence on those drag calculations based on the use of the momentum method as against those based on the pressure integral method. Any discrepancy between the drag calculated with either method is reduced as the number of spanwise divisions is increased. A further indication of the accuracy and validity of the EVD method can be obtained by observing the convergence characteristics of the induced drag span-efficiency factor  $e$ . It is the authors' opinion that, at this time, the momentum analysis method would be regarded as more accurate than the integral method. In both cases, however, the span-efficiency factor  $e$  is apparently converging to an expected value which, for a rectangular jet-wing, is slightly less than unity.

To conclude, it is apparent the EVD method will provide an accurate estimate of aerodynamic characteristics with a relatively small number of EVD elements. Also, in contrast to a number of alternative lifting surface theories, the present method is, in general, convergent. In the case of the jet-wing configuration considered in the spacing study, a 13 x 11-8 element arrangement seems more than adequate for accurate aerodynamic data (say  $\pm 1\%$ ). A further improvement in the accuracy resulting from an increase in the total number of EVD elements would, in view of the increased computing time, be difficult to justify.



### 2.2.6 Method Validation

The EVD approach to the solution of mixed boundary value problems can, of course, be much simplified when dealing with two-dimensional jet-wing problems. Although the corresponding results of research in this field have yet to be published, it should be noted that a two-dimensional EVD method has permitted the calculation of  $\Delta c_p$ ,  $c_l$ , and  $c_m$  for arbitrary cambered jet-flap airfoils. An extensive comparison of analytic calculations of chordwise loading with those obtained by the use of Spence's<sup>17,18</sup> loading function method have indicated, for example, that better results could not be obtained by the use of alternative methods (e.g., vortex lattice).

In order to assess the validity of the EVD jet-wing lifting-surface theory, comparisons were made between the present method and other theory and experimental data. This section contains a summary and discussion of the results.

#### 2.2.6.1 Some Comparisons with the Results of Other Theories

Some indication of the accuracy with which the EVD method is capable of predicting the aerodynamic characteristics of conventional wings can be given by comparing the results with those obtained by more rigorous mathematical treatments of the lifting-surface problem. For example, Kinner<sup>31</sup> has considered the case of a wing of circular planform and Krienes<sup>32</sup> has presented results for some elliptic wings.

The results obtained for the lift curve slope and aerodynamic center of elliptic wings using the present method are compared with those of Krienes in figures (2.11) and (2.12). Figure (2.11) also includes results for the limiting cases of very small aspect ratio (Jones) and of very large aspect ratio (Prandtl). Küchemann's<sup>33</sup> general theory for wings of any given planform includes the limiting cases of Jones and Prandtl and the agreement with the results of Kinner and Krienes is such that it can be regarded as an interpolation between these results. Considering the various approximations

adopted in the formulation of the present method, the agreement with other methods is regarded as excellent.

Figures (2.13), (2.14), and (2.15) show typical examples of the spanwise variation of sectional lift curve slope, center of pressure, and chordwise loading distribution obtained by the EVD method and Kinner theories for the circular wing. The span loading is found to be nearly elliptic (i.e., constant sectional lift curve slope  $\frac{\partial C_l}{\partial \alpha}$ ) by both methods with the greatest discrepancy occurring in the small region near the wing "tip". The chordwise loading distribution in this region also contains oscillations. Since the present method replaces the wing surface by rectangular elements and since the bound vorticity is assumed constant across each element, this lack of agreement was not unexpected. It will also be noted that, although 364 EVD elements (14 semi-span x 13 chord divisions) were used to represent each wing, in view of the symmetry in planform geometry about the 0x axis, it was only necessary by selecting the symmetry option in the EVD Jet-Wing Computer Program, to solve 182 linear equations. It is possible that the calculation of chordwise and spanwise loading with a larger number of EVD elements might be more accurate. There is definitely every indication from the numerical experimentation conducted to date that an increase in the number of EVD elements will insure convergence in, for example, lift and pitching moment. This has been discussed in detail in Section 2.2.5.

As was mentioned earlier, the method presented in the report is based on the use of a theoretical model of the jet-wing problem which is similar to that adopted by Maskell and Spence<sup>20</sup>. Typical results calculated with equation (2.4) using the expression for  $\sigma$  given by equation (2.5) are presented in figure (2.16). A comparison of these results with those obtained with the present method indicate excellent agreement for both the angle of attack and jet deflection fundamental cases.

The approximations adopted by Maskell and Spence and briefly described require that the error in  $w_i(x)$  be small, which implies a large aspect ratio, AR, and that its minimum permissible value increases with jet momentum. The present theory should give more accurate results at appreciably higher jet

coefficients and/or lower aspect ratio elliptic wings than that of Maskell and Spence.

As stated earlier, Maskell and Spence derived an exact overall relation between the total lift and induced drag equation (2.7), for the special case of constant  $\alpha_{j_\infty}$  by considering the momentum flow through a large control volume enclosing a wing in which both the chord and the jet momentum flux per unit span are elliptically distributed, the jet deflection is constant over the span and the camber is zero. Figure (2.17) shows that, within the accuracy of the numerical approach adopted by the present theory, the same relation between the lift and induced-drag coefficients is obtained.

Figures (2.18) and (2.19) present results for a large aspect ratio rectangular jet-wing with uniform blowing (angle of attack and jet deflection cases) in order to compare the predictions with Spence's two-dimensional results and those obtained with the Douglas 2-D EVD jet-augmented-flap method. (Note the EVD element notation is defined as  $M \times N_w - N_j$  where  $M$  is the number of semispan divisions and  $N_w$  and  $N_j$  are the number of chordwise divisions on the wing and jet, respectively). Two jet momentum coefficients,  $C_j$ , are considered, namely: 0 and 2. In view of the finite aspect ratio of the wing considered, the results obtained with the present method were expected to underpredict total two-dimensional circulation lift by approximately 2% at a  $C_j$  of 0 and 4% at a  $C_j$  of 2.0. Remarkably close agreement between the expected three-dimensional lift and the observed values of  $C_{L_T}$  is, therefore, obtained in all cases.

The comparisons of the results obtained with the present method with appropriate theoretical results for conventional elliptical wings without a jet flap as well as comparable jet-flap results have been shown to be very favorable. Also, in the limit as  $AR \rightarrow \infty$  the EVD approach to the solution of the jet-wing problem gives excellent agreement with the theory of Spence over the range of  $c_\mu$ 's investigated. The authors have also obtained good agreement with the published theoretical results of Multhopp<sup>21,36</sup>,

Malavard<sup>22</sup>, Das<sup>15</sup>, etc., and some comparisons between results obtained with the present method and this data are presented in figures (2.20) through (2.25)

## 2.2.6.2 Comparisons with Experiments

### 2.2.6.2.1 Rectangular Wings

The overall lift coefficients for a series of conventional rectangular wings have been calculated and compared with the measured values obtained from several experimental programs. Figure (2.20) presents some of the results of this correlation study. The measured lift curve slope is well predicted throughout the whole aspect ratio range.

Experimental results for rectangular wings with uniform full span blowing have been published by Williams and Alexander<sup>13</sup> and Das<sup>37</sup>. Both of these test programs were conducted using semi-span models. The intrinsic difficulties encountered when reducing test results for the effects of the finite size of the half-model end plates are well known and are briefly discussed in Appendix IV. In the case of the jet-wing, it is difficult to justify the application of simple methods that correct for these effects. Wind tunnel wall effects on the aerodynamic characteristics become important when the jet sheet is either steeply inclined to the wing chord or if the wing span, for example, is large relative to the cross section width or height of the tunnel working section. The rate of change of momentum and the orientation of the jet sheet, in the case of a jet-wing, must also be established. These parameters are often derived from measurements made in the tunnel when the wind is off. Many investigators usually do not bother to investigate the degree of inaccuracy involved in the assumption that the conditions of jet emission are independent of, for example, a given angle of attack, flap deflection, and free-stream velocity. Thus, any conclusions deduced from a comparison of analytical results with their test data can often be misleading. Experimental data on basic jet-wing configurations considered essential to establishing the validity of the present theoretical method is, however, limited. In fact, the results published by Das represent, at this time, the major source of test information for the validation of analytical methods. Despite these misgivings, the analytical predictions of the aerodynamic characteristics of rectangular jet-wings are

in satisfactory quantitative agreement with known experimental results. Typical examples of the comparison of theory and experiment are presented in figures (2.21) through (2.25).

It has been suggested by Spence<sup>17</sup> that the circulation part of the lift predicted by linearized theory should be multiplied by  $(1 + t/c)$ , where  $t/c$  is the airfoil thickness chord ratio. There is also some evidence to suggest (references 1, 17, and 20) that such a correction would lead to a better agreement between predicted and test data. The examples presented in these publications should not be interpreted, however, as an indication that it is always possible to obtain an equally close agreement between analytically derived and experimental results. No attempt has, therefore, been made to correct the aerodynamic data presented in this report for the effects of wing thickness.

#### 2.2.6.2.2 Swept Wings

Additional experimental data (reference 38) which provides evidence of the ability of the EVD method to correctly predict the aerodynamic characteristics of conventional wings is presented in figures (2.26) through (2.28). At angles of attack below which viscous effects are not considered significant the agreement between the analytic and experimental total lift, total pitching moment, and sectional aerodynamic characteristics is quite good. In the case of drag, it should be noted that  $C_{D_0}$  (i.e., profile drag coefficient) was not taken into account in the calculations. The noticeable divergence between measured and calculated aerodynamic characteristics above an angle of attack of approximately seven degrees is the result of viscous separation at the wing tip which becomes more pronounced at higher angles of attack.

The analytical results for the spanwise distribution of circulation lift on a swept jet wing are compared with experimental data in figures (2.29) and (2.30). Also presented in these figures are the theoretical results based on Das' lifting surface theory. In the case of uniform blowing, the results obtained with the present method agree well with the theoretical values of Das. One thing to note, however, is the inability, figure (2.30)

of Das' loading function theory to correctly predict the section lift coefficient distribution in the case of a partial span blowing jet-wing configuration.

#### 2.2.6.2.3 Dynamic Stability Derivatives

An extension of the basic EVD jet-wing lifting surface theory that enables a qualitative prediction of certain stability derivatives to be accomplished was described in Section 2.2.4. The evaluation of dynamic derivatives is based on a quasi-steady approach, and it was argued that this should suffice for most stability calculations. A comparison of theory and experiment (reference 39) of those dynamic derivatives due to pitching, rolling, and yawing for an unswept and swept, untapered wing for  $C_j = 0$  are presented in figures (2.31) and (2.32). The observations made in comparing experimental and calculated derivatives indicate that the assumptions adopted in the present analytical method are likely to be inadequate in the prediction of some derivatives. The calculated contributions of the wing to those stability derivatives likely to be considered important (e.g.,  $C_{lp}$ ,  $C_{np}$ ,  $C_{lr}$ ) appear, however, to be fairly reliable. The large discrepancies between calculated and experimental values at high lift coefficients, for which the flow is believed to be partially separated, is not unexpected. Even a more rigorous approach, if based on potential flow concepts, is unlikely to provide much improvement in the estimation of these derivatives under these conditions.

Since there is no published experimental data on the effects of a jet flap on the dynamic derivatives of a basic conventional wing, it is impossible to establish at this time, the limitations and accuracy of the present method. This field obviously deserves further investigation. For example, experimental measurements of the stability derivatives due to yawing, pitching, and rolling should be made in order to ascertain whether unsteady variations in the equivalent jet bound and wing and jet trailing vorticity can introduce phase lags of practical importance. In the meantime, the method outlined in this report represents the only known available method for the calculation of the dynamic derivatives of arbitrary jet-wing configurations.

### 2.2.6.3 Ground Effect

Validation of the ground effect method is a more difficult task than for the free-air EVD method because of a lack of general, well-proven three-dimensional ground effect methods, even for basic planform shapes. However, a large number of investigators have studied the two-dimensional ground effect problem, most notably Tomotika (references 41 and 42) who solved the problem by conformal mapping. In addition, two-dimensional potential flow methods for both wings and jet-wings developed at Douglas Aircraft Company have been used extensively to study the nature of the ground effect problem and to assess the validity of the assumptions employed in the three-dimensional method. Hence, the discussion presented here will first center on the two-dimensional problem and will then be expanded to include three-dimensional aspects.

The question of the applicability of the linearized approach in ground effect is of prime importance and has been given considerable attention in this two-dimensional analysis of the problem. Both linear and non-linear potential flow methods utilizing the Elementary Vortex Distribution loading concept have been used in this study. The linear approach, known as the Two-Dimensional EVD Method (reference 44), is analogous to the three-dimensional method presented here. That is, the deflection of the wing and jet are assumed to be small such that the boundary condition of no-flow through the wing and jet can be satisfied in the plane of the undeflected wing rather than on the actual jet-wing surface. This method offers the advantage of relative simplicity, in that the jet-wing and its image are planar and the downwash matrix need be solved only once per ground height. It fails, however, to fully include the effects of surface inclination. The non-linear approach, known as the Douglas Two-Dimensional Non-Linear Jet-Flap Potential Flow Method (reference 45), represents the wing and jet by their actual shape and the loading by a set of EVD's. However, since the jet shape is not known at the outset of the solution, an initial jet shape must be assumed and the solution must be iterated until convergence is obtained. This method is comparable to the rigorous three-dimensional method outlined in Section 2.2.1.5, and it offers the advantages of being fully non-planar and hence fully

non-linear. However, because of the complexity of its non-planar nature and the need for an iterative solution, computation time for this method will be considerably more than for the linear solution.

The methods described above have been used to analyze a variety of airfoils, both in and out of ground effect, including a flat plate and a hinged flat plate, with and without a jet. Some of these results are presented in figure (2.33) in which the ratio of lift for hinged flat plates without a jet calculated by the linear method to the lift calculated by the non-linear method is plotted versus the height of the airfoil above the ground, non-dimensionalized by wing chord. Since in the linear method the position of the airfoil relative to the ground is invariant with angle of attack and flap deflection while in the non-linear method the position is dependent on the deflections, there is some ambiguity in the definition of ground height. That is, the ground height is the same at any point on the airfoil in the linear method while it will differ from point to point along the airfoil chord in the non-linear method. Hence, the quantitative results in these figures will vary with the point chosen to measure ground height, although the qualitative results should apply irrespective of the point chosen. The non-linear data used to prepare figure (2.33) were calculated with the ground height measured relative to the airfoil leading edge.

For a flat plate airfoil in ground proximity, figure (2.33a), the linear and non-linear theories are shown to be within ten percent agreement for ground heights as low as  $h/c = 0.5$  and angles of attack as large as 20 degrees. The asymptotic values plotted in this figure indicate the magnitude of the non-linear effects in free air for each particular angle of attack and flap deflection. Note that for the flat plate airfoil in free air the non-linear effect is only two percent at an angle of attack of 20 degrees. However, for flapped airfoils, where the flap is significantly closer to the ground than the main airfoil, the non-linearities of the problem become significantly more important [figures (2.33b), (2.33c), (2.33d)]. Differences as large as 50 percent between the linear and non-linear methods were calculated for flapped airfoils at angle of attack for height-to-chord ratios of less than 1.0. It should be noted, however, that the magnitude of the free



air non-linear effects is also significantly increased for the flapped airfoil case, as can be seen from the plotted asymptotic values in these figures.

The comparisons presented to this point have been for unblown airfoils only and have indicated large non-linear effects for airfoils in close proximity to the ground. However, when ground heights typical of STOL transport aircraft are considered, and when the magnitude of the non-linear effects in free air are considered, it can be seen that the adoption of a linearized approach in the solution of the ground effect problem will provide a reasonable capability to predict the effects of ground proximity.

The nature of the ground effect phenomenon for hinged flat plate airfoils without jet flaps has been thoroughly examined using the two-dimensional linearized method described earlier. Since this method is analogous to the linearized three-dimensional method described in Section 2.2.1.5, these two-dimensional results will provide some insight into the ground effect phenomenon over a wide range of conditions. In figure (2.34) is plotted the ratio of lift in ground proximity to lift in free air versus height-to-chord ratio for a hinged flat plate airfoil with a 40 percent chord flap deflected 0, 20, 40, and 60 degrees. It is observed, first of all, that there is a smaller percentage increase in lift (or a larger percentage decrease) relative to the free air case as angle of attack is increased. This is a result of the freestream flow perturbations induced by the image airfoil, which increase more rapidly with angle of attack than does the airfoil vorticity. Secondly, as ground height decreases there is in some cases an increase in lift relative to the free air value while in other cases there is a decrease. This effect is shown in figure (2.34) to be a complex function of angle of attack and flap deflection. In addition, in three dimensions aspect ratio, taper ratio, sweep, etc., will also influence whether the ground effect will be favorable or adverse. In order to qualitatively understand these phenomena, if the airfoil and its image are visualized as being represented by a distribution of vortices, it can be seen that aft loading (e.g., flap deflection or aft camber) results in additional downwash being induced over most of the chord of the airfoil by its mirror image which results in a decrease in vortex strength. For a flat

plate airfoil, however, the loading is more concentrated on the forward portion of the airfoil and hence most of the airfoil is in an upwash field induced by the image. Thus, there is an increase in vortex strength. In all cases, lift is decreased by the perturbation to the freestream flow induced by the image airfoil on the real airfoil, so the relative magnitude of this effect compared to the change in vortex strength is paramount in determining the nature of the ground effect.

Having looked at the unblown airfoil in ground effect problem thoroughly, the effects of adding a jet will be discussed, primarily to determine what additional non-linearities are added by the jet and to determine the importance of ground impingement of the jet. The non-linear behavior of a flat plate airfoil with a deflected jet is shown in figure (2.35) to be not significantly different than that for the unblown case. That is, the non-linear effects in ground proximity are generally less than ten percent, and figure (2.36) shows, surprisingly, that for a hinged airfoil with jet the non-linear effects are considerably less important than for the unblown case. This apparent paradox has been resolved by the realization that false conclusions regarding the non-linear effects can be formulated by looking at lift alone. Looking at pressure distributions has shown, for example, that there can be a cross-over in the linear and non-linear pressure distributions, as illustrated in figure (2.37) for a hinged flat plate airfoil with jet. This shows that although there are significant differences in the chordwise loading on both the airfoil and the jet, there may be little difference in the lift since

$$\Delta c_{l_T} = c_{l_{\text{non-linear}}} - c_{l_{\text{linear}}} = \frac{1}{c} \int_0^c \left\{ \Delta c_{p_{\text{non-linear}}} - \Delta c_{p_{\text{linear}}} \right\} ds$$

In addition, when there is blowing, the non-linear effect on circulation lift  $\Delta c_{l_T}$  may be cancelled by the non-linear jet reaction lift, where the difference may be expressed by

$$\Delta c_{l_J} = c_{l_{J_{\text{non-linear}}}} - c_{l_{J_{\text{linear}}}} = c_{\mu} (\sin \theta - \theta)$$

Hence, with a jet it becomes quite difficult to establish the nature of the non-linear effects.

The discussion to this point has been concerned solely with a two-dimensional airfoil in ground proximity. What has been said is qualitatively applicable to the three-dimensional method, which is the actual subject of this work. In other words, the effects of non-linearities presented for the two-dimensional case should lend some insight into the non-linearities of the three-dimensional problem. However, the three-dimensional problem is considerably more complex, and there are additional factors which must be considered to assess the magnitude of the non-linearities. For example, a swept wing at angle of attack in proximity to the ground has variations in ground height not only in the chordwise direction but also in the spanwise direction. But in the present linear three-dimensional method, the entire wing is assumed to be at a constant height above the ground, so again an ambiguity exists in the definition of ground height. Unfortunately it has not been possible to assess the magnitude of the three-dimensional non-linearities, so at this point the two-dimensional study must be retained as the only guide.

Figure (2.38) is a comparison of the lift curve slope in ground proximity prediction of the present three-dimensional linear ground effect method with the experimental results of Saunders (reference 46) for a simple rectangular wing of aspect ratio 4.0. Excellent agreement has been obtained, although the case is rather simple, being a rectangular wing with no camber. In addition, non-linear effects may be masked by the 22 percent thickness of the airfoil section used in the test. Nevertheless, this comparison is an encouraging verification of the basic method.

Figure (2.39) presents another comparison of the present method with experiment, these data being for an aspect ratio 8.3 rectangular wing with full span jet flap (reference 47). For a jet momentum coefficient  $C_j$  of 1.0 [figure (2.39a)], reasonable agreement between theory and experiment is obtained for moderate ground heights. However, for smaller ground heights the theory is seen to considerably over-predict the lift. As observed experimentally, the jet sheet impinges on the ground for the smaller ground heights before significant turning of the jet to the freestream direction has occurred. Tuft studies of the flow show the jet to be deflected upstream by the ground

board which results, in the words of reference 47, in a "captive vortex" between the wing and ground. A large area behind the wing and jet sheet is seen to be turbulent flow. As jet momentum increases, the penetration of the jet normal to the freestream is greater and impingement losses in lift are even more significant, as shown by the experimental data in figures (2.39b) and (2.39c). Further experimental data not presented here show even greater impingement losses as the jet deflection angle increases, as would be expected.

The comparisons with fundamental wind tunnel tests presented here are representative of the type of agreement obtained with the present method. That is, excellent agreement with experiment is obtained for those cases where non-linear effects are not important. The present method may fail to adequately model the ground proximity problem for cases in which the wing is quite close to the ground ( $h/c < 1.0$ ), for wings with large surface deflections, or for jet-wings with a strong deflected jet which may impinge on the ground. The authors recognize the need for further research on the ground effect problem and recommend development of a fully non-linear, non-planar jet-wing ground-effect solution, possibly based on the solution described in Section 2.2.1.5. However, within the scope of the present program, the linear solution developed here is considered to be a significant advancement and should prove valuable as a preliminary engineering design tool.

### 2.2.7 Summary and Concluding Remarks

During the last two decades, the jet flap has been established as an effective method for improving lifting efficiency. The aerodynamic principles of basic jet-flapped wings in steady motion are now reasonably well established. Several interesting problems have, however, emerged from design studies of STOL and V/STOL aircraft which utilize powered lift concepts employing the jet-flap principle. Some of these problems can be attributed to a lack of a rational basis for the evaluation and design of such aircraft. To provide this rational basis requires, in part, a capability to predict the aerodynamic and stability and control characteristics of a given configuration.

The jet-wing lifting surface theory presented in Section 2.2 provides a much needed capability to predict the aerodynamic characteristics of arbitrary wings with arbitrary trailing edge jet momentum distribution. The theoretical model of the jet wing problem adopted by Maskell and Spence<sup>20</sup> was selected as a basis for the present theory. The approach adopted for its solution utilizes the Douglas Elementary Vortex Distribution (EVD) method. This method was developed as a basis for the solution of two- and three-dimensional mixed boundary-value potential flow problems and has been successfully applied to the two-dimensional jet-flap problem. In summary, the EVD jet-wing lifting surface theory and associated computer program (Volume II) will, for arbitrary planform wings, provide in or out of ground effect the following:

1. Spanwise and chordwise loading
2. Spanwise variation of induced drag
3. A capability to investigate the effects of
  - (a) part span flaps
  - (b) part span blowing
  - (c) rolling, yawing, pitching, and sideslipping
4. Total lift and induced drag (momentum method), pitching moment, yawing and rolling moments, and side force.

Although the versatility of the EVD method is obvious, several advantages associated with the approach adopted for the solution of the jet-wing

problem should be noted. For example,

1. The EVD method reduces the complicated set of integro-differential equations for the jet-wing problem to a set of linear equations in a straightforward manner. One can truly appreciate its simplicity by comparing the present method with Spence's two-dimensional jet-flap theory and Das' method for the three-dimensional jet-wing.
2. The EVD method is not subject to a stringent collocation requirement. Collocation is only an empirical means to compensate for the error resulting from the unrealistic assumption of vortex distribution. Since the true vorticity is represented closely by the present method, no collocation is, therefore, necessary.
3. Due to the close approximation of the vorticity distribution by the EVD method, which uses both linear and singular distributions, the resulting solution can be very accurate.
4. For the same reason that contributes to accuracy, relatively few EVD's are required in the solution of a specific problem, thus minimizing the computer time involved.

Comparison of analytical results with those available from other methods and with experimental data has, in general, confirmed the validity of the present theory. The adequacy of quasi-steady treatments for the determination of the dynamic stability derivatives of jet-flap wings has yet, however, to be established. It is worth adding that much of the experimental work conducted to date on jet-flap concepts has been undertaken using complete aircraft models and that the validity of the limited experimental data on basic jet-flap wings can be questioned. There is, therefore, an outstanding requirement for basic or fundamental experimental data that would primarily provide an understanding of the physical mechanism of the flow problems involved and would assist the validation and/or development of analytical methods.

The authors have earlier suggested that an analogy can be established between, for example, the externally blown jet flap and ejector jet flap and

the circulation control characteristics of basic jet-flap schemes, at least insofar as the aerodynamic/propulsive interactions are concerned. If this is so, then jet-flap theory can provide the theoretical framework for the development of appropriate analytical methods. The application of jet-flap theoretical methods to externally blown jet flaps would, however, involve a number of additional assumptions which, though possible as a means of making the problem tractable; would have to be justified on fundamental grounds. For example, there would be little justification for neglecting the presence of the jet beneath the wing and its entrainment properties. In addition, the application of jet-flap theory would require the postulation of a physically acceptable momentum distribution at the trailing edge. A clarification of the fundamental mechanism by which the jet is turned and spread would be valuable for this purpose. In the case of the augmentor wing, the performance of the ejector system would have to be known a priori and the effects of the intake flow (i.e., sink effect) on circulation lift, pitching moment, and drag must be accounted for. Despite all these misgivings, comparison of theoretical and experimental results (reference 1) and more recent research conducted by the authors and their colleagues at Douglas so far suggest that jet-flap theory provides a realistic and useful working basis for the prediction of externally blown jet-flap and augmentor wing aerodynamic characteristics as well as other jet-flap concepts.

Although past and present achievements, partly those at the Douglas Aircraft Company, have provided a theoretical basis for predicting the aerodynamic characteristics of jet-flap concepts, this methodology cannot, necessarily, be regarded as adequate. More theoretical ground work must be accomplished and relevant experimental programs must be conducted so as to assure validated engineering prediction methods. For example, there is a need for improved two-dimensional airfoil methods capable of handling multi-energy flows. There are also many questions left unresolved regarding the limitations of linearized two- and three-dimensional jet-flap methods. Are thickness corrections to circulation lift justified? Why is such good agreement obtained between theory and experiment at, for example, large jet angles?

## 2.3 JET-WING FLOW FIELD METHOD

In the analysis of complete STOL aircraft configurations employing jet-wings, it is necessary to be able to calculate the external flow field induced by the jet-wing so that interferences with other aircraft components can be determined. For example, it is necessary to be able to calculate the downwash field induced on the empennage by the jet-wing in order to calculate the aerodynamic and stability and control contributions of the empennage. The jet-wing flow field method described in this section is an approximate analytical method for calculating perturbation velocities induced at arbitrary points in the vicinity of a jet-wing powered lift system. The method requires a knowledge of the chordwise and spanwise loading distributions on both the wing and jet sheet, which is usually obtained from the EVD Jet-Wing Lifting Surface Theory (Section 2.2). The wing and jet, which are confined to the x-y plane in the linearized EVD method, must be fully non-planar in the flow field method in order to account for the orientation of the complete vortex sheet relative to the flow field point. Because of its non-planar nature, the flow field method is non-linear and hence it should be capable of predicting non-linear aerodynamic characteristics of jet-wing/empennage configurations, for example. The present method is applicable to conventional wings (i.e., unblown) as well as jet-wings.

### 2.3.1 Background

Over the years numerous investigators have studied the flow field problem both theoretically and experimentally, primarily to develop rational methods for determining the downwash characteristics at the tailplane. Much of the work on conventional airplane downwash methods has been compiled into extensive charts and tables (e.g., reference 48) based on experimental data and extended to additional configurations using a lifting line theory approach. Silverstein et al (reference 49) present a comprehensive analysis of the various methods commonly used for plain and flapped wings and discuss in some detail the problems associated with various theoretical downwash methods. In particular, they discuss the problem of vortex roll up and its effect on downwash at the tailplane and conclude that "it is usually sufficient to neglect the distention of the vortex sheet and to take into account the



distortion simply by considering the entire vortex sheet to be displaced vertically by an amount equal to the displacement of the centerline of the actual distorted sheet." Silverstein presents data to substantiate this statement, but only for simple unflapped wings.

Ross (reference 50) has presented a theoretical analysis of the jet-wing flow field problem based on the three-dimensional solution of Maskell and Spence (reference 20). However, it is the opinion of the authors that there seem to be several simplifications in Ross' work that are likely to seriously affect the accuracy of the method. Ross has assumed the jet sheet to be flat, as in the linearized model used in the EVD method, and has shifted the flow field points accordingly to account for the jet deflection. Not only does this method neglect jet curvature, but it has been shown using the Douglas Two-Dimensional Jet Flap Potential Flow Method (reference 45) that Ross' prediction of jet deflection for the infinite aspect ratio case is considerably in error. Thus, in Ross' work both the shape and orientation of the jet relative to the flow field points are incorrect. Also, Ross has assumed all the trailing vorticity to emanate from one chordwise position on the wing, so not only has jet curvature been neglected but also the additional vorticity shed by the jet has been improperly positioned.

The early flow field work by Silverstein and others is applicable only to conventional wings and then only for a specific set of configurations. It is clearly not applicable to jet-wings necessary for STOL aircraft which are characterized by mechanical and propulsive high lift systems which produce high lift coefficients and hence large downwash angles downstream. The method developed in the subsequent sections is an analytical method intended to provide the needed high lift flow field capability.

### 2.3.2 Theoretical Analysis of the Jet-Wing Flow Field Problem

The basic jet-wing system considered in the present analysis is illustrated in figure (2.2 ), in which the basic geometric quantities are defined. The present method is not unlike the mathematical model used by Silverstein although it is considerably more complex owing to its capability to handle jet-wings, non-planar surfaces, and complex wing loadings. As in

the EVD method, the origin of the coordinate system coincides with the wing apex; the x-axis is in the freestream direction; the z-axis is perpendicular to the x-axis, is in the plane of symmetry, and is positive up; and the y-axis forms a right-handed coordinate system, positive on the right wing. In the present method the wing is not required to lie in the x-y plane as it does in the EVD method, but rather the wing and jet sheet are allowed to be fully non-planar. The wing and jet sheet are divided into a lattice of quadrilateral elements in both the chordwise and spanwise directions [figure (2.4)]. Each of these elements on the wing is inclined such that it lies on the mean camber line of its section so that the equation for the location of the vortex sheet on the wing is

$$z(x,y) = z_\ell(y) - \int_{x_\ell}^x \left[ \epsilon_c(\xi,y) + \alpha \right] d\xi \quad (2.185)$$

where  $x_\ell$  and  $z_\ell$  are the leading edge coordinates of the y-section,  $\alpha$  is the wing angle of attack, and  $\epsilon_c(x,y)$  is the camber angle in radians. For computational purposes equation (2.185) would be replaced by a finite summation with the camber treated as constant on each quadrilateral element. Each element on the jet is inclined such that it approximately satisfies the jet dynamic boundary condition,

$$\frac{dw}{dx} = - \frac{2}{c(y)c_\mu(y)} \gamma(x,y) \quad (2.186)$$

where  $w$  is the induced downwash on the jet sheet and  $\gamma(x,y)$ , the vorticity distribution, is known from the EVD solution. Equation (2.186) must be integrated twice to determine the shape of the jet sheet. First, the downwash on the jet is

$$w(x,y) = \theta(y) - \frac{2}{c(y)c_\mu(y)} \int_{x_t}^x \gamma(\xi,y) d\xi \quad (2.187)$$

where  $x_t$  is the trailing edge x-coordinate of the y-section and  $\theta(y)$  is the total jet turning angle relative to the freestream at spanwise station  $y$ . The jet shape is then

$$z(x,y) = z_t(y) - \int_{x_t}^x w(\xi,y) d\xi \quad (2.188)$$

where  $z_t$  is the trailing edge  $z$ -coordinate of the  $y$ -section. Once again, the integrals are replaced by finite summations. Although the vorticity is shed from the jet sheet continuously, it has been assumed here that all the vorticity shed by the last jet element on a  $y$ -section is shed from the leading edge of that element. This last jet element has been assumed to be infinitely long, to be planar, and to be inclined to the freestream at an angle equal to  $\alpha_{j_\infty}(y)$ , the sectional downwash at infinity. Choice of  $\alpha_{j_\infty}(y)$ , which is calculated in the Trefftz plane, for the inclination of the jet infinity element is not theoretically correct except downstream at infinity; but if the last jet element is chosen to be sufficiently far downstream, further curvature of the jet can be neglected.

The shape of the trailing vortex sheet behind conventional (unblown) wings or behind unblown sections of jet-wings cannot be treated in the relatively simple manner as for blown wing sections since there is no longer a simple condition relating wake shape to vorticity. For an unblown wing, no additional vorticity is shed in the wake. However, as was first observed by Lanchester, the trailing vortex sheet behind a wing is unstable and tends to roll up as shown in figure (2.40). The roll up phenomenon is a result of the necessity of the free trailing vorticity to be parallel to the local free-stream, which in turn is determined by the vortex distribution itself. Methods have been developed to calculate the wake shape approximately (e.g., reference 51, 52, and 53), but these methods are iterative schemes which converge rapidly for only the most simple wing loadings [figure (2.41)]. For most practical configurations, such as part span jets or flaps, these iterative roll up methods give only a qualitative picture of the wake shape and orientation [figure (2.42)]. However, these roll up methods do indicate clearly that the simplified wake deflection suggested by Silverstein is not applicable to complex configurations with discontinuities in spanwise loading. Thus, some alternate scheme is necessary to locate the trailing vortex sheet behind unblown wings or unblown sections. The scheme adopted for the current flow field method is a major simplification of the wake geometry but it does, in an

approximate sense, make account for wake discontinuities. The trailing vortex sheet on each  $y$ -section is assumed to be planar and to extend infinitely far downstream inclined to the freestream at an angle  $\epsilon_\infty(y)$  midway between the freestream and a tangent to the sectional camber line at the trailing edge; that is,

$$\epsilon_\infty(y) = \frac{1}{2} \left[ \alpha + \epsilon_c(x_t, y) \right] \quad (2.189)$$

This particular angle was suggested by Rubbert (reference 54) in his non-planar vortex lattice lifting surface theory, and although there is no theoretical basis for its choice, comparison of this simplified wake shape with those predicted by roll up methods show that the approximation is reasonable.

With the entire non-planar jet-wing geometry established, it is now only a matter to superimpose the proper vorticity distribution on the wing and jet sheet. Since it is off-body induced velocities which are desired, the details of the loading distribution are not important and hence the continuous distribution of vorticity employed in the EVD method can be replaced by a lattice of discrete horseshoe vortices which are considerably simpler mathematically. This requires that the EVD vortex strengths  $\gamma(x, y)$  be properly integrated to determine the strengths of the corresponding concentrated vortices  $\Gamma(x, y)$ . This can be expressed by

$$\Gamma_i = \begin{cases} \delta_i \left( \gamma_i + \frac{1}{2} \gamma_{i+1} \right), & \text{Leading edge element} \\ \frac{1}{2} \delta_i \left( \gamma_i + \gamma_{i+1} \right), & \text{Regular element} \\ \gamma_i x_i, & \text{Jet Infinity element} \end{cases} \quad (2.190)$$

where  $\delta_i$  is the streamwise length of the  $i^{\text{th}}$  element and  $x_i$  is the streamwise position of the  $i^{\text{th}}$  element. The strength of the trailing vorticity on any element is easily found by integrating the bound vortex strengths from the leading edge of the  $y$ -section; that is

$$\Gamma_{i \text{ trail}} = \int_{x_l(y)}^x \gamma(\xi, y) d\xi \quad (2.191)$$

Up to this point the non-planar geometry of the wing and jet sheet have been determined and the proper vorticity distribution has been placed on them. All that remains to be done is to calculate the perturbation velocities induced by the jet-wing at each desired flow field point. Since the vorticity distribution has been replaced by a lattice of concentrated horseshoe vortices, the induced velocities can be calculated by repeated application of the Biot-Savart Law for straight line vortex filaments which is discussed in Appendix II. The off-body induced velocity is then simply the sum of the contributions of all the horseshoe vortices.

Although the theoretical development of the flow field method is essentially complete, there are several areas which require further discussion. Use of the concentrated singularity approach to represent the wing and jet sheet, desirable because of its mathematical simplicity, restricts the range of applicability of the method to the "far field" only. It can be shown from vortex lattice discretization theory that the no-flow boundary condition (i.e., the condition that there be no flow through the wing and jet sheet) can be satisfied at only one point per element, that point being the collocation point. At other points on the wing and jet sheet the flow normal to the surface will differ considerably from zero, which is physically impossible. However, at points which are not close to the jet-wing, the details of the vorticity distribution become less important mathematically since the discrete singularities are no longer nearby. This implies that use of the flow field method is restricted to points removed from the wing and jet sheet. It has been determined that a reasonable criterion to be used to avoid these singularity problems is that no flow field point be closer than one element length from the wing or jet sheet, where an element length is defined as the maximum linear dimension of a jet-wing element nearest to the flow field point of interest.

### 2.3.3 Method Validation

The lack of theoretical methods for calculating the flow field induced by arbitrary wings and jet-wings restricts method validation studies to comparisons with two-dimensional analytical methods and with experiment. Fortunately, there have been numerous experimental programs to explore the nature

of the flow field induced by a finite wing, including several for jet-wings, and therefore, comprehensive comparisons of the present method with experiment have been made. The experimental programs discussed here are limited to those for wing or jet-wing alone configurations so that the effects of fuselage, empennage, nacelles, etc., do not interfere with the basic method validation. Some of the problems associated with calculating the flow field induced by wing-body combinations will be discussed later.

Silverstein (references 48 and 49) has done extensive theoretical and experimental investigations of the flow field induced by a finite conventional wing with and without flaps. Comparison of some of these data with predictions of the present analytical method are presented in figure (2.43) for the USA 45 tapered wing of aspect ratio 6.2 without flaps. The comparison indicates good agreement with experiment except in a region near the wake. As discussed previously, near the vortex wake the present method is not expected to adequately predict the flow field perturbations because of the close proximity of the discrete singularities used to represent the wake. Also, viscous effects can become quite important near the vortex wake. Finally, it may be quite difficult to obtain accurate flow field data in the vicinity of the wake by the technique employed in the work of reference 49 because of the possibility of significant velocity gradients across the face of the yaw head probe used to measure flow direction. What is important to note is that outside the region of the wake there is excellent agreement in both the magnitude and spatial variation of downwash which indicates that the basic assumptions employed to locate the trailing vortex wake are valid.

Reference 47 provides a comprehensive experimental investigation of the flow field induced by a jet-wing high lift system. These data were obtained for a semispan model of an aspect ratio 8.3 rectangular jet-wing mounted on the ceiling of the Langley 7 x 10-foot tunnel. The model was equipped with a full-span jet-augmented flap in which the jet exited from a narrow slot in the wing upper surface near the trailing edge and followed the upper surface of the flap, leaving the wing at experimentally determined deflection angles of  $55^\circ$  and  $85^\circ$  for the two flap deflections tested. Because of the small model size relative to the tunnel cross-section, no wind-tunnel

jet-boundary corrections were applied to either the force or flow field data. The jet-wing loading distribution used in the present analytical method for this comparison was obtained from the EVD Jet-Wing Lifting Surface Theory (Section 2.2). However, in order to account for discrepancies in total lift between EVD predictions and experiment, which are in part attributable to thickness effects, end plate effects (whose magnitude may not be small for jet-wings), etc., the wing circulation loadings obtained from EVD have been increased by the ratio of experimental circulation lift

$$C_{L_T} = C_L - C_J \sin \theta \quad (2.192)$$

to the EVD predicted value.

Representative results of this comparison are presented in figures (2.44) and (2.45). In the first of these figures, the comparison between theory and experiment for the variation of jet-wing induced downwash with position behind the wing indicate generally good agreement except in those regions that are in close proximity to either the wing or jet. Parts (a) through (f) of this figure show comparisons for positions typical of empennage locations behind the wing. Parts (g) through (o) indicate the wide range of applicability of the present method. Figure (2.45) illustrates the variation in induced downwash with jet momentum coefficient,  $C_J$ . With the variation of  $C_J$  over the range 0.67 to 6.46, both theory and experiment show a large increase in induced downwash. Agreement is again good, except in the vicinity of the jet sheet. Again this is not surprising because of the discrete singularity approach adopted in the flow field mathematical model. In addition, near the jet sheet measurements of flow inclination are likely to be considerably in error because of the relatively large yaw head probe (3/16-inch diameter) used to measure the flow direction and the large velocity gradients across its face. What is important to note from these figures is that outside the region of the jet sheet the present analytical method predicts both the magnitude and spatial variation of flow inclination quite well and also predicts the variation of flow inclination with jet momentum coefficient with reasonable accuracy. Implicit in this data is the indication that the jet sheet location is also being properly predicted. The comparisons presented in

figures (2.44) and (2.45) are only a portion of those made with the experimental work of reference 47. Comprehensive comparisons have also been made for variation of angle of attack and for a wider range of positions, and these comparisons also indicate excellent agreement.

The preceding comparisons verify that the fundamental assumptions and the mathematical procedures of the present analytical method are valid. However, in a strict sense this method is only capable of handling pure wings or jet-wings and is unable to account for the perturbing effects of fuselage, nacelles, stores, etc. In the EVD Jet-Wing Lifting Surface Theory the effect of a fuselage, for example, is accounted for by extending the wing planform to the plane of symmetry. This approximation has been shown to reasonably predict the fuselage carryover lift. However, the shed vorticity from the fuselage is not as simple to treat mathematically as for the wing because there is no requirement on the fuselage for the flow to leave at the trailing edge as for the wing (i.e., the Kutta condition). Hence, in calculating the flow field velocities induced by a wing-body combination, extension of the wing planform to the plane of symmetry to represent the fuselage and use of the present analytical method may prove to be an over-simplification of the problem. This will be further discussed in Volume III where comparisons with experiment for wing-body combinations will be made.

#### 2.3.4 Summary and Concluding Remarks

A method has been presented to calculate the off-body velocities induced at arbitrary points by a jet-wing high lift system. The method requires a knowledge of the chordwise and spanwise loading distribution on the wing and jet sheet, which is usually obtained from the EVD Jet-Wing Lifting Surface Theory. The wing and jet sheet are modelled mathematically by a fully non-planar sheet upon which a lattice of discrete horseshoe is placed to represent the loading. The flow field induced velocities are calculated by application of the Biot-Savart Law.

Extensive comparisons with experiment have shown that the present method can adequately predict the induced flow in the vicinity of an



arbitrary jet-wing high lift system except for points which are in close proximity to the singularity sheet which represents the jet-wing. To evaluate the flow fields at points close to the wing a jet would require that the bound and/or trailing vorticity be continuous in both the chordwise and spanwise directions. This is not an intractable problem but was considered beyond the scope of the present investigation. The adoption of a spline procedure and a doublet singularity scheme might well be considered appropriate techniques that should be considered here.

### 3.0 MECHANICAL FLAP SYSTEMS WITH VECTORED THRUST

With conventional aircraft it is possible to add either auxiliary lift engines or to deflect the efflux from the cruise engines to augment airframe lift and thus provide a STOL capability. It would be logical to expect that the change in lift and drag, for example, would be, with the vectoring of the efflux, equivalent to the corresponding components of the rate of ejection of exhaust gas momentum. It has been established, however, that significant aerodynamic interferences may arise through the viscous-inviscid interactions of the efflux of the vectored-jet with the surrounding flow, which has already been significantly altered by the deflection of the mechanical flap system. The ability to analytically predict the aerodynamic characteristics of this type of STOL aircraft, already complicated by the deflection of the mechanical high lift system is, therefore, further impaired.

The difficulties associated with the prediction of the aerodynamic characteristics of STOL aircraft employing mechanical flap systems with vectored thrust are not insurmountable. If the propulsive system with its associated efflux vectoring device is not fully integrated with the wing (e.g., mounted in pods beneath the wing), then the analysis of the jet-efflux/airframe viscous-inviscid interaction problem might possibly be limited to the evaluation of aerodynamic interferences. In fact, there is sufficient experimental evidence to suggest that such an assumption would be more than justified in the case of STOL transport aircraft.

An integrated theoretical approach to the evaluation of the aerodynamic interferences for arbitrary configurations is still far beyond the state of the art. Initial attempts at an analytical analysis of the complex jet interference effects either involved order of magnitude arguments or attempts at the correlation of experimental results from various models. Unfortunately, little consideration was given to the fundamental mechanism involved. In view of this, several theoretical and fundamental experimental studies of this problem were initiated both in this country and abroad. It was found helpful to consider first the behavior and influence of a single jet at an

angle to the mainstream. In attempting to model this jet flow to reproduce the proper induced effects, a distribution of singularities located on a surface surrounding the jet (i.e., the jet envelope) might be used. This would require, however, a prior knowledge not only of the location of the jet, but also its cross-sectional shape and the velocity normal to its surface. Unfortunately, at this time our ability to evaluate these boundary conditions is, at best, qualitative. In fact, a point that should not be overlooked here is that the jet induced and the aircraft induced flow field are, in a strict sense, mutually dependent. Thus, any rigorous analytical approach to the present problem would have to employ a convergent iterative procedure. If, however, the jet-efflux does not pass close to a solid boundary (i.e., any aircraft component), it seems logical to assume that the problem can be uncoupled, at least insofar as the calculation of the jet envelope is concerned. Further, it could be argued that approximations would be justified in the formulation of the aircraft problem which are consistent with the approximations made in evaluating the jet envelope and velocity normal to it and which, in turn, determine the jet-induced flow field.

Although there may be misgivings as regards to the assumption that the jet envelope must be relatively far from the aircraft, several essentially "far-field" theoretical treatments of the efflux interferences have met with some success. Two theoretical models of the jet suggested by Wooler (reference 55), for example, have been used to predict "far-field" effects which are consistent with experimental observation. The first of these two models, a vortex representation of the jet, requires only a knowledge of the jet trajectory and the momentum flux of the jet for the computation of the induced velocity at a "far-field" point outside the jet. An interesting point worth noting is that the analytical treatment is similar to that adopted in jet-flap theory. In other words, the jet deflection and curvature are assumed to be solely related by inviscid theory to the pressure difference across the jet sheet. The second treatment, a sink-doublet model of the jet, describes the flow in more detail. This is still essentially a "far-field" theory, since any point at which the induced velocity is calculated is assumed to be far from the jet envelope. The equations of continuity and momentum for the jet are developed in terms of an unknown rate of entrainment and arbitrary cross-sectional jet envelope. These equations are solved not

only for the singularity strength but also the trajectory of the jet. To solve these equations, it is still necessary to postulate the cross-sectional shape of the jet and to establish the value of the coefficients in the empirical equation for jet entrainment. The latter are chosen to give a satisfactory correlation with available test data for the trajectory of the jet.

Although either theoretical model of the jet proposed by Wooler facilitates the analytical treatment of the interference problem, there are still, of necessity, a number of assumptions which can be strongly criticized. Despite any misgivings, the concepts employed have some physical justification and Wooler, who has undertaken (see reference 56) the extensive development and application of the second approach, has made comparisons with experimental results that provide some assurance that this method, which has been adopted herein, will have some practical value in predicting aerodynamic interferences.

In the sections that follow, Wooler's method for predicting the jet envelope and the sink-doublet model for predicting the vectored jet "far-field" induced velocities will be discussed. Aerodynamic interferences are calculated by classical potential flow arguments using a "small-perturbation" approach.

### 3.1 JET FLOW FIELD METHOD

If the mutual interaction between two or more jets is neglected, it is only necessary to consider the problem of a single jet exhausting at some arbitrary direction to the free stream. In other words, multiple-vectored jet configurations will be treated as a combination of discrete jets. The theoretical treatment proposed by Wooler for obtaining the flow field induced by a single circular jet exhausting into a cross flow is divided into two parts: (a) calculation of the jet envelope, and (b) following the mathematical representation of the jet by a distribution of sinks and doublets, the calculation of the jet induced velocity components.

#### 3.1.1 Jet Envelope

On leaving the vectored nozzle, the jet efflux is deflected downstream and rapidly distorts into a horseshoe shape, with a pair of strong counter-rotating vortices which trail downstream at the outer edge of the jet, growing in size and strength with increasing jet deflection. As mentioned earlier, the detailed flow mechanism responsible for the actual deflection and distortion of the jet in a mainstream are still, unfortunately, not understood. Pure inviscid theoretical treatments for the jet path have not met with much success. Other analytical treatments based on the assumption that the deflection is caused by a cross-flow drag force on the jet, similar to the drag on a solid cylinder, have been suggested. Although the situation still remains fundamentally unsatisfactory, these methods have nominally provided good agreement with experimental measurements. Wooler has made several refinements to the second type of approach by considering the deflection of the jet to be partly dependent on viscous entrainment in addition to a force on the jet boundary. It is assumed that the flow is everywhere incompressible and inviscid, except for the viscous phenomenon of mass entrainment by the jet. The latter effect is accounted for by the following empirical expression for the mass entrainment per unit length,  $E$ , of the jet:

$$E = \rho E_1 U d_j \sin \theta + \frac{\rho k_1 E_2 C (V_j - U \cos \theta)}{1 + E \frac{U}{3V_j} \sin \theta} \quad (3.1)$$

where  $U$ ,  $V_j$ ,  $\theta$ ,  $C$ , and  $d_j$  are the free-stream velocity, local jet velocity, the angle between the local jet velocity vector and the cross-flow vector or free-stream, the local jet circumference, and diameter, respectively. This expression was chosen for several reasons. First, it reduces to the Recon-Spalding expression for the free-jet case (i.e.,  $U = 0$ ). Second, the parameter  $E_2$  can be adjusted to agree, in the fully developed region of the jet, with the Ricou-Spalding experimental result of constant rate of change of integrated jet momentum per unit distance along the jet, equal to 0.32. This requires that  $E_2 = 0.08$ . In the development region, the entrainment characteristics will be dependent on the jet exit condition. In this region, therefore,  $E_2$  is allowed to vary in such a way that it approaches its asymptotic value of 0.08. The reader is referred to figure 1 of reference 55 for additional information regarding the variation of  $E_2$  in the development region. The third and final reason for selecting the expression for  $E$  is that  $E_1$ ,  $E_3$ , and  $k_1$  can be selected to give good agreement with experimental jet centerline measurements.

The assumption of the mass entrainment characteristics of the jet are not, by themselves, sufficient to allow the calculation of the jet envelope. It is at this point that Wooler assumes that there is a cross flow drag force acting perpendicular to the local jet centerline direction and, that along with the mainstream momentum contribution, this supplies the necessary force to produce a centripetal acceleration of the local jet mass, thus causing the jet to bend. This cross flow drag force can, for a jet element of unit length, be written as

$$F_p = C_D \frac{1}{2} \rho U^2 \sin^2 \theta d_j \quad (3.2)$$

where  $C_D$  is the cross flow drag coefficient of the jet.

Considering the jet to be divided into a development region and a fully developed region, termed (figure 3.1) Region I and Region II, respectively, Wooler assumes that the cross-sectional shape of the jet envelope changes linearly from circular to elliptical in Region I and remains elliptical in Region II. The elliptical cross-section is also assumed to have a major to minor axis ratio of 4.0. The length of Region I,  $H_I$ , is given by

$$\frac{H_I}{d/J_0} = \begin{cases} \left(0.3 \frac{V_{J_0}}{U}\right) \sec \theta_J, & \text{for } \theta_J \leq \frac{\pi}{2} \\ \left(0.3 \frac{V_{J_0}}{U}\right) \sin \theta_J, & \text{for } \theta_J \geq \frac{\pi}{2} \end{cases} \quad (3.3)$$

where  $V_{J_0}$  and  $\theta_J$  are the initial jet velocity and angle relative to the freestream. In this region, the cross-flow drag coefficient is allowed to vary from 1.0 at the jet exit to 1.8 at the end of Region I. Throughout Region II, the cross-flow drag coefficient remains constant and, therefore, equal to 1.8.

With entrainment into and the pressures forces on the jet envelope prescribed, the jet-efflux equations of motion can be expressed as follows:

Continuity:

$$\rho \frac{d(A_J V_J)}{ds} = E \quad (3.4)$$

Momentum:

$$\rho \frac{d(A_J V_J^2)}{ds} = EU \cos \theta \quad (3.5)$$

Force:

$$\rho \frac{A_J V_J^2}{R} = EU \sin \theta + \frac{1}{2} \rho \left( U \sin \theta \right)^2 d_J C_D \quad (3.6)$$

where  $R$  is the radius of curvature of the jet centerline and  $A_J$  is the local jet cross sectional area. Before proceeding to a solution of the equations of motion, Wooler establishes a functional relationship between the cross sectional area  $A_J$ , the circumference  $C$  of the jet, and the jet growth.

On the basis of assumptions made earlier, the geometric characteristics  $A_J$  and  $C$  of the jet can be treated in two regions, namely Region I and Region II.

- Region I: In this region, the jet has been assumed to deform from a circular to an elliptical cross section and that the ratio of minor to

major axis decreases linearly with  $z$  from 1 at  $z/d_{J0} = 0$  to  $1/4$  at  $z/d_{J0} = -H_I/d_{J0} = -0.3 \frac{V_{J0}}{U} (\sin \theta_J)^a$  where  $a = (\theta_J - \frac{\pi}{2}) / |\theta_J - \frac{\pi}{2}|$ . In this case, therefore, the ratio of minor to major axis can be written as

$$1 + \frac{5}{2} (\sin \theta_J)^{-a} (z/d_{J0}) (U/V_{J0})$$

which yields the following expressions for  $A_J$  and  $C$  in Region I:

$$A_J = \frac{\pi d_J^2}{4} \left[ 1 + \left(\frac{5}{2}\right) (\sin \theta_J)^{-a} (U/V_{J0}) \right] \quad (3.7)$$

$$C \approx \frac{\pi d_J}{\sqrt{2}} \left[ 1 + \left( 1 + \left(\frac{5}{2}\right) (\sin \theta_J)^{-a} (U/V_{J0}) \right)^2 \right]^{1/2} \quad (3.8)$$

- Region II: In this region (i.e.,  $z/d_{J0} \leq H_I/d_{J0}$ ) the jet is assumed to retain a similar cross section. Hence,  $A_J$  and  $C$  can be written as

$$A_J = \frac{\pi d_J^2}{16} \quad (3.9)$$

$$C \approx \frac{\pi}{4} (8.5)^{1/2} d_J = 2.29 d_J \quad (3.10)$$

It is important to note here that Wooler has incorrectly assumed that  $C = 2.24d_J$ . To be consistent with the approximate equation used earlier for the circumference of the ellipse, the expression given in equation (3.10) has been used in the present work.

The next step in the solution of the equations of motion for the jet envelope requires the consolidation of equations (3.4), (3.5), and (3.6). Consider first equation (3.4). The left hand side can alternatively expressed as

$$\rho \frac{d(A_J V_J)}{ds} = \rho \frac{d(A_J V_J^2 / V_J)}{ds}$$



Hence,

$$E = \frac{\rho}{V_J} \frac{d(A_J V_J^2)}{ds} + \rho A_J V_J^2 \frac{d(1/V_J)}{ds} \quad (3.11)$$

which by substituting equation (3.5), yields

$$E = \frac{1}{V_J} EU \cos \theta - \rho A_J \frac{d V_J}{ds} \quad (3.12)$$

Substituting for  $A_J$  and  $C$ , the following two equations for  $\frac{d V_J}{dz}$  in Regions I and II are obtained:

● Region I

$$\begin{aligned} \frac{d V_J}{dz} = & - \left\{ E_1 \sin \theta + \frac{k_1 E_2 (m V_J - \cos \theta) \pi}{1 + E_3 \sin \theta / V_J m} \right. \\ & \times \left. \left[ \frac{1 + \left(1 + \frac{5}{2} (\sin \theta)^{-a} (z/m)\right)^2}{2} \right]^{1/2} \right\} \\ & \times \left\{ \frac{4(\cos \theta - m V_J)}{\pi \left(1 + \frac{5}{2} (\sin \theta)^{-a} (z/m)\right) d_J m^2 V_J \sin \theta} \right\} \end{aligned} \quad (3.13)$$

● Region II

$$\begin{aligned} \frac{d V_J}{dz} = & - \left\{ \frac{16}{\pi d_J^2 m^2 V_J \sin \theta} \right\} (\cos \theta - m V_J) \\ & \times \left\{ E_1 \sin \theta + \frac{E_2 (m V_J - \cos \theta) 2.29}{(1 + E_3 \sin \theta / V_J m)} \right\} \end{aligned} \quad (3.14)$$

where  $V_J$  and  $z$  and  $d_j$  have been normalized by  $V_{J0}$  and  $d_{J0}$  respectively and have retained their same symbols, and  $m = V_{J0}/U$ .

Considering the continuity and force expressions (i.e., equations (3.4) and (3.6)) and substituting for  $A_J$  and  $C$ , Wooler obtains an additional set of equations, in this case for  $dd_J/dz$  and  $d^2x/dz^2$ , that apply to Regions I and II. It can be shown that these equations in their non-dimensional form can be written as

$$\begin{aligned} \frac{d d_J}{dz} = & - \left\{ \left[ E_1 \sin \theta + \frac{\pi E_2 k_1 (mV_J - \cos \theta)}{(1 + E_3 \sin \theta / V_J m)} \left[ \frac{1 + \left(1 + \frac{5}{2} (\sin \theta)^{-a} (z/m)\right)^2}{2} \right]^{1/2} \right] \right. \\ & \times \frac{d_J}{m \sin \theta} + \pi \frac{5}{8} \pi d_J^2 \frac{V_J}{m} - \frac{\pi}{4} d_J^2 \left( 1 + \frac{5}{2} (\sin \theta)^{-a} \left(\frac{z}{m}\right) \right) \\ & \left. \frac{d V_J}{dz} \right] \frac{2}{\pi d_J V_J \left( 1 - \frac{5}{2} (\sin \theta)^{-a} (z/m) \right)} \end{aligned} \quad (3.15)$$

$$\begin{aligned} \frac{d^2 x}{dz^2} = & \left[ 1 + \left( \frac{dx}{dz} \right)^2 \right]^{3/2} \left\{ \frac{4 \sin \theta}{m^2 \pi d_J V_J^2 \left( 1 - \frac{5}{2} (\sin \theta)^{-a} (z/m) \right)} \right\} \\ & \times \left\{ \left( E_1 + .5C_D \right) \sin \theta \right. \\ & \left. + \left( \frac{\pi E_2 k_1 (mV_J - \cos \theta)}{1 + E_3 \sin \theta / V_J m} \right) \left( \frac{1 + \left(1 + \frac{5}{2} (\sin \theta)^{-a} \right)^2}{2} \right) \right\} \end{aligned} \quad (3.16)$$

● Region II

$$\begin{aligned} \frac{d d_J}{dz} = & \left\{ \frac{8}{\pi m \sin \theta V_J} \right\} \left\{ \frac{\pi}{16} m \sin \theta dz \frac{d V_J}{dz} \right. \\ & \left. - E_1 \sin \theta - \frac{2.29 E_2 (mV_J - \cos \theta)}{(1 + E_3 \sin \theta / V_J m)} \right\} \end{aligned} \quad (3.17)$$

$$\frac{d^2x}{dz^2} = \left[ 1 + \left( \frac{dx}{dz} \right)^2 \right]^{3/2} \left[ \frac{16 \sin \theta}{\pi m^2 d_J V_J^2} \right. \\ \left. \times \left\{ (E_1 + .5C_D) \sin \theta + \frac{2.29 E_2 (m V_J - \cos \theta)}{(1 + E_3 \sin \theta / V_J m)} \right\} \right] \quad (3.18)$$

With the additional substitution

$$\sin \theta = \frac{1}{\left[ 1 + \left( \frac{dx}{dz} \right)^2 \right]^{1/2}}$$

$$\cos \theta = - \frac{dx/dz}{\left[ 1 + \left( \frac{dx}{dz} \right)^2 \right]^{1/2}}$$

equations (3.13), (3.15), and (3.16) applicable to Region I and equations (3.13), (3.17), and (3.18) applicable to Region II are seen to constitute a set of differential equations to be solved for  $V_J$ ,  $d_J$ , and  $x$  as functions of  $z$  and the parameters  $E_1$ ,  $E_2$ ,  $E_3$ , and  $C_D$ .

The numerical procedure employed for solving the two resulting sets of three simultaneous linear differential equations, as per the approach taken by Wooler, consists of an Adams predictor-corrector scheme with a Runge-Kutta starting condition. The initial conditions at the jet exit are

$$z = 0., \quad x = 0., \quad V_J = 1., \quad \text{and} \quad \frac{dx}{dz} = \cot \theta_J.$$

Since  $k_1 E_2$  is allowed to vary in Region I,  $E_2$ , as mentioned earlier, is determined to be 0.08 while  $k_1$  becomes

$$\begin{aligned} &= 1.0 \text{ for } z > 10 \\ &= 21/32 \text{ for } z > 0.8H_I \\ &= 12/32 \text{ for } z > 0.6H_I \\ &= 10/32 \text{ for } z \leq 0.6H_I \end{aligned} \quad (3.19)$$

The parameters  $E_1$  and  $E_3$  were selected by Wooler to give good correlation between experimentally and theoretically evaluated jet centerlines and jet-induced surface pressures. This approach resulted in an  $E_1 = 0.45$  and an  $E_3 = 30.0$ . The cross flow drag coefficient,  $C_D$ , as mentioned earlier, varies in Region I, and is given by:

$$C_D = \frac{1}{6} \left\{ 4 + 6.6 \left( \frac{1}{1 - \frac{5}{2} (\sin \theta_J)^{-a} (z/m)} \right) - \frac{1}{\left[ 1 - \frac{5}{2} (\sin \theta_J)^{-a} (z/m) \right]^2} \right\} \quad (3.20)$$

### 3.1.2 Jet Induced Velocity Field

To obtain the jet induced velocity field, Wooler assumed the entrained fluid to be represented by a uniform sink distribution placed orthogonal to the plane of the jet and the mainstream [see figure (3.1)] and a distribution of doublets with their axis perpendicular to the jet centerline to represent the so-called jet "blockage" phenomenon. The strength of the doublet distribution is obtained from a questionable two-dimensional analogy. In effect, the flow considered is that past an equivalent circular cylinder since the strength is obtained from the  $1/z$  term in the complex velocity expansion  $w(z)$  for the two-dimensional flow past an ellipse. In addition to the sink and doublet distribution, Wooler has recently introduced a third set of singularities which are also distributed along the calculated jet centerline. This latter is a set of point sources which are blindly added to compensate for the invalidity of the hypothesized entrainment expression. The source strength are made proportional to the local curvature, which are justified by Wooler mainly through comparison with experimental results. The total jet induced velocity at a point  $(x, y, z)$  in space can be obtained by integrating the effects of all singularities. The details of the calculation procedure will be discussed below.

Consider an element of the jet of length  $\delta_s$  with centerline coordinates  $(\xi, 0, \zeta)$ . The sink distribution per unit distance in the  $y$  direction will

be given by

$$\bar{m}(s) = \delta_s U \left\{ E_1(s) \sin \theta(s) + \frac{k_1 E_2(s) [V_J(s) m - \cos(s) C(s)]}{d_J(s) (1 + E_3(s) \sin \theta(s) / V_J(s) m)} \right\} \quad (3.21)$$

The total "sink" perturbation velocity ( $u_s, v_s, w_s$ ) at ( $x, y, z$ ) induced by an element of jet of length  $\delta_s$  can be obtained by substituting for  $\bar{m}(s)$  in the following equations for  $\Delta u_s, \Delta v_s$  and  $\Delta w_s$  and integrating these expressions over the extent of the jet.

$$\begin{aligned} \frac{\Delta u_s}{U}(x, y, z) &= \frac{\bar{m}}{4\pi U} \int_{-d_J/2}^{d_J/2} \frac{(\xi-x) d\eta}{[(\zeta-z)^2 + (\xi-x)^2 + (\eta-y)^2]^{3/2}} \\ &= \frac{-\bar{m}}{4\pi U} \frac{(\xi-x)}{[(\zeta-z)^2 + (\xi-x)^2]} \\ &\quad \times \left\{ \frac{y-d_J/2}{[(\zeta-z)^2 + (\xi-x)^2 + (d_J/2-y)^2]^{1/2}} \right. \\ &\quad \left. - \frac{y+d_J/2}{[(\zeta-z)^2 + (\xi-x)^2 + (d_J/2+y)^2]^{1/2}} \right\} \quad (3.22) \end{aligned}$$

$$\frac{\Delta v_s}{U}(x, y, z) = -\frac{\bar{m}}{4\pi U} \int_{-d_J/2}^{d_J/2} \frac{(y+\eta) d\eta}{[(\zeta-z)^2 + (\xi-x)^2 + (\eta-y)^2]^{3/2}}$$

$$= - \frac{\bar{m}}{4\pi U} \left\{ \frac{1}{\left[ (\zeta-z)^2 + (\xi-x)^2 + (d_j/2-y)^2 \right]^{1/2}} - \frac{1}{\left[ (\zeta-z)^2 + (\xi-x)^2 + (d_j/2+y)^2 \right]^{1/2}} \right\} \quad (3.23)$$

$$\begin{aligned} \frac{\Delta w_s}{U}(x,y,z) &= - \frac{\bar{m}}{4\pi U} \int_{-d_j/2}^{+d_j/2} \frac{(\zeta-z) d\eta}{\left[ (\zeta-z)^2 + (\xi-x)^2 + (\eta-y)^2 \right]^{3/2}} \\ &= + \frac{\bar{m}}{4\pi U} \frac{(\xi-z)}{\left[ (\zeta-z)^2 + (\xi-x)^2 \right]} \\ &\quad \times \frac{y-d_j/2}{\left[ (\zeta-z)^2 + (\xi-x)^2 + (\eta-d_j/2)^2 \right]^{1/2}} \\ &\quad - \frac{y+d_j/2}{\left[ (\zeta-z)^2 + (\xi-x)^2 + (\eta+d_j/2)^2 \right]^{1/2}} \quad (3.24) \end{aligned}$$

It should be noted that  $\Delta w_s$  in equation (3.24) represents the downwash.

As mentioned earlier, the strength of the doublet distribution utilized to represent the blockage effect of the jet is obtained from the complex velocity potential for the two-dimensional flow past an ellipse. By equating the strength of the doublet to the coefficient of the  $1/2$  term, the flow past an equivalent circular cylinder is being considered.

The complex velocity potential for an ellipse can be written as

$$W_{\alpha=0}(z) = \frac{1}{2} U \sin \theta (a+b) \left[ \frac{z+(z^2-c^2)^{1/2}}{(a+b)} + \frac{z-(z^2-c^2)^{1/2}}{(a-b)} \right] \quad (3.25)$$

where  $a$  and  $b$  are the minor and major semi-axis of the ellipse. Considering a binomial expansion of equation (3.25), the leading two terms in a series of inverse powers are

$$w(z) = Uz + \frac{1}{2} U (a+b) b (1/z)$$

where it is possible to equate the strength of the doublet,  $\mu$ , with the coefficient of the  $1/z$  term. In other words,  $\mu$ , becomes

$$\mu = \frac{1}{2} U(a+b)(b) \sin \theta$$

alternatively

$$\left. \begin{aligned} \mu &= \frac{\pi}{4} U d_J^2 \sin \theta \left[ 1 - \frac{5}{2} (\sin \theta_J)^{-a} z/m \right], & \text{(in Region I)} \\ &= \frac{5\pi U d_J^2 \sin \theta}{32}, & \text{(in Region II)} \end{aligned} \right\} \quad (3.26)$$

With the notation of figure (3.1), the induced velocity field at a point  $(x,y,z)$  due to a doublet of strength  $\mu$  at  $(\xi, \eta, \zeta)$  is given by

$$\left. \begin{aligned} \frac{\Delta U_D}{U} &= \frac{\Delta u'_D}{U} \cos \theta + \frac{\Delta w'_D}{U} \sin \theta \\ \frac{\Delta V_D}{U} &= - \frac{\Delta v'_D}{U} \\ \frac{\Delta W_D}{U} &= \frac{\Delta w'_D}{U} \sin \theta - \frac{\Delta u'_D}{U} \cos \theta \end{aligned} \right\} \quad (3.27)$$

where

$$\frac{\Delta u'_D}{U} = - \frac{6}{4\pi} \left( \frac{\mu}{U} \right) x' z' \left( x'^2 + y'^2 + z'^2 \right)^{-5/2}$$

$$\frac{\Delta v'_D}{U} = -\frac{6}{4\pi} \left(\frac{\mu}{U}\right) y' z' (x'^2 + y'^2 + z'^2)^{-5/2}$$

$$\frac{\Delta w'_D}{U} = \frac{2\mu/U}{4\pi(x'^2 + y'^2 + z'^2)^{3/2}} \left[ 1 - \frac{3z'^2}{x'^2 + y'^2 + z'^2} \right]$$

in which  $x'$ ,  $y'$ , and  $z'$  are given by

$$x' = (\xi - x) \cos \theta + (\zeta - z) \sin \theta$$

$$y' = -\eta$$

$$z' = (\xi - x) \sin \theta - (\zeta - z) \cos \theta$$

and  $\mu$  is obtained from equation (3.26). The total "doublet perturbation velocity ( $u_s, v_s, w_s$ ) is determined from an integration of equation (3.27) over the extent of the jet.

There remains the induced velocity field ( $u'_s, v'_s, w'_s$ ) associated with the additional source distribution. Wooler assumes this distribution to be proportional to jet curvature and has established that the best correlation with experimental data, over the range of velocity ratios  $.1 \leq U/V_{j0} \leq .3$ , is obtained by taking the source strength equal to three times the jet curvature. Hence, to obtain the velocity field induced by both the sink and source distribution, it is simply necessary to substitute  $\bar{m}$  in equations (3.22), (3.23), and (3.24) not by equation (3.21) but by the following expression

$$\bar{m} = -3 \frac{d\theta}{ds} + \delta_s U \left\{ E_1(s) \sin \theta(s) + \frac{E_2(s)(V_j(s) - \cos(s) C(s))k_1}{d_j(s)(1 + E_3(s) \sin \theta(s)/V_j(s)m)} \right\} \quad (3.28)$$

The total interference velocity at the point ( $x, y, z$ ) is now obtained from a summation of the component velocities induced by the sink, source, and doublet distributions.



### 3.1.3 Summary and Concluding Remarks

Wooler has undertaken an extensive correlation of analytical results obtained with the method described in the previous section and experimental data. Some typical results obtained by the authors with the computer program described in Volume II are presented in figure (3.2). Estimates of the trajectory of the jet, for example, reproduce effectively the trajectory determined experimentally, while the analytical results give reasonable predictions of the experimental pressure measurements on an infinite plane wall from which a single jet issues normally.

Extensions of the Jet Flow Field method to include the effects of ground proximity and to provide a basis for the evaluation of aircraft rotary dynamic derivatives have been considered. In ground effect, the authors have adopted the approach suggested by Wooler. That is, it is assumed that the jet envelope is unaffected by the presence of the ground up to the point of impingement. From the point of impingement, the jet is then considered to be parallel to the ground and freestream. The induced flow field then simply requires the computation of the velocities induced by both the jet and its image. The effect of rotary variables (i.e., pitching, rolling, and yawing) on the development of the jet can be considered in the basic method as a change in the mainstream velocity vector. Wooler (reference 56) presents a detailed discussion of this approach; but in general concludes that the effects of rotary variables can be considered as negligible. Frankly, the overall accuracy of the basic method should be improved before the satisfactory estimation of the effects of rotary variables can proceed. Thus, the authors are of the opinion that the effect of rotary variables should not be taken into account. But, more evidence and analysis is needed to support this.

Although valuable progress has been made by the formulation of the sink/doublet mathematical model, further attempts at development along such lines seem of doubtful value until the mechanism of jet deflection is better understood. Despite the progress made in the development of the sink/doublet model and the alternative vortex sheet model mentioned earlier, there still remain objections to each theory. It might be argued, for example, that there is little justification for the adoption of an inviscid model of the

flow, except by invoking the arguments that the major region of the flow field can be treated in inviscid terms providing the boundary conditions take account of the viscous flow on the envelope of the jet. Next, the assumptions made in arriving at the momentum equation (i.e., equation 3.5) imply that, with the exception of the momentum of the entrained freestream air, the momentum flux along the jet is constant - an assumption difficult to justify at large jet deflections or low values of the velocity ratio  $V_{j0}/U$ . Finally, a closer examination of the mathematical model will reveal that the concepts employed are naturally questionable as the jet angle,  $\theta_j$ , approaches zero. Nevertheless, the authors have had some success in predicting aerodynamic interference at jet angles greater than or equal to five degrees.

### 3.2 AERODYNAMIC/PROPULSION INTERFERENCES

The extension of the "far field" jet-flow field theory discussed in Section (3.1) to the practical case of a STOL aircraft employing mechanical high lift systems in conjunction with vectored thrust will now be considered. This involves nothing more than simply the computation of the velocity field induced over the wing, fuselage, and empennage, followed by the derivation of, for example, the wing aerodynamic loading consistent with the induced downwash distribution. Two important factors might discourage the adoption of such an approach. Firstly, the jet flow field method discussed earlier suggests that a large downwash variation might be induced by the jet. Theoretical methods currently available for estimating, for example, wing loading might not, therefore, be adequate. Secondly, there has been difficulty in explaining, for example, wing surface-pressure distributions as effected by the jet efflux. Evidence and analysis are, therefore, needed to clarify and subsequently to solve these problems. From the point of view of the prediction of lift interferences, however, the experimental data (reference 57) is to a degree consistent [figure (3.3a)] with the simple argument that the jet flow merely induces a downwash velocity past the wing which combines with the freestream velocity to produce a change in the effective camber and twist of the wing. Results also give a reasonable prediction [figure (3.3b)] of the experimental chordwise loading measurements considering the complexity of the flow field. In fact some of the discrepancy between experimental and calculated results are, in part, due to the inability of the present method, in particular EVD lifting surface theory, to consider more than one wing element (e.g., a single or double slotted flap).

In view of the above, the present technique for calculating aerodynamic propulsion interferences, in particular those associated with the vectoring of the propulsive thrust, comprises the following two steps:

- Calculate the jet location and envelope for each jet followed by the perturbation velocities induced on the aircraft surface boundaries by all jets by the Jet-Flow Field method.
- Calculate the aircraft aerodynamic performance and stability and control

characteristics with or without these perturbation velocities as boundary conditions by the wing, fuselage, and empennage methods presented in this report.

To obtain satisfactory results, two important assumptions must be adopted. The first requires that the mutual interaction between one jet and the remaining jets, as well as the mutual interaction between any jet and the aircraft, be neglected. The second requires that the jets neither impinge on, nor are in close proximity to any of the aircraft surfaces. In other words, the Jet Flow Field method is a "far-field" theory.

#### 4.0 METHODS FOR THE ANALYSIS OF THE AERODYNAMICS OF AIRCRAFT COMPONENTS

In the preceding sections, analytical methods have been presented for calculating the aerodynamic and stability and control characteristics of jet-wings and wings with vectored jets. In addition, it is necessary to provide a capability to calculate the contributions of other aircraft components, particularly for stability and control analyses. However, it is necessary to consider the mutual aerodynamic interferences between aircraft components to properly calculate complete aircraft aerodynamic characteristics. The approach adopted in this work is to approximately account for these interferences by determining the flow field induced on these components by the jet-wing and/or vectored jets, but to neglect the influence of these components on the jet-wing or vectored jets. It is shown in the following sections that treating interferences in this manner is a reasonable approximation for transport aircraft-type configurations where the influences of the components on the wing are small. However, for aircraft with low aspect ratio wings and/or low fineness ratio bodies, the mutual interferences are not likely to be small, and a fully integrated solution is likely to be required.

Treating the interference problem in the manner just described eliminates the need for an iterative solution, which otherwise would be required since the location of the jet sheet and/or vortex wake, which is a function of the loading on all aerodynamic surfaces, would be unknown a priori. It is the opinion of the authors that the approach adopted here should be adequate for the purposes of most STOL transport design and analysis work.

In the following sections methods for calculating the contributions to the aircraft aerodynamic characteristics of the fuselage and empennage (horizontal tail and vertical tail) are presented. Interferences due to the jet-wing and/or vectored jets are treated in the manner discussed here.

## 4.1 FUSELAGE ANALYSIS

A method based, in part, on slender body theory has been developed as a basis for predicting the contributions of the fuselage to the overall static and dynamic stability and control characteristics of STOL configurations employing internally ducted and externally blown jet flaps and mechanical flap systems with vectored thrust. A rigorous analytical solution of the integrated jet-wing-fuselage problem is considered to be desirable but is beyond the scope of this study. However, the method described herein should be adequate for the preliminary aerodynamic design and evaluation of turbofan powered STOL transport aircraft.

Although slender body theory has been used as a basis for the method presented, modifications to the theory have been made to account for, in an approximate sense, bodies with non-circular cross-sectional geometry, body camber (e.g., fuselage upsweep), and jet-wing or vectored jet induced downwash and sidewash on the fuselage. No account is made for flow separation from the fuselage afterbody, but even a fully integrated jet-wing-fuselage analysis could not account for flow separation or vortex shedding from the fuselage. There are no general methods for the solution of the flow about a body with separation from the afterbody.

In the following sections a review of classical slender body theory<sup>58</sup> will be made followed by modifications to the method and an analysis of the fuselage contributions to the aerodynamic characteristics of a complete aircraft.

### 4.1.1 Slender Body Theory

The concept of slender body theory for the flow past a body of revolution was originated by Munk (reference 59) in his studies of airship hulls. The concept has been developed to cover a wide variety of applications because of its relative simplicity as compared to exact methods and because, for a wide variety of useful body shapes, it produces excellent agreement with exact methods.

Consider the steady flow of an incompressible fluid past a body of revolution at an angle of attack relative to the freestream. The body is oriented with its axis coincident with the x-axis and its leading edge (nose) at the origin (see figure 4.1). It will be convenient to use the cylindrical coordinate system  $(r, \theta, x)$  as shown in figure (4.1), related to the Cartesian system  $(x, y, z)$  by

$$x = x, \quad y = r \sin \theta, \quad z = -r \cos \theta \quad (4.1)$$

The unconventional choice of  $\theta = 0$  on the  $-z$  axis was made to facilitate symmetry considerations, as will be discussed in Section 4.1.2. The surface of the body may be described by

$$r = R(x) \quad (4.2)$$

which may also be expressed as

$$F(r, \theta, x) = r - R(x) = 0 \quad (4.3)$$

The basic equation to be solved is Laplace's equation

$$\nabla^2 \phi = 0 \quad (4.4)$$

subject to the boundary condition that there be no flow through the surface of the body, expressed by

$$\vec{\nabla} \phi \cdot \vec{\nabla} F = 0 \quad \text{on} \quad F(r, \theta, x) = 0 \quad (4.5)$$

where  $\vec{\nabla} \phi$  is the total velocity vector  $\vec{V}$  and  $\vec{\nabla} F$  is the normal to the surface of the body. Also, the flow must be undisturbed at infinity, so

$$\vec{\nabla} \phi = U_{\infty} \quad (\text{at infinity}) \quad (4.6)$$

It is convenient to reformulate the problem in terms of a perturbation velocity potential  $\phi(r, \theta, x)$ , whereby equations (4.4), (4.5), and (4.6) become

$$\nabla^2 \phi = 0$$

$$(\vec{V}_\infty + \vec{v}_\phi) \cdot \vec{\nabla} F = 0 \text{ or } F(r, \theta, x) = 0 \quad (4.7)$$

$$\vec{\nabla} \phi = \vec{q} = 0 \text{ at infinity}$$

Expressing equations (4.7) fully in cylindrical coordinates yields

$$\frac{\partial^2 \phi}{\partial r^2} + \frac{1}{r} \frac{\partial \phi}{\partial r} + \frac{1}{r^2} \frac{\partial^2 \phi}{\partial \theta^2} + \frac{\partial^2 \phi}{\partial x^2} = 0$$

$$(U_\infty \sin \alpha \cos \theta + u_r) \frac{\partial F}{\partial r} + (U_\infty \cos \alpha + u_x) \frac{\partial F}{\partial x} = 0 \text{ on } F = 0 \quad (4.8)$$

$$(u_r, u_\theta, u_x) = 0 \text{ at infinity}$$

where  $(u_r, u_\theta, u_x)$  are perturbation velocities. Since Laplace's equation is linear in  $\phi$ , the velocity potential may be expressed as the sum of two perturbation potentials

$$\phi = \phi_1 + \phi_2 \quad (4.9)$$

and the solution to equation (4.8) may be formed by the superposition of solutions for  $\phi_1$  and  $\phi_2$ . From equation (4.3) it can be seen that

$$\frac{\partial F}{\partial r} = 1 \text{ and } \frac{\partial F}{\partial x} = -\frac{dR}{dx} \quad (4.10)$$

so the boundary condition equation of (4.8) can be rewritten as

$$\frac{\partial \phi}{\partial r} = u_r = (U + u_x) \frac{dR}{dx} + W \cos \theta \quad (4.11)$$

where  $U = U_\infty \cos \alpha$  and  $W = U_\infty \sin \alpha$ . Using equation (4.9) and noting that it follows that

$$u_x = u_{x_1} + u_{x_2} \quad (4.12)$$



the boundary condition can finally be expressed as

$$\frac{\partial \phi_1}{\partial r} (R, \theta, x) = (U + u_{x_1}) \frac{dR}{dx}, \quad (4.13)$$

$$\frac{\partial \phi_2}{\partial r} (R, \theta, x) = u_{x_2} \frac{dR}{dx} + W \cos \theta \quad (4.14)$$

Having divided the solution in this manner, it can be seen that equation (4.13) is the boundary condition for the axisymmetric flow past a body of revolution in a freestream of speed  $U$  and equation (4.14) is the boundary condition for the cross flow past the same body of revolution in a freestream of speed  $W$ .

Up to this point the analysis has been exact. It is now that the concept of a slender body of revolution is introduced to make the solution of equation (4.4) subject to the boundary conditions, equations (4.13) and (4.14), tractable. Consider a body of revolution whose cross-sectional radius changes slowly with distance along its axis; that is,  $dR/dx$  is small. Now, since  $u_{x_1}$  and  $u_{x_2}$  are perturbation quantities that will be small for a slender body, the terms  $u_{x_1}(dR/dx)$  and  $u_{x_2}(dR/dx)$  in (4.13) and (4.14), respectively, are second order small and may be neglected. Hence, the surface conditions reduce to the simple form

$$\frac{\partial \phi_1}{\partial r} (R, \theta, x) = U \frac{dR}{dx} \quad (4.15)$$

$$\frac{\partial \phi_2}{\partial r} (R, \theta, x) = W \cos \theta \quad (4.16)$$

It must be emphasized that the assumption of small perturbations is not valid at or near stagnation points of the body or near the ends of a body with rounded ends where  $dR/dx$  is not small compared to unity. For many bodies of interest, however, the regions where the slender body assumption is not valid are small.

The solution of Laplace's equation subject to boundary condition (4.15) is the solution for an axisymmetric flow past a slender body of revolution. Based on past experience it is known that such a flow may be represented by

a suitable distribution of sources (and sinks) on the body axis. Letting  $q(x)$  denote the source distribution, the velocity potential is

$$\phi_1(r,x) = -\frac{1}{4\pi} \int_0^{\ell} q(\xi) \frac{d\xi}{\sqrt{(x-\xi)^2+r^2}} \quad (4.17)$$

where  $\ell$  is the length of the body. It is now necessary to relate the source strength  $q(x)$  to the body geometry. First it should be noted that one necessary condition is

$$\int_0^{\ell} q(x)dx = 0 \quad (4.18)$$

since the body is closed and no mass is added to or taken from the flow. The linearized form of the surface condition, equation (4.15), can be used to develop an approximate relationship between  $q(x)$  and  $R(x)$ . Consider a small cylinder of radius  $r$  and length  $dx$  surrounding an element of source distribution. As  $r \rightarrow 0$  the volume outflow becomes

$$q(x)dx = \lim_{r \rightarrow 0} (2\pi u_r r dx)$$

or

$$\lim_{r \rightarrow 0} (ru_r) = \frac{q(x)}{2\pi} \quad (4.19)$$

For small  $r$  this shows that

$$u_r \sim \frac{1}{r}$$

and hence  $u_r$  must be infinite as  $r \rightarrow 0$ . In order to make use of the surface condition, it is necessary to relate  $(ru_r)_{r \rightarrow 0}$  to  $(ru_r)_{r=R(x)}$ , which is similar to transferring the boundary condition from the surface to the camber line of a thin airfoil. Hence, the slender body approximation implies that

$$(ru_r)_{r=R(x)} = (ru_r)_{r \rightarrow 0} \quad (4.20)$$

and, therefore, the source strength can be determined from (4.15), (4.19) and (4.20) to be

$$q(x) = 2\pi UR \frac{dR}{dx} = U \frac{dS}{dx} \quad (4.21)$$

where  $S(x)$  is the distribution of cross-sectional area. Finally, the perturbation velocity potential can be expressed as

$$\phi_1(x, r) = - \frac{U}{4\pi} \int_0^l \frac{dS}{d\xi} (\xi) \frac{d\xi}{\sqrt{(x-\xi)^2 + r^2}} \quad (4.22)$$

for the axial flow solution.

The solution of Laplace's equation subject to boundary condition (4.16) is the solution for the cross flow past a slender body of revolution. Since the cross-section of the body is circular, the flow can be represented by doublet distribution along the axis of the body. Letting  $\mu(x)$  be the strength of the doublet distribution, it can be shown that

$$\phi_2(r, \theta, x) = - \frac{1}{4\pi} \int_0^l \mu(\xi) \frac{r \cos \theta}{[(x-\xi)^2 + r^2]^{3/2}} d\xi \quad (4.23)$$

By using arguments analogous to those employed in the axial flow problem for the transfer of the boundary condition from the surface to the axis, it can be shown that

$$\mu(x) = 2\pi WR^2(x) = 2WS(x) \quad (4.24)$$

For small values of  $r$ , equation (4.23) can be integrated, using (4.24), so that approximately

$$\phi_2(r, \theta, x) = - \frac{WS(x) \cos \theta}{\pi r} \quad (4.25)$$

for the cross flow solution.

The total surface perturbation potential is expressed by (4.9),

$$\phi = \phi_1 + \phi_2$$

where  $\phi_1$ , is determined by (4.22) and  $\phi_2$  by (4.25). Once the surface perturbation velocity potential has been determined, the surface velocities can easily be calculated by differentiation of (4.9) to determine  $(u_r, u_\theta, u_x)$  or  $(u_x, u_y, u_z)$ . Finally the surface pressure distribution is calculated from

$$c_p(x,y,z) = 1 - \frac{(U+u_x)^2 + u_y^2 + (W + u_z)^2}{U_\infty^2} \quad (4.26)$$

#### 4.1.2 Modification of Slender Body Theory for Non-Axisymmetric Bodies in Non-Uniform Flows

For bodies which are not axisymmetric, the analysis of Section 4.1.1 does not apply. However, for nearly axisymmetric bodies, that is, for bodies whose cross-sections are nearly circular and/or whose axis is nearly straight, the assumptions of slender body theory can still be employed with certain modification.<sup>61</sup> Examples of bodies which fall into this category are fuselages with oval, elliptical, or nearly circular cross-sections, moderately upswept fuselages, or fuselages with moderately small protuberances. In addition, a modification to slender body theory is desirable such that non-uniform onset flows on the body can be considered.

The classical slender body theory discussed in Section 4.1.1 is composed of two superpositioned solutions. The first is axisymmetric in form and provides a source distribution to generate the proper distribution of cross-sectional area. In the general case of non-circular cross-sections and non-cylindrical shape (i.e., a non-straight axis), if the geometry is "sufficiently axisymmetric" so there are no significant velocities in the theta direction ( $u_\theta$ , see figure 4.1), then the axial flow can be calculated in the slender body sense over an equivalent body of revolution having the same distribution of cross-sectional area as the actual body. Therefore, a perturbation velocity potential for the axial flow  $\phi_1(x,r)$  can be calculated in

a manner analogous to the axisymmetric case, except equation (4.22) must be changed to

$$\phi_1(x,r) = -\frac{U}{4\pi} \int_0^{\ell} \frac{d\tilde{S}}{d\xi}(\xi) \frac{d\xi}{\sqrt{(x-\xi)^2+r^2}} \quad (4.27)$$

where  $\tilde{S} = S(x)$  is the area distribution of the equivalent body of revolution.

In the actual numerical solution developed here, the body is divided into a series of streamwise segments by planes normal to the body axis [figure (4.2)]. Then the velocity potential can be determined by numerical integration of (4.27); but since it is actually the surface velocities rather than surface velocity potential that is desired for the final solution,

$$u_{x_1}(x,r) = \frac{U}{4\pi} \int_0^{\ell} \frac{d\tilde{S}}{d\xi}(\xi) \frac{(x-\xi)}{[(x-\xi)^2+r^2]^{3/2}} d\xi \quad (4.28)$$

and

$$u_{r_1}(x,r) = \frac{U}{4\pi} \int_0^{\ell} \frac{d\tilde{S}}{d\xi}(\xi) \frac{r}{[(x-\xi)^2+r^2]^{3/2}} d\xi \quad (4.29)$$

will be integrated numerically directly. Since it has been assumed that the body is slender, it is reasonable to assume that the area gradient,  $d\tilde{S}/dx$ , is nearly constant over a segment. If it is not, then a closer segment spacing can always be chosen so that the assumption is valid. Thus,  $d\tilde{S}/dx$  can be taken piecewise outside the integrals in (4.28 and (4.29). Finally,  $u_{x_1}$  and  $u_{r_1}$  on the  $i$ th segment can be calculated from

$$u_{x_1}(x_i, r_i) = \frac{1}{4\pi} \sum_j^{\bar{M}} \left( \frac{d\tilde{S}}{dx} \right)_j \left\{ \frac{1}{[(\xi_{j+1}-x_i)^2+r_i^2]^{1/2}} - \frac{1}{[(\xi_j-x_i)^2+r_i^2]^{1/2}} \right\} \quad (4.30)$$

$$u_{r_1}(x_i, r_i) = \frac{1}{4\pi} \sum_j^{\bar{M}} \left( \frac{d\tilde{S}}{dx} \right)_j \left\{ \frac{\xi_{j+1}-x_i}{r_i[(\xi_{j+1}-x_i)^2+r_i^2]^{1/2}} - \frac{\xi_j-x_i}{r_i[(\xi_j-x_i)^2+r_i^2]^{1/2}} \right\} \quad (4.31)$$

where the summations are carried out over the entire body (i.e.,  $\bar{M}$  stream-wise segments) and the terms  $x_i$ ,  $\xi_j$ ,  $r_i$ , etc., are defined in figure (4.2).

The second of the superimposable solutions, the cross flow solution, accounts for angle of attack effects. For the axisymmetric case it is simply represented by the flow past a distribution of doublets on the body axis. The doublet is the natural choice of singularity for the axisymmetric case since it is well-known that a doublet can be used to model the flow about a two-dimensional circular cylinder in a freestream. For the general case of a non-circular cross-section, however, a doublet inside the body is no longer adequate. Instead, the body cross-section is represented by a continuous source distribution on the boundary of the cross-section. The Neumann boundary condition of no flow across the boundary is imposed and the problem is solved two-dimensionally to determine the source strength distribution. The Neumann solution is well developed (references 62 and 63) and is reviewed in Appendix III. The two-dimensional cross flow solution is computed for each streamwise segment of the fuselage to determine  $u_{r_1}(r, \theta, x)$  and  $u_{\theta}(r, \theta, x)$ . Returning momentarily to the axisymmetric cross flow solution, equation (4.25) for the perturbation cross flow potential clearly shows that there is a contribution to the axial perturbation velocity,  $u_x$ , from the cross flow solution, since

$$u_{x_2}(r, \theta, x) = \frac{\partial \phi_2}{\partial x} = -\frac{W}{\pi r} \frac{dS}{dx}(x) \cos \theta \quad (4.32)$$

However, the Neumann solution for the cross flow in the general case is strictly two-dimensional in the  $(r, \theta)$ -plane, so no  $x$ -dependence is obtained. Thus, it is again necessary to revert to the equivalent body of revolution concept, yielding in place of (4.32)

$$u_{x_2}(r, \theta, x) = \frac{-W}{\pi r} \frac{d\tilde{S}}{dx}(x) \cos \theta \quad (4.33)$$

Finally, the cross flow solution must be modified to account for non-straight body axis and non-uniform cross flow velocities. This has been done by replacing the constant cross flow freestream velocity vector  $W\vec{k}$  with a variable velocity that allows for both vertical and lateral cross flow freestreams,  $V(x)\vec{j} + W(x)\vec{k}$ . The vertical cross flow freestream  $W(x)$  can

be composed of angle of attack contributions ( $U_\infty \sin \alpha$ ), wing induced downwash ( $w(x)$ ), and a downwash induced by the upsweep of the fuselage axis ( $-dz_{CL}/dx$ ). Hence,

$$w(x) = U_\infty \cos \beta \sin \alpha - \frac{dz_{CL}}{dx}(x) + w(x) \quad (4.34)$$

The lateral cross-flow freestream  $V(x)$  is composed of sideslip terms and wing induced terms; that is,

$$V(x) = -U_\infty \sin \beta + v(x) \quad (4.35)$$

where a positive sideslip angle  $\beta$  is defined as shown in figure (2.7a). The modified cross flow freestream, (4.34) and (4.35), can be included in the Neumann solution merely by modifying the boundary conditions. However, for the axial perturbation velocity contribution of the cross flow, equation (4.33) must be modified to be

$$u_{x_2}(r, \theta, x) = -\frac{1}{\pi r} \frac{d\tilde{S}}{dx}(x) \left[ w(x) \cos \theta - V(x) \sin \theta \right] \quad (4.36)$$

The complete surface velocity distribution is then obtained by summing vectorially the freestream velocity, the axial contribution [(4.30) and (4.31)], and the cross flow contribution [the Neumann solution and (4.33)]. Finally, the surface pressure distribution can be calculated from equation (4.26).

#### 4.1.3 Jet-Wing Interference

The fuselage analysis developed in the preceding sections is approximate because of the slender body assumptions ( $dR/dx \ll 1$ ) and because of the assumptions required to handle non-axisymmetries. Further approximations are made in the consideration of jet-wing interference. The flow induced on the fuselage by the jet-wing system is a function of  $(R(x), \theta, x)$ . However, since the fuselage is slender and the wing is of at least moderately high aspect ratio, it is reasonable to assume that the flow induced on the fuselage by the jet-wing can be approximated by the downwash and sidewash on the fuselage axis. Thus, it is assumed that

$$\begin{aligned}
v(R(x),\theta,x) &\approx v(x)|_{\text{axis}} \\
w(R(x),\theta,x) &\approx w(x)|_{\text{axis}}
\end{aligned}
\tag{4.37}$$

Obviously this assumption will be more valid at the leading and trailing edges of the fuselage than near the wing/fuselage junction. However, since moments rather than pressure distributions are the desired end result, the errors introduced near the center of the fuselage by this assumption should be small.

#### 4.1.4 Aerodynamic Characteristics

Within the context of the assumptions and limitations of the method described in the preceding sections, the aerodynamic characteristics of a fuselage in the presence of a jet-wing can be determined by suitably integrating the surface pressure distribution obtained. Since the singularities used to represent the fuselage are single-valued (i.e., no circulation), however, by D'Alembert's paradox it is known that there can be no total force on the body. However, there is a distribution of force along the body and, hence, there can be non-zero total moments on the body.

As mentioned previously, the body is divided into streamwise segments by planes normal to the freestream [figure (4.2)]. In addition, each streamwise segment is divided into circumferential segments [figure (4.3)] so that the surface of the fuselage is effectively divided into a lattice of quadrilateral elements [figure (4.4)]. Hence, knowing the pressure coefficient on each quadrilateral element, the area of the element, its normal, and its position in space, differential force and moment vectors can be calculated from

$$d \vec{F} = qSc_p(r,\theta,x) \vec{n} r d\theta dx \tag{4.38}$$

$$d \vec{M} = qSc_p(r,\theta,x) \vec{\rho} \times \vec{n} r d\theta dx \tag{4.39}$$



which can be readily integrated for the total forces and moments. Since in the actual numerical method the differentials in (4.38) and (4.39) are replaced by finite values (i.e., the dimensions of the quadrilateral elements), it is obvious that more accurate results will be obtained as the fineness of the element lattice is increased. In addition, these equations show that finer divisions are required for areas where the loading gradients are larger (e.g., near the ends of the body).

#### 4.1.4.1 Pitching Moment

The fuselage pitching moment can be calculated by integrating the y-component of (4.39). It is first necessary to determine the unit normal  $\vec{n}$  on each element. Referring to figures (4.3) and (4.5), the unit normal can be expressed in rectangular Cartesian coordinates by

$$\vec{n} = -\sin \psi \vec{i} + \cos \psi \sin \beta \vec{j} - \cos \psi \cos \beta \vec{k} \quad (4.40)$$

where  $\psi = \tan^{-1} (dr/dx)$  and  $\beta = \tan^{-1} (dz/dy)$ . Hence

$$\vec{n} = -\frac{dr}{dS} \vec{i} + \frac{dx}{dS} \sin \beta \vec{j} - \frac{dx}{dS} \cos \beta \vec{k} \quad (4.41)$$

Therefore, in non-dimensional form equation (4.39) can be integrated to yield

$$C_m = \frac{-1}{S\bar{c}} \int_0^l \int_0^{2\pi} \left[ c_p(r, \theta, x) \right] \left\{ (x - x_{mc}) \frac{dx}{dS} \cos \beta - r \frac{dr}{dS} \cos \theta \right\} r d\theta dx \quad (4.42)$$

where the moment arm  $\vec{\rho}$  in (4.39) is

$$\vec{\rho} = (x - x_{mc}) \vec{i} + r \sin \theta \vec{j} - r \cos \theta \vec{k} \quad (4.43)$$

and  $x_{mc}$  is the desired moment center on the body axis.

#### 4.1.4.2 Yawing Moment

The fuselage yawing moment can be calculated by integrating the

z-component of (4.39). In non-dimensional form the result is

$$C_n = \frac{-1}{5b} \int_0^l \int_0^{2\pi} [c_p(r, \theta, x)] \left\{ (x-x_{mc}) \frac{dx}{dS} \sin \beta - r \frac{dr}{dS} \sin \theta \right\} r d\theta dx \quad (4.44)$$

#### 4.1.5 Dynamic Stability Derivatives

In Section 2.2.4 it has been argued that the assumption of quasi-steady flow conditions should suffice for the calculation of jet-wing dynamic stability derivatives. This implies that the entire jet wing/fuselage flow field adjusts instantaneously to oscillatory motions. The same assumption will be used in analyzing the dynamic stability contribution of the fuselage. This reduces the problems to calculating the dynamic stability derivatives for an isolated fuselage in a freestream. Since fuselage cross-sections are nearly circular, it has been assumed that the rolling dynamic stability derivatives for the fuselage are negligible.

##### 4.1.5.1 Pitching Fuselage

The pitching fuselage can be considered by assuming an induced downwash distribution along the fuselage axis

$$\frac{\Delta w}{U_\infty} = \left( \frac{q \tilde{c}}{2U_\infty} \right) \left( \frac{b}{\tilde{c}} \right) \left( \frac{x-x_{cg}}{b/2} \right) \quad (4.45)$$

where  $q$  is the rate of pitch (radians/sec.) about the aircraft center of gravity. The quantity

$$\hat{q} = \left( \frac{q \tilde{c}}{2U_\infty} \right) \quad (4.46)$$

is the non-dimensional rate of pitch. Using the downwash distribution (4.45) with  $\hat{q} = 1.0$  and calculating the pressure distribution by the method of the preceding sections, equation (4.42) yields

$$C_{mq} = \frac{\partial C_m}{\partial \hat{q}} \quad (4.47)$$

#### 4.1.5.2 Yawing Fuselage

The yawing fuselage can be considered by assuming an induced sidewash distribution along the fuselage axis

$$\frac{\Delta v}{U_\infty} = - \left( \frac{rb}{2U_\infty} \right) \left( \frac{x-x_{cg}}{b/2} \right) \quad (4.48)$$

where  $r$  is the rate of yaw (radians/sec) about the aircraft center of gravity. The quantity

$$\hat{r} = \left( \frac{rb}{2U_\infty} \right) \quad (4.49)$$

is the non-dimensional rate of yaw. Using the sidewash distribution (4.48) with  $\hat{r} = 1.0$  and calculating the pressure distribution by the method of the preceding sections, equation (4.44) yields

$$C_{n_r} = \frac{\partial C_n}{\partial r} \quad (4.50)$$

#### 4.1.6 Method Validation

In order to assess the validity of the modified slender body approach to the solution of the fuselage problem, comparisons have been made between the present method, exact analytical methods, and experiment. In addition, the method validation summary presented here includes a brief study of spacing criteria and convergence of the numerical method for a set of body shapes whose analytical solution is well known. Finally, the non-potential aspects of the problem, particularly vortex separation from the fuselage afterbody, are discussed.

What must be first established in assessing the validity of the present method is the range of applicability of classical slender body theory. In other words, how slender must a body be in order for it to be classified as a slender body? Although there are many excellent treatments of this topic (e.g., references 58 and 60), the present method has been used to verify these findings and to provide the reader unfamiliar with slender body theory with a feeling for its worth. Since there exists an exact analytic solution for

the potential flow about an ellipsoid, bodies of this type have been employed for this comparison. In particular, spheroids (ellipsoids of revolution) of varying thickness/chord ratios have been used in the initial comparison with classical slender body theory. Figure (4.6) shows typical comparisons between analytic theory and the present numerical method for the pressure distribution for a body at zero angle of attack for several different arrangements of streamwise elements. The distributions of streamwise divisions along the body axis include 16, 24, and 32 divisions, spaced closely near the ends of the body where the slope of the surface is large and spaced more widely near the center of the body. The calculated pressure distribution for a body of thickness/chord ratio 0.1 indicates excellent agreement with exact theory except when only 16 divisions were used, and the good agreement is maintained over nearly the entire body length. The strange behavior of the 16-division solution near the mid-section of the body is indicative of the type of solution that can be obtained by under-defining the body geometry. The 24 and 32 point solutions demonstrate the adequate convergence characteristics of the numerical method for well-defined body geometries. For a spheroid of thickness/chord ratio 0.2, the calculated results are in generally good agreement with the exact result, although the effects of increased body thickness are apparent in comparison to the previous result. Figure (4.6c) for a spheroid of thickness/chord ratio 0.4 is indicative of the results obtained when the body deviates significantly from the assumptions of slender body theory.

Figure (4.7) presents additional body pressure distribution data at 20 degrees angle of attack for both the present method and the exact analytic result. What these data show is consistent with the zero angle of attack result, indicating excellent agreement for the spheroid of  $t/c = 0.1$  over the entire length of the body and increasingly poorer agreement as the body becomes less slender. Although the 32 streamwise element solution is plotted in figure (4.7), similar results were obtained for the 24 element solution.

These results can be alternately summarized as in figure (4.8), which presents a comparison for the body moment versus angle of attack between the present slender body method and the exact analytic result. The slender body

result which can be shown to be simply

$$C_m = \sin(2\alpha) \quad (4.50)$$

where  $C_m$  is non-dimensionalized by the body volume, is invariant with body thickness/chord ratio. The comparison with exact theory in figure (4.8) leads to the same general conclusions as were reached from the pressure distribution comparisons. That is, excellent agreement is obtained for the  $t/c = 0.1$  spheroid; adequate results are obtained for the  $t/c = 0.2$  spheroid (approximately 12 percent error); while rather poor results (approximately 35 percent error) are obtained for the  $t/c = 0.4$  spheroid.

It becomes increasingly more difficult to assess the validity of the present modified slender body approach for bodies of non-circular cross-section because of the complexity of the analytic solutions available. In fact, the only known analytic solution for a fully three-dimensional body is for a tri-axial ellipsoid, which is a body whose meridian shape in each of the coordinate planes is an ellipse. Remembering that the present method treats the axial flow solution (i.e., the zero angle of attack solution) using an equivalent body of revolution technique, it is shown in figure (4.9) that the small variation in circumferential pressure obtained from the exact solution is unimportant and that the axial pressure distribution predicted by the slender body technique is a reasonable average. Of course, for less slender bodies or for bodies whose cross-sectional eccentricity is larger (the eccentricity of the tri-axial ellipsoid analyzed in figure (4.9) is .125), the assumptions of slender body theory and the assumption of replacing the body by an equivalent body of revolution for the axial flow solution will become less valid. Figure (4.10) presents additional body pressure distribution comparisons at several circumferential stations at 20 degrees angle of attack for the same tri-axial ellipsoid. Excellent agreement is evident, verifying the cross-flow solution for non-circular cross-sections using the Neumann solution approach. Unfortunately no analytic solution for the momentson a tri-axial ellipsoid for comparison was found. However, based on the good agreement obtained for pressure distributions, it is certain that comparisons similar to figure (4.8) would be obtained.

Having established the behavior of the present approximate solution relative to the exact analytic result, it is necessary to examine the magnitude of the errors expected to ascertain if they are tolerable in typical STOL transport aircraft aerodynamic and stability and control analyses. In particular, consider the pitching moment contribution of the fuselage relative to the overall wing body combination pitching moment. Since a typical thickness-chord ratio for a STOL transport is 0.2, from figure (4.8) it would be expected that the fuselage pitching moment predictions would be in error by approximately 12 percent. In general, however, the absolute magnitude of the error, when expressed in a form non-dimensionalized by the wing area and reference chord, may be only 2 to 5 percent of the total pitching moment. Hence, the range of applicability of the present method may be more than that established in the body alone studies presented here because of the masking of errors by other component contributions to pitching moment.

The discussion to this point has been solely concerned with potential flow aspects of the body problem. However, the phenomenon of vortex shedding from the afterbody of a fuselage is well-known and usually occurs when the body is at a large angle of attack or if there is considerable afterbody upsweep. The vortex shedding can significantly alter the pressure distribution on the afterbody which means that the pitching moment contributions of the body can be changed. Although body vortex shedding is a topic of current research interest, no attempt has been made to treat this phenomenon here because so little is yet known about it analytically. Reference is made to the experimental work of Peake (reference 64) and Wickens (reference 65) of Canada which clearly demonstrates the nature of the phenomenon. Empirical modifications to the present method to account for such effects are discussed in Volume III of this report. However, the authors are of the opinion that further analytical research in this area is warranted.

#### 4.1.7 Summary and Concluding Remarks

A method has been presented to predict approximately the aerodynamic and stability and control contributions of a fuselage in the presence of a jet-wing high lift system. Based in part on slender body theory, the method has been structured to allow non-circular body cross-sections, body camber,

and interference effects due to the jet-wing. The method calculates the pressure distribution on the body and then integrates the surface pressures to determine the pitching and yawing moments due to the body. The method cannot predict any forces on the body, however, because of D'Alembert's paradox. Based on quasi-steady assumptions, a capability to calculate the dynamic stability contributions of the fuselage has also been provided.

Method validation studies have been presented for a variety of analytic body shapes to establish the general range of applicability of the method. Good agreement with the exact analytic solutions was obtained for a wide class of bodies that fall within the scope of slender body theory, including typical STOL transport fuselages.

## 4.2 EMPENNAGE ANALYSIS

A method based on approximate interference techniques has been developed to analyze the aerodynamic and stability and control characteristics of a jet-wing/empennage configuration. A rigorous solution of an integrated jet-wing/empennage must, of necessity, be iterative in nature because of the jet sheet (or vortex wake) whose position is a function of the loading and hence is unknown a priori. Although such an iterative solution is conceptually possible, the mathematical complexity and iterative nature of the solution make it unattractive to the design engineer because of the potentially restrictive computation requirements. It is the opinion of the authors that, for the purposes of preliminary design and analysis of STOL transport aircraft, an approximate solution to calculate the aerodynamic and stability and control characteristics of a jet-wing/empennage configuration should be adequate. The method developed here considers the influence of the jet-wing on the empennage but neglects the influence of the empennage on the jet-wing. Hence, the jet sheet location is assumed to be independent of the empennage loading and, therefore, the need for an iterative solution is removed. This approximation should be adequate for typical STOL transport configurations which are characterized by a tail which is at least a wing semi-span aft of the wing and which usually have T-tail type arrangements. However, for other configurations, such as V/STOL fighters, where the empennage may be in close proximity to the jet-wing, the approximate interference techniques of this method are likely to be invalid and a complete iterative solution may be required.

The flow field behind a jet-wing high-lift system is characterized by large downwash angles and, in some cases, abrupt changes in the downwash field. Therefore, the aerodynamic characteristics of the empennage in the jet-wing flow field will be considerably different from those of an empennage in a uniform freestream. On the other hand, the flow field perturbations induced by the empennage on the jet-wing are likely to be small since the flow field upstream of a lifting surface rapidly returns to its undisturbed state with distance upstream from it. Hence, if the empennage is sufficiently downstream of the wing, its influence on the wing should be negligible. The validity of this assumption will break down if the empennage is close to the wing (i.e., short coupled aircraft), if the empennage lift becomes large, or if the tail



planform area becomes comparable to that of the wing.

The method of solution discussed here may be divided into three distinct segments:

1. Calculate the jet-wing loading and jet shape using the linearized EVD Jet-Wing Lifting Surface Theory (Section 2.2).
2. Calculate the flow field induced on the empennage using the Jet-Wing Flow Field Method (Section 2.3).
3. Treating the jet-wing flow field effects as induced camber, calculate the empennage loading using a lifting surface theory for multi-planar systems (Section 4.2.1).

Although the jet-wing loading is linear in angle of attack or in any of the deflections (Section 2.2.1.4), the jet shape and flow field are non-linear and hence the aerodynamic characteristics of the empennage are also non-linear.

#### 4.2.1 Lifting Surface Theory for Multiplanar Systems

Before the jet-wing/empennage problem can be solved in the manner outlined in the previous section, it is necessary to be able to calculate the self-induced effects of the empennage. Since most empennage arrangements are composed of a horizontal tail and a vertical tail, a multiplanar lifting surface theory is required to calculate the horizontal tail/vertical tail interaction. A capability to consider conventional tail geometries and T-tail geometries is required. Although such a lifting surface theory is not a new development, the method presented here has been developed specifically for tail geometries and should be more efficient than a fully non-planar method. The present method can only consider a horizontal tail in the  $xy$ -plane and a vertical tail in the  $xz$ -plane.

For simplicity and computational expediency, the loading on the empennage has been modelled by the most simple vortex distribution, a lattice of discrete horseshoe vortices. Vortex lattice theory (references 54 and 66) requires that the wing be divided into a lattice of elements and that on each element be placed a discrete bound vortex at the  $1/4$ -chord position of the

element. Trailing vortices emanate from each bound vortex and extend parallel downstream to infinity. It is then required that the total flow normal to the wing surface be zero at the 3/4-chord position of each element. Hedman (reference 29) discusses the theory behind the 1/4-chord-3/4-chord criterion on each element. Basically, it is based on the thin airfoil theory result that the 1/4-chord is the aerodynamic center of a flat plate airfoil.

To proceed with the solution, the tail surfaces are divided into a finite number of small elements, each with a horseshoe vortex of unknown strength  $\Gamma_j$ . The inclination of each element to the freestream direction is  $\epsilon_j$ . The flow induced by the empennage normal to the  $i^{\text{th}}$  element is then

$$w_i = \sum_{j=1}^N A_{ij} \Gamma_j \quad (4.51)$$

where  $A_{ij}$  is the normal-wash influence coefficient and the summation is carried out over the entire empennage ( $N$  elements). The freestream contribution to the normal-wash on the horizontal tail is

$$w_{i_\infty} = U_\infty \sin(\alpha + \epsilon_j) \approx U_\infty (\alpha + \epsilon_j) \quad (4.52)$$

and on the vertical tail is

$$w_{i_\infty} = U_\infty \sin(\beta + \epsilon_j) \approx U_\infty (\beta + \epsilon_j) \quad (4.53)$$

where the linearization approximation is based on small perturbation assumptions analogous to those used in the EVD Theory (Section 2.2). In equations (4.52) and (4.53)  $\alpha$  and  $\beta$  are the angle of attack and angle of sideslip, respectively. By requiring the normal-wash to be zero on each element, the following matrix equation for the unknown vortex strengths  $\Gamma_j$  can be formed:

$$\sum_{j=1}^N A_{ij} \Gamma_j = \begin{cases} -(\alpha + \epsilon_j), & \text{on the horizontal tail} \\ -(\beta + \epsilon_j), & \text{on the vertical tail} \end{cases} \quad (4.54)$$

The systems of equations can be solved by standard matrix techniques on a digital computer.

The normal-wash influence coefficients  $A_{ij}$  can be divided into four distinct types:

1. Horizontal-on-horizontal
2. Horizontal-on-vertical
3. Vertical-on-vertical
4. Vertical-on-horizontal

The basis for determining each of the coefficients is the Biot-Savart Law for straight line vortex filaments which is discussed in detail in Appendix II. Unlike the wing alone problem, however, there is a basic asymmetry in the horizontal/vertical tail normal-wash matrix. This can be seen in figure (4.11) by observing that, in the case shown, the vertical tail induces a downwash on the right panel of the horizontal tail and an upwash on the left panel. Since the horizontal-on-horizontal segment of the matrix is symmetric for symmetric planforms, the overall matrix is asymmetric. It is necessary, therefore, to treat the entire planform of the horizontal tail. The vertical tail can be considered as only one panel of a symmetric planform. However, since the fuselage effectively endplates the vertical, the loading at the root of the vertical cannot be zero so the single panel model cannot be used. It has been assumed here that the fuselage acts as an infinite endplate and thus a mirror image of the vertical tail is required. Obviously the fuselage does not provide a complete endplate effect, but this approximation should be fairly reasonable.

Because of the discrete singularity approach adopted in this method, there are certain restrictions which must be noted. A horseshoe vortex cannot pass through the normal-wash control point of another element since an infinite velocity would be induced. This is particularly important at the juncture between the horizontal and vertical tails where the elements must be properly oriented so that singularity problems do not occur.

Once the matrix equation (4.51) has been solved for the vortex strengths  $\Gamma_i$ , the chordwise loading distribution can be determined from

$$\Delta c_{p_i} = \frac{2\Gamma_i}{\Delta x_i} \quad (4.55)$$

where  $\Delta x_i$  is the streamwise length of the  $i^{\text{th}}$  element. The pressure jump coefficients will be integrated for aerodynamic and stability and control characteristics in Section 4.2.3.

#### 4.2.2 Jet-Wing Interference

The effects of the flow field induced on the empennage by the jet-wing can be treated as an additional camber distribution on the empennage. Thus, if the jet-wing induces perturbation velocities  $[u(x,y,z), v(x,y,z), w(x,y,z)]$  on the empennage, then the induced camber on the horizontal tail is

$$\epsilon(x,y) = -\tan^{-1} \left[ \frac{w(x,y,z)}{U_\infty + u(x,y,z)} \right] \quad (4.56)$$

and the induced camber of the vertical tail is

$$\epsilon(x,z) = \tan^{-1} \left[ \frac{v(x,y,z)}{U_\infty + u(x,y,z)} \right] \quad (4.57)$$

#### 4.2.3 Aerodynamic Characteristics

Within the context of the assumptions and limitations of the method described in the preceding sections, the aerodynamic characteristics of the empennage in the presence of a jet-wing can be determined by suitably integrating the vorticity distribution obtained in the solution. Total empennage aerodynamic coefficients are non-dimensionalized by wing area and reference chord, and moments are referenced to the aircraft moment center and center of gravity.

##### 4.2.3.1 Tail Lift

The lift contribution of the empennage is derived solely from the horizontal tail. The sectional tail lift  $c_{L_H}(y)$  can be obtained from an

integration of the chordwise loading distribution  $\Delta c_p(x,y)$  obtained in the preceding sections, expressed by

$$c_{\ell_H}(y) = \frac{1}{c_H(y)} \int_{x_{\ell}(y)}^{x_t(y)} \Delta c_p(x,y) dx = \int_0^1 \Delta c_p(\bar{x},y) d\bar{x} \quad (4.58)$$

where the auxiliary non-dimensional coordinate  $\bar{x} = \frac{x-x_{\ell}(y)}{c_H(y)}$  has been introduced.

The total horizontal tail lift follows directly from a spanwise integration of equation (4.58).

$$C_{L_H} = \frac{1}{S} \int_{-b_H/2}^{b_H/2} c_H(y) c_{\ell_H}(y) dy \quad (4.59)$$

where  $b_H$  is the horizontal tail span.

#### 4.2.3.2 Tail Side Force

The side force contribution of the empennage is assumed to be derived solely from the vertical tail. The sectional vertical tail side force  $c_{y_V}(z)$  can be obtained from an integration of the chordwise loading distribution  $\Delta c_p(x,z)$  on the vertical

$$c_{y_V}(z) = \frac{1}{c_V(z)} \int_{x_{\ell}(z)}^{x_t(z)} \Delta c_p(x,z) dx = \int_0^1 \Delta c_p(\bar{x},z) d\bar{x} \quad (4.60)$$

The total vertical tail side force is

$$C_{Y_V} = \frac{1}{S} \int_0^{b_V} c_V(z) c_{y_V}(z) dz \quad (4.61)$$

where here  $b_V$  is the vertical tail span.

#### 4.2.3.3 Tail Induced Drag

Both the vertical and horizontal tails contribute to the empennage induced drag. The calculation cannot be made using a pressure integral as in Section 2.2.3.1.3 for the jet-wing, however, because the discrete singularity approach adopted here does not provide the singular loading at the leading edge necessary to calculate leading edge suction. Instead, the induced drag will be calculated by application of the Kutta-Joukowski Law again, but this time using the induced flow normal to the wing plane on each bound vortex. That is, since the wing is represented by a vortex lattice, the flow normal to the wing is zero only at the aforementioned collocation points, there being flow through the wing everywhere else. Hence, the bound vortices are immersed in a "normal flow" which results in a chordwise force. Letting  $D_{ij}$  be the normal flow influence coefficient relating the flow induced at the  $i^{\text{th}}$  bound vortex by the  $j^{\text{th}}$  horseshoe vortex of strength unity, the normal flow at  $i$  is then

$$w_i = \sum_{j=1}^N D_{ij} \Gamma_j \quad (4.62)$$

and by the Kutta-Joukowski Law the induced drag due to the  $i^{\text{th}}$  element is

$$d_i = \rho w_i \Gamma_i \quad (4.63)$$

The sectional induced drag is simply

$$c_{d_{i_H}}(y) = \frac{1}{q_{\infty} c_H(y)} \int_0^1 \rho w(\bar{x}, y) \Gamma(\bar{x}, y) d\bar{x} \quad (4.64)$$

on the horizontal tail and

$$c_{d_{i_V}}(z) = \frac{1}{q_{\infty} c_V(z)} \int_0^1 \rho w(\bar{x}, z) \Gamma(\bar{x}, z) d\bar{x} \quad (4.65)$$

on the vertical tail. Finally, the total induced drag of the empennage is

$$C_{D_i} = \frac{1}{S} \left\{ \int_{-b_H/2}^{b_H/2} c_H(y) c_{d_i}(y) dy + \int_0^{bv} c_V(z) c_{d_i}(z) dz \right\} \quad (4.66)$$

The leading edge suction is actually distributed along the chord in this method. The reader is referred to references 29 and 67, for a further discussion of calculating induced drag at the wing for the vortex lattice method.

#### 4.2.3.4 Tail Pitching Moment

Both the lift and induced drag of the horizontal tail contribute to the aircraft pitching moment, the drag effect being of importance only for T-tail configurations. The induced drag of the vertical tail also contributes to the pitching moment, but it is small and has been neglected in this analysis. Sectional tail pitching moment can be calculated from a chordwise pressure integration expressed by

$$c_{m_H}(y) = - \int_0^1 \Delta c_p(\bar{x}, y) \bar{x} d\bar{x} + c_{d_{iH}}(y) \left[ z_H / c_H(y) \right] \quad (4.67)$$

where  $c_{m_H}(y)$  is referenced to the leading edge of the section,  $z_H$  is the height of the horizontal tail above the aircraft moment center, and the last term accounts for the induced drag effect on  $c_m$ . The total horizontal tail pitching moment is then

$$C_m = \frac{1}{S\bar{c}} \int_{-b_H/2}^{b_H/2} \left\{ c_H^2(y) c_{m_H}(y) - \left[ \ell_H + x_{\ell_H}(y) - x_{mc} \right] c_H(y) c_{\ell_H}(y) \right\} dy + C_{D_{iH}} \left[ z_H / \bar{c} \right] \quad (4.68)$$

where  $C_m$  is referenced to the aircraft moment center  $x_{mc}$ ,  $\ell_H$  is the distance between the wing apex and the horizontal tail apex, and  $x_{\ell_H}(y)$  is the section leading edge on the horizontal tail.

#### 4.2.3.5 Tail Rolling Moment

Both the horizontal tail lift and the vertical tail side force

contribute to the tail rolling moment. The total rolling moment due to the horizontal tail can be obtained by a spanwise integration of tail lift expressed by

$$C_{l_H} = -\frac{1}{Sb} \int_{-b_H/2}^{b_H/2} c_H(y) c_{\ell_H}(y) y dy \quad (4.69)$$

where right wing down is defined as a positive rolling moment. The vertical tail rolling moment is similarly calculated to be

$$C_{l_V} = \frac{1}{Sb} \int_0^{b_V} c_V(z) c_{y_V}(z) z dz \quad (4.70)$$

#### 4.2.3.6 Tail Yawing Moment

Vertical tail side force and horizontal tail induced drag contribute to the empennage yawing moment, but the drag effects have been neglected here since they are considerably smaller than the side force effect. Hence, the sectional vertical tail yawing moment is

$$c_{n_V}(z) = - \int_0^1 \Delta c_p(\bar{x}, z) \bar{x} d\bar{x} \quad (4.71)$$

where  $c_{n_V}(z)$  is referenced to the leading edge of the section. The total yawing moment is then

$$C_{n_V} = \frac{1}{Sb} \int_0^{b_V} \left\{ c_V^2(z) c_{n_V}(z) - [\ell_V + x_{\ell_V}(z) - x_{mc}] c_V(z) c_{y_V}(z) \right\} dz \quad (4.72)$$

where  $\ell_V$  is the distance between the wing apex and the vertical tail apex and  $x_{\ell_V}(z)$  is the section leading edge on the vertical tail.

#### 4.2.4 Dynamic Stability Derivatives

In Section 2.1.5 it has been argued that the assumption of quasi-steady flow conditions should suffice for the calculation of jet-wing dynamic stability



derivatives. This implies that the flow field adjusts instantaneously to oscillatory motions. The same assumption will be adopted in the analysis of the empennage contribution to the dynamic stability derivatives, which reduces the problem to the determination of the dynamic stability derivatives for an isolated empennage. Thus, the problem becomes quite similar to the isolated wing problem, complicated primarily by the multiplanar nature of the empennage.

#### 4.2.4.1 Pitching Tail

The pitching tail can be considered by assuming an induced downwash distribution  $\frac{\Delta w}{U_\infty}$  which can, in the quasi-steady state, be considered as equivalent to an effective camber distribution on the horizontal tail. This can be expressed by

$$\frac{\Delta w}{U_\infty} = \left( \frac{q \tilde{c}}{2U_\infty} \right) \left( \frac{b}{\tilde{c}} \right) \left( \frac{x}{b/2} - \frac{x_{cg}}{b/2} \right) \quad (4.73)$$

where  $q$  is the rate of pitch in radians per second about the aircraft center of gravity. Defining the non-dimensional rate of pitch  $\hat{q}$  as in equation (4.46) and letting  $\hat{q} = 1.0$ , the tail aerodynamic characteristics can be calculated by the method of the preceding sections using the camber distribution (4.73) to yield

$$C_{Lq_H} = \frac{\partial C_{m_H}}{\partial \hat{q}} \quad (4.74)$$

from equation (4.59) and

$$C_{mq_H} = \frac{\partial C_{m_H}}{\partial \hat{q}} \quad (4.75)$$

from equation (4.68).

#### 4.2.4.2 Rolling Tail

Both the vertical and horizontal tails contribute to the rolling dynamic stability derivatives. On the horizontal tail an induced downwash

distribution  $\frac{\Delta w}{U_\infty}$  can be considered as equivalent to an effective camber distribution

$$\frac{\Delta w}{U_\infty} = \left( \frac{pb}{2U_\infty} \right) \frac{y}{b/2} \quad (4.76)$$

where  $p$  is the rate of roll in radians per second. It must be noted that the induced camber distribution on the horizontal tail is antisymmetric for symmetric planforms because of the  $y$ -dependence of (4.76). On the vertical tail an induced sidewash distribution  $\frac{\Delta v}{U_\infty}$  can be considered as an effective camber distribution, where

$$\frac{\Delta v}{U_\infty} = - \left( \frac{pb}{2U_\infty} \right) \frac{z}{b/2} \quad (4.77)$$

Since the vertical tail is treated as endplated, antisymmetry must again be treated. Defining the non-dimensional rolling rate  $\hat{p}$  by

$$\hat{p} = \left( \frac{pb}{2U_\infty} \right) \quad (4.78)$$

and setting  $\hat{p} = 1.0$ , the rolling dynamic stability derivatives can be calculated by the method of the preceding sections using the camber distributions (4.76) and (4.77).

Both the horizontal and vertical tails contribute to the  $C_{l_p}$  derivative which can be calculated from equations (4.69) and (4.70), respectively, to yield

$$C_{l_{pH}} = \frac{\partial C_{l_H}}{\partial \hat{p}} \quad (4.79)$$

$$C_{l_{pV}} = \frac{\partial C_{l_V}}{\partial \hat{p}} \quad (4.80)$$

Neglecting the induced drag contribution of the horizontal tail, only the vertical tail contributes to the  $C_{n_p}$  derivative which can be calculated from (4.72) to yield

$$C_{n_{pV}} = \frac{\partial C_{n_V}}{\partial \hat{p}} \quad (4.81)$$

Similarly, equation (4.61) may be used to calculate the vertical tail contribution to  $C_{Yp}$ , as

$$C_{Yp} = \frac{\partial C_Y}{\partial \hat{p}}$$

#### 4.2.4.3 Yawing Tail

Only the vertical tail has a significant contribution to the yawing stability derivatives. An induced sidewash distribution  $\frac{\Delta v}{U_\infty}$  can be considered as equivalent to an effective camber distribution on the vertical tail, expressed by

$$\frac{\Delta v}{U_\infty} = -\left(\frac{rb}{2U_\infty}\right)\left(\frac{x}{b/2} - \frac{x_{cg}}{b/2}\right) \quad (4.82)$$

where  $r$  is the rate of yaw in radians per second. Note that, unlike the case for the wing (Section 2.1.5.5), the vertical tail yawing case is not antisymmetric but rather is analogous to the pitching case for the horizontal tail in its treatment. Defining the non-dimensional yaw rate  $\hat{r}$  as in equation (4.49) and letting  $\hat{r} = 1.0$ , the yawing dynamic stability derivatives can be calculated by the method of the preceding sections using the camber distribution (4.82) to yield

$$C_{lrv} = \frac{\partial C_{l_v}}{\partial \hat{r}} \quad (4.83)$$

from (4.70);

$$C_{nr_v} = \frac{\partial C_{n_v}}{\partial \hat{r}} \quad (4.84)$$

from (4.72); and

$$C_{Yrv} = \frac{\partial C_{y_v}}{\partial \hat{r}} \quad (4.85)$$

from (4.61).

#### 4.2.5 Summary and Concluding Remarks

A method to calculate the contributions of the empennage to the aerodynamic and stability and control characteristics of a STOL aircraft, including,

in an approximate sense, the interference due to a jet-wing high lift system, has been presented. The treatment is based on classical vortex lattice lifting surface techniques and allows multiplanar systems, such as a T-tail. Dynamic stability contributions of the empennage are treated in a manner similar to that for the jet-wing based on quasi-steady assumptions.

## 5.0 REFERENCES

1. Lopez, M.L. and Shen, C.C.: Recent Developments in Jet Flap Theory and Its Application to STOL Aerodynamic Analysis. AIAA Paper No. 71-578, AIAA 4th Fluid and Plasma Dynamics Conference, June 1971. Also revised as Douglas paper 5928, Douglas Aircraft Company, McDonnell Douglas Corporation, July 1971.
2. Goldhammer, M.I. and Wasson, N.F.: Methods for Predicting the Aerodynamic and Stability and Control Characteristics of STOL Aircraft. Volume II - STOL Transport Aerodynamic Methods Program. McDonnell Douglas Corporation Report No. MDC J5965-02, 1973.
3. Schubauer, G.B.: Jet Propulsion with Special Reference to Thrust Augmentation. NACA TN442, 1933.
4. Hagedorn, H. and Ruden, P.: Wind Tunnel Investigation of a Wing with Junkers Slotted Flap and the Effect of Blowing Through the Trailing Edge of the Main Surface over the Flap. Report by the Institut für Aeromechanik und Flugtechnik der Technischen Hochschule Hannover, LGL Bericht A64, 1938. RAE Translation No. 442, 1953.
5. Davidson, I.M.: The Jet Flap. J. Roy. Aero. Soc. 60, pp. 25-50, 1956.
6. Stratford, B.S.: Early Thoughts on the Jet Flap. Aero. Quart. 8, pp. 45-49, 1956.
7. Poisson-Quinton, Ph.: Recherches Theoretiques et Experimentales sur le Controle de la Couche Limite. Proceedings of the Seventh International Congress of Applied Mechanics, Vol. 2, Part II, London, 1948.
8. Malavard, L.; Jousserandot, P.; and Poisson-Quinton, Ph.: Jet-Induced Circulation Control. Part I through Part III. Aero Digest 73, No. 3 to 4, Sept., Oct., and Nov., 1956.
9. Dimmock, N.A.: Some Early Jet Flap Experiments. Aero. Quart. 8, pp. 331-345, 1957.
10. Williams, J. and Alexander, A.J.: Some Exploratory Three-Dimensional Jet-Flap Experiments. Aero. Quart. 8, pp. 21-30, 1957.

11. Lowry, J.G. and Vogler, R.D.: Wind Tunnel Investigation at Low Speeds to Determine the Effect of Aspect Ratio and End Plates on a Rectangular Wing with Jet Flaps Deflected 85°. NACA TN 3863, 1956.
12. Gainer, T.G.: Low Speed Wind Tunnel Investigation to Determine the Aerodynamic Characteristics of a Rectangular Wing Equipped with a Full-Span and an Inboard Half-Span Jet-Augmented Flap Deflected 55°. NASA Memo 1-27-59L, 1959.
13. Williams, J. and Alexander, A.J.: Three-Dimensional Wind-Tunnel Tests of a 30° Jet Flap Model. ARC CP No. 304, 1957.
14. Butler, S.F.J.; Guyett, M.B.; and Moy, B.A.: Six Component Low-Speed Tunnel Tests of Jet-Flap Complete Models with Variation of Aspect Ratio, Dihedral and Sweepback, Including the Influence of Ground Proximity. ARC R&M 3441, 1961.
15. Das, A.: Tragflüchentheorie für Tragflügel mit Strahlklappen. Jahrbuch der Wissenschaftlichen Gesellschaft für Luftfahrt, pp. 112-133, 1960. Translated into English as T.T. 1122, National Research Council of Canada, 1964.
16. Maskell, E.C. and Gates, S.B.: Preliminary Analysis for a Jet Flap System in Two-Dimensional Inviscid Flow. RAE Aero Report No. 2552, 1955.
17. Spence, D.A.: The Lift Coefficient of a Thin Jet-Flapped Wing. Proc. Roy. Soc. A238, pp. 46-68, 1956.
18. Spence, D.A.: The Lift of Thin Aerofoil with a Jet-Augmented Flap. Aero. Quart. 9, pp. 287-299, 1958.
19. Küchemann, D.: A Method for Calculating the Pressure Distribution Over Jet-Flapped Wings. ARC R&M 3036, 1956.
20. Maskell, E.C. and Spence, D.A.: A Theory of the Jet Flap in Three Dimensions. Proc. Roy. Soc. A251, pp. 407-425, 1959.
21. Multhopp, H.: Methods for Calculating the Lift Distribution of Wings (Subsonic Lifting Surface Theory). ARC R&M 2884, 1955.
22. Malavard, L.: Application of the Rheoelectric Analogy for the Jet Flap Wing of Finite Span. Boundary Layer and Flow Control, ed. by G.V. Lachmann, pp. 365-389, Pergamon Press, New York, 1961.

23. Erickson, J.G., Jr. and Kaskel, A.L.: Theoretical Solutions and Numerical Results for Low-Aspect Ratio Rectangular Jet-Flap Control Surfaces. Therm Advanced Research, Inc., TR 6603, 1966.
24. Tokuda, N.: An Asymptotic Theory of the Jet Flap in Three Dimensions. JFM 46, Part 4, pp. 705-726, 1971.
25. Lissaman, P.B.S.: A Linear Theory for the Jet Flap in Ground Effect. AIAA J., Vol. 6, pp. 1356-1362, 1968.
26. Taylor, A.S.: A Theoretical Investigation of the Longitudinal Stability, Control and Response Characteristics of Jet-Flap Aircraft, Part I and II, ARC R&M 3272, 1960.
27. Thomas, H.H.B.M. and Ross, A.J.: The Calculation of the Rotary Lateral Stability Derivatives of a Jet-Flapped Wing. ARC R&M 3277, 1958.
28. Ashley, H. and Landahl, M.: Aerodynamics of Wings and Bodies. Addison-Wesley, Massachusetts, 1965.
29. Hedman, S.G.: Vortex Lattice Method for Calculation of Quasi-Steady State Loadings on Thin Elastic Wings in Subsonic Flow. The Aeronautical Research Institute of Sweden, Report 105, 1966.
30. Woodward, F.A.: Analysis and Design of Wing Body Combinations at Subsonic and Supersonic Speeds. J. Aircraft, Vol. 5, No. 6, pp. 528-534, 1968.
31. Kinner, W.: Die Kriesförmige Tragfläche auf Potentialtheoretischer Grundlage. Ing. Arch., pp. 47-80, 1937.
32. Krienes, K.: The Elliptical Wing Based on the Potential Theory. NACA TM 931, 1941. Translated from "Die Elliptische Tragfläche auf Potentialtheoretischer Grundlage." ZAMM, Vol. 20, No. 2, 1940.
33. Kuchemann, D.: A Simple Method for Calculating the Span and Chordwise Loading on Straight and Swept Wings of Any Given Aspect Ratio at Subsonic Speeds. ARC R&M 2953, 1952.
34. Jordan, P.F.: Remarks on Applied Subsonic Lifting Surface Theory. WGLR Jahrbuch 1967.
35. Van Spiegel, E.: Boundary Value Problem in Lifting Surface Theory. National Aeronautical Research Institute, Amsterdam, TR W1, 1959.

36. Lamar, J.E.: A Modified Multhopp Approach for Predicting Lifting Pressures and Camber Shape for Composite Planforms in Subsonic Flow. NASA TN D-4427, 1968.
37. Das, A.: Theoretische und Experimentelle Untersuchungen an Tragflügeln endlicher Spannweite mit Strahlklappen. Deutsche Forschungsanstalt für Luft- und Raumfahrt, FB 64-40, 1964.
38. Graham, R.R.: Low Speed Characteristics of a 45° Sweepback Wing of Aspect Ratio 8 from Pressure Distributions and Force Tests at Reynolds Numbers from 1,500,000 to 4,800,000. NACA RM L51H13, 1951.
39. Toll, T.A. and Queijo, M.J.: Approximate Relations and Charts for Low-Speed Stability Derivatives of Swept Wings. NACA TN 1581, 1948.
40. Woods, L.C.: The Theory of Subsonic Plane Flow. Cambridge University Press, Cambridge, England, 1961.
41. Tomotika, S.; Tamada, K.; and Umemoto, H.: The Lift and Moment Acting on a Circular Arc Airfoil in a Stream Bounded by a Plane Wall. The Quarterly J. of Fluid Mechanics and Applied Mathematics, Vol. 4, 1951, pp. 1-22.
42. Tomotika, S.; Hasimoto, Z.; and Urano, K.: The Forces Acting on an Aerofoil of Approximate Joukowski Type in a Stream by a Plane Wall. The Quarterly J. of Fluid Mechanics and Applied Mathematics, Vol. 4, 1951, pp. 289-307.
43. Kida, T. and Miyai, T.: Jet-Flapped Wings in Very Close Proximity to the Ground. AIAA J., Vol. 10, No. 5, May 1972, pp. 611-616.
44. Hayashi, T.T.: Solution of the Two-Dimensional Jet-Flap Problem by the EVD Method. McDonnell Douglas Report, in publication.
45. Halsey, N.D.: Two-Dimensional Nonlinear Jet-Flap Potential Flow Method. Unpublished work. McDonnell Douglas Corporation proprietary information.
46. Saunders, G.H.: Aerodynamic Characteristics of Wings in Ground Proximity. M.Sc. Thesis, Dept. of Aeronautics and Astronautics, Massachusetts Institute of Technology, 1963.
47. Vogler, R.D. and Turner, T.R.: Wind-Tunnel Investigation at Low Speeds to Determine Flow-Field Characteristics and Ground Influence on a Model with Jet-Augmented Flaps. NACA TN 4116, 1957.



48. Silverstein, A. and Katzoff, S.: Design Charts for Predicting Downwash Angles and Wake Characteristics Behind Plain and Flapped Wings. NACA TR 648, 1939.
49. Silverstein, A.; Katzoff, S.; and Bullivant, W.K.: Downwash and Wake Behind Plain and Flapped Airfoils. NACA Report No. 651, 1939.
50. Ross, A.J.: The Theoretical Evaluation of the Downwash Behind Jet-Flapped Wings. R&M 3119, Aeronautical Research Council, Great Britain, 1935.
51. Goldhammer, M.I.: An Analytic Method for Calculating the Roll Up of the Trailing Vortex Sheet Behind Swept Wings. McDonnell Douglas Corporation Report No. MDC J5610, Jan. 1973. (McDonnell Douglas proprietary information.)
52. Butter, D.J. and Hancock, G.J.: A Numerical Method for Calculating the Trailing Vortex System Behind a Swept Wing at Low Speed. J. Roy. Aero. Soc., Vol. 75, Aug. 1971, pp. 564-568.
53. Spreiter, J.R. and Sacks, A.H.: The Rolling Up of the Trailing Vortex Sheet and Its Effect on the Downwash Behind Wings. J. Aero. Sci., Vol. 18, No. 1, Jan. 1951, pp. 21-32.
54. Rubbert, P.E.: Theoretical Characteristics of Arbitrary Wings by a Nonplanar Vortex Lattice Method. Boeing Company Document No. D6-9244, Feb. 1964.
55. Wooler, P.T.: Development of an Analytical Model for the Flow of a Jet into a Subsonic Cross Wind. NASA SP-218, pp. 101-108, 1969.
56. Wooler, P.T., et. al: V/STOL Aircraft Aerodynamic Prediction Methods Investigation. Vol. I. Theoretical Development of Prediction Methods. AFFDL-TR-72-26, Jan. 1972.
57. Carter, A.W.: Effect of Jet Exhaust Location on the Longitudinal Aerodynamic Characteristics of a Jet V/STOL Model. NASA TN D5333, July 1969.
58. Karamcheti, K.: Principles of Ideal-Fluid Aerodynamics. John Wiley & Sons, New York, 1966.
59. Munk, M. M.: The Aerodynamic Forces on Airship Hulls. NACA Report No. 184, 1924.

60. Adams, M.C. and Sears, W.R.: Slender-Body Theory — Review and Extension. J. Aero. Sci., Feb. 1953, pp. 85-98.
61. Barnett, L. and Stevens, W.A.: Calculation of Pressure Distributions on Cambered Bodies of Arbitrary Cross Section at Angle of Attack with Application to Transport Fuselage Afterbody Design. AIAA Paper No. 65-718, Nov. 1965.
62. Smith, A.M.O. and Pierce, J.: Exact Solution of the Neumann Problem. Calculation of Noncirculatory Plane and Axially-Symmetric Flows About or Within Arbitrary Boundaries. Douglas Aircraft Company Report No. ES 26988, April 1958.
63. Hess, J.L. and Smith, A.M.O.: Calculation of Potential Flow About Arbitrary Bodies. Progress in Aeronautical Sciences. Pergamon Press, 1966.
64. Peake, D.J.: Three-Dimensional Flow Separations on Upswept Rear Fuselages. Canadian Aeronautics and Space Journal. Vol. 15, No. 10, Dec. 1969.
65. Wickens, R.H.: Observations of the Vortex Wake of a Lifting Fuselage Similar to Those on Rear-Loading Transport Aircraft. National Research Council of Canada Aeronautical Report LR-395, (NRC No. 7911), Jan. 1964.
66. Giesing, J.P.: Lifting Surface Theory for Wing-Fuselage Combinations. McDonnell Douglas Corporation Report No. DAC 67212, Aug 1968.
67. Kalman, T.P.; Giesing, J.P.; and Rodden, W.P.: Spanwise Distribution of Induced Drag in Subsonic Flow by the Vortex Lattice Method. J. Aircraft, Vol. 7, No. 6, Nov.-Dec. 1970, pp. 574-576.
68. USAF Stability and Control Datcom, Air Force Flight Dynamics Laboratory, Flight Control Division, Wright-Patterson Air Force Base, Ohio. October, 1960, revised February 1972.
69. Aiken, Thomas N. and Cook, Anthony M.: Results of Full-Scale Wind Tunnel Tests on the H.126 Jet-Flap Aircraft. NASA TN D-7252, April 1973.
70. Lissaman, P.B.S.: Analysis of High-Aspect-Ratio Jet-Flap Wings of Arbitrary Geometry. NASA CR-2179, February 1973.
71. Kerney, Keith P.: A Theory of the High-Aspect-Ratio Jet-Flap. AIAA Jour., Vol. 9, No. 3, March 1971.

APPENDIX I.1  
DOWNWASH INFLUENCE COEFFICIENTS

According to the EVD model constructed in Section 2.2.2, an EVD is generally represented by equation (2.61) and its downwash influence coefficients are defined by equations (2.63) and (2.64). To simplify the presentation the indices  $i$  and  $j$  are now dropped and the equations are rewritten as:

$$\gamma^* (\xi, \eta) = \gamma g(\xi) + \beta h(\xi) \quad (\text{I.1})$$

and

$$a(x, y) = -\frac{1}{4\pi} \iint_{\Delta A} \frac{g(\xi)}{(y - \eta)^2} \left( 1 + \frac{x - \xi}{r} \right) d\xi d\eta \quad (\text{I.2})$$

$$b(x, y) = -\frac{1}{4\pi} \iint_{\Delta A} \frac{h(\xi)}{(y - \eta)^2} \left( 1 + \frac{x - \xi}{r} \right) d\xi d\eta \quad (\text{I.3})$$

It has already been stated that the downwash influence coefficients represent the downwash at a point  $(x, y)$  induced by an EVD of unit magnitude ( $\gamma = 1$ , or  $\beta = 1$ ) at the base  $\Delta A$ . Since the induced downwash depends only on the relative distance between the downwash point and the EVD base, the coefficient may be calculated using any coordinate system, not necessarily the one adopted in the formulation of the jet-wing problem. Thus, for convenience, the following derivations will be based on a local coordinate system parallel to the original one and with its origin located inside the EVD base.

In order to simplify the calculation of the downwash influence coefficients, it has been assumed that all the EVD elements and hence their bases are rectangular in shape. Suppose that for a rectangular base, the limit of integration is from  $x_1$  to  $x_2$  in the  $\xi$  direction, and from  $-\Delta$  to  $\Delta$  in the  $\eta$  direction; then the integrals given by equations (I.2) and (I.3) are reduced to

$$a(x,y) = -\frac{1}{4\pi} \int_{x_1}^{x_2} g(\xi) F(\xi, x, y) d\xi \quad (I.4)$$

$$b(x,y) = -\frac{1}{4\pi} \int_{x_1}^{x_2} h(\xi) F(\xi, x, y) d\xi \quad (I.5)$$

where the function  $F(\xi, x, y)$  is the result of the  $n$ -integration (Mangler's principal value is taken) of the original integrals, or

$$\begin{aligned} F(\xi, x, y) &= \int_{-\Delta}^{\Delta} \frac{1}{(y-n)^2} \left( 1 + \frac{x-\xi}{r} \right) dn \quad (I.6) \\ &= \frac{1}{y-\Delta} \left( 1 + \frac{\sqrt{(x-\xi)^2 + (y-\Delta)^2}}{x-\xi} \right) - \frac{1}{y+\Delta} \left( 1 + \frac{\sqrt{(x-\xi)^2 + (y+\Delta)^2}}{x-\xi} \right) \end{aligned}$$

A considerable simplification has thus been achieved, since the calculations are now reduced to one-dimensional integrations only. Nevertheless, these integrals remain singular at  $\xi = x$ , for which the Cauchy principal value has to be taken. To complicate matters further, the EVD functions  $g(\xi)$  and  $h(\xi)$  may also contain singularities. Consequently, careful attention must be given to the computation of these integrals.

In the following sections each of the four types of EVD will be defined, and their corresponding downwash influence coefficients will be derived.

### I.1.1 Regular EVD

A Regular EVD and its associated coordinate system are shown in figure (I.1a). The triangular shape arises as a result of assuming a linear chord-wise vortex distribution in an element, because the linear distribution can be built up by two overlapping triangles. The vortex distribution in this case can be expressed simply by

$$\gamma^*(\xi) = \gamma g(\xi) \quad (I.7)$$

where

$$g(\xi) = \begin{cases} \frac{1}{\delta_1} (\xi + \delta_1), & (-\delta_1 \leq \xi \leq 0) \\ -\frac{1}{\delta_2} (\xi - \delta_2), & (0 \leq \xi \leq \delta_2) \end{cases}$$

where  $\gamma$  designates the peak value of the triangular distribution. Hence, the downwash influence coefficient calculated from equation (I.2) becomes

$$\begin{aligned} a(x,y) &= -\frac{1}{4\pi} \left\{ \int_{-\delta_1}^0 \frac{\xi + \delta_1}{\delta_1} F(\xi, x, y) d\xi + \int_0^{\delta_2} -\frac{\xi - \delta_2}{\delta_2} F(\xi, x, y) d\xi \right\} \\ &= -\frac{1}{8\pi} \left\{ (\delta_1 + \delta_2) \left( \frac{1}{y - \Delta} - \frac{1}{y + \Delta} \right) \right. \\ &\quad + \frac{x + \delta_1}{\delta_1} \left( \frac{R_1' - R_0'}{y - \Delta} - \frac{R_1'' - R_0''}{y + \Delta} \right) + \frac{x - \delta_2}{\delta_2} \left( \frac{R_2' - R_0'}{y - \Delta} - \frac{R_2'' - R_0''}{y + \Delta} \right) \\ &\quad - 2 \left( \frac{x + \delta_1}{\delta_1} \right) \log \left| \frac{y - \Delta + R_1'}{y + \Delta + R_1''} \cdot \frac{y + \Delta + R_0''}{y - \Delta + R_0'} \right| - 2 \left( \frac{x - \delta_2}{\delta_2} \right) \log \left| \frac{y - \Delta + R_2'}{y + \Delta + R_2''} \cdot \frac{y + \Delta + R_0''}{y - \Delta + R_0'} \right| \\ &\quad - \left( \frac{y - \Delta}{\delta_1} \right) \log \left| \frac{x + \delta_1 + R_1'}{x + R_0'} \right| + \left( \frac{y + \Delta}{\delta_1} \right) \log \left| \frac{x + \delta_1 + R_1''}{x + R_0''} \right| \\ &\quad \left. - \left( \frac{y - \Delta}{\delta_2} \right) \log \left| \frac{x - \delta_2 + R_2'}{x + R_0'} \right| + \left( \frac{y + \Delta}{\delta_2} \right) \log \left| \frac{x - \delta_2 + R_2''}{x + R_0''} \right| \right\} \quad (I.8) \end{aligned}$$

where

$$\begin{aligned}
 R_1' &= \sqrt{(x + \delta_1)^2 + (y - \Delta)^2} & R_1'' &= \sqrt{(x + \delta_1)^2 + (y + \Delta)^2} \\
 R_0' &= \sqrt{x^2 + (y - \Delta)^2} & R_0'' &= \sqrt{x^2 + (y + \Delta)^2} \\
 R_2' &= \sqrt{(x - \delta_2)^2 + (y - \Delta)^2} & R_2'' &= \sqrt{(x - \delta_2)^2 + (y + \Delta)^2}
 \end{aligned}$$

### I.1.2 Leading Edge EVD

According to classical thin airfoil theory, the leading edge vortex distribution can be expanded into the following form:

$$\gamma(\xi) = C_0 \xi^{-1/2} + C_1 \xi^{1/2} + O(\xi^{3/2}), \quad (\xi \rightarrow 0) \quad (I.9)$$

which includes a square root singularity. The EVD formulation requires a linear distribution, as shown by the dashed line in figure (I.1b), to be subtracted from the real leading edge distribution, thus the leading edge EVD is defined as

$$\gamma^*(\xi) = C_0 \xi^{-1/2} + C_1 \xi^{1/2} + O(\xi^{3/2}) - \frac{\gamma_1}{\delta} \xi \quad (I.10)$$

Such a distribution is illustrated by the shaded area in figure (I.1b). If it is assumed that the higher order terms (i.e., term of  $O(\xi^{1/2})$  and higher) in the above expansion are approximated by a linear distribution  $D\xi$  then

$$\gamma^*(\xi) = C_0 \xi^{-1/2} + \left(D - \frac{\gamma_1}{\delta}\right) \xi \quad (I.11)$$

Since, by definition,  $\gamma^*(\xi)$  approaches zero as  $\xi$  goes to  $\delta$ , the Leading-Edge EVD can be reduced to the following expression:

$$\gamma^*(\xi) = C_0 (\xi^{-1/2} - \delta^{-3/2} \xi) \quad (I.12)$$

It follows by integration that the mean value of  $\gamma^*$  over its base is given by:

$$\bar{\gamma} = \frac{3}{2} \delta^{-1/2} C_0 \quad (I.13)$$

In terms of this mean value, a final expression for the Leading-Edge EVD is established as follows:

$$\gamma^*(\xi) = \bar{\gamma} g(\xi) \quad (I.14)$$

where

$$g(\xi) = \frac{2}{3} \left[ \left( \frac{\xi}{\delta} \right)^{-1/2} - \left( \frac{\xi}{\delta} \right) \right]$$

With the above definition, the downwash influence coefficient  $a(x,y)$  due to the Leading-Edge EVD according to equation (A.2) becomes

$$\begin{aligned} a(x,y) &= -\frac{1}{4\pi} \int_0^\delta \frac{2}{3} \left[ \left( \frac{\xi}{\delta} \right)^{-1/2} - \left( \frac{\xi}{\delta} \right) \right] F(\xi, x, y) d\xi \\ &= -\frac{1}{6\pi} \left\{ \frac{3}{2} \delta \left( \frac{1}{y-\Delta} - \frac{1}{y+\Delta} \right) + \left( \frac{R_0'}{y-\Delta} - \frac{R_0''}{y+\Delta} \right) P(x) + Q(x) \right\} \end{aligned} \quad (I.15)$$

where

$$P(x) = \begin{cases} -\sqrt{\frac{\delta}{x}} \log \left| \frac{\sqrt{x} - \sqrt{\delta}}{\sqrt{x} + \sqrt{\delta}} \right| + \frac{x}{\delta} \log \left| \frac{x - \delta}{x} \right| + 1, & (x \geq 0) \\ -2\sqrt{\frac{\delta}{-x}} \tan^{-1} \sqrt{\frac{\delta}{-x}} + \frac{x}{\delta} \log \left| \frac{x - \delta}{x} \right| + 1, & (x < 0) \end{cases}$$

$$Q(x) = \begin{cases} \int_0^\delta q_1(x, \xi) d\xi, & (x < 0, x > \delta) \\ -[f'(x, x) - f''(x, x)] \log \left| \frac{x - \delta}{x} \right| + \int_0^\delta q_2(x, \xi) d\xi, & (0 \leq x \leq \delta) \end{cases}$$

$$R_0' = \sqrt{x^2 + (y - \Delta)^2}, \quad R_0'' = \sqrt{x^2 + (y + \Delta)^2}$$

where in  $Q(x)$  the functions  $f'(x, \xi)$  and  $f''(x, \xi)$  are defined as

$$f'(x, \xi) = \left[ \left( \frac{\xi}{\delta} \right)^{-1/2} - \frac{\xi}{\delta} \right] \frac{\sqrt{(x - \xi)^2 + (y - \Delta)^2} - \sqrt{x^2 + (y - \Delta)^2}}{y + \Delta}$$

$$f''(x, \xi) = \left[ \left( \frac{\xi}{\delta} \right)^{-1/2} - \frac{\xi}{\delta} \right] \frac{\sqrt{(x - \xi)^2 + (y + \Delta)^2} - \sqrt{x^2 + (y + \Delta)^2}}{y + \Delta}$$

and the integrands  $q_1(x, \xi)$  and  $q_2(x, \xi)$  are given by

$$q_1(x, \xi) = \frac{f'(x, \xi) - f''(x, x)}{x - \xi}$$

$$q_2(x, \xi) = \frac{f'(x, \xi) - f'(x, x)}{x - \xi} - \frac{f''(x, \xi) - f''(x, x)}{x - \xi}$$

It should be noted that the integrands  $q_1(x, \xi)$  and  $q_2(x, \xi)$  are bounded in their respective regions of integration. Hence, the corresponding integrals can be readily evaluated by a numerical technique. In this case, a Gaussian integration method is utilized.

Numerical problems still arise when computation is made directly with the above formulas. To avoid them, various limiting values associated with certain terms must be evaluated beforehand and represented by separate expressions. See Volume II, Appendix I.

### I.1.3 Hinge EVD

To derive the Hinge EVD, it may first be seen that near the hinge (in general, this includes the knee of either a leading or trailing edge flap and the point of jet emission) the vortex distribution can be expressed in terms of the following expansion:

$$\gamma(\xi) = -\frac{2\beta}{\pi} \log|\xi| + C_0 + C_1\xi + O(\xi^2), \quad (\xi \rightarrow 0) \quad (I.16)$$



which follows from either linearized thin airfoil or jet-flap theory. The first term (i.e., a logarithmic singularity) guarantees that the downwash distribution across the hinge (at  $\xi = 0$ ) exhibits a jump equal in magnitude to the deflection angle  $\beta$ , thus, satisfying the boundary condition exactly for an ideal leading or trailing edge flap or jet deflection.

Next, on each side of the hinge, a linear distribution must be subtracted from equation (A.16). This is illustrated in figure (I.1c), in which the dashed lines represent the linear quantities to be subtracted (denoted by  $E_1\xi$  with  $E_1 = -\gamma_1/\delta_1$  for  $\xi < 0$  and  $E_1 = \gamma_2/\delta_2$  for  $\xi > 0$ ). The remaining shaded area in the figure thus defines the Hinge EVD. With the second-order quantity  $O(\xi^2)$  in equation (I.16) approximated by a linear term  $D_1\xi$ , the Hinge EVD may be expressed as

$$\gamma^*(\xi) = -\frac{2}{\pi} \log|\xi| + C_0 + (C_1 + D_1 - E_1)\xi \quad (I.17)$$

Finally, the Hinge EVD requires the  $\gamma^*$  value to vanish at both ends. Consequently,  $\gamma^*$  is expressed as

$$\gamma^*(\xi) = C_0 g(\xi) + \beta h(\xi) \quad (I.18)$$

$$g(\xi) = \begin{cases} \frac{1}{\delta_1} (\xi + \delta_1), & (-\delta_1 \leq \xi < 0) \\ -\frac{1}{\delta_2} (\xi - \delta_2), & (0 < \xi \leq \delta_2) \end{cases}$$

and

$$h(\xi) = \begin{cases} -\frac{2}{\pi} (\log|\xi| + \frac{\xi}{\delta_1} \log \delta_1), & (-\delta_1 \leq \xi < 0) \\ -\frac{2}{\pi} (\log|\xi| - \frac{\xi}{\delta_2} \log \delta_2), & (0 < \xi \leq \delta_2) \end{cases}$$

Thus, the Hinge EVD actually consists of two parts. The first part  $C_0 g(\xi)$ , is identical to the Regular EVD except that now  $C_0$  replaces  $\gamma$ . The second part  $h(\xi)$  is an additional hinge distribution which is found to be proportional to the deflection angle  $\beta$  and which contains the logarithmic singularity.

Accordingly, the downwash influence coefficients for the Hinge EVD will also have two parts, that is,  $a(x,y)$  and  $b(x,y)$ . The regular part,  $a(x,y)$ , corresponding to the Regular EVD, has already been given in equation (I.8); while the additional part,  $b(x,y)$ , corresponding to the additional hinge distribution, can be derived from equation (I.5) and expressed as follows:

$$\begin{aligned}
 b(x,y) &= -\frac{1}{4\pi} \int_{-\delta_1}^0 -\frac{2}{\pi} \left( \log|\xi| + \frac{\xi}{\delta_1} \log \delta_1 \right) F(\xi,x,y) d\xi \\
 &\quad - \frac{1}{4\pi} \int_0^{\delta_2} -\frac{2}{\pi} \left( \log|\xi| - \frac{\xi}{\delta_2} \log \delta_2 \right) F(\xi,x,y) d\xi \\
 &= \frac{1}{2\pi^2} \left\{ - \left( \delta_1 + \delta_2 + \frac{1}{2} \delta_1 \log \delta_1 + \frac{1}{2} \delta_2 \log \delta_2 \right) \left( \frac{1}{y-\Delta} - \frac{1}{y+\Delta} \right) \right. \\
 &\quad \left. + \left( \frac{R_0'}{y-\Delta} - \frac{R_0''}{y+\Delta} \right) P(x) + Q(x) \right\} \tag{I.19}
 \end{aligned}$$

In the above,

$$\begin{aligned}
 P(x) &= -\frac{\pi^2}{4} S(x) - \log \frac{\delta_1}{\delta_2} \\
 &\quad + \left( \log \left| \frac{x}{\delta_1} \right| + \frac{x + \delta_1}{\delta_1} \log \delta_1 \right) \log \left| \frac{x + \delta_1}{x} \right| \\
 &\quad - \left( \log \left| \frac{x}{\delta_2} \right| - \frac{x - \delta_2}{\delta_2} \log \delta_2 \right) \log \left| \frac{x - \delta_2}{x} \right|
 \end{aligned}$$

$$+ \int_1^{\delta_1/|x|} \frac{\log t dt}{S(x)+t} + \int_1^{\delta_2/|x|} \frac{\log t dt}{S(x)-t} \quad , \quad (x \neq 0)$$

$$P(x) = -\frac{\pi^2}{2} S(x) - \left(1 - \frac{1}{2} \log \delta_1 \delta_2\right) \log \frac{\delta_1}{\delta_2} \quad , \quad (x \rightarrow 0)$$

$$Q(x) = \begin{cases} \int_{-\delta_1}^0 q_1(x, \xi) d\xi + \int_0^{\delta_2} q_1(x, \xi) d\xi & , \quad (x \leq -\delta_1, x \geq \delta_2) \\ -[f'(x, x) - f''(x, x)] \log \left| \frac{x - \delta_2}{x + \delta_1} \right| + \int_{-\delta_1}^0 q_2(\xi) d\xi + \int_0^{\delta_2} q_2(\xi) d\xi, & (-\delta_1 < x < \delta_2) \end{cases}$$

$$R_0' = \sqrt{x^2 + (y - \Delta)^2} \quad , \quad R_0'' = \sqrt{x^2 + (y + \Delta)^2}$$

where by definition,

$$q_1(x, \xi) = \frac{f'(x, \xi) - f''(x, \xi)}{x - \xi}$$

$$q_2(x, \xi) = \frac{f'(x, \xi) - f'(x, x)}{x - \xi} - \frac{f''(x, \xi) - f''(x, x)}{x - \xi}$$

$$f'(x, \xi) = h_0(\xi) \frac{\sqrt{(x - \xi)^2 + (y - \Delta)^2} - \sqrt{x^2 + (y - \Delta)^2}}{y - \Delta}$$

$$f''(x, \xi) = h_0(\xi) \frac{\sqrt{(x - \xi)^2 + (y + \Delta)^2} - \sqrt{x^2 + (y + \Delta)^2}}{y + \Delta}$$

$$h_0(\xi) = \begin{cases} \log |\xi| + \frac{\xi}{\delta_1} \log \delta_1 \quad , & (-\delta_1 \leq \xi < 0) \\ \log |\xi| - \frac{\xi}{\delta_2} \log \delta_2 \quad , & (0 < \xi \leq \delta_2) \end{cases}$$

$$S(x) = \begin{cases} -1, & (x < 0) \\ +1, & (x > 0) \end{cases}$$

All the integrands which cannot be integrated analytically have been reduced to the bounded functions as shown, so that a numerical procedure (in this case a Gaussian integration method) can be applied. Several limiting values (reference 2) or expressions still have to be derived before the computation is made by a computer.

#### 1.1.4 Infinity (far-jet) EVD

As the jet leaves the trailing edge of a wing in the downstream direction, its bound vortex strength gradually decays. In view of the Kutta condition, it will finally vanish at infinity. Therefore, far enough downstream, the vorticity distribution on the jet may be approximated by a polynomial of negative powers; that is,

$$\gamma(\xi) = C_n(\xi + d)^{-n} + C_{n+1}(\xi + d)^{-(n+1)} + \dots, (\xi > 0) \quad (I.20)$$

for which the coordinate system is shown in figure (I.1d). The origin is located at a distance  $d$  from the trailing edge.

It is also essential that the total vorticity contained in the far-jet interval (from  $\xi = 0$  to  $\infty$ ) should be a finite value so that the wing loading caused by it is not unlimited. The smallest power  $n$  which satisfies this condition is 2. Thus,

$$\gamma(\xi) = C_2(\xi + d)^{-2} \quad (I.21)$$

The higher order terms are negligible when  $d$  is chosen sufficiently large. Suppose that the peak vortex value at  $\xi = 0$  is  $\gamma$ , it is easily verified that  $C_2 = \gamma d^2$ .

In deriving an expression for the Infinity EVD, it should be noted that

a linear vortex distribution which has been left over from the formation of a Regular EVD immediately ahead of  $\xi = 0$  must be accounted for. This is also illustrated in figure (I.1d). Thus, the Infinity EVD may be expressed as

$$\gamma^*(\xi) = \gamma g(\xi) \quad (I.22)$$

where

$$g(\xi) = \begin{cases} \frac{1}{\delta} (\xi + \delta), & (-\delta \leq \xi \leq 0) \\ \left(\frac{\xi}{d} + 1\right)^{-2}, & (\xi > 0) \end{cases}$$

The downwash influence coefficient  $a(x,y)$  corresponding to the Infinity EVD is obtained from equation (I.9), as follows:

$$\begin{aligned} a(x,y) &= -\frac{1}{4\pi} \int_{-\delta}^0 \frac{1}{\delta} (\xi + \delta) F(\xi, x, y) d\xi - \frac{1}{4\pi} \int_0^{\infty} \left(\frac{\xi}{d} + 1\right)^{-2} F(\xi, x, y) d\xi \\ &= -\frac{1}{8\pi} \left\{ (\delta + 2d) \left( \frac{1}{y - \Delta} - \frac{1}{y + \Delta} \right) - \left( \frac{R_0'}{y - \Delta} - \frac{R_0''}{y + \Delta} \right) \right. \\ &\quad + \frac{x + \delta}{\delta} \left( \frac{R_1'}{y - \Delta} - \frac{R_1''}{y + \Delta} \right) \\ &\quad - 2 \left( \frac{x + \delta}{\delta} \right) \log \left| \frac{y - \Delta + R_1'}{y + \Delta + R_1''} \cdot \frac{y + \Delta + R_0''}{y - \Delta + R_0'} \right| \\ &\quad - \frac{y - \Delta}{\delta} \log \left| \frac{x + \delta + R_1'}{x + R_0'} \right| + \frac{y + \Delta}{\delta} \log \left| \frac{x + \delta + R_1''}{x + R_0''} \right| \\ &\quad \left. + P(x) \right\} \end{aligned}$$

where

$$P(x) = -2 \frac{d^2}{x + d} \left( \frac{1}{y - \Delta} - \frac{1}{y + \Delta} \right) + 2 \frac{d}{x + d} \left( \frac{R_0'}{y - \Delta} - \frac{R_0''}{y + \Delta} \right)$$

$$\begin{aligned}
& -2\left(\frac{d}{x+d}\right)^2 \log \left| \frac{y-\Delta+R_0'}{y+\Delta+R_0''} \right| \\
& +2\left(\frac{d}{x+d}\right)^2 \left[ \frac{y-\Delta}{R_d'} \log \left| \frac{-(x+d)+R_d' \frac{R_0'+R_d'}{d}}{-(x+d)+R_d'} \right| \right. \\
& \quad \left. - \frac{y+\Delta}{R_d''} \log \left| \frac{-(x+d)+R_d'' \frac{R_0''+R_d''}{d}}{-(x+d)+R_d''} \right| \right], \quad (x \neq -d)
\end{aligned}$$

$$\begin{aligned}
P(x) = & -\left(\frac{R_0'}{y-\Delta} - \frac{R_0''}{y+\Delta}\right) \\
& - \left[ \left(\frac{d}{y-\Delta}\right)^2 \log \left| \frac{y-\Delta+R_0'}{d} \right| - \left(\frac{d}{y+\Delta}\right)^2 \log \left| \frac{y+\Delta+R_0''}{d} \right| \right] \\
& (x = -d)
\end{aligned}$$

$$R_0' = \sqrt{x^2 + (y - \Delta)^2} \quad R_0'' = \sqrt{x^2 + (y + \Delta)^2}$$

$$R_1' = \sqrt{(x + \delta)^2 + (y - \Delta)^2} \quad R_1'' = \sqrt{(x + \delta)^2 + (y + \Delta)^2}$$

$$R_d' = \sqrt{(x + d)^2 + (y - \Delta)^2} \quad R_d'' = \sqrt{(x + d)^2 + (y + \Delta)^2}$$

### I.1.5 Ground Effect Influence Coefficients

The infinitesimal horseshoe vortex distribution representing the image jet-wing in the solution of the ground effect problem has been represented by a lattice of discrete horseshoe vortices, as discussed in Section 2.2.2.3. The downwash influence coefficients due to the image,  $\bar{a}_{ij}$ , represent the downwash induced at the point  $(x_i, y_i, z = 0)$  by a discrete horseshoe vortex of unit strength located on the element of the image jet-wing including the point  $(x_j, y_j, -2h)$ , where  $h$  is the height of the wing above the ground plane, normalized by the wing semi-span  $b/2$ . Just as for the EVD influence functions, the formulation here will be based on a local coordinate system parallel to the original one with its origin located inside the

influencing element base.

Since the singularities representing the image are discrete while those representing the real jet-wing are EVDs, it is necessary to establish the relationship between the EVD value (either the peak or average value) and the integrated (or discrete) value  $\Gamma$ . Placing the discrete vortex at the leading edge of each element in the plane of the image wing and integrating the Elementary Vortex Distribution over the chord of the element, the relationship between the EVD strength  $\gamma_i$  and the discrete horseshoe vortex strength  $\Gamma_i$  for the vortex located at the leading edge is

$$\Gamma_i = \gamma_i \delta_i \quad (I.23)$$

where  $\delta_i$  is the length of the leading edge element. For all other elements the relationship is

$$\Gamma_i = \frac{1}{2} \gamma_i (\delta_{i-1} + \delta_i) \quad (I.24)$$

with the exception of the jet infinity or far field element which is given by

$$\Gamma_i = \gamma_i \left( \frac{1}{2} \delta_{i-1} + d \right) \quad (I.25)$$

where  $d$  is the streamwise distance from the wing trailing edge to the leading edge of the jet infinity element.

The actual downwash influence coefficient is calculated by application of the Biot-Savart Law for straight line vortex filaments. Although the equations derived in Appendix II are applicable here, because the horseshoe vortices in this case are in a plane parallel to the  $x$ - $y$  plane and because the bound segments are always parallel to the  $y$ -axis and the trailing segments to the  $x$ -axis, considerable simplification is possible. Hence, with  $\gamma_i$  in equations (I.23), (I.24), and (I.25) equal to unity, the downwash influence coefficient is

$$\bar{a}(x,y) = -\frac{g(\delta)}{4\pi} \left\{ \left( \frac{y-\Delta}{R_L} - \frac{y+\Delta}{R_R} \right) \frac{x}{R_B^2} + \left( \frac{x}{R_L} + 1.0 \right) \frac{y-\Delta}{R_L'^2} - \left( \frac{x}{R_R} + 1.0 \right) \frac{y+\Delta}{R_R'^2} \right\} \quad (I.26)$$

where

$$g(\delta) = \begin{cases} \delta_i & , \text{(leading edge element)} \\ \frac{1}{2} (\delta_{i-1} + \delta_i) & , \text{(regular element)} \\ \frac{1}{2} \delta_{i-1} + d & , \text{(jet infinity element)} \end{cases} \quad (I.27)$$

and

$$\begin{aligned} R_L &= \sqrt{x^2 + (y-\Delta)^2 + (2h)^2} & R_L' &= \sqrt{(y-\Delta)^2 + (2h)^2} \\ R_R &= \sqrt{x^2 + (y+\Delta)^2 + (2h)^2} & R_R' &= \sqrt{(y+\Delta)^2 + (2h)^2} \\ R_B &= \sqrt{x^2 + (2h)^2} \end{aligned} \quad (I.28)$$

The perturbation freestream velocity influence coefficient,  $a_{ij}$ , represents the perturbation to the freestream flow induced at a point  $(x_i, y_i, 0)$  by a discrete horseshoe vortex of unit strength located on the element of the image including the point  $(x_j, y_j, -2h)$ . In a manner similar to the downwash influence coefficient  $\bar{a}(x,y)$ , the perturbation freestream velocity influence coefficient can be expressed in the following form:

$$c(x,y) = \frac{g(\delta)}{4\pi} \left\{ \left( \frac{y-\Delta}{R_L} - \frac{y+\Delta}{R_R} \right) \frac{2h}{R_B^2} \right\} \quad (I.29)$$



APPENDIX I.2  
INTEGRATION COEFFICIENTS

The integration coefficients  $e_{ij}$  and  $f_{ij}$  as defined in equation (2.71) are given by

$$\int_{x_{i-1}}^{x_i} \gamma(\xi, y_i) d\xi = \sum_{j=1}^N e_{ij} \gamma_j + \sum_{j=1}^N f_{ij} \beta_j \quad (i, \text{ on the jet}) \quad (I.30)$$

The evaluation of these coefficients depends on the location of the  $i$ -th control point on the jet. It also depends on the relative location of the control point with respect to an element. In the following, the derivation is made for the control point situated in the center (chordwise) of the rectangular element.

i. The Leading Control Point on the Jet

The integration in this case should start from the trailing edge  $x_t$  rather than the preceding control point  $x_{i-1}$  because the latter happens to be outside the jet. Thus by using the EVD definition and with the aid of figure (I.2)

$$\begin{aligned} \int_{x_t}^{x_i} \gamma(\xi, y_i) d\xi &= \int_0^{\delta_i/2} \left[ -\frac{\gamma_i}{\delta_i} (t - \delta_i) + \frac{\gamma_{i+1}}{\delta_i} t - \frac{2\beta_i}{\pi} \left( \log |t| - \frac{\log \delta_i}{\delta_i} t \right) \right] dt \\ &= \frac{3}{8} \delta_i \gamma_i + \frac{1}{8} \delta_i \gamma_{i+1} + \frac{1}{\pi} \left( 1 + \ln 2 - \frac{3}{4} \log \delta_i \right) \delta_i \beta_i \end{aligned} \quad (I.31)$$

ii. The Second Control Point on the Jet

$$\begin{aligned} \int_{x_{i-1}}^{x_i} \gamma(\xi, y_i) d\xi &= \int_{\delta_{i-1}/2}^{\delta_{i-1}} \left[ -\frac{\gamma_{i-1}}{\delta_{i-1}} (t - \delta_{i-1}) + \frac{\gamma_i}{\delta_{i-1}} t - \frac{2\beta_{i-1}}{\pi} \left( \log |t| - \frac{\log \delta_{i-1}}{\delta_{i-1}} t \right) \right] dt \\ &\quad + \int_0^{\delta_i/2} \left[ -\frac{\gamma_i}{\delta_i} (s - \delta_i) + \frac{\gamma_{i+1}}{\delta_i} s \right] ds \end{aligned} \quad (I.32)$$

$$\begin{aligned}
&= \frac{1}{8} \delta_{i-1} \gamma_{i-1} + \frac{3}{8} (\delta_{i-1} + \delta_i) \gamma_i + \frac{1}{8} \delta_i \gamma_{i+1} \\
&+ \frac{1}{\pi} \left( 1 - \log 2 - \frac{1}{4} \log \delta_{i-1} \right) \delta_{i-1} \beta_{i-1}
\end{aligned} \tag{I.32}$$

iii. Internal Control Points

$$\int_{x_{i-1}}^{x_i} \gamma(\xi, y_i) d\xi = \frac{1}{8} \delta_{i-1} \gamma_{i-1} + \frac{3}{8} (\delta_{i-1} + \delta_i) \gamma_i + \frac{1}{8} \delta_i \gamma_{i+1} \tag{I.33}$$

iv.

The Last Control Point (at Infinity) on the Jet

$$\begin{aligned}
\int_{x_{i-1}}^{x_i} \gamma(\xi, y_i) d\xi &= \int_{-\delta_{i-1}/2}^0 \left[ -\frac{\gamma_{i-1}}{\delta_{i-1}} s + \frac{\gamma_i}{\delta_{i-1}} (s + \delta_{i-1}) \right] ds \\
&+ \int_0^{\infty} \gamma_i \left( \frac{s+d}{d} \right)^{-2} ds \\
&= \frac{1}{8} \delta_{i-1} \gamma_{i-1} + \left( \frac{3}{8} \delta_{i-1} + d(y_i) \right) \gamma_i
\end{aligned} \tag{I.34}$$

Now the integration coefficients  $e_{ij}$  and  $f_{ij}$  may be identified from the above formulas; that is,

$$\begin{aligned}
e_{ij} = 0, \quad f_{ij} = 0, \quad (i = 1, 2, \dots, N) \\
(j = 1, 2, \dots, N)
\end{aligned}$$

except for the following:

i, the leading jet control point:

$$e_{i,i} = \frac{3}{8} \delta_i, \quad f_{i,i} = \frac{1}{\pi} (1 + \ln 2 - \frac{3}{4} \ln \delta_i) \delta_i,$$

$$e_{i,i+1} = \frac{1}{8} \delta_i,$$

i, the second jet control point:

$$e_{i,i-1} = \frac{1}{8} \delta_{i-1} \quad f_{i,i-1} = \frac{1}{\pi} (1 - \ln 2 - \frac{1}{4} \ln \delta_{i-1}) \delta_{i-1}$$

$$e_{i,i} = \frac{3}{8} (\delta_{i-1} + \delta_i)$$

$$e_{i,i+1} = \frac{1}{8} \delta_i$$

i, the internal jet control points:

$$e_{i,i-1} = \frac{1}{8} \delta_{i-1}$$

$$e_{i,i} = \frac{3}{8} (\delta_{i-1} + \delta_i)$$

$$e_{i,i+1} = \frac{1}{8} \delta_i$$

i, the last jet control point (at infinity):

$$e_{i,i-1} = \frac{1}{8} \delta_{i-1}$$

$$e_{i,i} = \frac{3}{8} \delta_{i-1} + d(y_i)$$

APPENDIX I.3  
LEADING EDGE SUCTION

An expression for the leading edge suction compatible with the approximations adopted in the development of the EVD method and based on a two-dimensional analogy will be derived.

Consider a two-dimensional thin airfoil with its leading edge located at the origin ( $x = 0, y = 0$ ). The force acting on this leading edge may be conveniently obtained by applying the Blasius law to a small circle "C" surrounding the leading edge, that is,

$$F_x - iF_y = \frac{1}{2} \rho i \oint_C \omega^2(z) dz \quad (I.35)$$

where  $\omega(z)$  represents the complex velocity. The latter, in terms of the vorticity distribution  $\gamma(\xi)$  assumed in thin airfoil theory, may be written as

$$\omega(z) = Uz + \frac{i}{2\pi} \int_0^C \frac{\gamma(\xi) d\xi}{z - \xi} \quad (I.36)$$

Since only the singular part of the velocity can have a finite contribution to the integral in equation (I.35) when the circle C is allowed to diminish, the finite part of the velocity in equation (I.36) may now be dropped insofar as the force calculation is concerned. Incidentally, the singular velocity in this case is induced by the singular (i.e., square root) part of the vorticity distribution. Thus, without loss of generality, this singular vorticity distribution can be expressed as

$$\gamma(\xi) = A\xi^{-1/2} \quad (I.37)$$

and the integration limit of equation (I.36) may be carried to a small distance  $\epsilon$  from the leading edge instead of all the way to the trailing edge.

$$\omega(z) = \frac{iA}{2} \int_0^\epsilon \frac{\xi^{-1/2} d\xi}{z - \xi} \quad (I.38)$$

With the aid of the residue theorem, it leads to

$$\omega(z) = \frac{A}{2\sqrt{z}} \quad (I.39)$$

which is truly seen to be square root singular. Substituting this back into equation (I.35) and again using the residue theorem yields the following expressions:

$$F_x = -\frac{\pi}{4} \rho A^2 \quad (I.40)$$

$$F_y = 0$$

This is the so-called leading edge suction. It acts in the direction along which the vortex is distributed. Written in dimensionless form, it becomes

$$c_s = -\frac{F_x}{qc} = \frac{\pi}{2} \frac{A^2}{U^2 c} \quad (I.41)$$

The leading edge suction is seen to be dependent solely on the local singular flow behavior. But such a singular velocity is self-induced and unaffected by the nearby vorticity distribution. In other words, the leading edge suction depends on the local vorticity distribution. It would, therefore, be reasonable to assume that this two dimensional expression could be adopted in the finite wing case.

Since the present EVD method divides the wing into rectangular elements which locally forces the wing leading edge to be straight, it is suggested that the two-dimensional expression (I.41) be applied directly. It will be noted that the basis for adopting this approach has been substantiated elsewhere.

In the EVD method it has already been shown that the first term in the leading edge vorticity distribution can be expressed by

$$\gamma(x) = \frac{2}{3} U \sqrt{\delta} \bar{\gamma} x^{-1/2}$$

thus enabling the coefficient  $A$  to be identified. In terms of the EVD approach the leading edge suction coefficient  $c_s$  is, therefore, given by

$$c_s = \frac{2}{9} \pi \frac{\delta}{c} \bar{\gamma}^2 \quad (I.42)$$

In the above  $\delta$  denotes the leading edge element length and  $\bar{\gamma}$  is the average leading edge EVD value, obtained as a part of the  $\bar{\gamma}_j$  solution.

## APPENDIX I.4

### NUMERICAL TECHNIQUE FOR EVALUATING THE INDUCED DOWNWASH AT INFINITY

Two approaches to the calculation of induced drag have been outlined in this report. The first initially involves the calculation of the distribution of the drag forces on the wing. However, for most applications it is necessary to calculate only the overall drag, and this is done more conveniently by means of the momentum method described earlier in this report.

To determine the induced drag coefficient  $C_{Di}$  as given by equation (2.151), which can also be written as

$$C_{Di} = \frac{1}{2S} \int_{-1}^{+1} c(y) \alpha_{i\infty}(y) \left[ 2 \int_{x_\ell}^{x_t} \gamma(x,y) dx + c_\mu(y) \theta(y) \right] dy \quad (I.43)$$

it is necessary to evaluate the induced downwash angle  $\alpha_{i\infty}(y)$  according to the following formula

$$\alpha_{i\infty}(y) = \alpha_{i\infty W}(y) + \alpha_{i\infty I}(y) \quad (I.44)$$

where

$$\alpha_{i\infty W}(y) = \frac{1}{2\pi} \int_{-1}^{+1} \frac{d\Gamma(\eta)/d\eta}{y - \eta} d\eta$$

$$\alpha_{i\infty I}(y) = \frac{1}{2\pi} \int_{-1}^{+1} \frac{(y-\eta)d\Gamma(\eta)/d\eta}{(2h)^2 + (y-\eta)^2} d\eta$$

and

$$\Gamma(y) = \int_{x_\ell}^{\infty} \gamma(x,y) dx$$

In equation (I.44)  $\alpha_{i\infty I}(y)$  and  $\alpha_{i\infty W}(y)$  are the induced downwash contributions from the jet-wing wake and its image, respectively.

In principle, it is possible to obtain a solution for  $\alpha_{i\infty}(y)$  by simply considering the spanwise distribution of circulation  $\Gamma(\eta)$  as given by the EVD Jet-Wing Lifting Surface Theory. Unfortunately, the stepwise distribution of  $\Gamma(\eta)$  inherent in the formulation of the EVD method can be readily shown to give a low accuracy in the prediction of  $\alpha_{i\infty}(y)$ . This is not to imply that the accuracy in predicting aerodynamic loading should be questioned; but that since  $C_{D_i}$  is a second order quantity, higher order terms in the spanwise distribution of jet and wing bound vorticity must be considered.

Now, it has been found convenient to assume in evaluating  $\alpha_{i\infty}(y)$  the circulation across the spanwise strip "v" can be written in the form

$$\Gamma_v(\eta) = A_v(1-|\eta|)^{1/2} + B_v(1-|\eta|)^{3/2} + C_v(1-|\eta|)^{5/2} \quad (I.45)$$

where the coefficient  $A_v$ ,  $B_v$ , and  $C_v$  are determined with one exception from the values of  $\Gamma$  given by equation (I.44) at the center of each spanwise step and the center of its two adjacent strips. The one exception is at the wing tips where the coefficients are assumed to be identical to those at the nearest inboard strip. In general, therefore, if the subscript  $v$  refers to the centerline of each spanwise strip, then the coefficients  $A_v$ ,  $B_v$ ,  $C_v$  can be determined from the following matrix equation:

$$\begin{vmatrix} a^{1/2} & a^{3/2} & a^{5/2} \\ b^{1/2} & b^{3/2} & b^{5/2} \\ c^{1/2} & c^{3/2} & c^{5/2} \end{vmatrix} \begin{vmatrix} A_v \\ B_v \\ C_v \end{vmatrix} = \begin{vmatrix} \Gamma_{v-1} \\ \Gamma_v \\ \Gamma_{v+1} \end{vmatrix} \quad (I.46)$$

where

$$a = (1 - |\eta_{v-1}|)$$

$$b = (1 - |\eta_v|)$$

$$c = (1 - |\eta_{v+1}|)$$

It is important to note here that equation (I.45) will give the correct singular behaviors of the trailing vorticity,  $dr(y)/dy$ , at the wing-tip.

The incremental downwash  $\Delta\alpha_{i_{\infty kv}}$  at the point  $y_k$  due to the trailing vorticity associated with strip "v" of width  $2\Delta$  can now be simply obtained by substituting in the integral for  $\alpha_{i_{\infty v}}(y)$  given in equation (I.44)  $\frac{dr(y)}{dy}$  which can be obtained from equation (I.45). Hence, it follows that  $\Delta\alpha_{i_{\infty kv}}$  can be written as

$$\Delta\alpha_{i_{\infty kv}} = A_v H_{vk} + B_v I_{vk} + C_v J_{vk} \quad (I.47)$$

where

$$\begin{aligned} H_{vk} &= \frac{1}{4\pi} \int_{y_v - \Delta_v}^{y_v + \Delta_v} \frac{(1-|\eta|)^{-1/2}}{(y_k - \eta)} d\eta \\ &= \frac{1}{4\pi} \frac{1}{\sqrt{1-\bar{a}y_k}} \ln \left| \frac{(\sqrt{1-|y_v + \Delta_v|} - \sqrt{1-\bar{a}y_k})(\sqrt{1-|y_v - \Delta_v|} + \sqrt{1-\bar{a}y_k})}{(\sqrt{1-|y_v + \Delta_v|} + \sqrt{1-\bar{a}y_k})(\sqrt{1-|y_v - \Delta_v|} - \sqrt{1-\bar{a}y_k})} \right| \end{aligned}$$

$$\begin{aligned} I_{vk} &= \frac{3}{4\pi} \int_{\eta_v - \Delta_v}^{\eta_v + \Delta_v} \frac{(1-|\eta|)^{1/2}}{(\eta_k - \eta)} d\eta \\ &= \frac{3}{4\pi} \left\{ -2 \left( \sqrt{1-|y_v + \Delta_v|} - \sqrt{1-|y_v - \Delta_v|} \right) \right. \\ &\quad \left. + (1-\bar{a}y_k) \int_{y_v - \Delta_v}^{y_v + \Delta_v} \frac{(1-|\eta|)}{(y_k - \eta)} d\eta \right\} \end{aligned}$$



$$\begin{aligned}
J_{vk} &= \frac{5}{4\pi} \int_{\eta_v - \Delta_v}^{\eta_v + \Delta_v} \frac{(1-|\eta|)^{3/2}}{(\eta_k - \eta)} d\eta \\
&= \frac{5}{4\pi} \left\{ -\frac{2}{3} \left( \sqrt{1-|y_v + \Delta_v|}^3 - \sqrt{1-|y_v - \Delta_v|}^3 \right) \right. \\
&\quad \left. + (1-\bar{a}y_k) \int_{y_v - \Delta_v}^{y_v + \Delta_v} \frac{(1-|\eta|)^{3/2}}{(y_k - \eta)} d\eta \right\}
\end{aligned}$$

and  $\bar{a} = \frac{y_v}{|y_v|}$

The above procedure will give the exact result for  $\alpha_{i_{\infty W}}$  for an elliptical distribution of  $\Gamma$  and an acceptable accuracy under other conditions providing the distribution of  $c_\mu(y)$  is continuous. If this is not the case, the discontinuity in  $\Gamma$  is approximated by a discrete vortex equal in strength to the "jump" in  $\Gamma$ . This could cause some problems in the calculation of  $\alpha_{i_{\infty W}}$  which are avoided in the present method by calculating  $\alpha_{i_{\infty W}}$  at the midpoint of each spanwise strip.

The total downwash induced by the jet-wing wake at the point  $y_{kv}$  in the Trefftz plane can now readily be obtained from a summation of  $\Delta\alpha_{i_{\infty Wk}}$  for all  $M$  spanwise strips. In other words  $\alpha_{i_{\infty W}}(y_k)$  can be expressed as follows:

$$\alpha_{i_{\infty W}}(y_k) = \alpha_{i_{\infty Wk}} = \sum_{vk=1}^M \Delta\alpha_{i_{\infty Wk}} \tag{I.48}$$

There now remains the calculation of the induced downwash angle  $\alpha_{i_{\infty I}}(y)$  at the point  $(y_k)$  induced by the image of the jet-wing wake. The integral for  $\alpha_{i_{\infty I}}(y)$  given in equation (I.44) can, by integrating by parts, be expressed alternatively by

$$\alpha_{i_{\infty I}}(y) = -\frac{1}{2\pi} \int_{-1}^{+1} \frac{(2h)^2 - (y-\eta)^2}{[(y-\eta)^2 + (2h)^2]^2} \Gamma(\eta) d\eta \quad (\text{I.49})$$

The numerical integration of equation (I.49) presents no problems. In the present case, a quadrature integration procedure has been used.

APPENDIX I.5  
GROUND EFFECT — THIN AIRFOIL THEORY

An important example of the application of linear perturbation theory is the case of the flow past an airfoil placed near a single, solid boundary, a situation which occurs during the takeoff and landing of an aircraft. In this appendix a first approximation method for thin airfoils (i.e., a thin airfoil theory) will be described.

Thin airfoil theory was developed by Munk. Later contributions to the theory were made by Birnbaum, Glauert, Theodorsen, and Allen. The reader should refer, for example, to H. Glauert's, "The Elements of Aerofoil and Airscrew Theory," on which the present treatment of the thin airfoil in ground effect is based.

It will be observed that owing to the linearization of the boundary conditions adopted in thin airfoil theory, the effect of thickness and camber can be calculated separately. Indeed, if  $y_u(x)$  and  $y_l(x)$  are the ordinates of the upper and lower surfaces of an airfoil, then

$$y_u(x) = y_m(x) + y_t(x), \quad y_l(x) = y_m(x) - y_t(x),$$

where

$$y_m(x) = \frac{1}{2} [y_u(x) + y_l(x)]$$

is the mean camber line and

$$y_t(x) = \frac{1}{2} [y_u(x) - y_l(x)]$$

is one-half the local thickness.

The equation  $y = y_m(x)$  may be regarded as defining a very thin cambered airfoil, while  $y = \pm y_t(x)$  defines the upper and lower surfaces of a symmetrical airfoil. The pressure distributions around these airfoils can then be studied individually and the results superimposed to obtain the pressure

distribution about the original airfoil. In what follows only the problem of the thin cambered airfoil will be dealt with.

It is possible to derive a solution of the ground effect problem by the use of complex representation and conformal transformation methods. In this appendix another approach in which the airfoil is represented by a system of singularities is considered.

For very thin airfoils, where thickness effects are neglected, the horizontal and vertical induced velocities on the airfoil surface, according to thin airfoil theory, become

$$u(\theta) = U \left[ A_0 \cot \frac{1}{2} \theta + \sum_{n=1}^{\infty} A_n \sin n\theta \right] \quad (I.50)$$

$$v(\theta) = U \left[ A_0 + \sum_{n=1}^{\infty} A_n \cos n\theta \right] \quad (I.51)$$

where the variable  $\theta$  is related to the chordwise coordinate  $x$  by

$$x = \frac{1}{2} c(1 - \cos \theta)$$

where  $c$  is the airfoil chord. Providing the local slope of the airfoil camber line (i.e.,  $\tan^{-1}(dy_m/dx) = s(\theta)$ ) is small, the induced velocity tangential to the airfoil is also given by equation (I.50) and the normal velocity (I.51). The tangential velocity, therefore, takes equal and opposite values on the upper and lower surfaces of the airfoil. Hence, it follows that the airfoil can be replaced by a surface discontinuity in the form of a distribution of vorticity, the magnitude of which is given by

$$[u(\theta) - u(-\theta)] = 2u(\theta)$$

The complex potential due to an isolated vortex of unit strength is given by the formula

$$\Pi(z) = \frac{i}{2\pi} \log (z - z_0)$$

The corresponding velocity is

$$\omega(z) = \frac{i}{2\pi} \frac{\Gamma}{z - z_0} \quad (I.52)$$

It will be assumed that the same representation is possible for the airfoil in ground effect (i.e., two airfoils, one of which is the mirror image of the other), and, moreover, it will be assumed that the expansion (I.52) also holds for the self-induced velocity due to the vorticity distribution of the airfoil and its image. Thus, the vorticity distribution becomes

$$\gamma(\theta) = 2u(\theta) = 2U \left( A_0 \cot \frac{\theta}{2} + \sum_{n=1}^{\infty} A_n \sin n\theta \right), \quad (0 < \theta < \pi) \quad (I.53)$$

while for its image there is simply a change in sign.

The induced velocity at the point  $z_0$  of the airfoil is found by integration of equation (I.52) over the vorticity distribution of both the airfoil and its image:

$$\omega(z_0) = \frac{1}{2\pi i} \int_{ih}^{c+ih} \frac{\gamma(z)}{z_0 - z} |dz| - \frac{1}{2\pi i} \int_{-ih}^{c-ih} \frac{\gamma(z)}{z_0 - z} |dz| \quad (I.54)$$

where  $h$  is the distance of the airfoil from the ground. Separating (I.54) into real and imaginary parts, the components of the total velocity are obtained.

$$\begin{aligned} u(z_0) &= U \cos \alpha - \frac{1}{2\pi} \int_0^c \frac{\gamma(x) 2hx}{(x_0 - x)^2 + 4h^2} dx + \frac{\gamma(x)}{2\pi} \\ v(z_0) &= U \sin \alpha + \frac{1}{2\pi} \int_0^c \frac{\gamma(x)(x_0 - x)}{(x_0 - x)^2 + 4h^2} dx - \frac{1}{2\pi} \int_0^c \frac{\gamma(x) dx}{(x_0 - x)} \end{aligned} \quad (I.55)$$

The required vorticity distribution can be obtained by applying the linearized boundary condition of thin airfoil theory, namely:

$$\frac{v}{U \cos \alpha} = \frac{dy_m}{dx} = s(\theta)$$

Thus, substituting the second equation of (I.55) for  $v(z_0)$

$$\begin{aligned} U \cos \alpha s(\theta_0) = U \sin \alpha - \frac{1}{2\pi} \int_0^\pi \frac{\gamma(\theta)(\cos \theta_0 - \cos \theta)}{(\cos \theta_0 - \cos \theta)^2 + (4h/c)^2} \sin \theta d\theta \\ + \frac{1}{2\pi} \int_0^\pi \frac{\gamma(\theta)}{\cos \theta_0 - \cos \theta} \sin \theta d\theta \end{aligned} \quad (I.56)$$

Here the fact that  $x = c(1 - \cos \theta)/2$  has been used. Note that the expression for  $u(z_0)$  given in equation (I.55) becomes

$$\begin{aligned} u(\theta_0) = U \cos \alpha - \frac{1}{2\pi} \int_0^\pi \frac{\gamma(\theta)(4h/c)}{(\cos \theta_0 - \cos \theta)^2 + (4h/c)^2} \sin \theta d\theta \\ + \frac{\gamma(\theta)}{2} \end{aligned} \quad (I.57)$$

The next step involves substituting for  $\gamma$ . However, to simplify the situation, powers of  $(c/4h)^2$  greater than the first will be neglected. Then equation (I.56) becomes

$$\begin{aligned} s(\theta_0) \cos \alpha \approx \sin \alpha - \frac{1}{\pi} \left( \frac{c}{2h} \right)^2 \int_0^\pi \left( A_0 \cot \frac{\theta}{2} + \sum_{n=1}^{\infty} A_n \sin n\theta \right) \\ (\cos \theta_0 - \cos \theta) \sin \theta d\theta \\ + \frac{1}{\pi} \int_0^\pi \frac{\left( A_0 \cot \theta/2 + \sum_{n=1}^{\infty} A_n \sin n\theta \right)}{\cos \theta_0 - \cos \theta} \sin \theta d\theta \end{aligned}$$

where the A's are the coefficients in the expansion for  $\gamma$ . Using the fact that

$$\int_0^\pi \frac{\cos n\theta}{\cos \theta_0 - \cos \theta} d\theta = +\pi \frac{\sin n\theta_0}{\sin \theta_0}$$

it can be shown that

$$\begin{aligned} s(\theta_0) \cos \alpha &= \sin \alpha - \left(\frac{c}{4h}\right)^2 \left[ A_0 \left( \cos \theta_0 - \frac{1}{2} \right) + \frac{1}{2} A_1 \cos \theta_0 - \frac{1}{4} A_2 \right] \\ &\quad - A_0 + \sum_{n=1}^{\infty} A_n \cos n\theta_0 \end{aligned} \quad (I.58)$$

The coefficients A can be obtained by integration

$$\cos \alpha \frac{1}{2\pi} \int_0^{2\pi} s(\theta_0) d\theta_0 = \sin \alpha - A_0 \left[ 1 - \frac{1}{2} \left(\frac{c}{2h}\right)^2 \right] + A_2 \frac{1}{4} \left(\frac{c}{4h}\right)^2$$

$$\cos \alpha \frac{1}{\pi} \int_0^{2\pi} s(\theta_0) \cos \theta_0 d\theta_0 = A_1 - \left( A_0 - A_1 \frac{1}{2} \right) \left(\frac{c}{4h}\right)^2$$

$$\cos \alpha \frac{1}{\pi} \int_0^{2\pi} s(\theta_0) \cos n\theta_0 d\theta_0 = A_n, \quad (n \geq 2) \quad (I.59)$$

The lift and pitching moment coefficients are given by the following relations

$$\begin{aligned} c_\ell &= \frac{1}{1/2\rho U^2 c} \int_0^c \rho U \gamma(x) dx \\ &= 2\pi \left( A_0 + \frac{1}{2} A_1 \right) \end{aligned} \quad (I.60)$$

$$\begin{aligned} c_{m_{L.E.}} &= \frac{1}{1/2\rho U^2 c^2} \int_0^c \rho U \gamma(x) x dx \\ &= \frac{\pi}{4} (A_2 - A_1) - \frac{1}{4} c_\ell \end{aligned} \quad (I.61)$$

An example of the application of this approach to the two-dimensional ground effect problem is the flat-plate airfoil. In this case, from equations (I.59), (I.60), and (I.61), it can be shown that neglecting terms of  $(c/4h)^3$  and higher

$$c_l = 2\pi\alpha \left[ 1 + \frac{1}{4} \left( \frac{c}{2h} \right)^2 \right] \quad (I.62)$$

$$c_{m_{L.E.}} = -\frac{\pi\alpha}{2} \left[ 1 + \frac{3}{8} \left( \frac{c}{2h} \right)^2 \right] \quad (I.63)$$

To conclude this appendix, an expression for the perturbation velocity  $u'$  induced by the image will also be derived. Neglecting powers of  $(c/4h)^2$  greater than the first, equation (I.57) becomes

$$\begin{aligned} u'(\theta_0) &= u(\theta_0) - U \cos \alpha - \frac{\gamma(\theta)}{2} \\ &\approx -\frac{1}{2\pi} \left( \frac{c}{4h} \right) \int_0^\pi \gamma(\theta) \left[ 1 - \left( \frac{c}{4h} \right)^2 (\cos \theta_0 - \cos \theta)^2 \right] \sin \theta d\theta \\ &\approx -\frac{1}{2\pi} \frac{c}{4h} \int_0^\pi \gamma(\theta) \sin \theta d\theta \end{aligned} \quad (I.64)$$

Referring to equation (I.64), it will be noted that the integral is proportional to the lift coefficient  $c_l$ . Thus, equation (I.64) becomes

$$\frac{u'}{U}(\theta_0) = -\frac{1}{2\pi} \left( \frac{c}{4h} \right) c_l \quad (I.65)$$



## APPENDIX II

### NORMAL-WASH INFLUENCE COEFFICIENTS FOR AN ARBITRARILY ORIENTED DISCRETE HORSESHOE VORTEX

The flow induced at an arbitrary point  $P$  in space by a discrete horseshoe vortex arbitrarily oriented can be calculated quite simply by application of the Biot-Savart Law for straight line vortex filaments,

$$\vec{Q}_i = \frac{\Gamma}{4\pi h} (\cos \theta_1 + \cos \theta_2) \vec{s} \times \vec{r} \quad (\text{II.1})$$

where  $\vec{Q}_i$  is the induced velocity vector,  $\Gamma$  is the strength of the vortex filament,  $h$  is the normal distance from the vortex filament to the point  $P$ ,  $\theta_1$  and  $\theta_2$  are the angles between the vortex filament and lines joining the ends of the filament and  $P$  [see figure (II.1)],  $\vec{s}$  is a unit vector along the vortex filament, and  $\vec{r}$  is a unit vector in the plane including the filament and  $P$ . Although equation (II.1) is a simple expression, evaluation of the terms in it suitable for use in a computer program requires careful treatment of the geometric parameters. A vector approach has been adopted both here and in the computer programs associated with this work because of its simplicity. A horseshoe vortex with finite length trailing filaments is illustrated in figure (II.2). The bound segment of the horseshoe is a straight line between the points  $(x_1, y_1, z_1)$  and  $(x_2, y_2, z_2)$ , and the trailing filaments terminate at  $(x_3, y_3, z_3)$  and  $(x_4, y_4, z_4)$  for the right and left hand filaments, respectively. Choosing the point  $P$  as  $P(\xi, \eta, \zeta)$  and defining the vectors  $\vec{v}_A, \vec{v}_B, \vec{v}_C, \vec{v}_1, \vec{v}_2, \vec{v}_3$ , and  $\vec{v}_4$  as in figure (II.2), the cosine terms in equation (II.1) can be simply calculated from the vector scalar product. For the bound vortex filament;

$$\cos \theta_{1\text{bound}} = \frac{\vec{v}_2 \cdot \vec{v}_B}{|\vec{v}_2| |\vec{v}_B|} \quad \cos \theta_{2\text{bound}} = - \frac{\vec{v}_3 \cdot \vec{v}_B}{|\vec{v}_3| |\vec{v}_B|} \quad (\text{II.2})$$

for the right side trailing filament:

$$\cos \theta_{1R.\text{trail}} = \frac{\vec{v}_3 \cdot \vec{v}_c}{|\vec{v}_1| |\vec{v}_c|} \quad \cos \theta_{2R.\text{trail}} = - \frac{\vec{v}_4 \cdot \vec{v}_c}{|\vec{v}_4| |\vec{v}_c|} \quad (\text{II.3})$$

and for the lift trailing filament:

$$\cos \theta_{1L.\text{trail}} = \frac{\vec{v}_2 \cdot \vec{v}_A}{|\vec{v}_2| |\vec{v}_A|} \quad \cos \theta_{2L.\text{trail}} = - \frac{\vec{v}_1 \cdot \vec{v}_A}{|\vec{v}_1| |\vec{v}_A|} \quad (\text{II.4})$$

The normals from P to each of the vortex filaments can be easily calculated from the vector cross product. Referring to figure (II.2), it can be seen that

$$h_{\text{bound}} = \frac{|\vec{v}_2 \times \vec{v}_3|}{|\vec{v}_B|} \quad (\text{II.5})$$

$$h_{R.\text{trail}} = \frac{|\vec{v}_3 \times \vec{v}_4|}{|\vec{v}_c|} \quad (\text{II.6})$$

$$h_{L.\text{trail}} = \frac{|\vec{v}_2 \times \vec{v}_1|}{|\vec{v}_A|} \quad (\text{II.7})$$

It is now necessary to calculate the direction of  $\vec{Q}_i$  for each of the three vortex filaments comprising the horseshoe. Let  $\vec{n}$  be a unit normal in the direction of the  $\vec{s} \times \vec{r}$  term of equation (II.1). It can be seen from figure (II.2), therefore, that

$$\vec{n}_{\text{bound}} = \frac{\vec{v}_B \times \vec{v}_2}{|\vec{v}_B \times \vec{v}_2|} \quad (\text{II.8})$$

$$\vec{n}_{T.\text{right}} = \frac{\vec{v}_c \times \vec{v}_3}{|\vec{v}_c \times \vec{v}_3|} \quad (\text{II.9})$$

$$\vec{n}_{T.\text{left}} = \frac{\vec{v}_A \times \vec{v}_2}{|\vec{v}_A \times \vec{v}_2|} \quad (\text{II.10})$$

In summary, equation (II.1), the Biot-Savart Law for straight line vortex filaments, is evaluated for the bound vortex using equations (II.2), (II.5), and (II.8); for the right trailing vortex using equations (II.3), (II.6), and (II.9); and for the left trailing vortex using equations (II.4), (II.7), and (II.10).

### APPENDIX III

#### NEUMANN SOLUTION FOR THE POTENTIAL FLOW ABOUT A TWO-DIMENSIONAL BODY

Development of general methods for calculating the incompressible potential flow about arbitrary bodies has been an area of considerable research at the Douglas Aircraft Company (references 62 and 63) for many years. The method reviewed here utilizes a source density distribution on the surface of an arbitrary two-dimensional body and computes the distribution as the solution of a Fredholm integral equation of the second kind. The problem solved here is known as the Neumann problem since it is the Neumann boundary condition, that is, the normal derivative on the boundary, that is specified. The two-dimensional solution presented here is an exact potential flow solution in the sense that any degree of numerical accuracy desired can be obtained.

The irrotational flow of an incompressible, inviscid fluid satisfies Laplace's equation

$$\nabla^2 \phi = 0 \quad (\text{III.1})$$

where  $\phi$  is the perturbation velocity potential, subject to the Neumann boundary condition

$$(\vec{\nabla}\phi + \vec{U}_\infty) \cdot \vec{n} = 0$$

or

$$\frac{\partial \phi}{\partial n} = -\vec{U}_\infty \cdot \vec{n} \quad (\text{III.2})$$

and the condition at infinity that

$$\vec{\nabla}\phi|_\infty \rightarrow 0 \quad (\text{III.3})$$

Although in two-dimensional flow there are analytical solutions to the problem defined by (III.1), (III.2), and (III.3) which are obtained both by the

method of separation of variables and by conformal mapping, a numerical solution to the problem is desirable so that arbitrary body shapes in arbitrary potential onset flow fields can be treated.

The solution discussed here reduces the problem to an integral equation for the source density distribution on the body surface. Consider a unit point source located at the point  $(y_q, z_q)$  in figure(III.1). At the point  $(y_p, z_p)$  the velocity potential due to this source is then

$$\phi = \frac{1}{r(p,q)} \quad (III.4)$$

where  $r(p,q)$  is the distance between  $(y_p, z_p)$  and  $(y_q, z_q)$

$$r(p,q) = \sqrt{(y_p - y_q)^2 + (z_p - z_q)^2} \quad (III.5)$$

Thus, the potential at the point  $p$  due to a continuous distribution of source  $\sigma(y,z)$  on the boundary  $S$  of the body is

$$\phi(x_p, y_p) = \int_S \frac{\sigma(s)}{r(p,s)} ds \quad (III.6)$$

In order to apply the boundary conditions, equations (III.2) and (III.3), it is necessary to take the normal derivative of equation (III.6), but owing to the singular nature of the integral at the point  $p$  care must be taken in the differentiation of the integrand. Although the details are omitted here, it has been shown (reference 63) that combining the boundary conditions and equation (III.6) yields a Fredholm integral equation of the second kind of the form

$$2\pi\sigma(p) - \int_S \frac{\partial}{\partial n} \left[ \frac{1}{r(p,s)} \right] \sigma(s) ds = - \vec{U}_\infty \cdot \vec{n}(p) \quad (III.7)$$

This integral equation can be approximated by a set of linear algebraic equations. The boundary  $S$  about which the flow is computed is approximated by a large number of straight line surface elements [figure(II.1)] whose size is small compared to that of the body. Over each surface element the value of the source strength is assumed to be constant. Thus,  $\sigma$  can be removed from

the integral in equation (III.7) and the integral can be evaluated from the known body geometry on each element. The boundary condition can only be satisfied at one point on each element since there is only one unknown for each element. The resulting set of linear equations for  $\sigma$  can be expressed by

$$\sum_j A_{ij} \sigma_j = B_i \quad (\text{III.8})$$

where  $A_{ij}$  is the coefficient matrix which consists of the normal velocity induced by the  $j^{\text{th}}$  element on the  $i^{\text{th}}$  element for a source density of unity.  $B_i$  is the right side matrix and is essentially  $-\vec{U}_\infty \cdot \vec{n}_i$ .

The body is approximated by a large number of straight line surface elements as shown in figure (III.1). It is necessary to determine the velocity induced by one of these source line elements at some arbitrary point  $(y,z)$  in space. Referring to figure (III.2), the velocity induced at  $(y,z)$  parallel to the source line element is

$$\frac{v}{U_\infty}(y,z) = \frac{\sigma}{2\pi} \int_{\xi_1}^{\xi_2} \frac{\cos \theta}{r} d\xi \quad (\text{III.9})$$

and the velocity induced normal to the source line element is

$$\frac{w}{U_\infty}(y,z) = \frac{\sigma}{2\pi} \int_{\xi_1}^{\xi_2} \frac{\sin \theta}{r} d\xi \quad (\text{III.10})$$

where  $\xi$  is a dummy variable along the source element,  $r$  is the distance between a point on the element and  $(y,z)$ , and  $\theta$  is the angle between  $r$  and  $y$ . From figure (III.2),

$$r^2 = (y-\xi)^2 + z^2$$

$$\sin \theta = \frac{z}{r}, \cos \theta = \frac{y-\xi}{r}$$

Substituting these expressions into (III.9) and (III.10) and integrating yields

$$\frac{v}{U_\infty}(y,z) = \frac{\sigma}{2\pi} \int_{\ell_1}^{\ell_2} \frac{(y-\xi)}{z^2+(y-\xi)^2} d\xi = \frac{\sigma}{2\pi} \ln \frac{r_1}{r_2} \quad (\text{III.11})$$

and

$$\frac{w}{U_\infty}(y,z) = \frac{\sigma}{2\pi} \int_{\ell_1}^{\ell_2} \frac{z}{z^2+(y-\xi)^2} d\xi = \frac{\sigma}{2\pi} (\theta_2 - \theta_1) = \frac{\sigma}{2\pi} \theta_3 \quad (\text{III.12})$$

where

$$\begin{aligned} r_1 &= \sqrt{(\ell_1 - y)^2 + z^2} \\ r_2 &= \sqrt{(\ell_2 - y)^2 + z^2} \\ \theta_3 &= \cos^{-1} \left[ \frac{r_1^2 + r_2^2 - (\ell_2 - \ell_1)^2}{2r_1 r_2} \right] \end{aligned}$$

Finally, transforming (III.11) and (III.12) to the (Y,Z) coordinate system,

$$\begin{aligned} (A_{ij})_V &= \frac{1}{2\pi} \left[ \ln \frac{r_1}{r_2} \cos \beta_j - \theta_3 \sin \beta_j \right] \\ (A_{ij})_W &= \frac{1}{2\pi} \left[ \ln \frac{r_1}{r_2} \sin \beta_j + \theta_3 \cos \beta_j \right] \end{aligned} \quad (\text{III.13})$$

Considering now the right hand side of (III.8), it can be seen from figure (III.1) that

$$\vec{n} = \sin \beta_j \vec{j} - \cos \beta_j \vec{k} \quad (\text{III.14})$$

Finally the freestream velocity can be written as

$$\vec{U}_\infty = V_\infty \vec{j} + W_\infty \vec{k} \quad (\text{III.15})$$

so the final matrix equation is

$$\sum_j \left[ (A_{ij})_V \sin \beta_j - (A_{ij})_W \cos \beta_j \right] \sigma_j = W_\infty \cos \beta_j - V_\infty \sin \beta_j \quad (\text{III.16})$$

Equations (III.16) can easily be solved for the source strengths  $\sigma_j$  by standard matrix solution techniques on a digital computer. Once the source strengths have been determined it is necessary to calculate the velocities tangential to the surface of the body so that the pressure distribution and aerodynamic quantities can be computed. The total velocity on the  $i^{\text{th}}$  element of the body surface is simply

$$V_i \vec{j} + W_i \vec{k} = \left[ \sum_j (A_{ij})_V \sigma_j + V_\infty \right] \vec{j} + \left[ \sum_j (A_{ij})_W \sigma_j + W_\infty \right] \vec{k} \quad (\text{III.17})$$

where  $\sigma_j$  is now known. The tangential velocity is then

$$V_{T_i} = V_i \cos \beta_i + W_i \sin \beta_i \quad (\text{III.18})$$

and the pressure distribution on the body can be determined by application of Bernoulli's equation.



## APPENDIX IV

### GENERAL REMARKS — HALF SPAN WIND TUNNEL TESTING

There are several advantages associated with the use of half models. For example, a larger scale of model is permissible. Also, model manufacturing costs are considerably reduced, and the problems of model support, method of air supply for powered lift systems, and instrumentation are all greatly simplified. A disadvantage is that the model cannot be yawed, so that one is restricted to the evaluation of longitudinal aerodynamics. A more serious problem, however, is that associated with the selection of the location of a reflection plane or the size and location of an end plate. One arrangement often adopted involves the use of the tunnel floor as a reflection plane. Alternatively, a false wall or floor can be inserted in the tunnel or the model can be mounted on an end-plate. In either case, care has to be taken to ensure that the reflection-plane or end-plate boundary-layer does not significantly influence the aerodynamics of the model under investigation. This could be achieved either by using boundary layer control (e.g., suction or blowing) or a fuselage provided its thickness is at least an order of magnitude greater than the boundary layer displacement thickness. If a reflection plane is to be inserted in the tunnel, care must also be taken to ensure a uniform velocity field on the model side of the reflection plane. This requires that careful consideration be given to minimizing and/or correcting for the blockage on the two sides of the plane.

A thorough investigation of reflection plane or end plates in relation to high-lift circulation controlled models has not so far been made. Limited comparative high-lift jet flap experiments on a half-model and a similar complete model have not, however, always shown good agreement. In part, it might be argued that, in addition to the reasons mentioned earlier, some of the discrepancy could be attributed to the uncertainty of the validity of wind tunnel wall corrections applied and, in the case of half-model end plates, the classical correction\* made to wing aspect ratio because of the finite size of the plate.

\* Mangler, W.: Die Auftriebsverteilung am Tragflügel mit Endscheiben. Luftfahrtforschung, Vol. 14, p. 564, 1937.

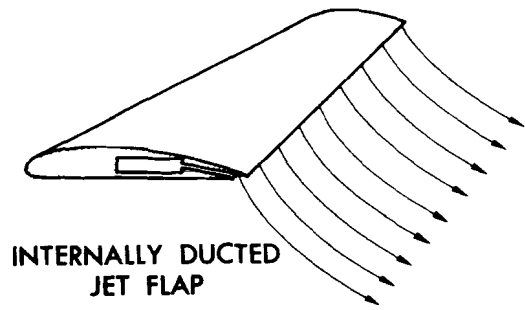
As mentioned earlier, the results published by Das<sup>37</sup> represent, at this time, the major source of fundamental test information for the validation of jet-flap analytical methods. Having adopted a half-model testing technique with an end plate of restricted dimensions, Das has computed the effective aspect ratio of the wings tested. It is not completely clear from the available translations of Das' work what corrections might also have been made for wind tunnel open jet boundary constraints, although it is suggested that the test data was corrected for lift interference effects. Since Das' experimental data has been used extensively in the validation of the EVD Jet-Wing Lifting Surface Theory, it is pertinent to ask here whether the accuracy of the finally corrected data is satisfactory.

There have been several recommendations on the size of end plates acceptable for jet flap models. For example, it has been suggested that the end plate should at least extend 1-1/2 chords upstream of the leading edge, 4 chords downstream of the trailing edge, 1-1/2 chords above the wing, and 3 chords below the wing. There is no reason to believe, however, that because the end plate used by Das does not satisfy this criteria that serious errors will be introduced. Providing a satisfactory method is available for correcting for the finite size of the plate, there would be no misgivings in this regard. Unfortunately, available methods, at least those with which the authors are familiar, do not address the end plate correction problem of arbitrary half-model jet-wings. Nor is it likely that such corrections could be expressed simply as a correction to the geometric aspect ratio of the wing. It is interesting to note here the magnitude of the classical corrections applied by Das, namely:

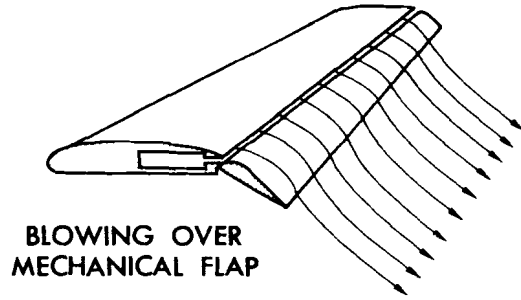
Aspect Ratio	
Geometric	Effective
3.0	2.75
4.0	3.50
5.0	4.50

and that these corrections are simply a function of the height of the end plate and the semi-span of the wing. These corrections are equivalent to a change in circulation lift or drag of up to 10%. A study recently initiated

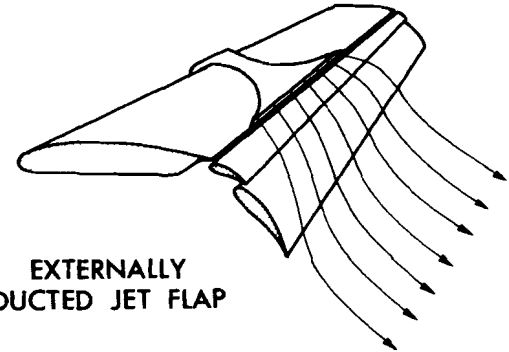
by the authors has, to date, provided some results that indicate that these corrections might be as much as 50% in error. In addition, as might well be expected, the finite end plate effects on wing spanwise and chordwise loading cannot be explained in terms of a simple correction to wing aspect ratio.



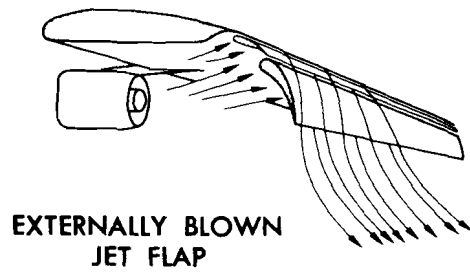
INTERNALLY DUCTED  
JET FLAP



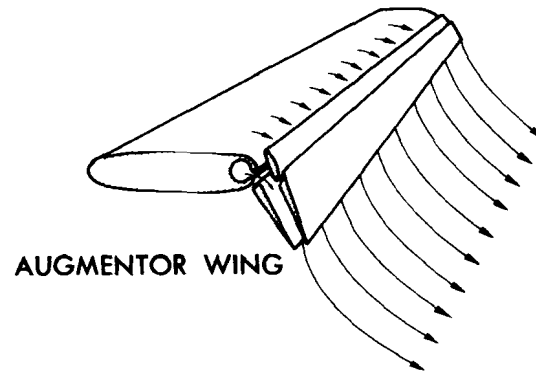
BLOWING OVER  
MECHANICAL FLAP



EXTERNALLY  
DUCTED JET FLAP

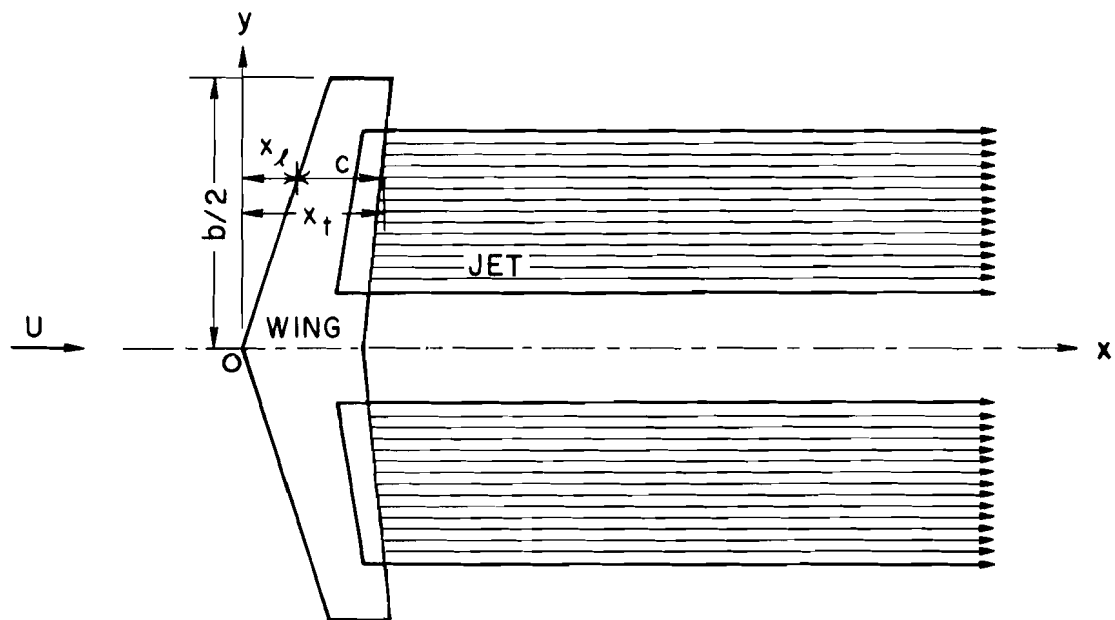


EXTERNALLY BLOWN  
JET FLAP

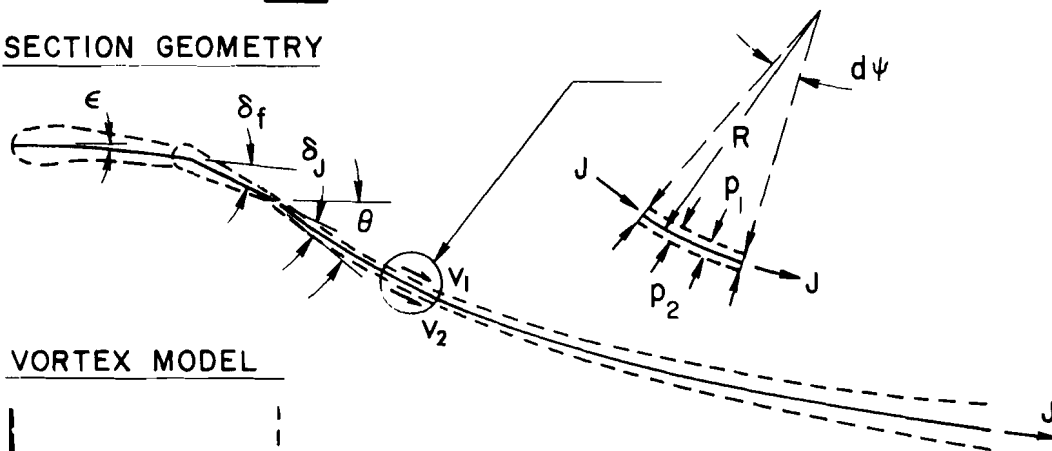


AUGMENTOR WING

Figure (2.1). Various Jet-Flap Schemes



**SECTION GEOMETRY**



**VORTEX MODEL**

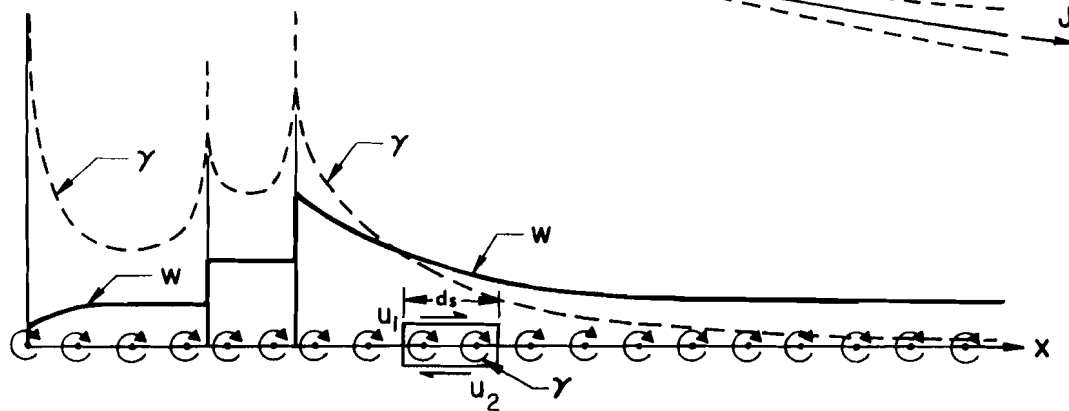
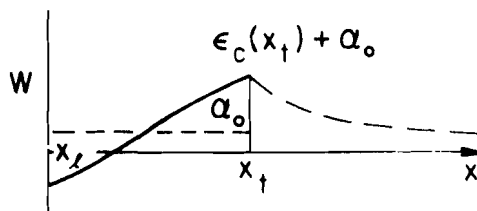
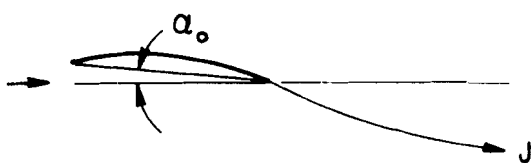
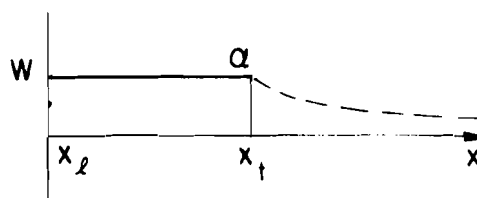
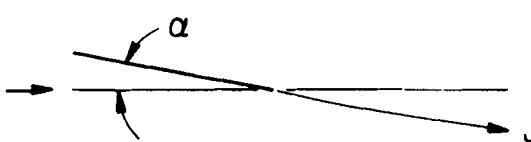


Figure (2.2). Theoretical Model of a Basic Jet-Wing System

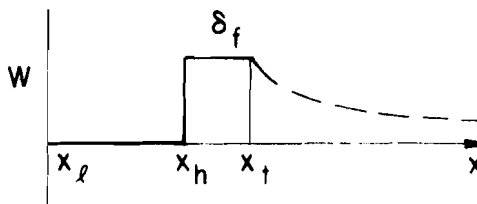
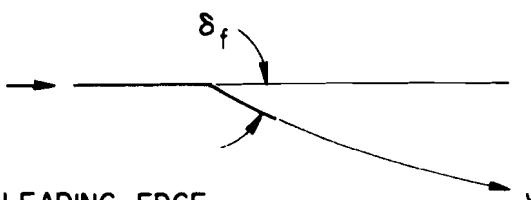
CAMBER & TWIST



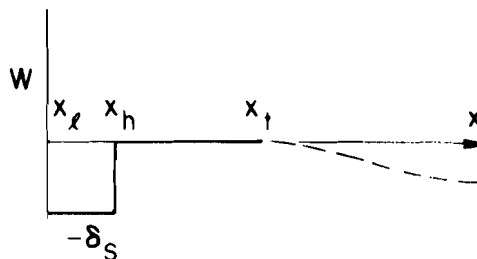
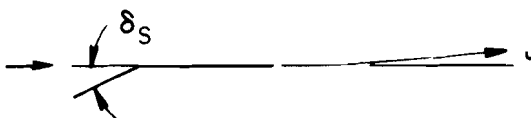
ANGLE OF ATTACK



FLAP DEFLECTION



LEADING EDGE FLAP DEFLECTION



JET DEFLECTION

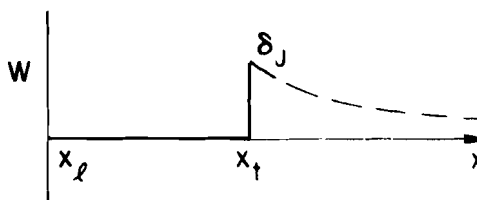
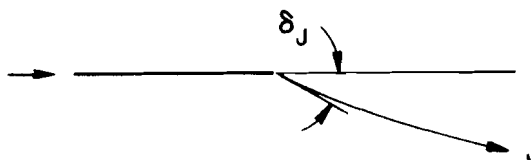


Figure (2.3). Jet-Wing Fundamental Cases

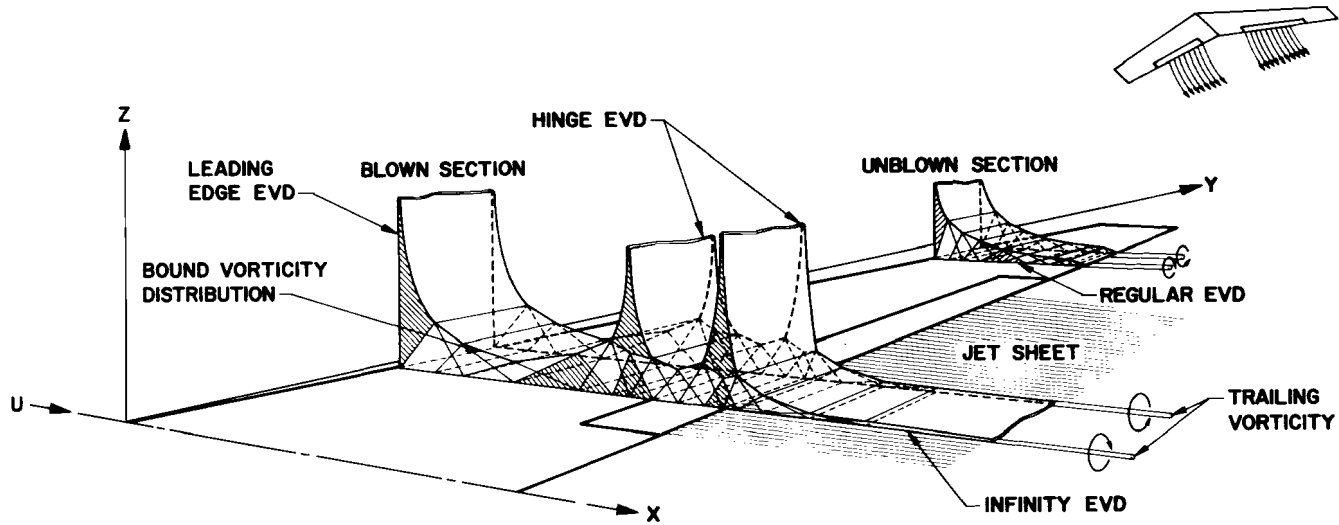


Figure (2.4a). Illustration of the EVD Jet-Wing Method

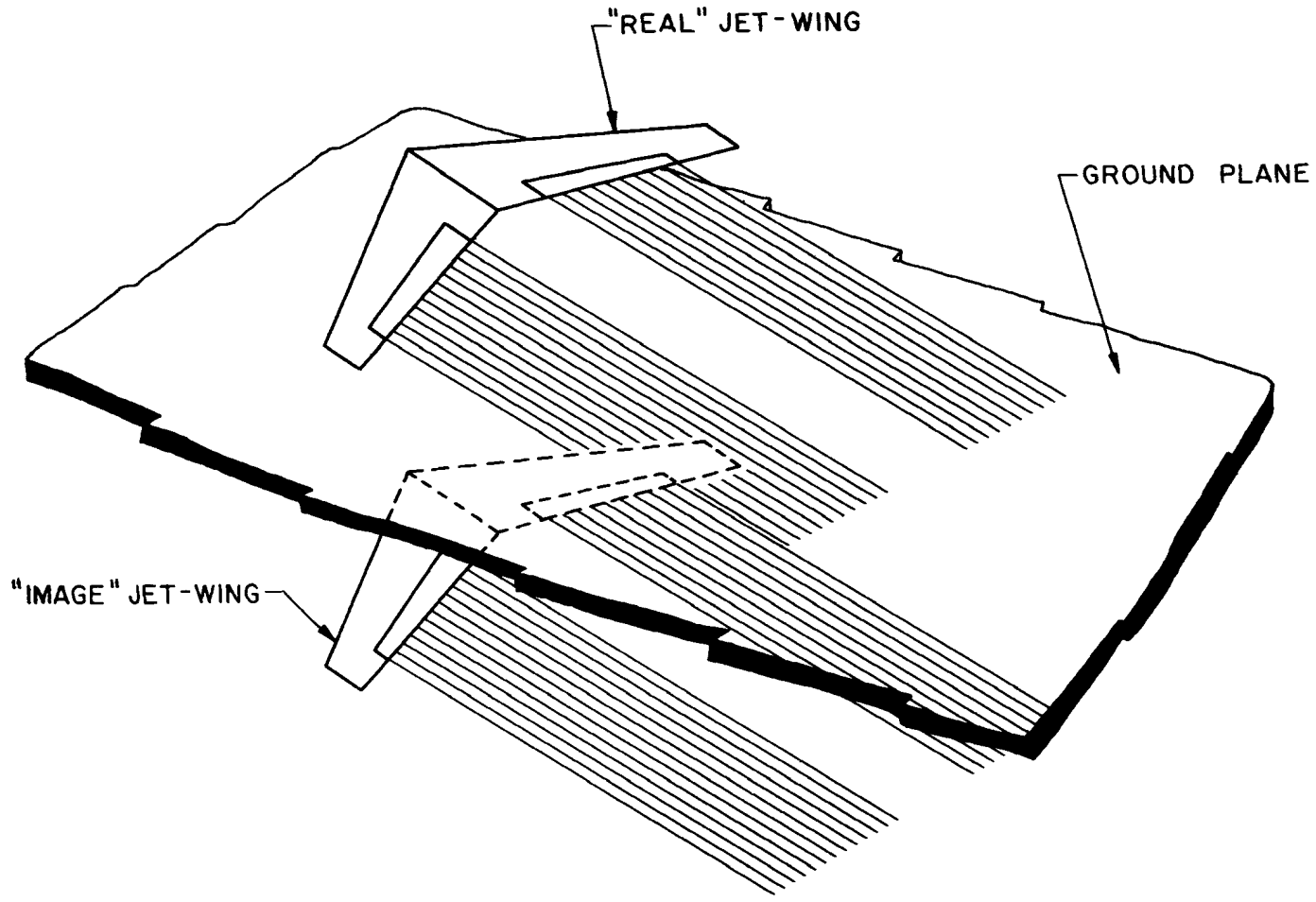


Figure (2.4b). Illustration of the EVD Jet-Wing Ground Effect Method



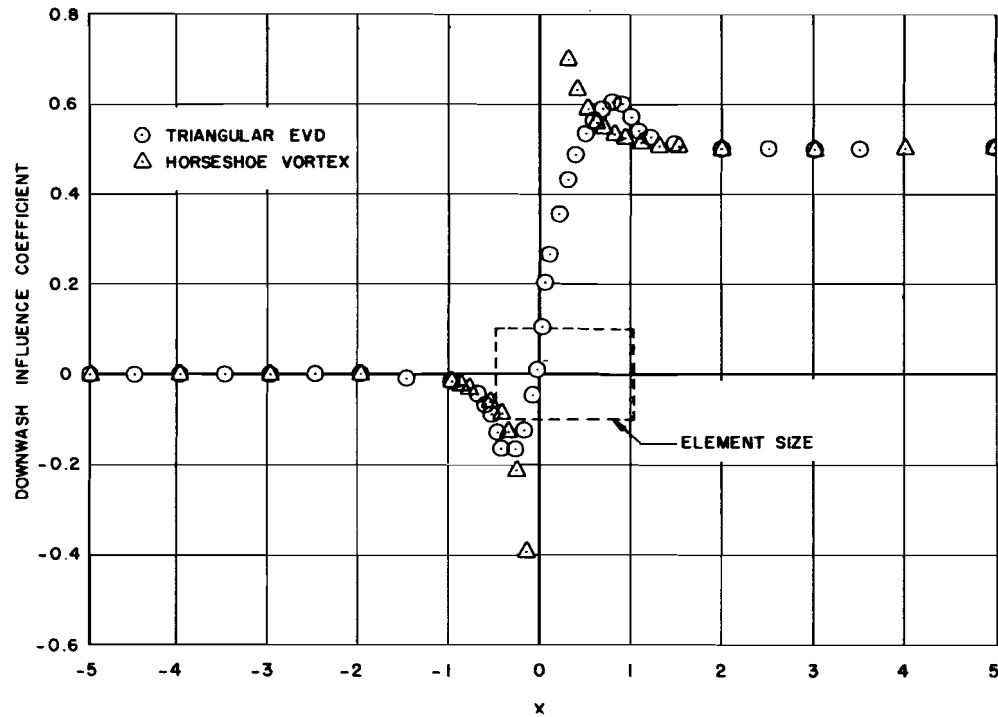


Figure (2.5). Comparison Between Downwash Induced by a Triangular EVD and by a Discrete Horseshoe Vortex of the Same Total Strength

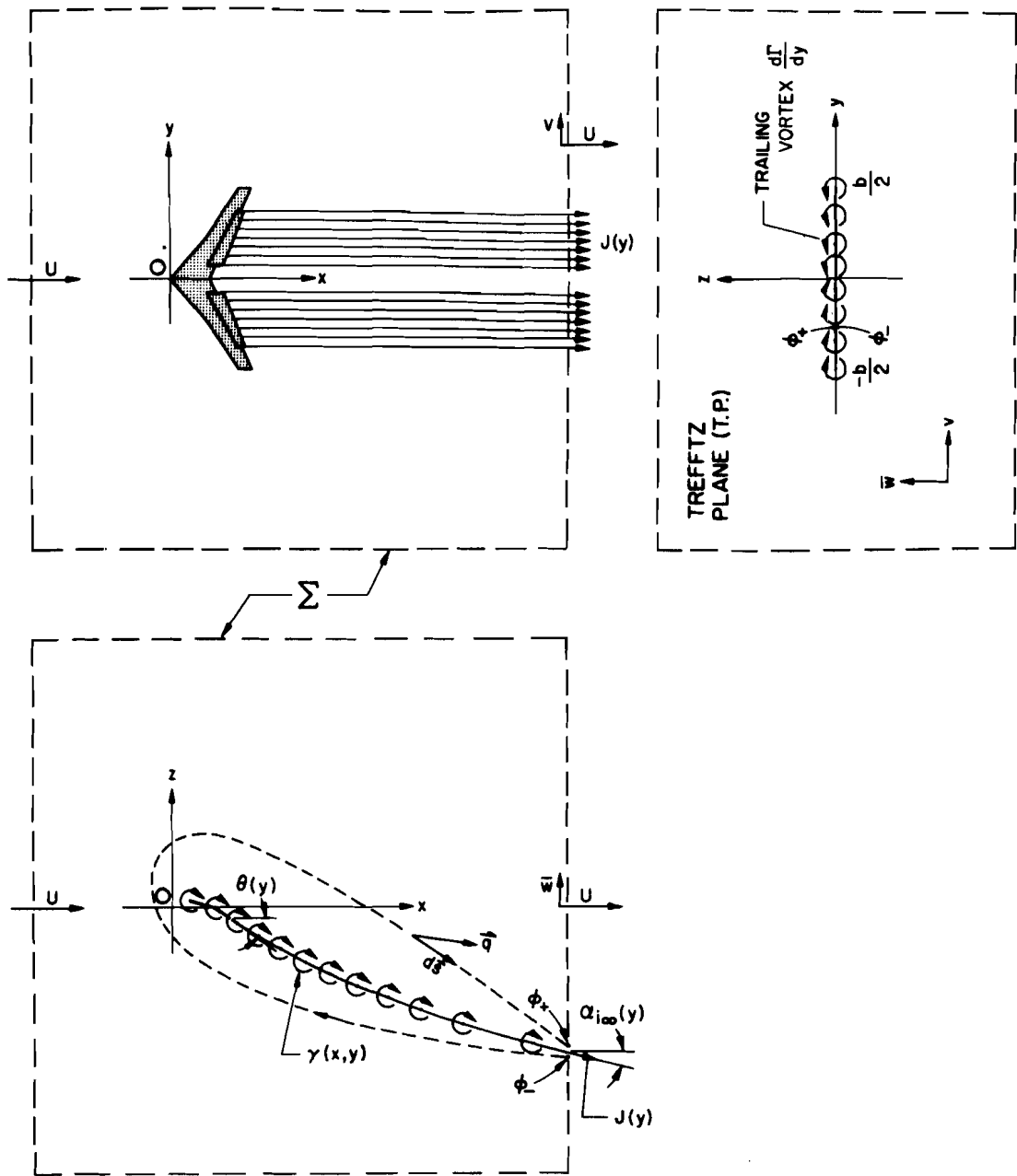


Figure (2.6). Illustration of the Jet-Wing Momentum Analysis

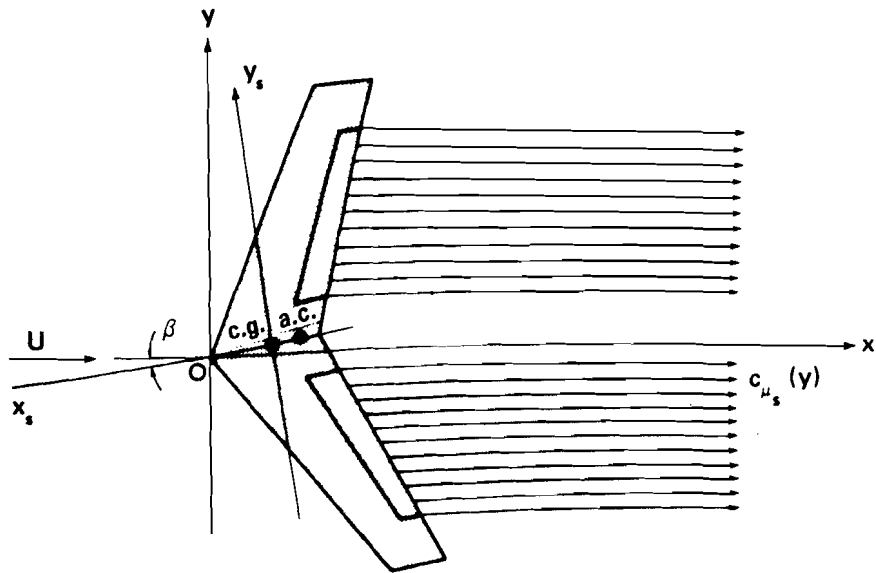


Figure (2.7a) Jet-Wing in Sideslip

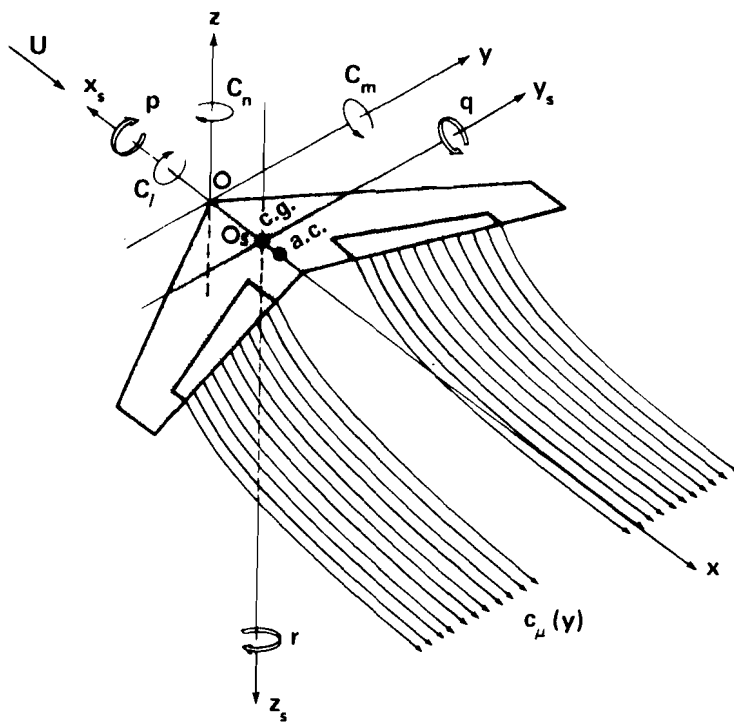


Figure (2.7b). Stability Axes for Jet-Wing

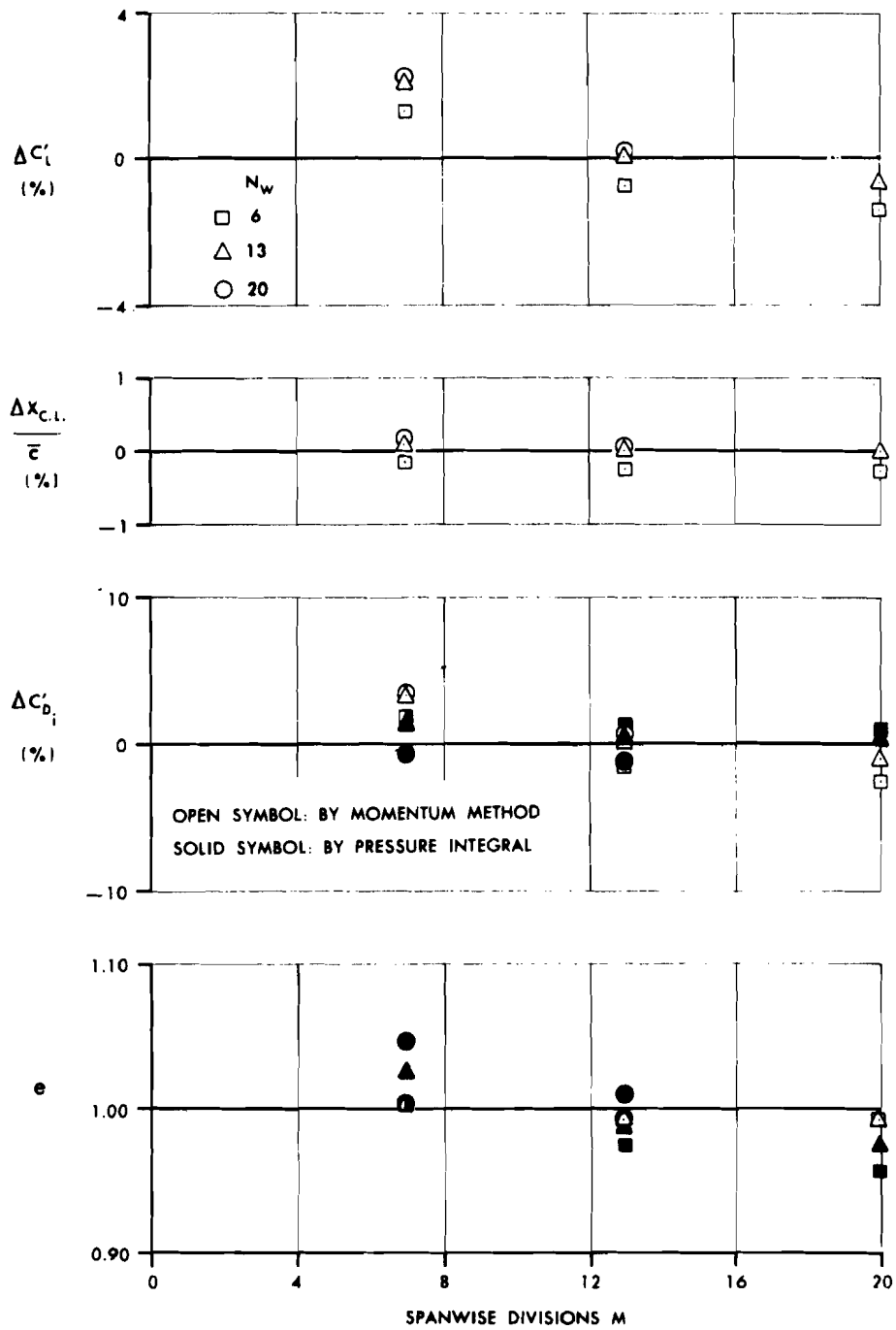


Figure (2.8). Effect of the EVD Element Spacing on the Aerodynamic Characteristics of a Rectangular Wing of Aspect Ratio 4.5

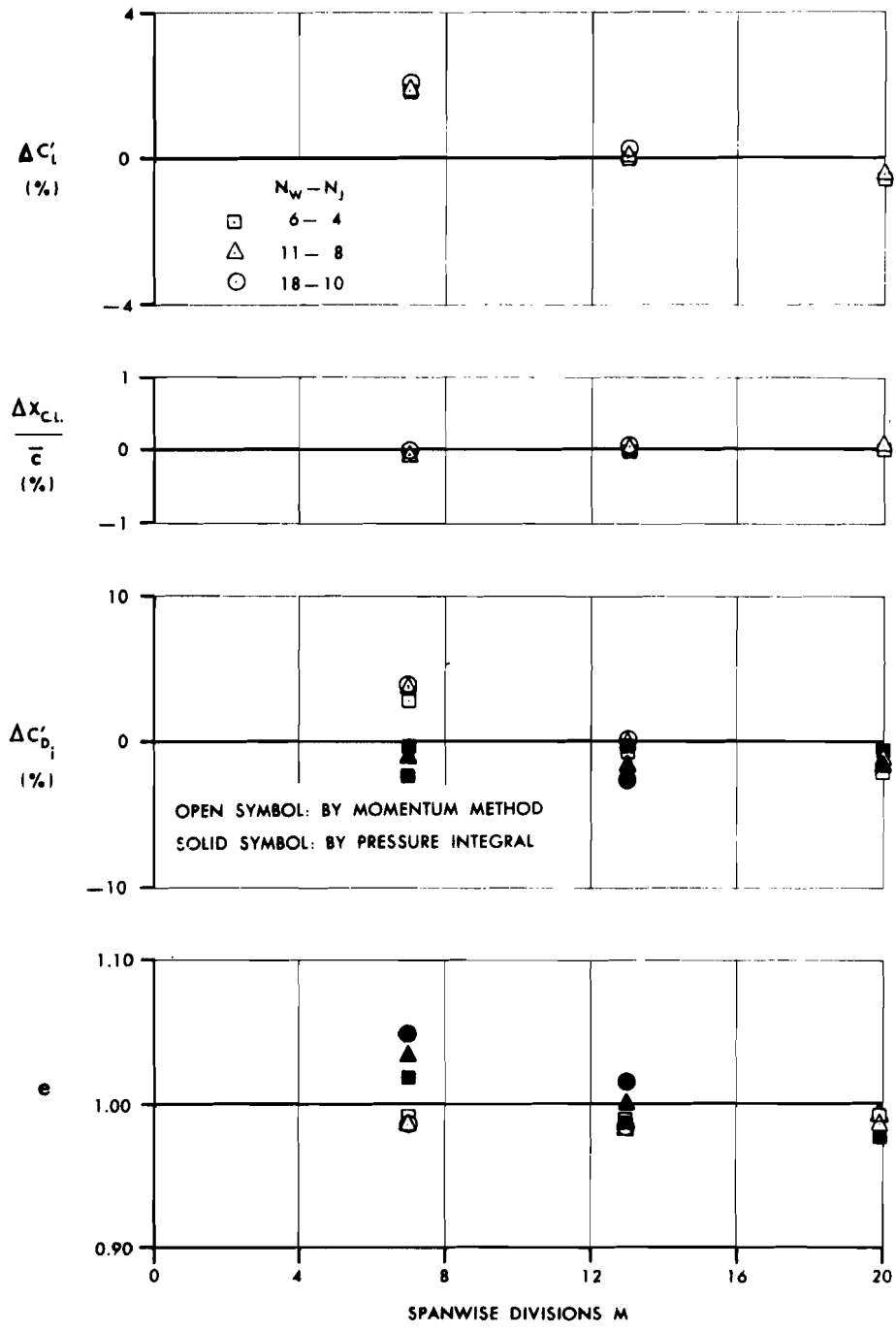


Figure (2.9). Effect of the EVD Element Spacing on the Aerodynamic Characteristics of a Rectangular Jet-Wing of Aspect Ratio 4.5 with Uniform Full-Span Blowing (Angle of Attack Case).

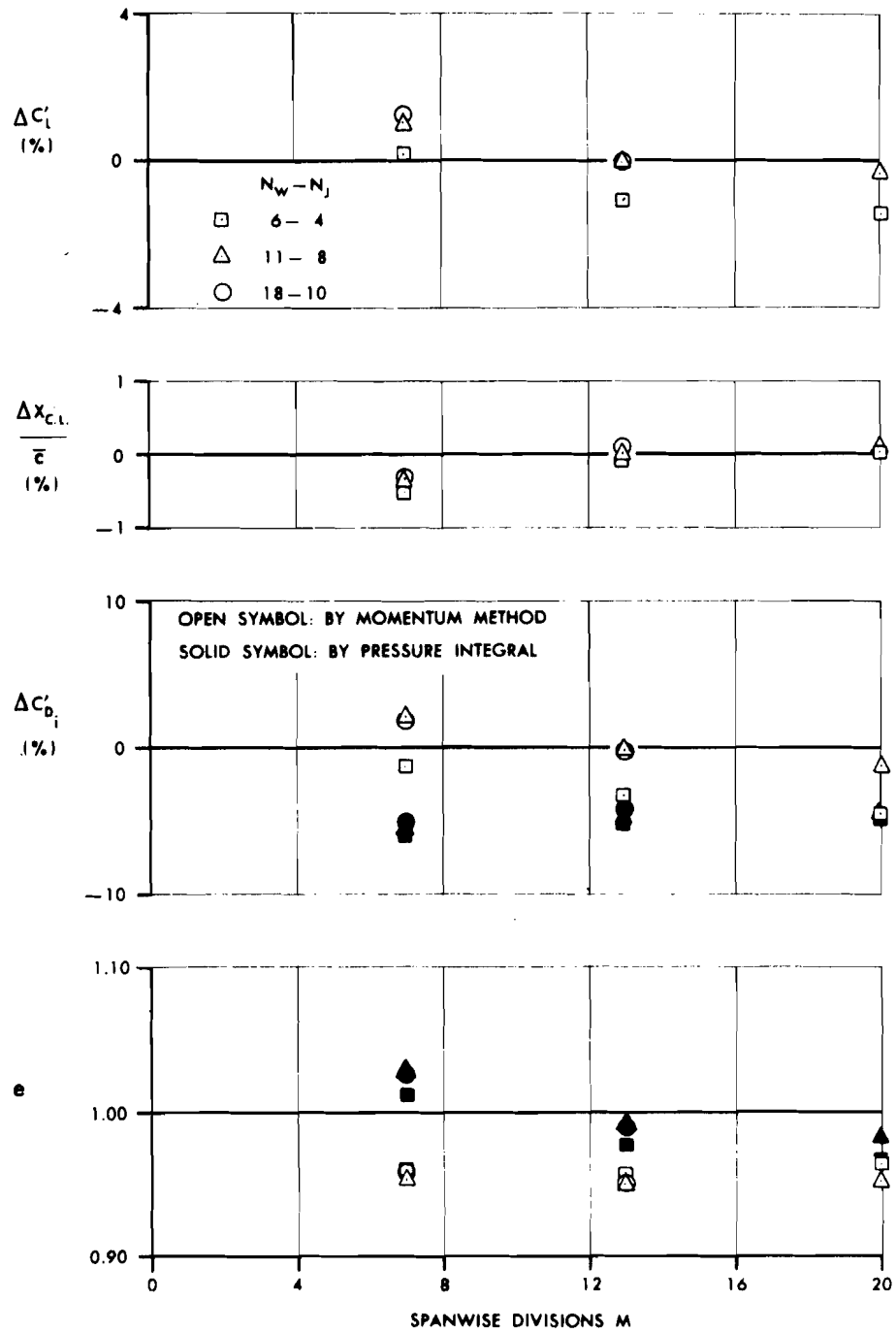


Figure (2.10). Effect of the EVD Element Spacing on the Aerodynamic Characteristics of a Rectangular Jet-Wing of Aspect Ratio 4.5 with Uniform Full-Span Blowing (Jet Deflection Case).

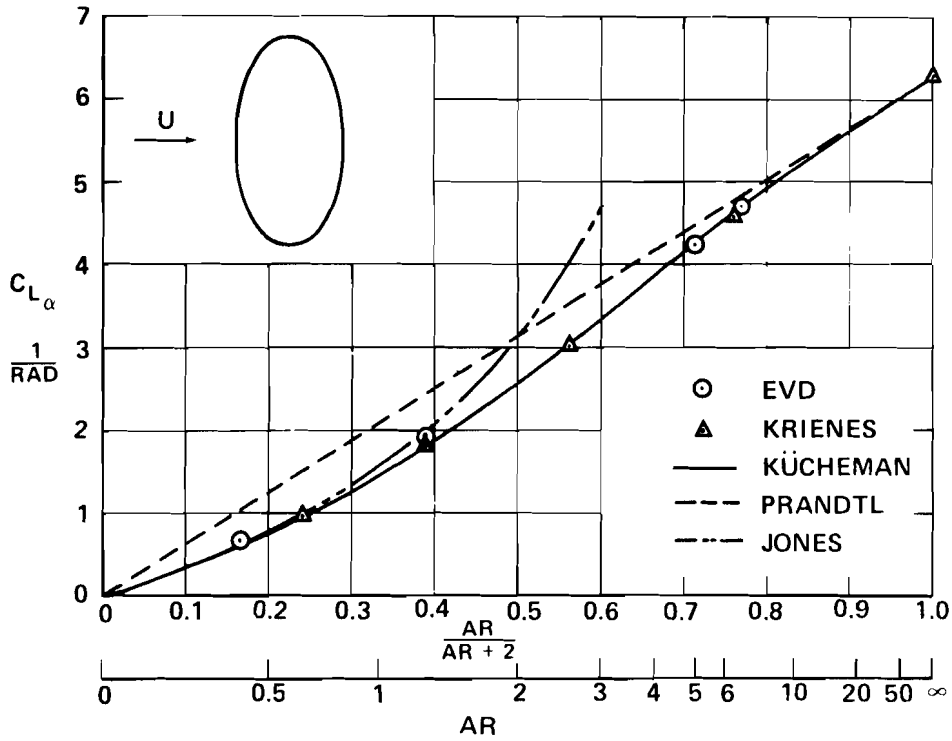


Figure (2.11). Lift Curve Slope of Elliptical Wings - Comparison of Results from Various Theoretical Methods

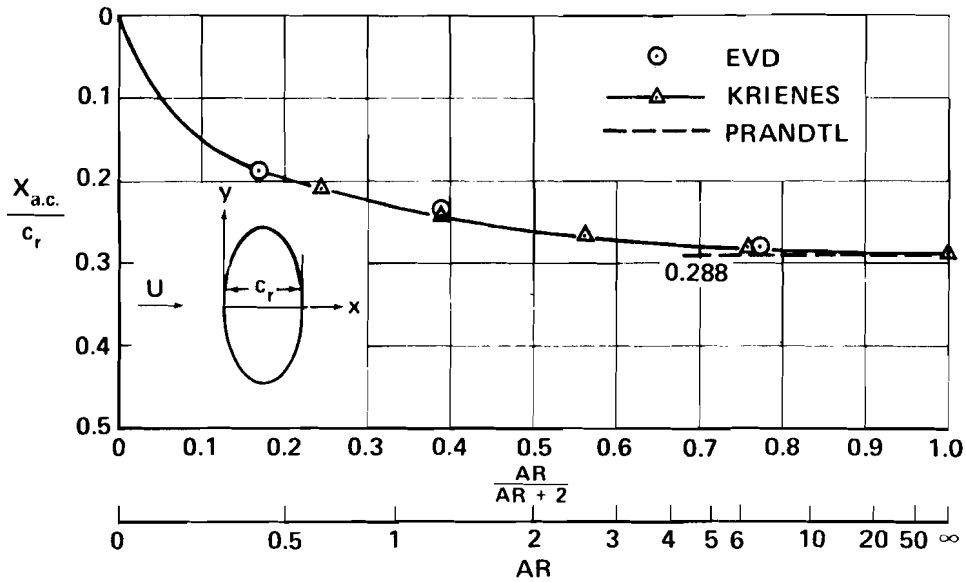


Figure (2.12). Aerodynamic Center of Elliptical Wings - Comparison of Results from Various Theoretical Methods

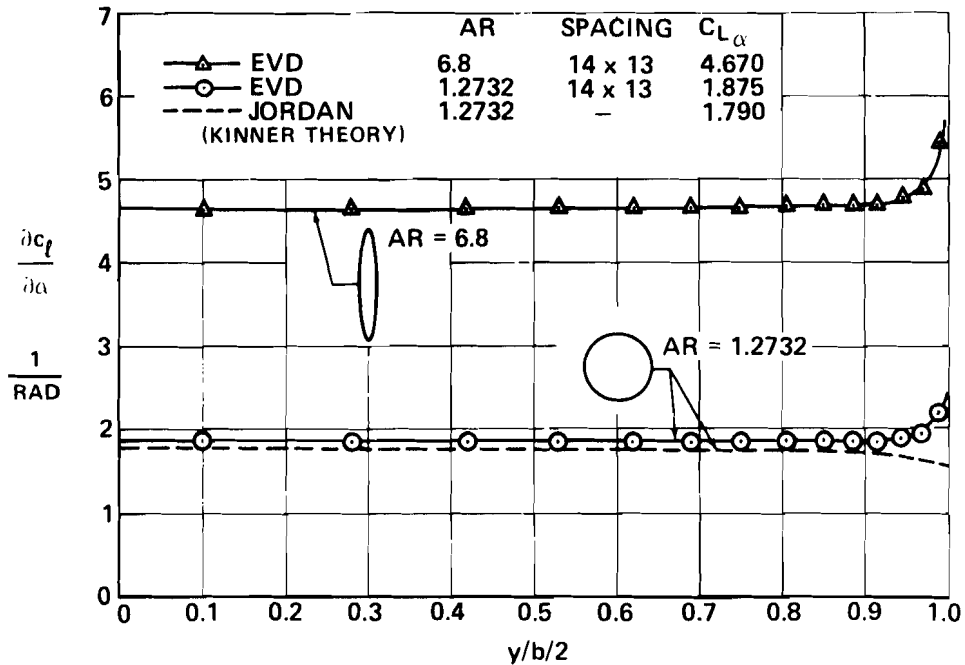


Figure (2.13). Comparison of the Spanwise Variation of Theoretical Sectional Lift Curve Slope for Elliptical Wings

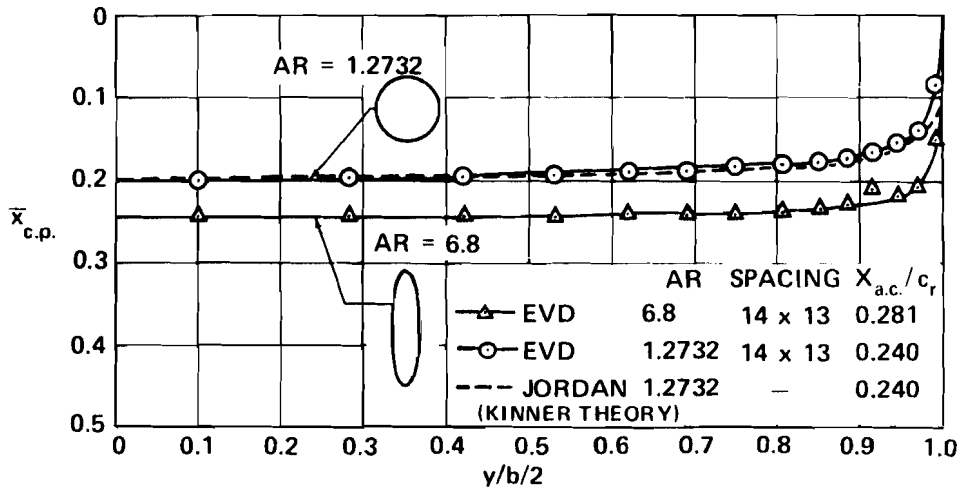


Figure (2.14). Comparison of the Spanwise Variation of Theoretical Sectional Center of Pressure for Elliptical Wings



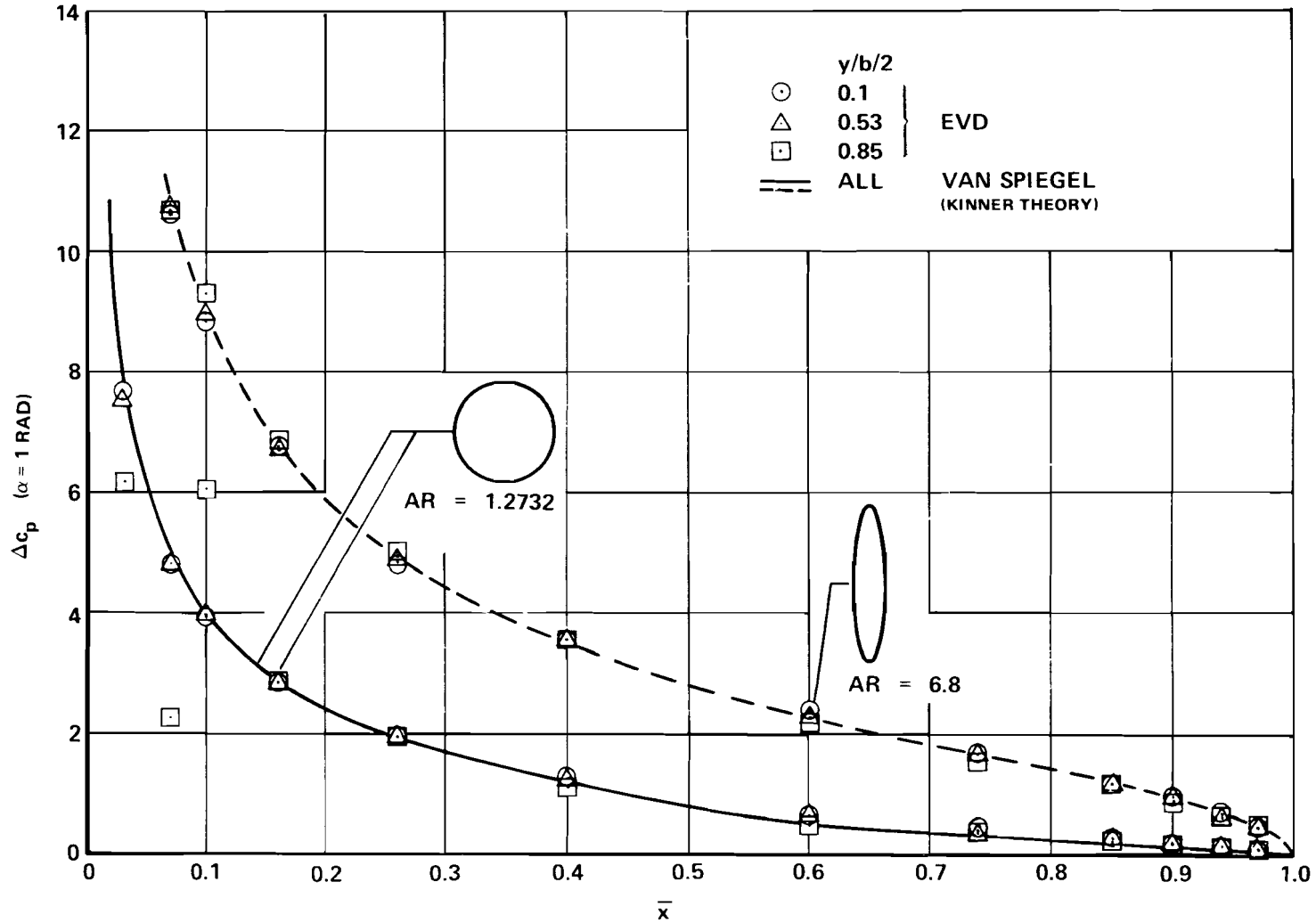


Figure (2.15). Comparison of the Theoretical Chordwise Loading Distributions for Elliptical Wings

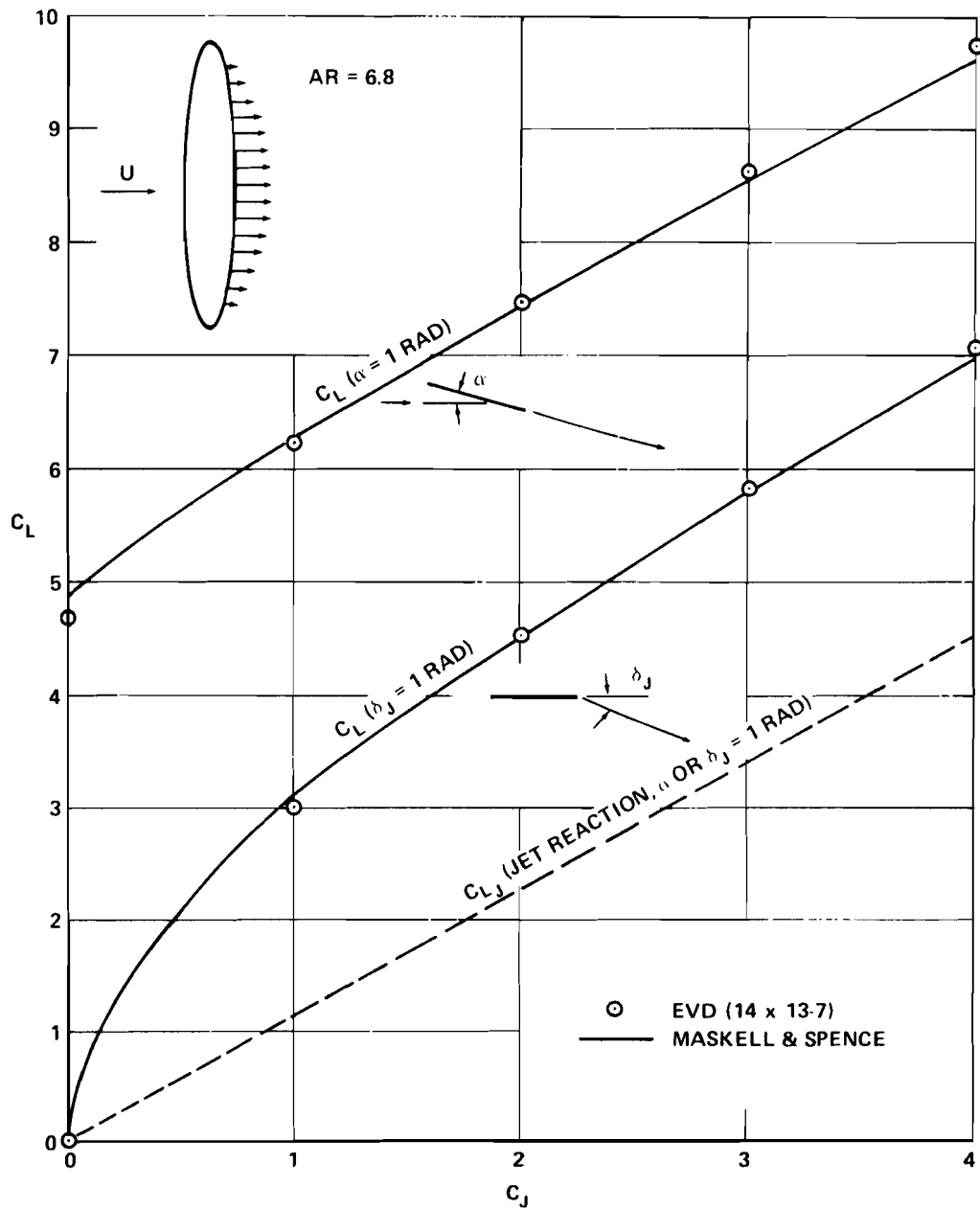


Figure (2.16). The Effect of Jet Momentum on the Lift of an Elliptical Jet-Wing of Aspect Ratio 6.8 - Comparison of Theoretical Results ( $c_{\mu}(y) = \text{constant}$ )

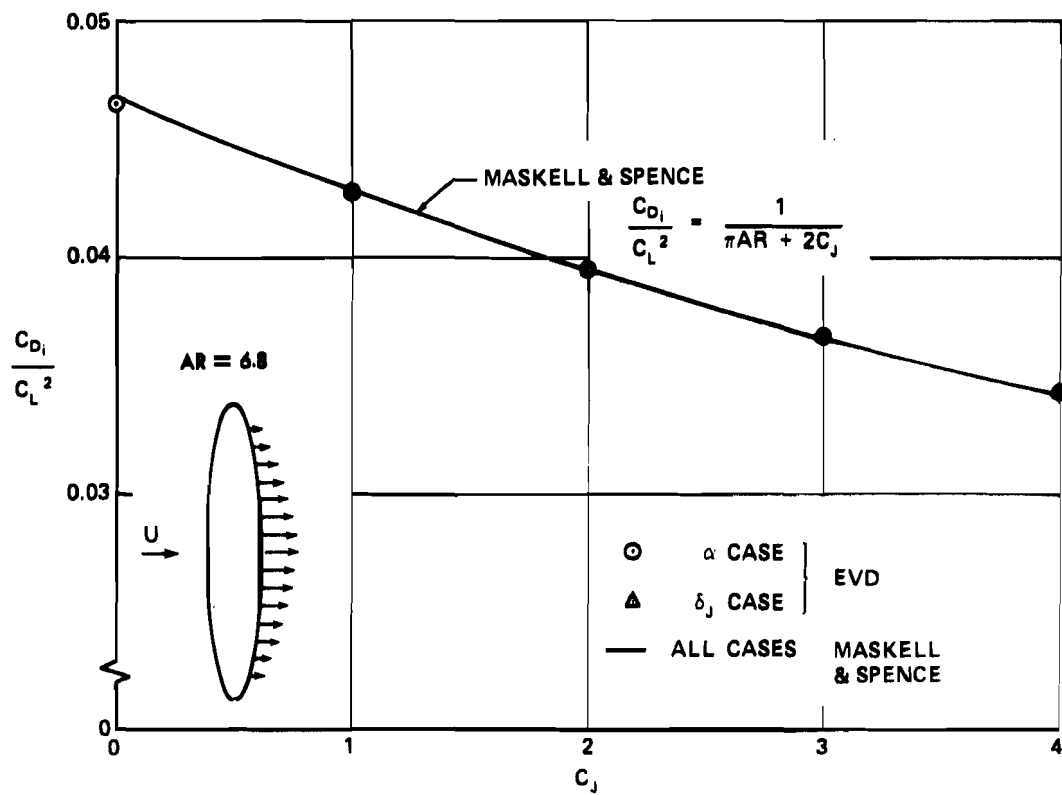


Figure (2.17). The Effect of Jet Momentum on the Induced Drag of an Elliptical Jet-Wing ( $c_u(y)$  - constant)

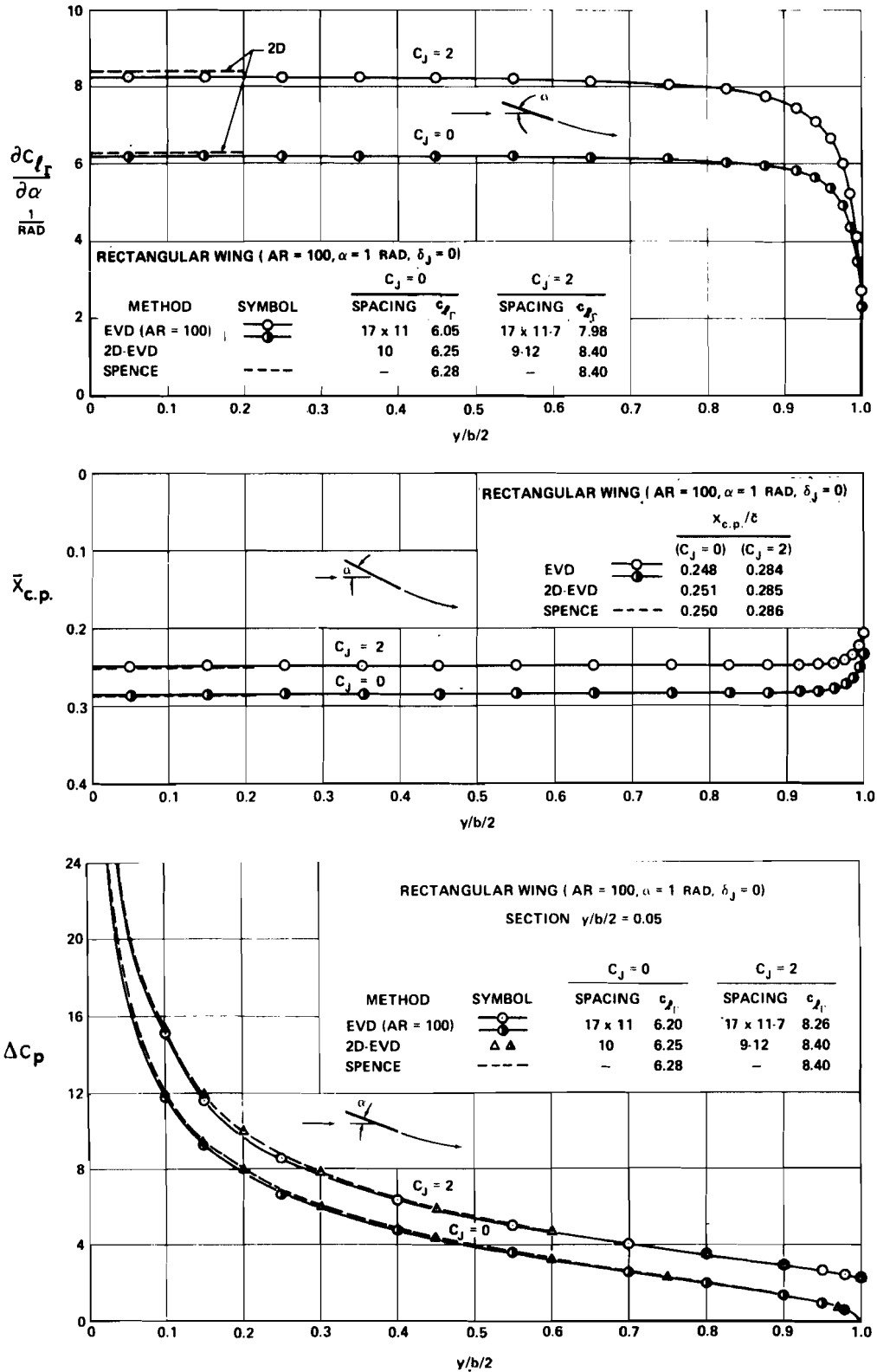


Figure (2.18). Comparison of the EVD Theoretical Aerodynamic Characteristics for a Large Aspect Ratio Wing (AR = 100) with 2-D Analytical Results ( $\alpha = 1.0$  rad.,  $\delta_J = 0$ ).

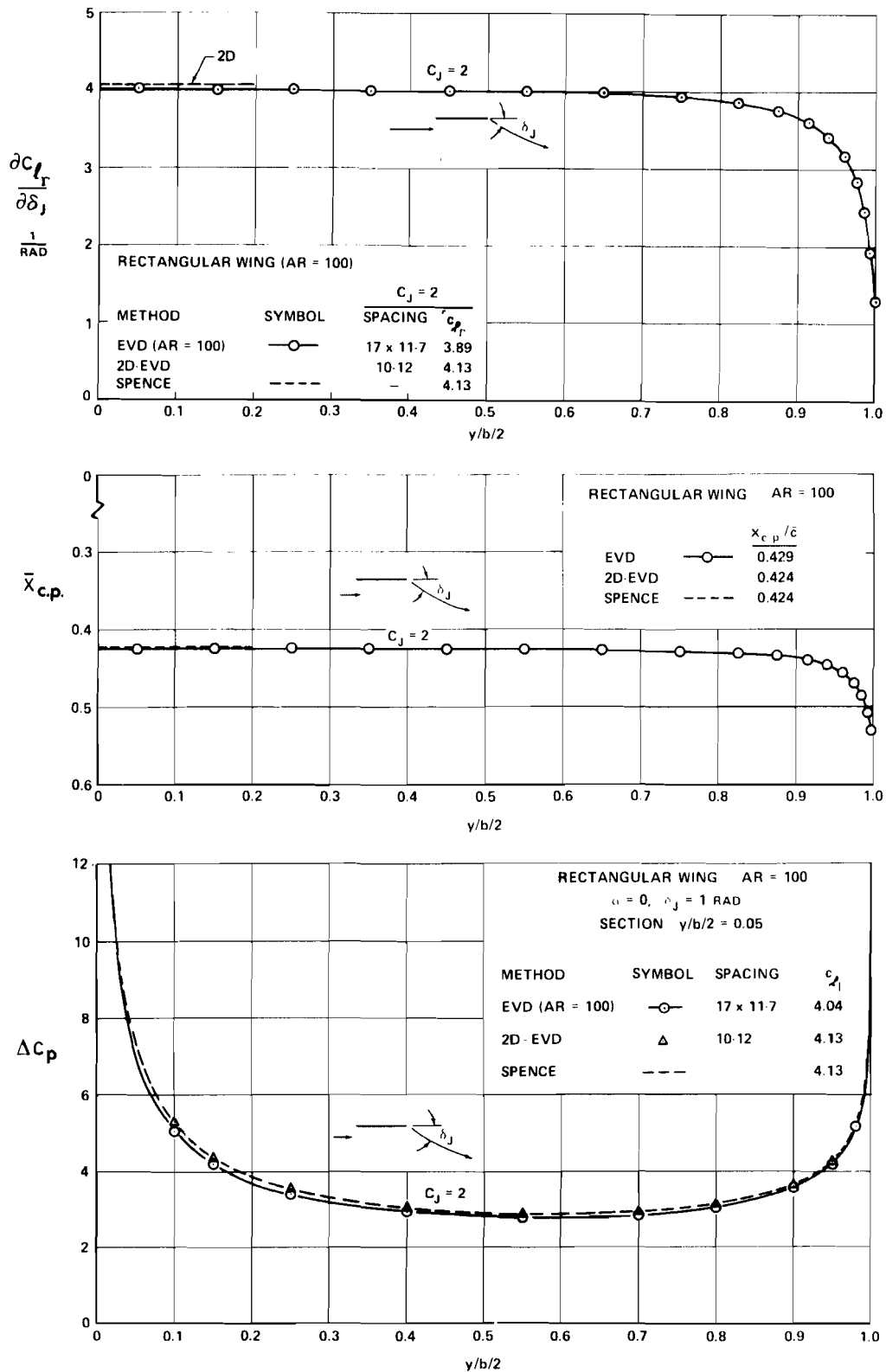


Figure (2.19). Comparison of the EVD Theoretical Aerodynamic Characteristics for a Large Aspect Ratio Wing (AR = 100) with 2-D Analytical Results ( $\alpha = 0, \delta_J = 1.0 \text{ rad.}$ )

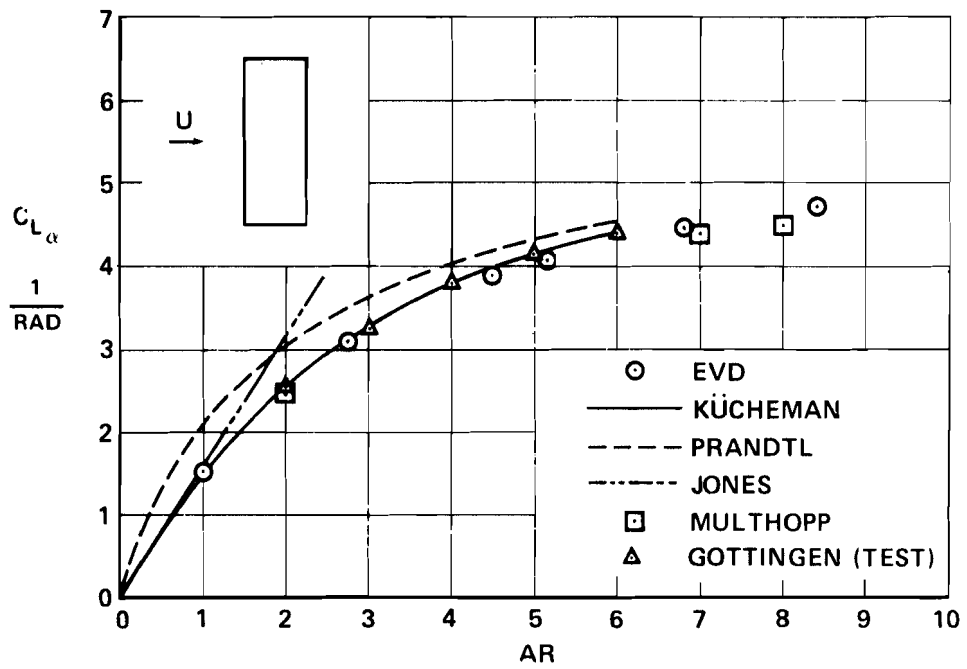


Figure (2.20). The Lift Curve Slope of Rectangular Wings ( $C_J = 0$ ) - Comparison of the EVD Method with Other Theories and Experiment

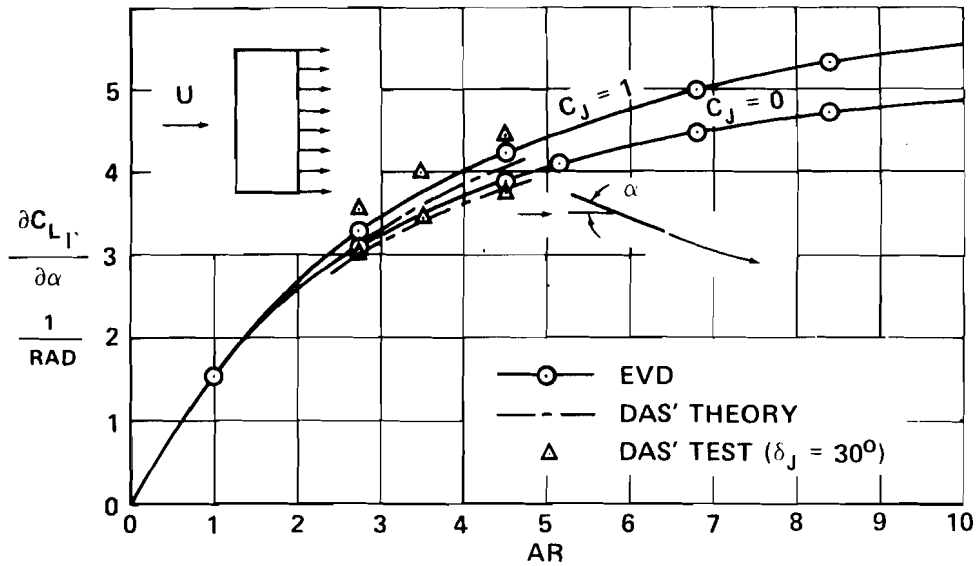


Figure (2.21). Lift of Rectangular Wings with Uniform Full-Span Blowing - Comparison Between Theory and Experiment.  $\partial C_{L_T} / \partial \alpha$  versus AR.

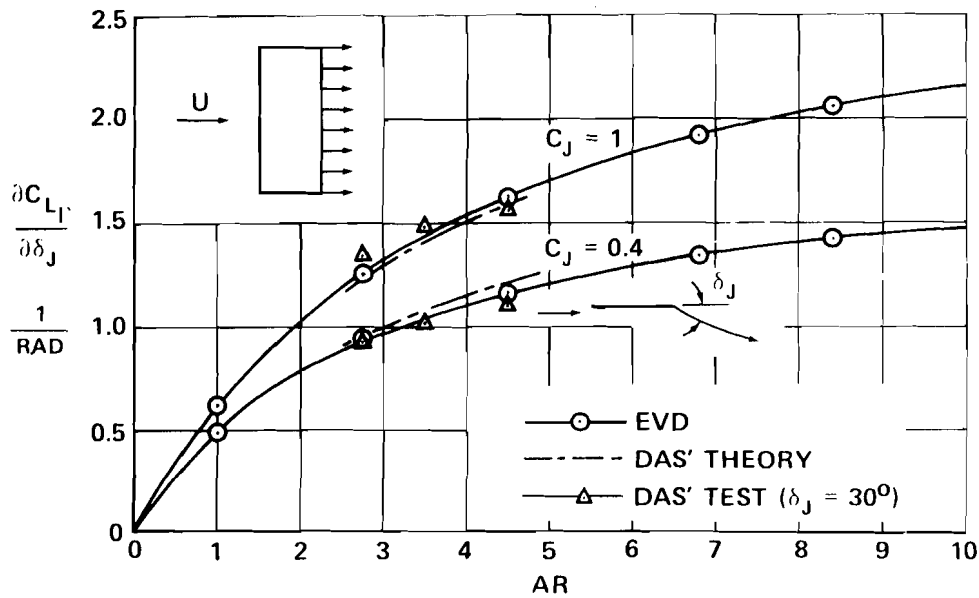


Figure (2.22). Lift of Rectangular Wings with Uniform Full-Span Blowing - Comparison Between Theory and Experiment.  $\partial C_{L_T} / \partial \delta_J$  versus AR

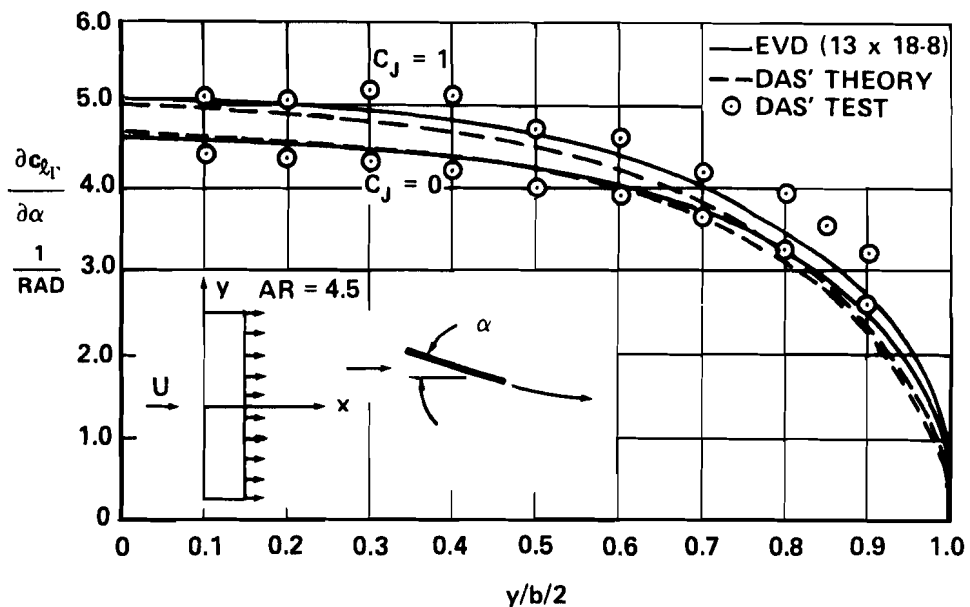


Figure (2.23). Spanwise Variation of Sectional Lift Curve Slope of a Rectangular Wing (AR = 4.5) with Uniform Full-Span Blowing - Comparison Between Theory and Experiment

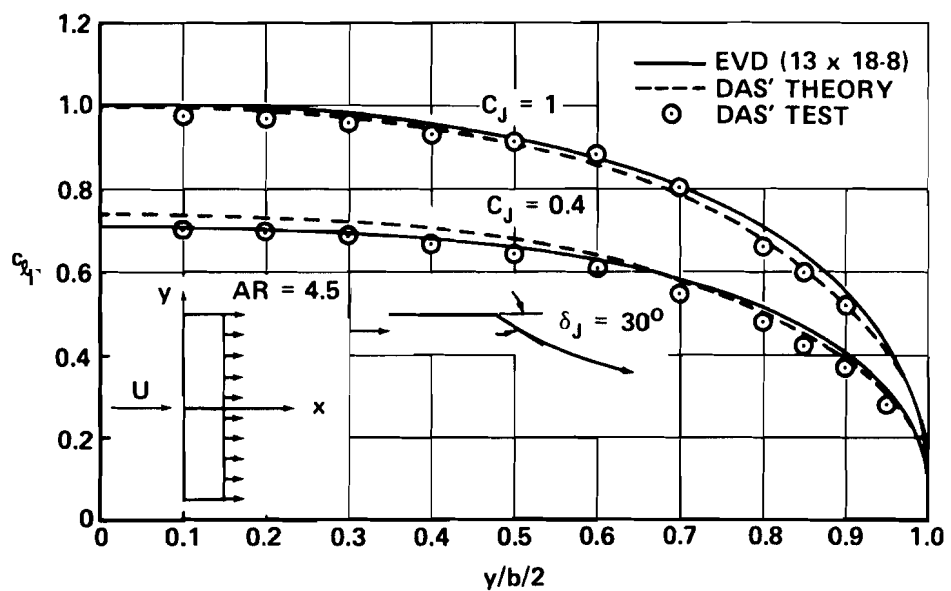


Figure (2.24). Spanwise Variation of Sectional Lift of a Rectangular Wing (AR = 4.5) with a Uniform Full-Span Jet Deflected at  $30^\circ$  - Comparison Between Theory and Experiment



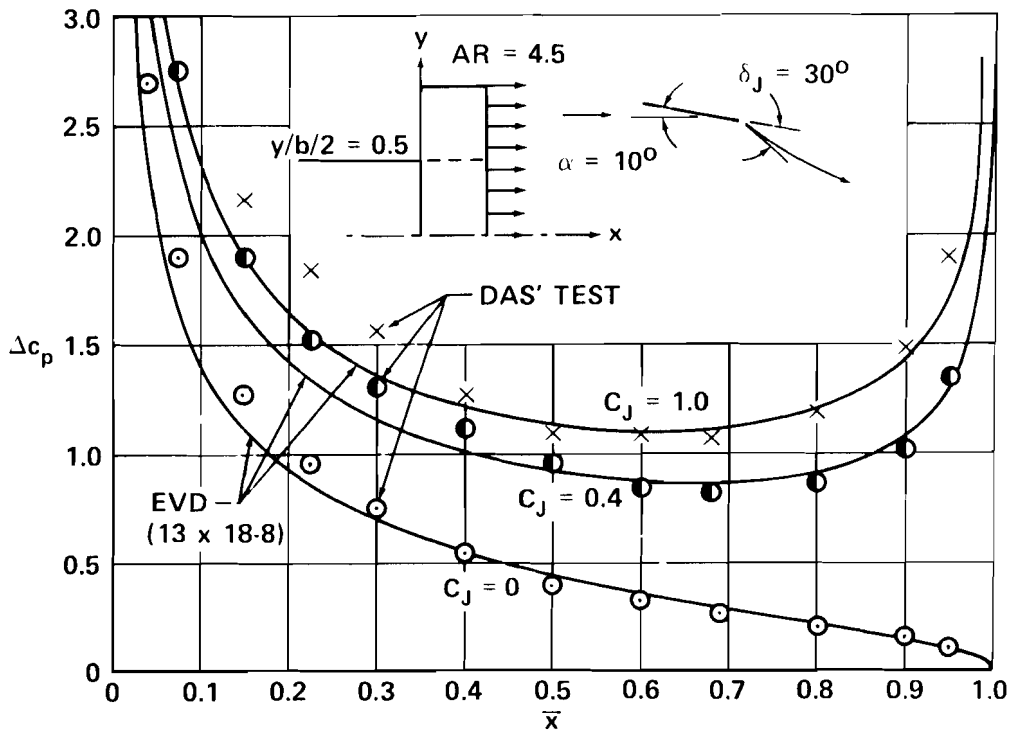
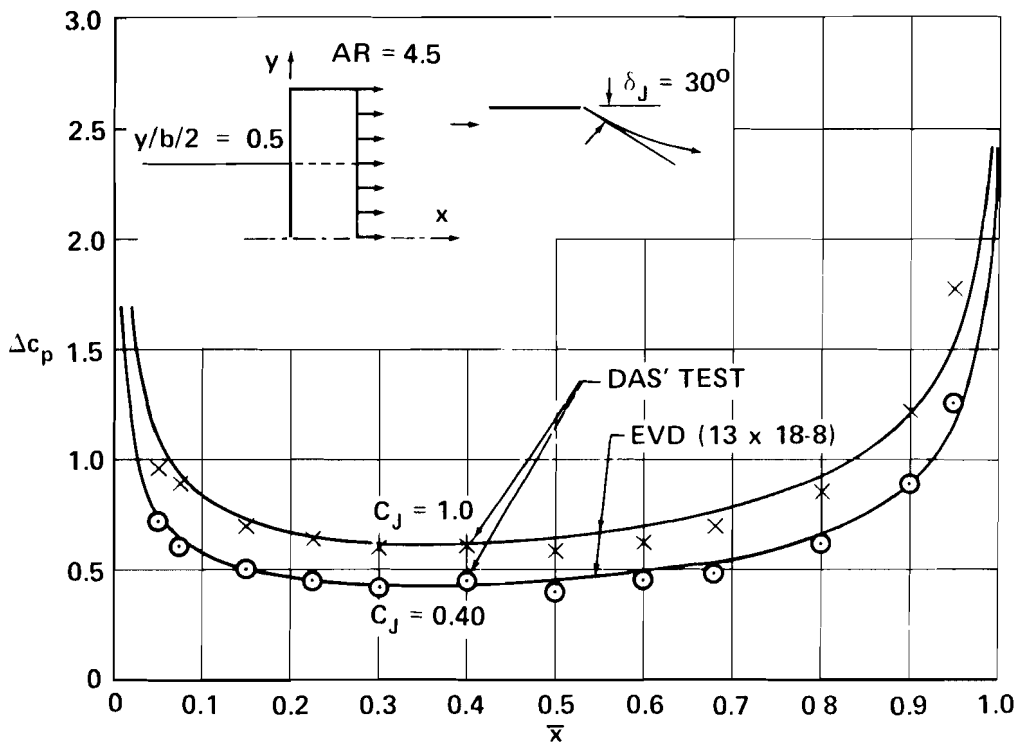


Figure (2.25). Comparison of the EVD Theory with Experimental Results for Chordwise Loading of a Rectangular Wing with Uniform Full-Span Blowing

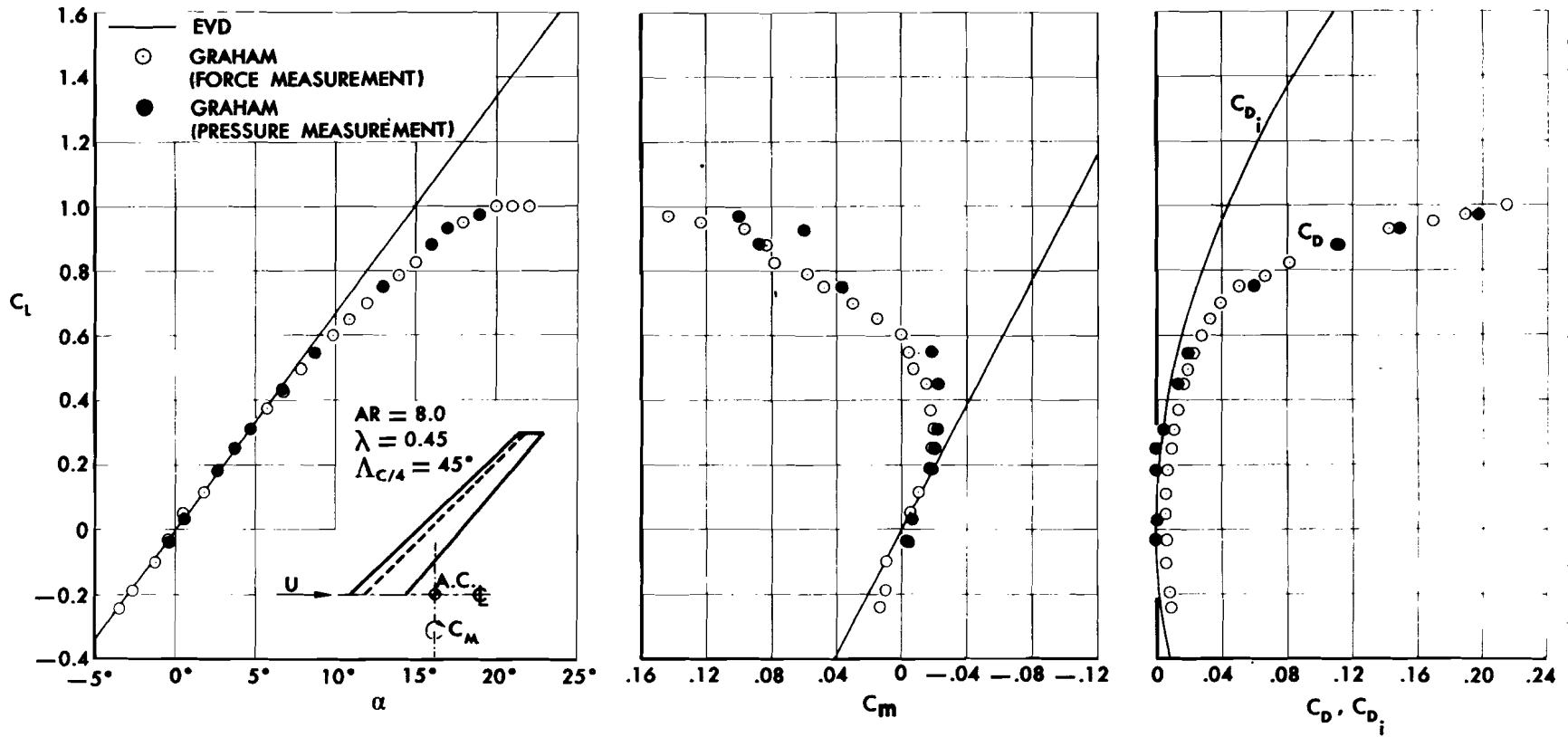


Figure (2.26). Theoretical and Experimental Lift, Pitching Moment, and Drag Characteristics of a Tapered Swept Wing ( $C_j = 0$ )

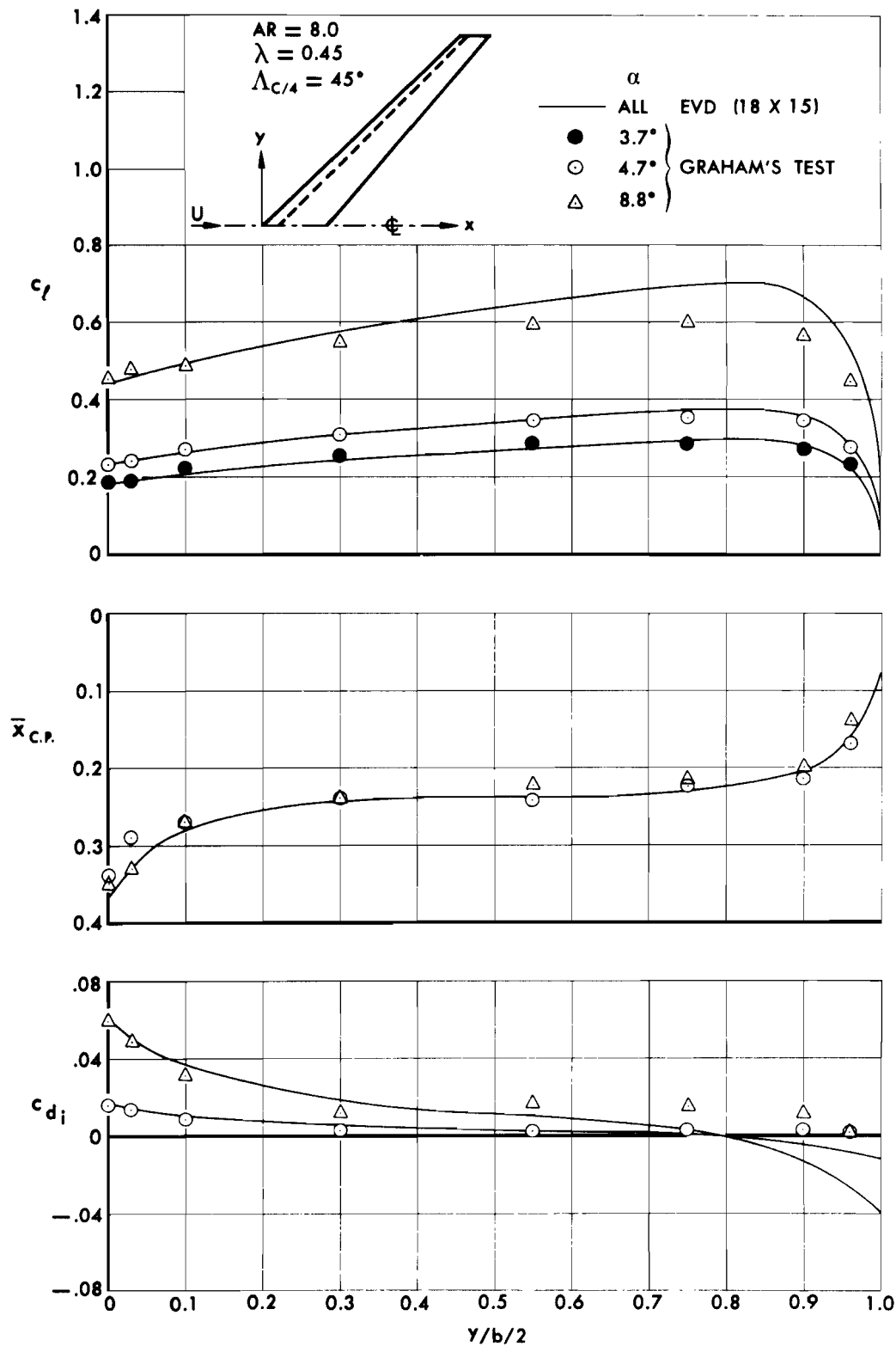


Figure (2.27). Spanwise Variation of Lift, Center of Pressure, and Induced Drag - Comparison of Theory and Experiment for a Tapered Swept Wing ( $C_j = 0$ )

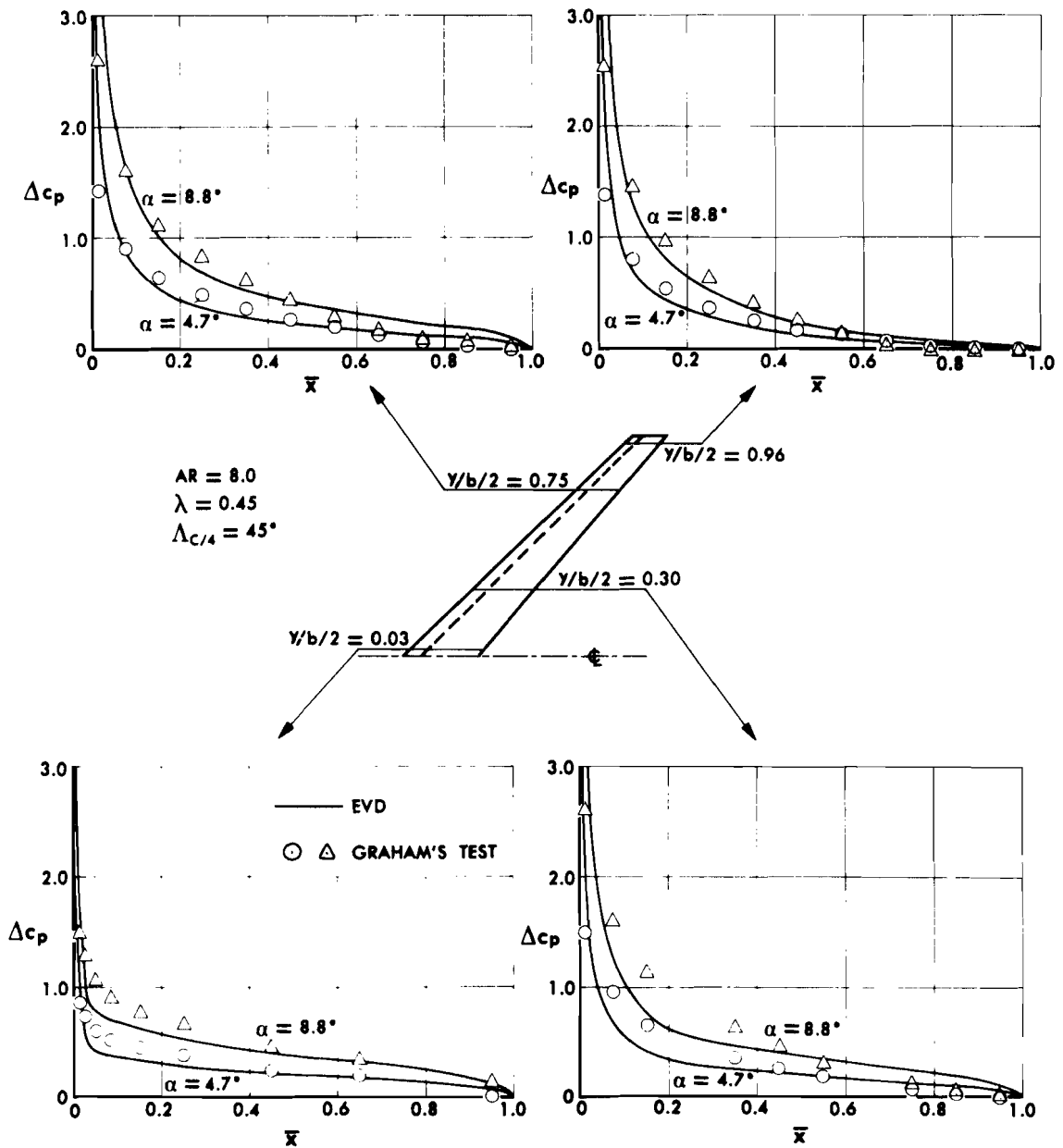


Figure (2.28). Comparison of the EVD Theory with Experimental Results - Chordwise Loading on a Tapered Swept Wing ( $C_j = 0$ )

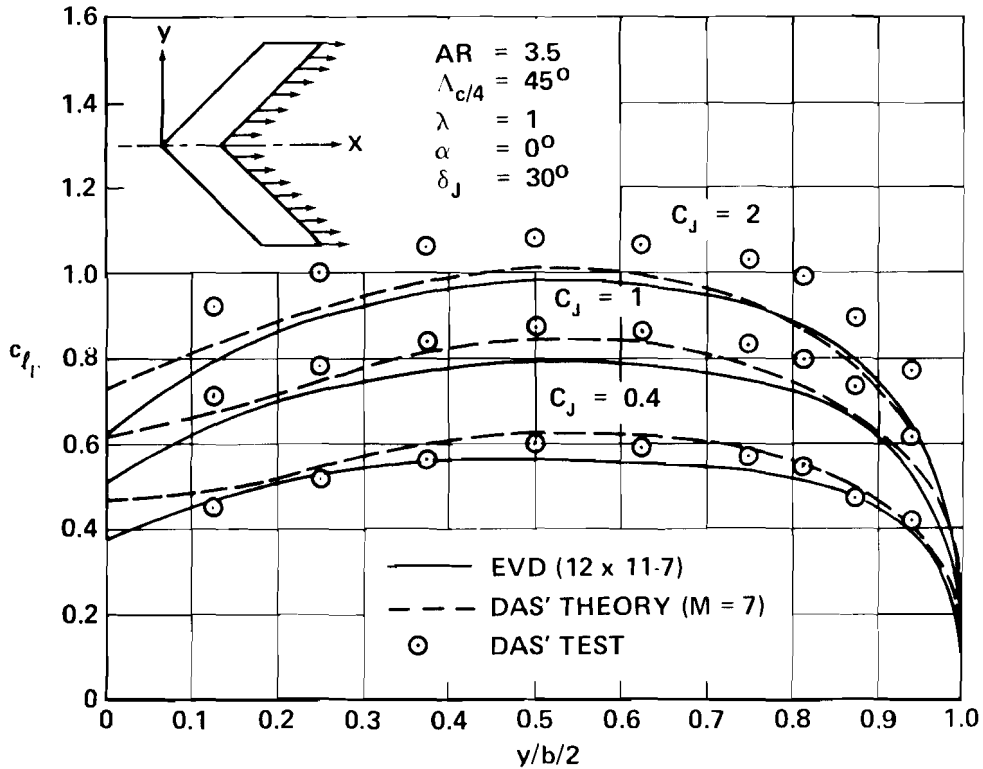


Figure (2.29). Comparison of Theory and Experiment - Spanwise Circulation Lift Distribution of a  $45^\circ$  Swept Wing with Uniform Full-Span Blowing

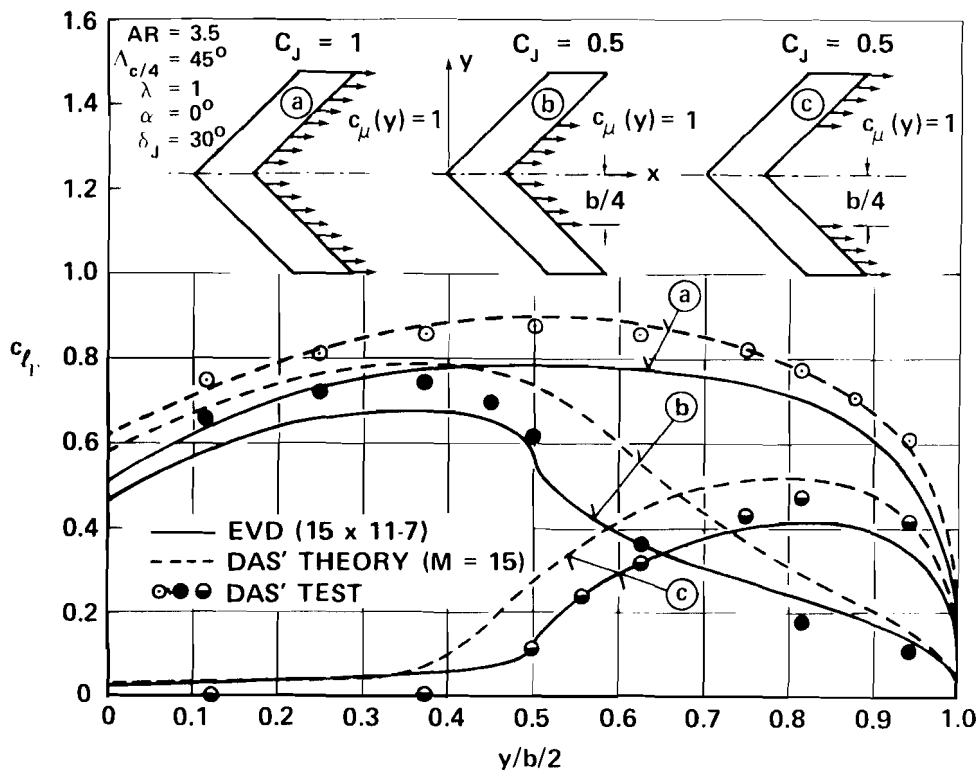


Figure (2.30). Comparison of Theory and Experiment - Spanwise Circulation Lift Distribution of a  $45^\circ$  Swept Wing with Partial Span Blowing

RECTANGULAR WING AR = 5.16

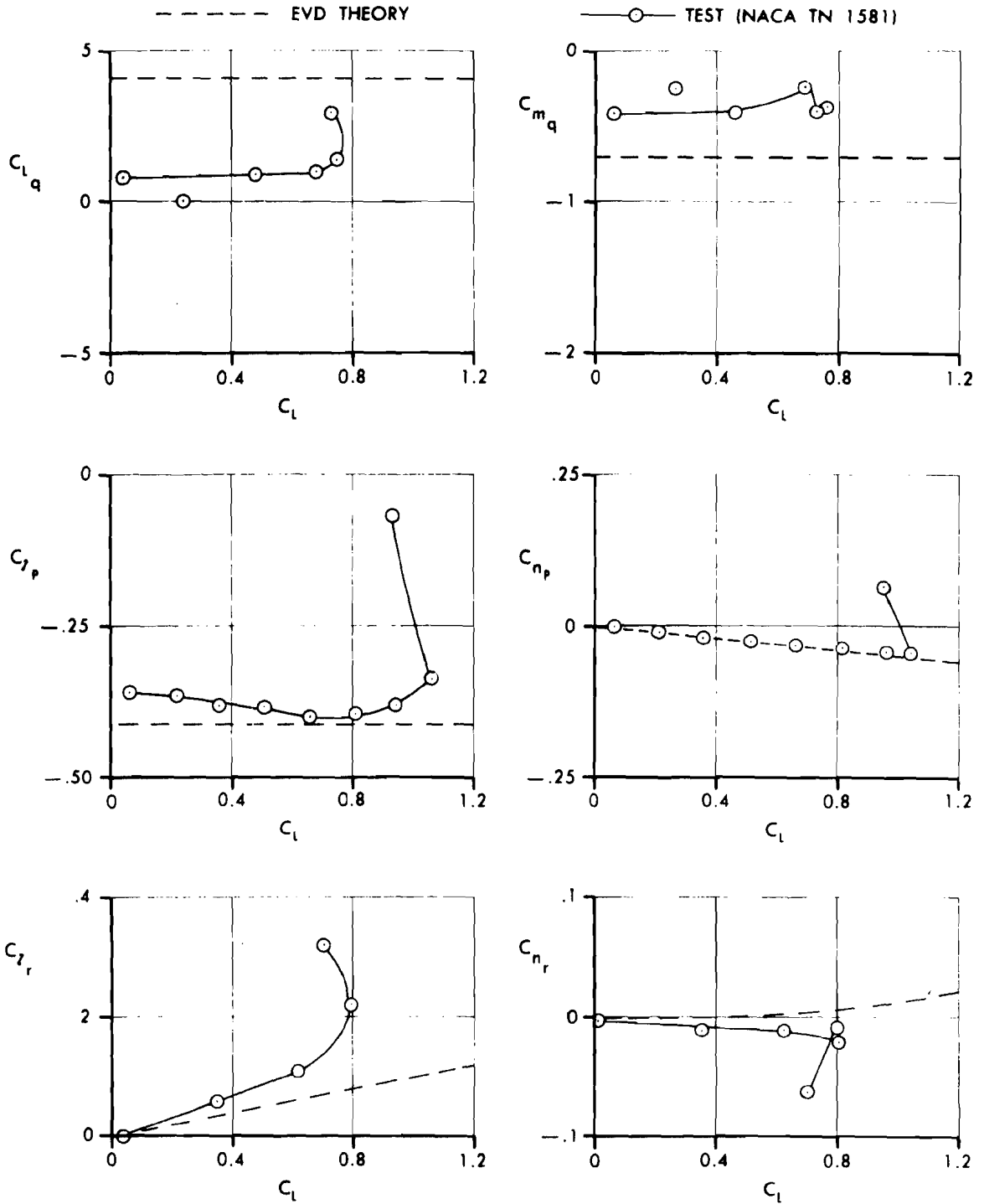


Figure (2.31). Measured and Calculated Stability Derivatives due to Pitching, Rolling, and Yawing for a Rectangular Wing of Aspect Ratio 5.16 ( $C_J = 0$ ). (Both c.g. and Moment Reference Center are at a.c.)

SWEPT WING AR = 2.61,  $\Lambda = 45^\circ$ ,  $\lambda = 1$

----- EVD THEORY

—○— TEST (NACA TN 1581)

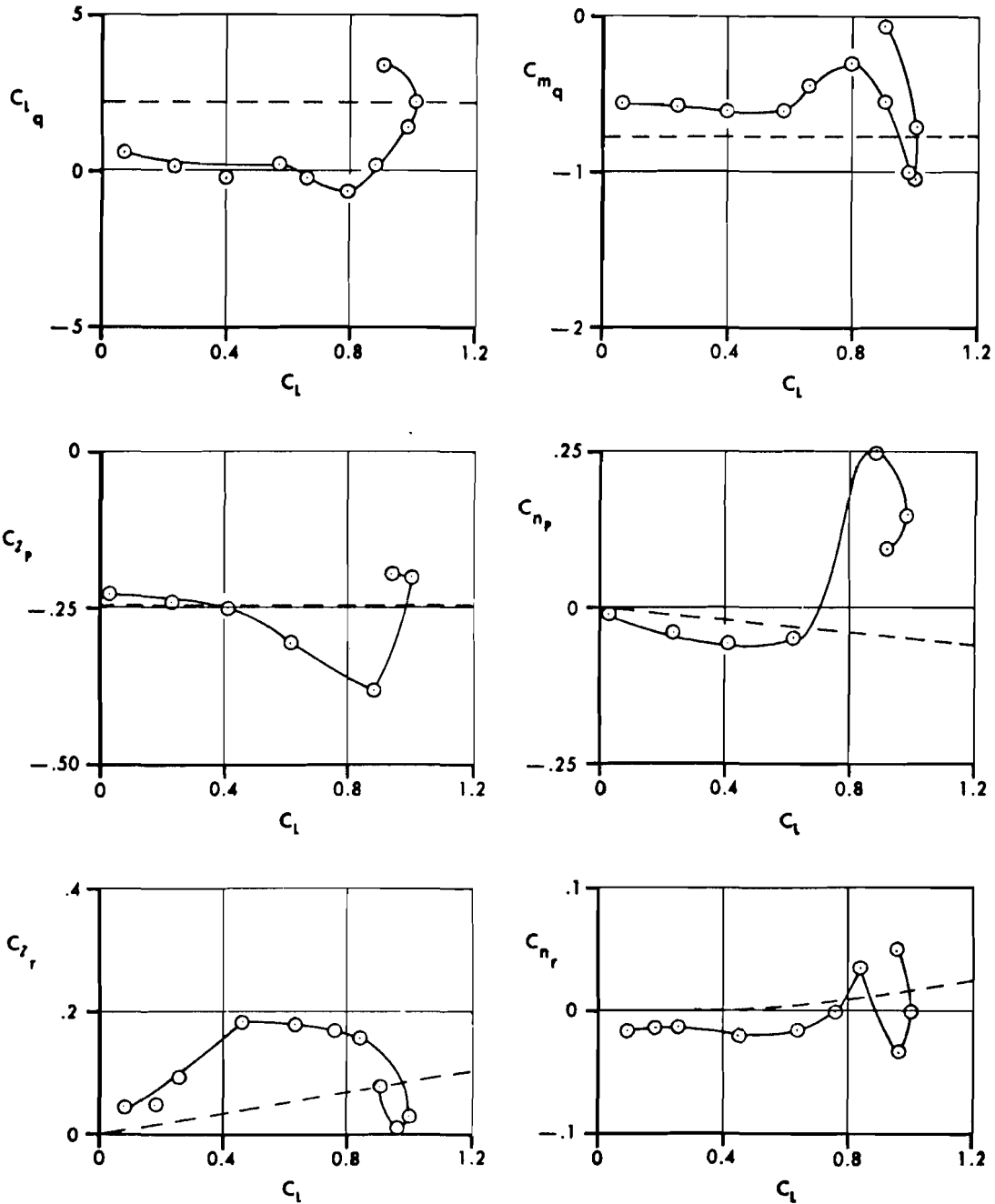


Figure (2.32). Measured and Calculated Stability Derivatives due to Pitching, Rolling, and Yawing for a  $45^\circ$  Swept, Constant-Chord Wing - AR = 2.61 ( $C_D = 0$ ). (Both c.g. and Moments Reference Center are at a.c.)

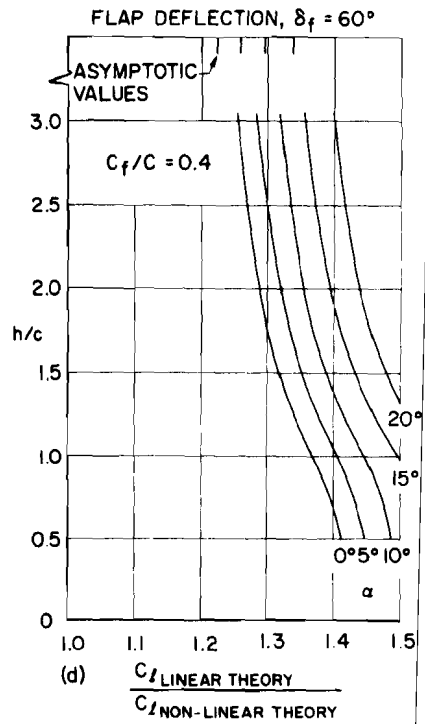
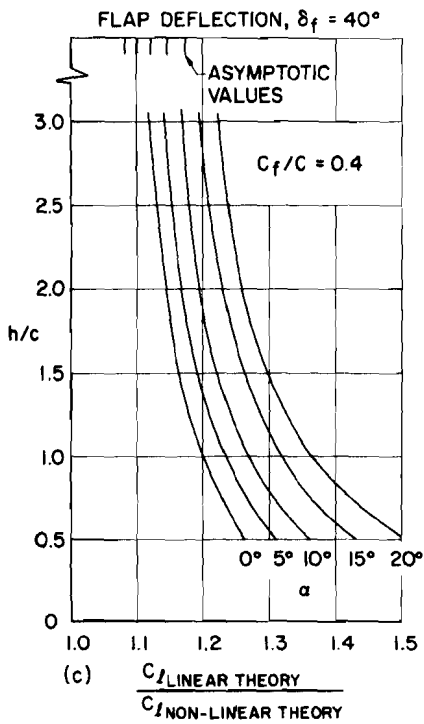
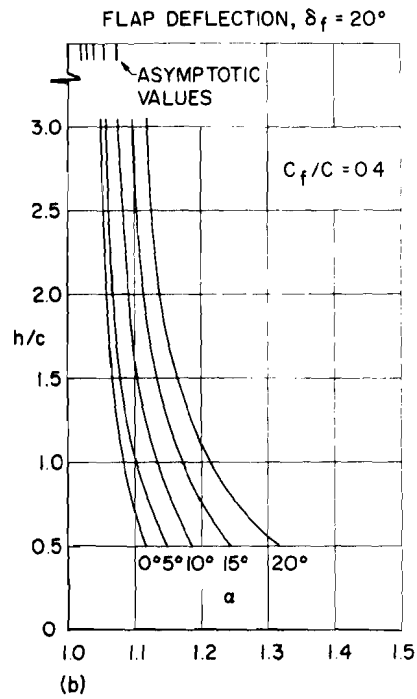
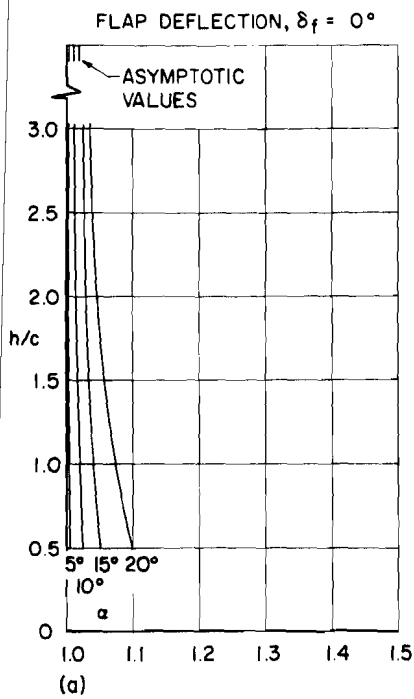
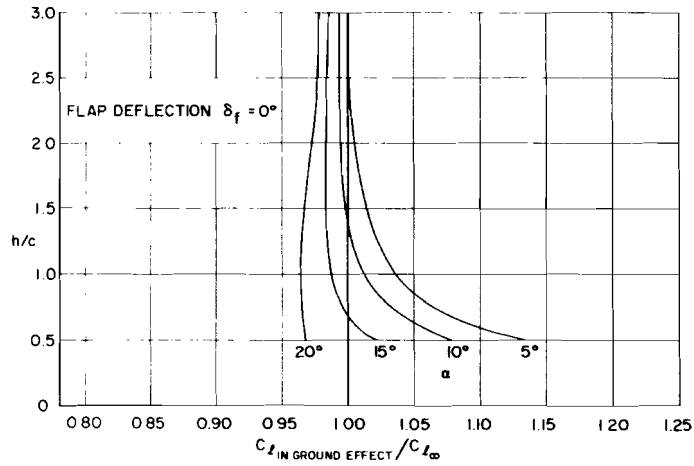
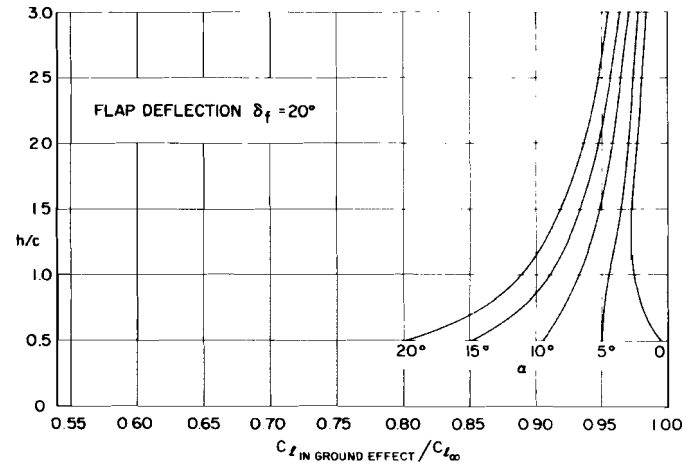


Figure (2.33). Lift on a Two-Dimensional Hinged Flat-Plate Airfoil in Ground Effect - Comparison Between Linear and Non-Linear Theory

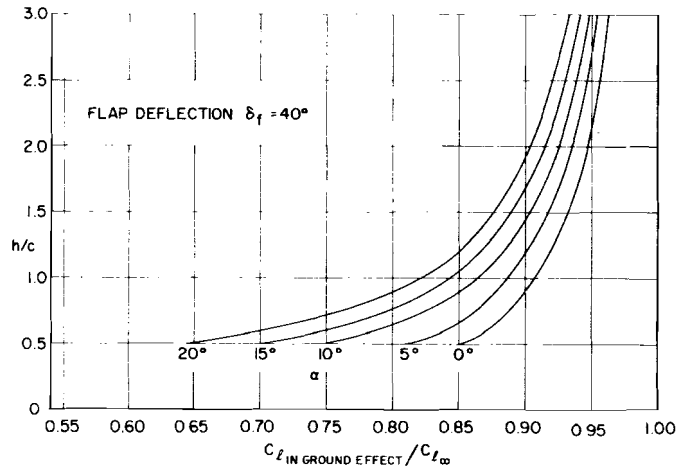




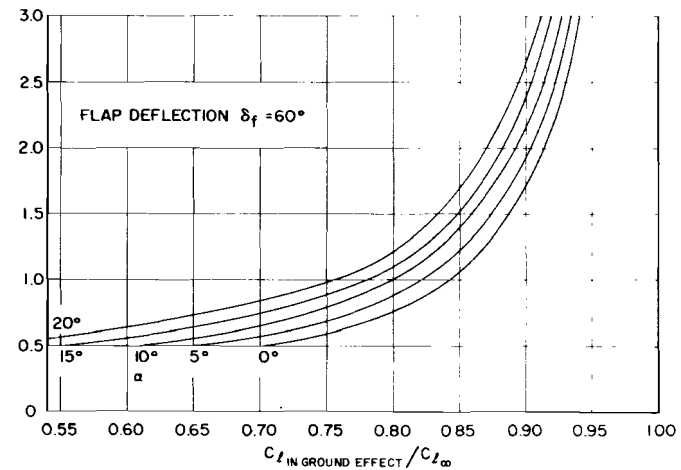
(a)



(b)



(c)



(d)

Figure (2.34). Lift on a Two-Dimensional Hinged Flat Plate Airfoil in Ground Effect Calculated by Linear Theory - Ratio of Lift in Ground Effect to Lift in Free Air.

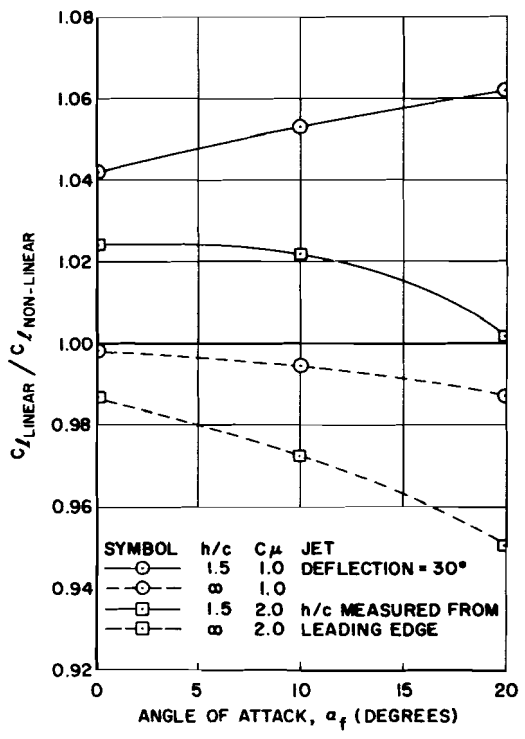


Figure (2.35). Lift on a Two-Dimensional Flat Plate Airfoil with Jet Flap in Ground Effect - Comparison Between Linear and Non-Linear Theory

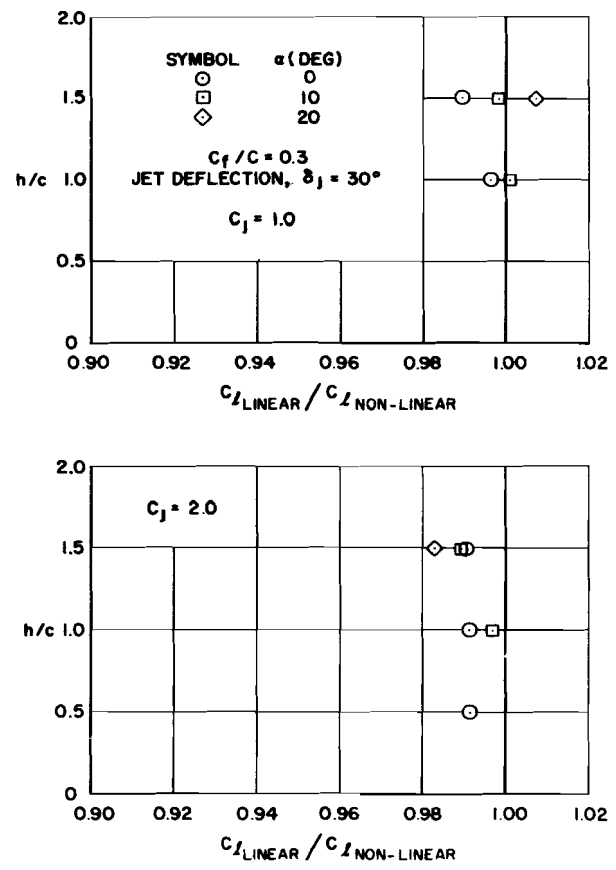


Figure (2.36). Lift on a Two-Dimensional Hinged Flat Plate Airfoil with Jet Flap in Ground Effect - Comparison Between Linear and Non-Linear Theory

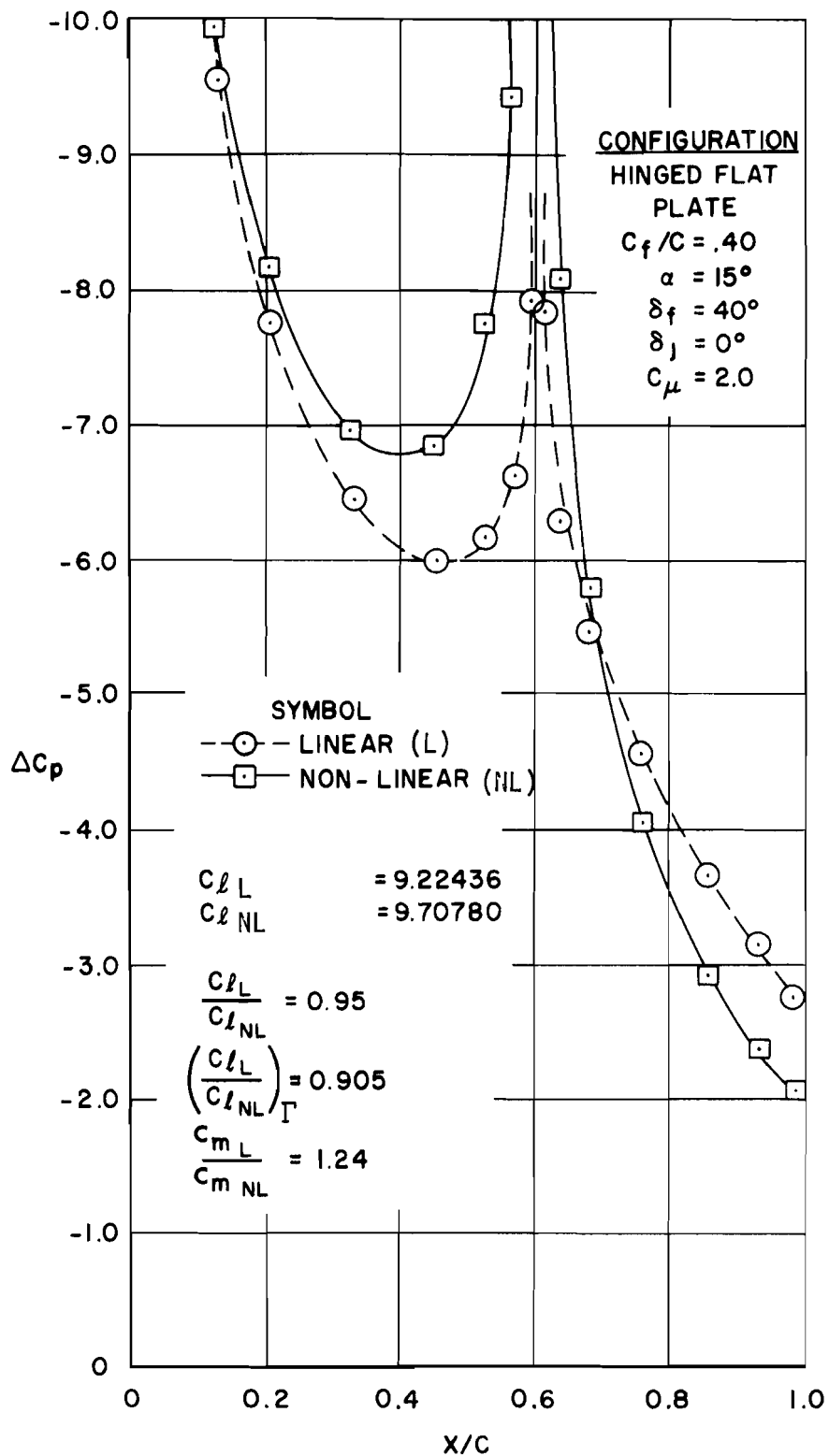


Figure (2.37). Pressure Distribution on a Two-Dimensional Hinged Flat Plate Airfoil with Jet Flap in Ground Effect - Comparison Between Linear and Non-Linear Theory

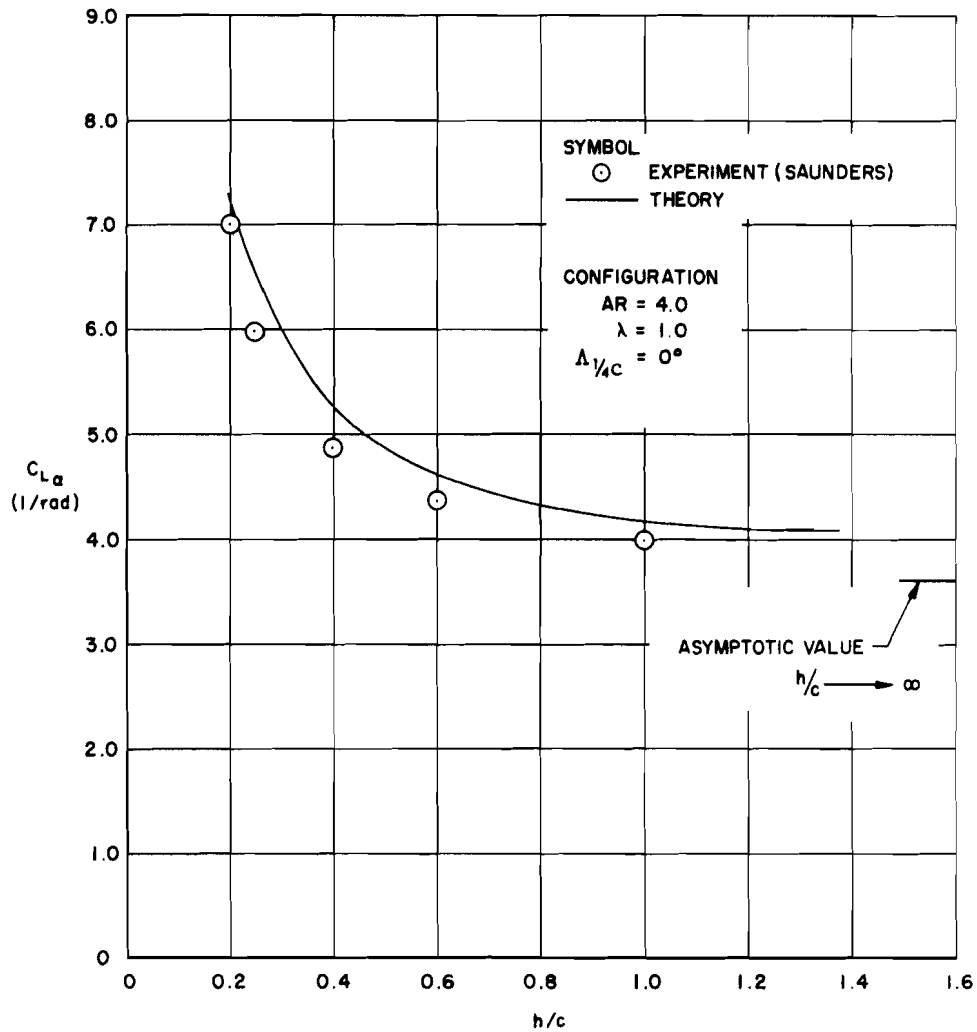


Figure (2.38). Effect of Ground Proximity on the Lift Curve Slope of a Rectangular Wing - Comparison Between Theory and Experiment

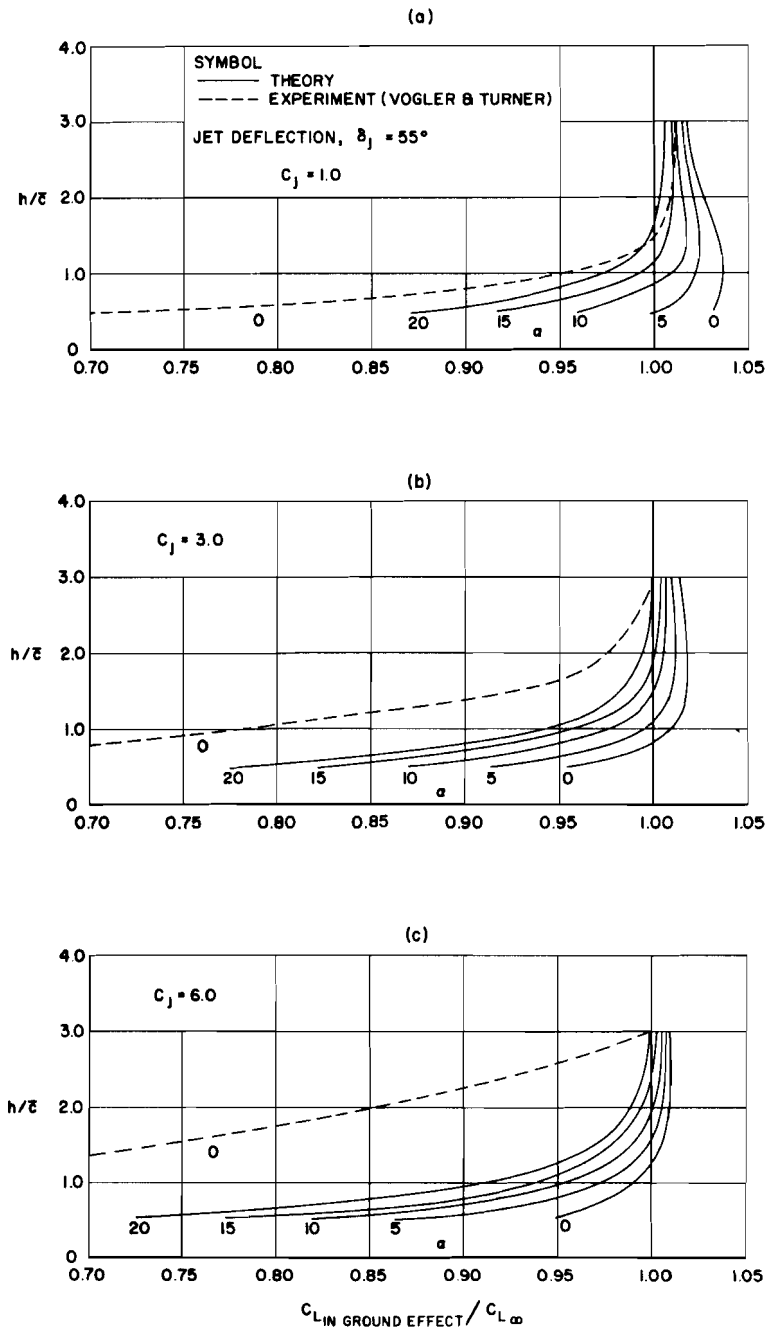


Figure (2.39). Effect of Ground Proximity on the Lift of a Rectangular Jet-Wing - Comparison Between Theory and Experiment.  
 (Configuration:  $AR = 8.3$ ,  $\lambda = 1.0$ ,  $\lambda_{1/4}c = 0$ )

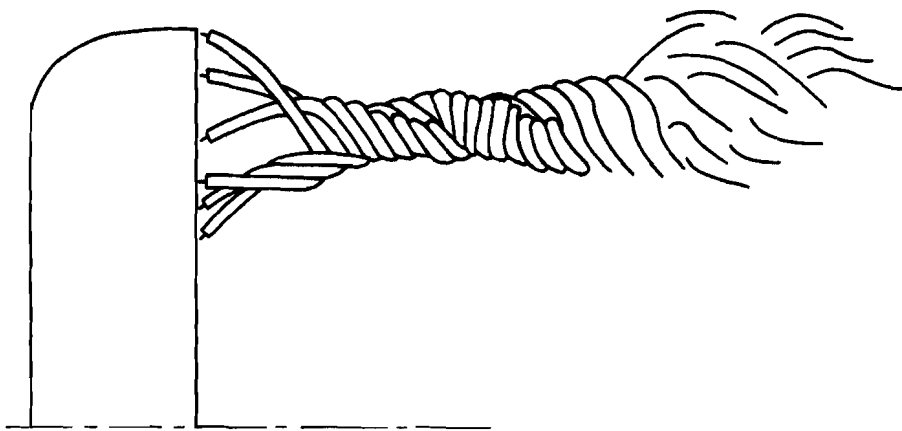


Figure (2.40). Lanchester's Representation of Vortex Roll Up

CONFIGURATION  
 USA 45 WING  
 ASPECT RATIO 6.2  
 1/4 CHORD SWEEP 0°  
 $C_L = 1.35$   
 $\alpha = 15.2^\circ$

—●— THEORY (2nd ITERATION)  
 - - - EXPERIMENT (SILVERSTEIN)

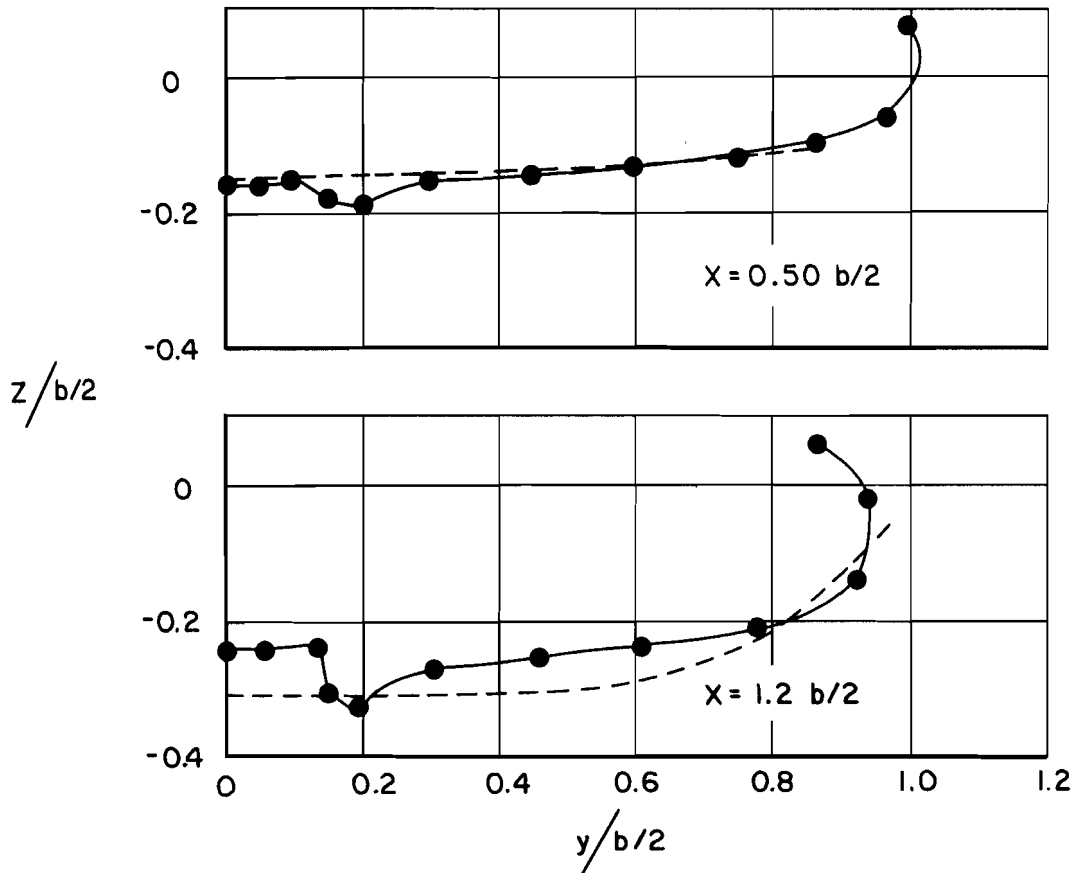


Figure (2.41). Typical Rolled Up Wake for a Wing with a Simple Spanwise Loading Distribution - Comparison Between Theory (reference 51) and Experiment

### CONFIGURATION

ASPECT RATIO	5.0	FLAP SPAN: 0.10 b/2 - 0.75 b/2
TAPER RATIO	0.3	FLAP DEFLECTION 30°
1/4 CHORD SWEEP	20°	$C_L \approx 3.0$

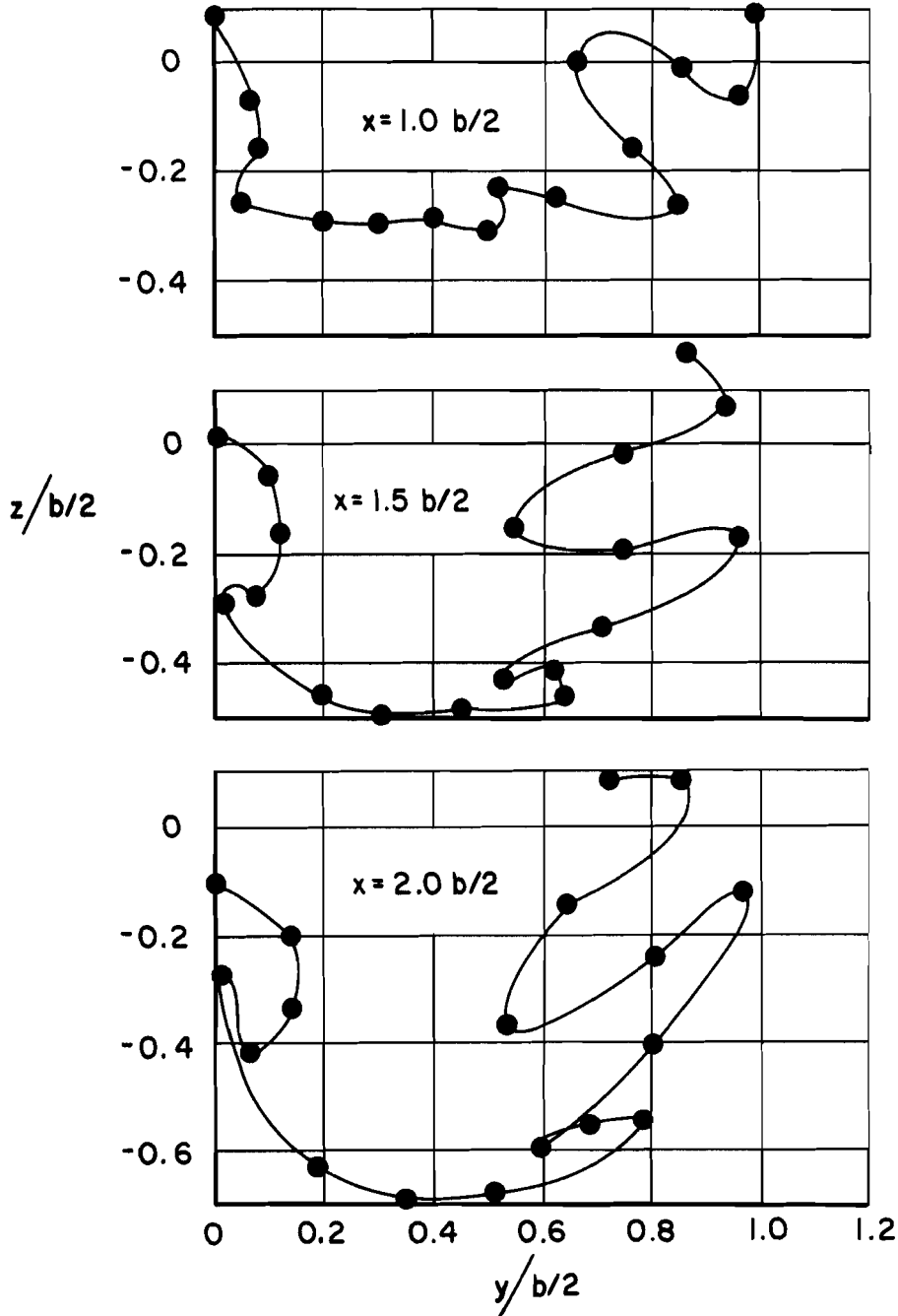
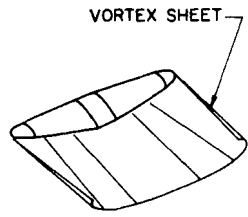


Figure (2.42). Typical Rolled Up Wake for a Wing with a Part-Span Flap - Theoretical Prediction (2nd Iteration) of the Method of Reference 51,





(a) USA 45 WING AND ROLLED UP VORTEX SHEET

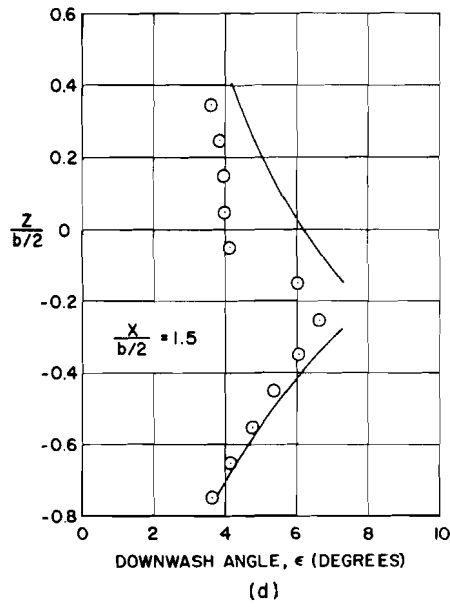
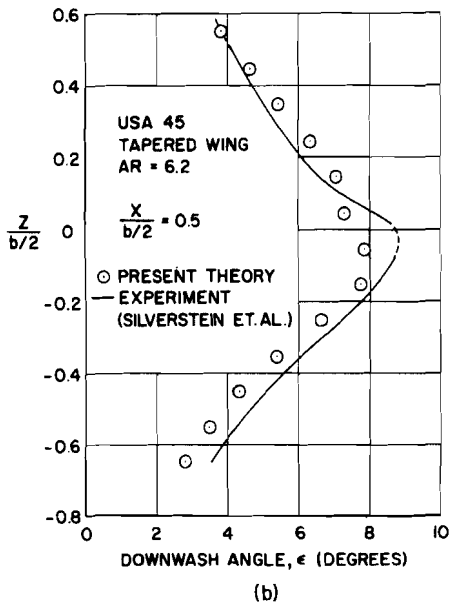
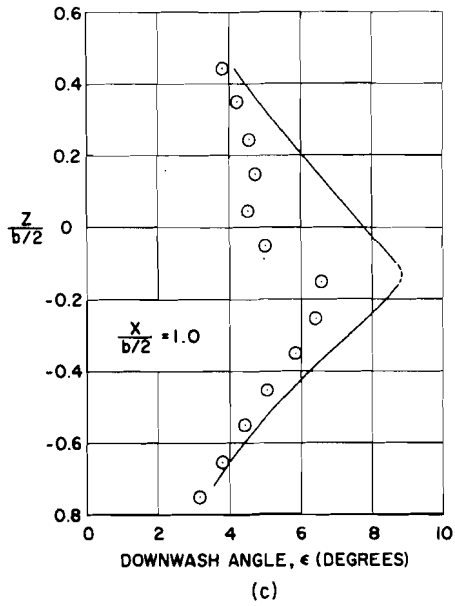


Figure (2.43). Variation of Wing Induced Downwash in the Plane of Symmetry Behind the USA 45 Wing - Comparison Between Theory and Experiment

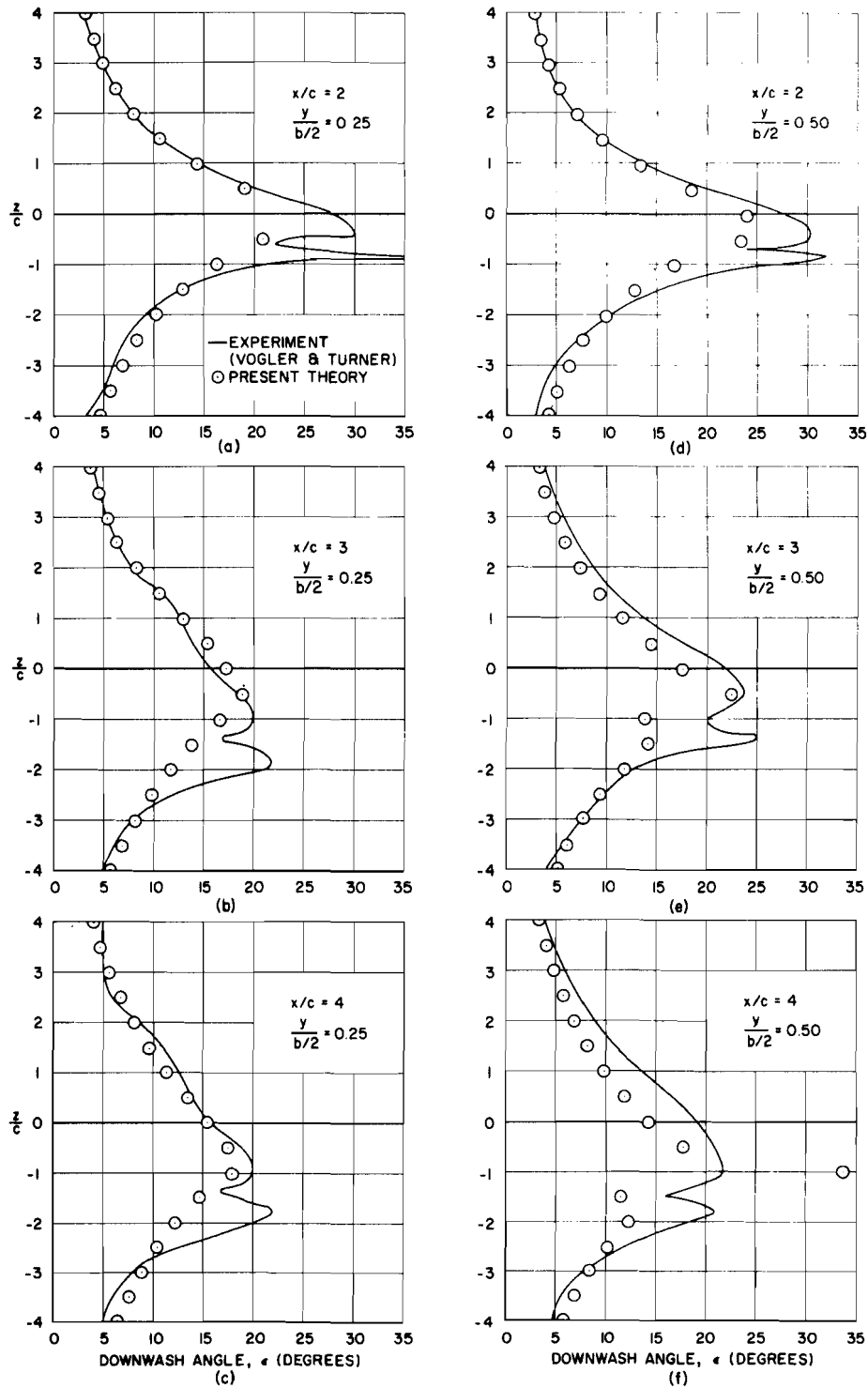


Figure (2.44). Variation of Jet-Wing Induced Downwash with Position - Comparison Between Theory and Experiment. (Configuration:  $AR = 8.3$ ,  $\lambda = 1.0$ ,  $\Lambda_{1/4c} = 0$ ,  $C_J = 1.67$ ,  $C_L = 5.3$ ),

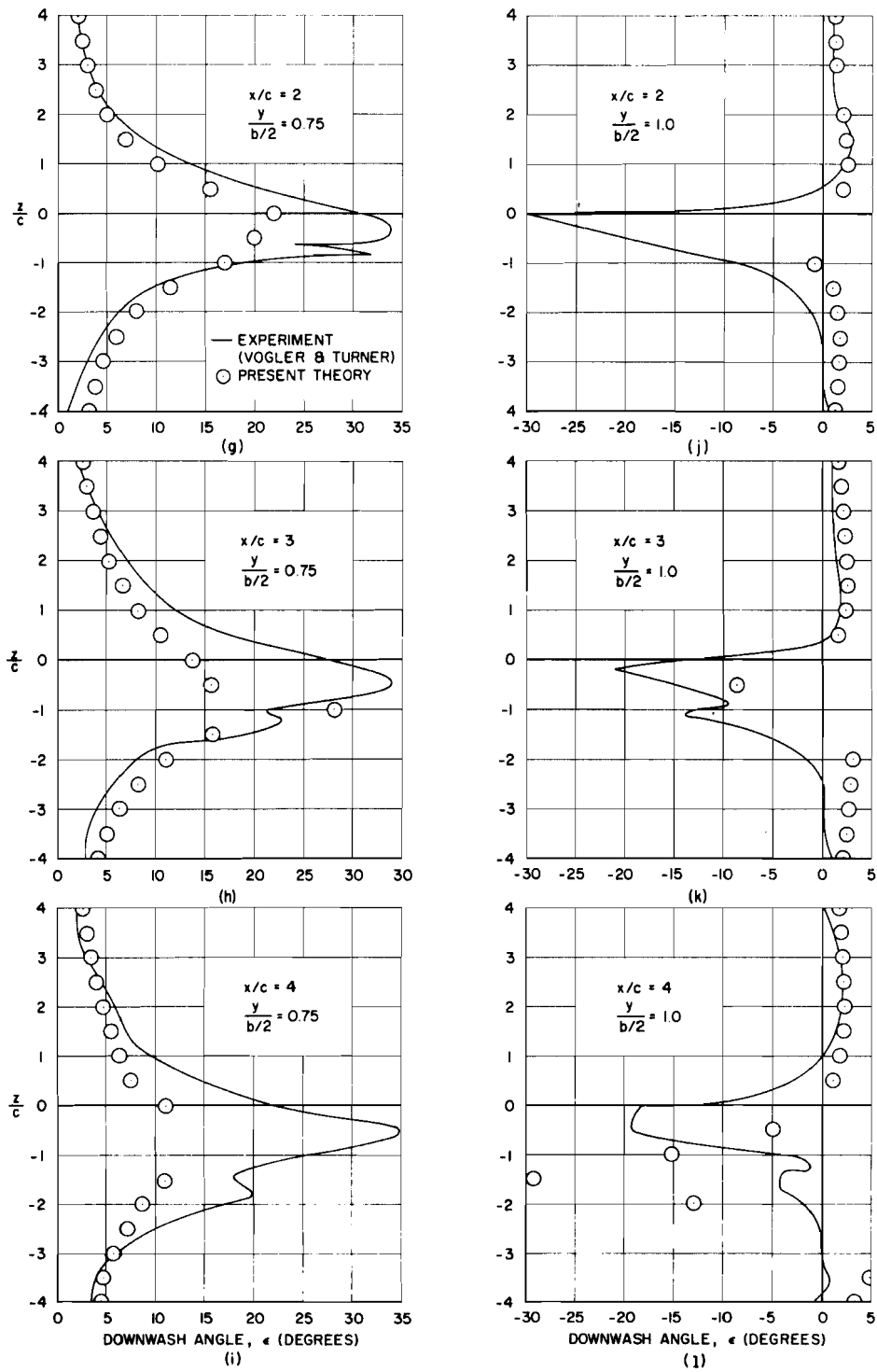


Figure (2.44). Continued

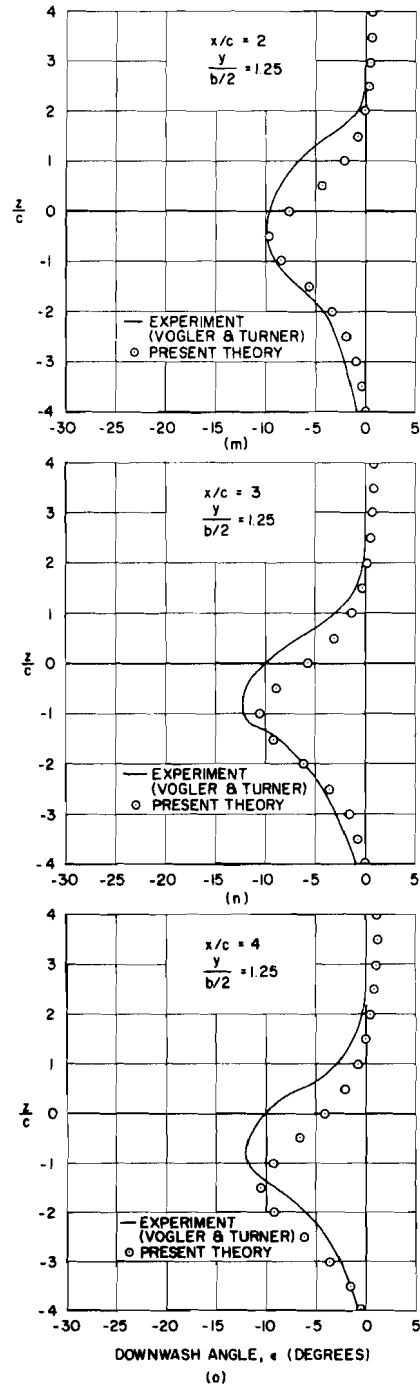


Figure (2.44) Continued

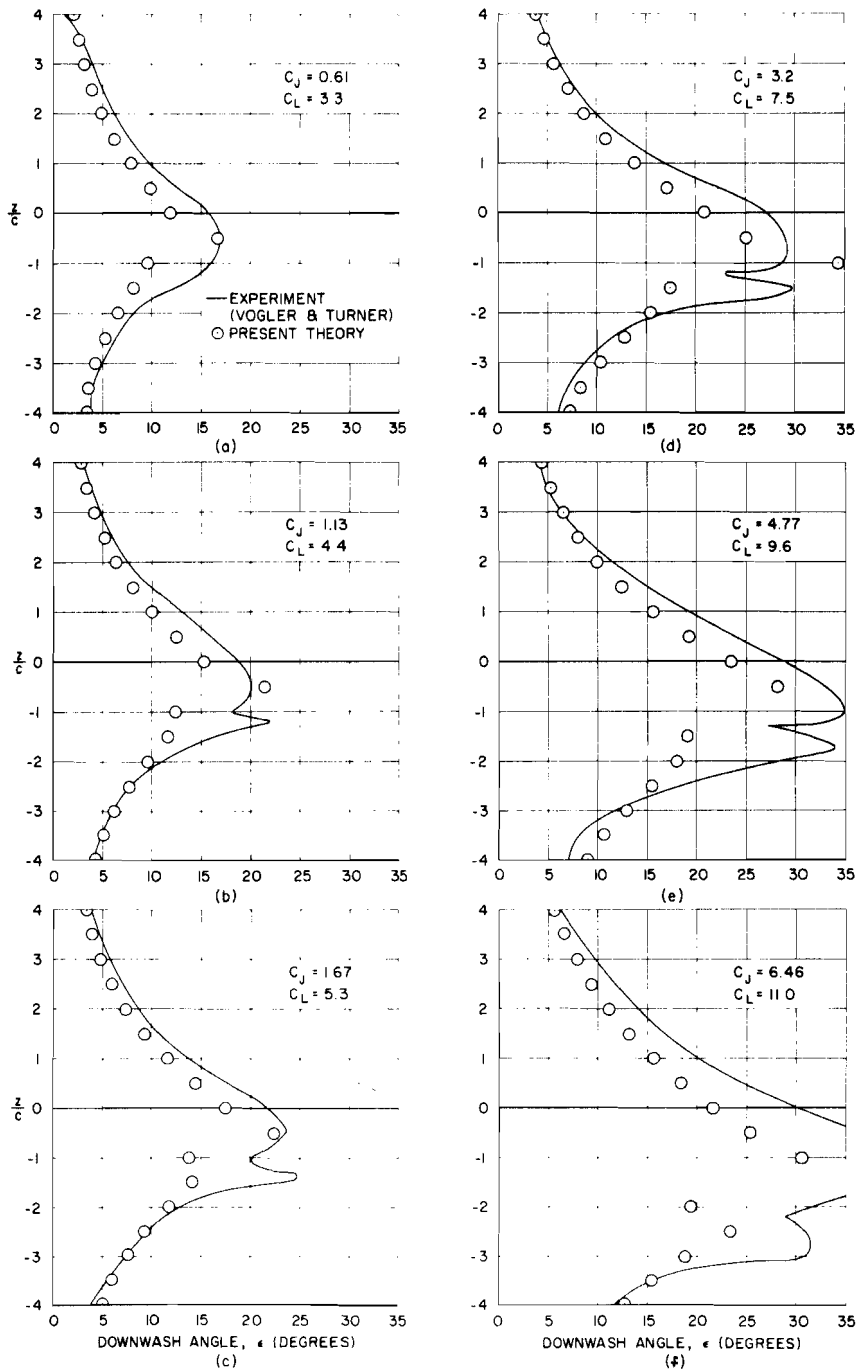


Figure (2.45). Variation of Jet-Wing Induced Downwash with Jet Momentum - Comparison Between Theory and Experiment. (Configuration:  $AR = 8.3, \lambda = 1.0, \Lambda_{1/4c} = 0$ )

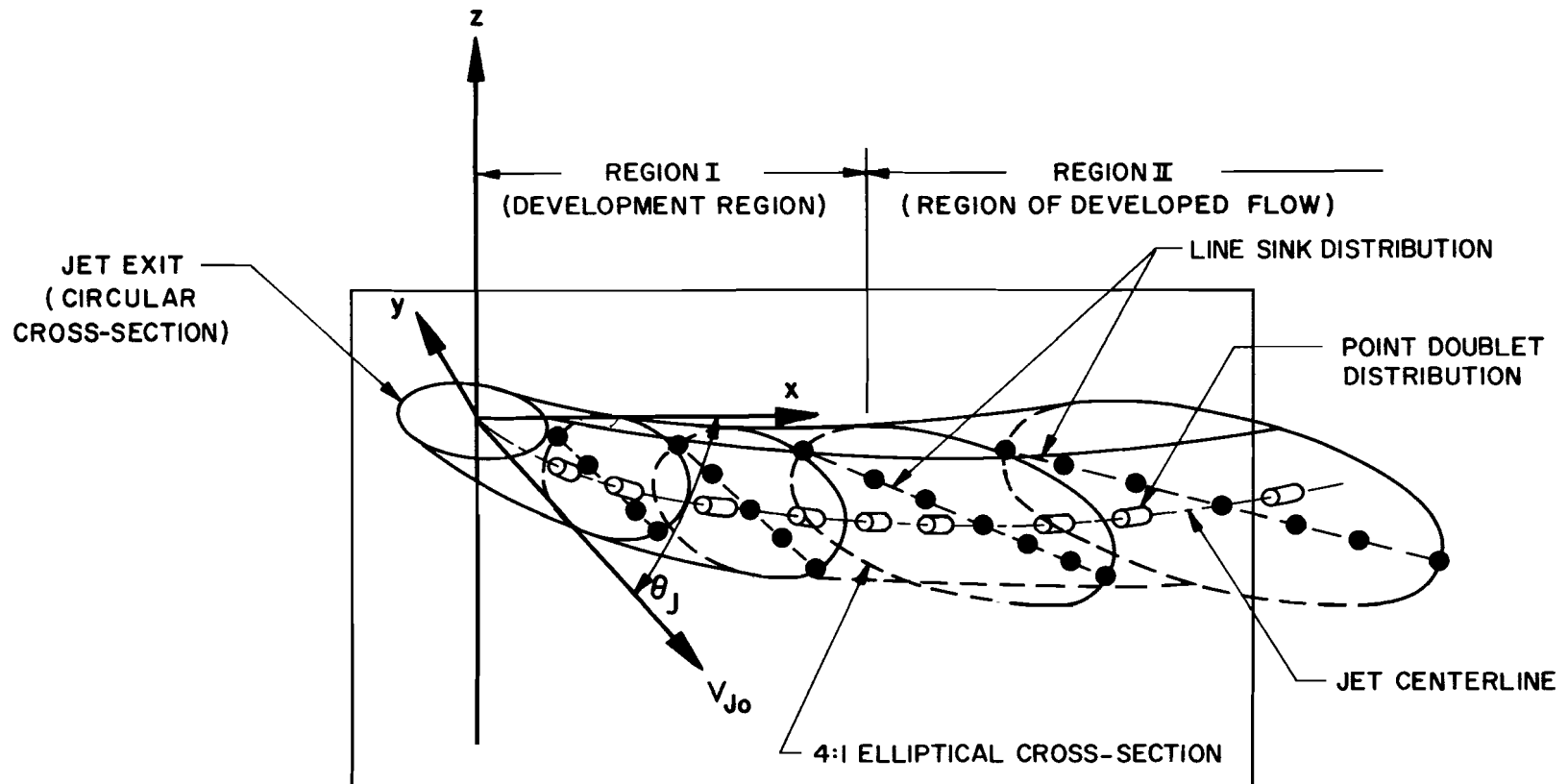
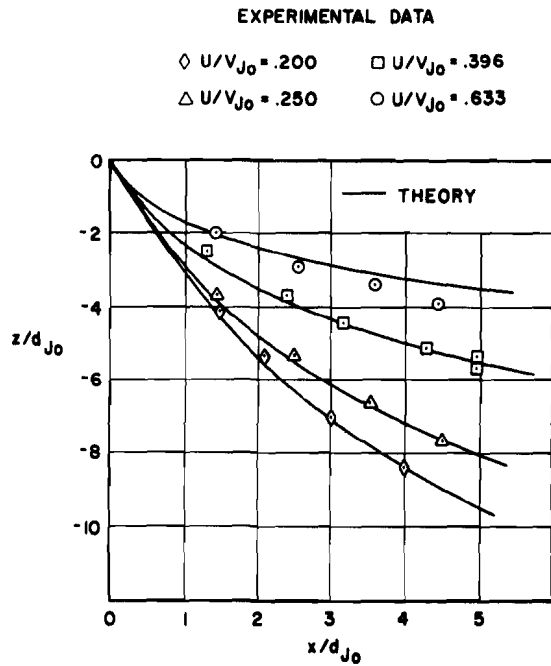
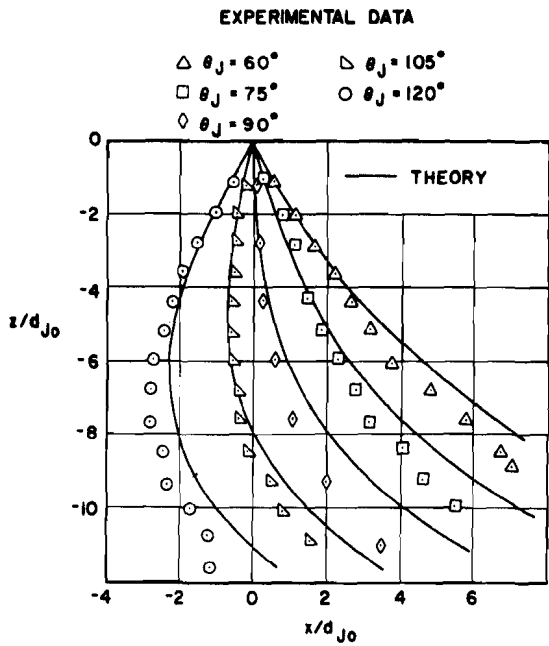
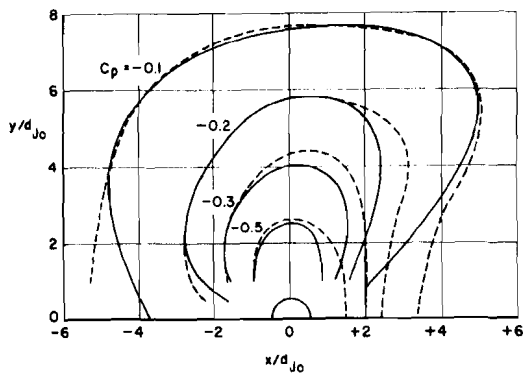


Figure (3.1). Illustration of a Vectored-Jet in a Cross Flow - Geometry and Mathematical Model

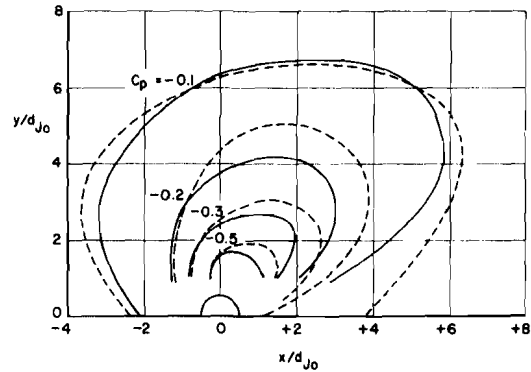


(a) The effect of jet angle,  $\theta_J$ , on the trajectory of a circular jet exhausting into a freestream ( $U/V_{J_0} = 0.120$ ).

(b) The effect of velocity ratio on the trajectory of a jet exhausting at an angle  $\theta_J = 60^\circ$  into a freestream.



(c)



(d)

Comparison of predicted and experimental induced pressure distributions around a single circular jet. (c)  $\theta_J = 90^\circ$ ,  $U/V_{J_0} = 0.125$ . (d)  $\theta_J = 60^\circ$ ,  $U/V_{J_0} = 0.125$ .

Figure (3.2). Comparison of Predicted and Experimental Jet Parameters

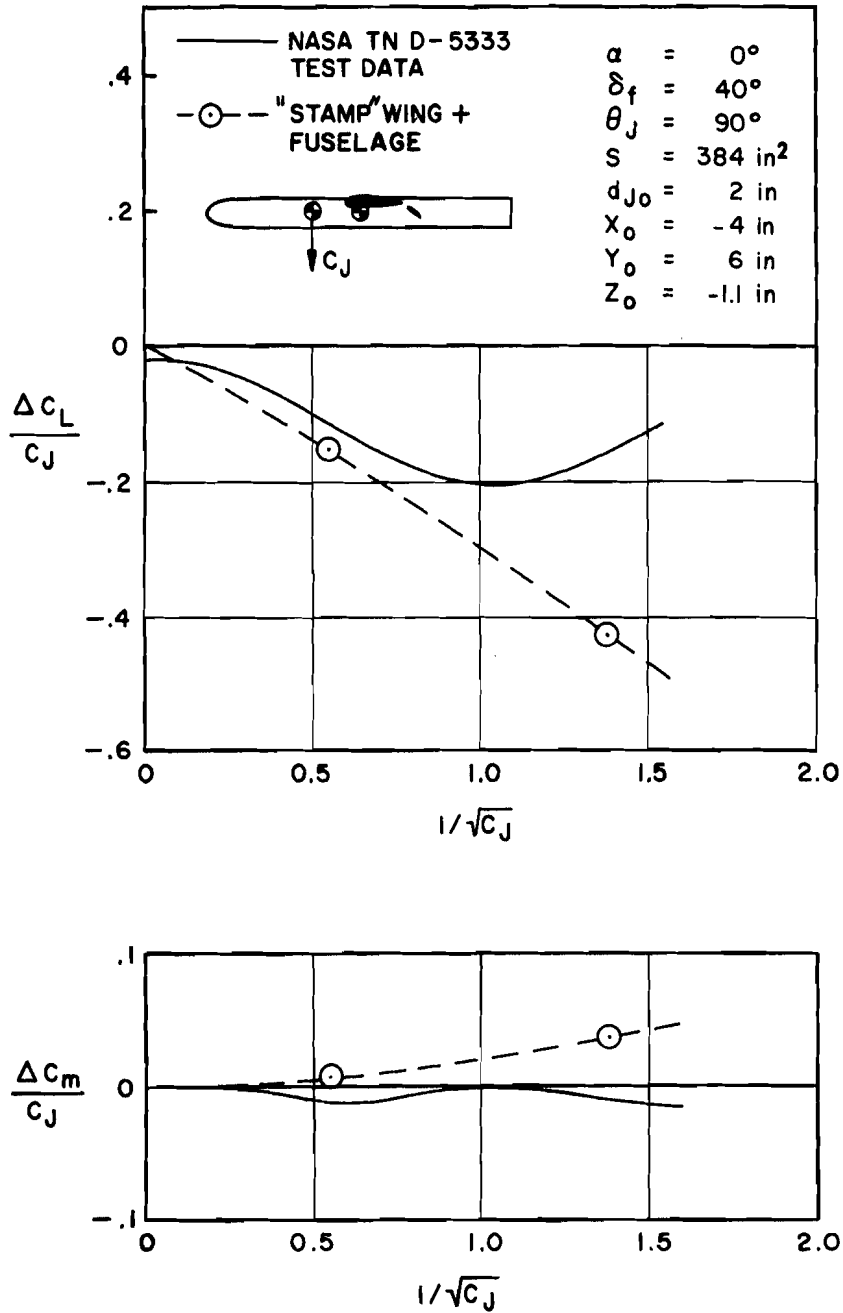


Figure (3.3a). Typical Wing/Vectored Jet Aerodynamic Interferences



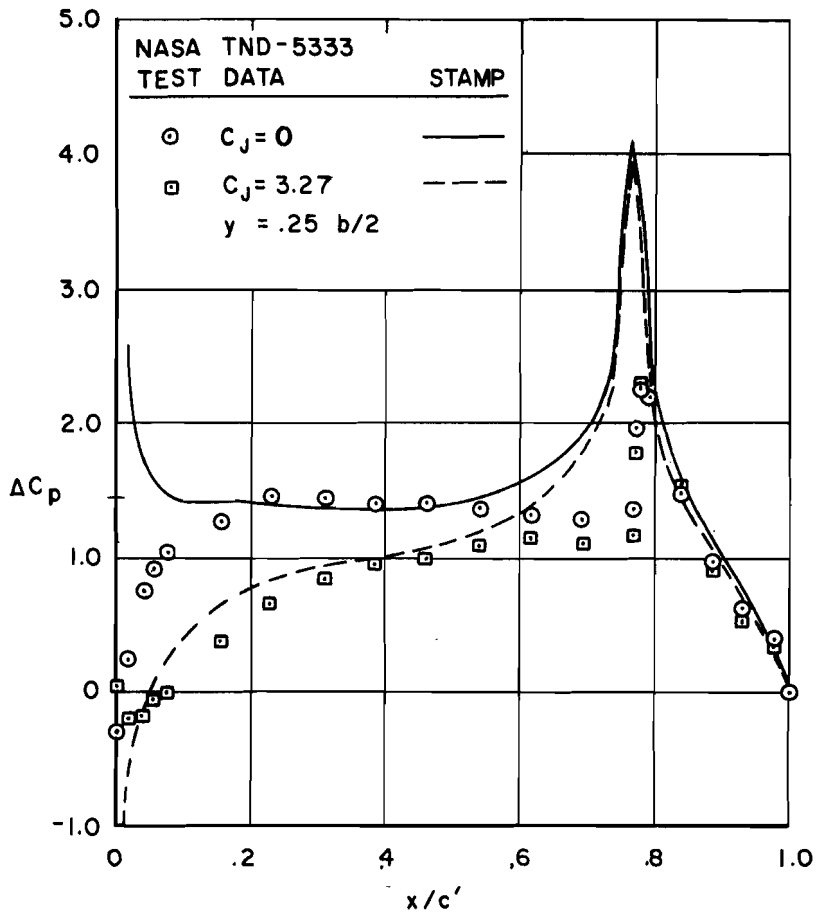
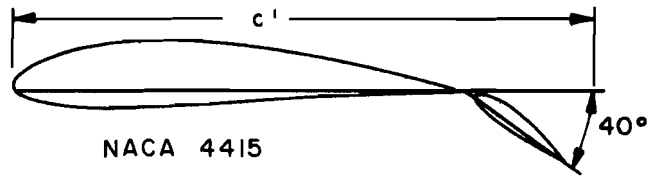


Figure (3.3b). Typical Wing/Vectored Jet Aerodynamic Interferences

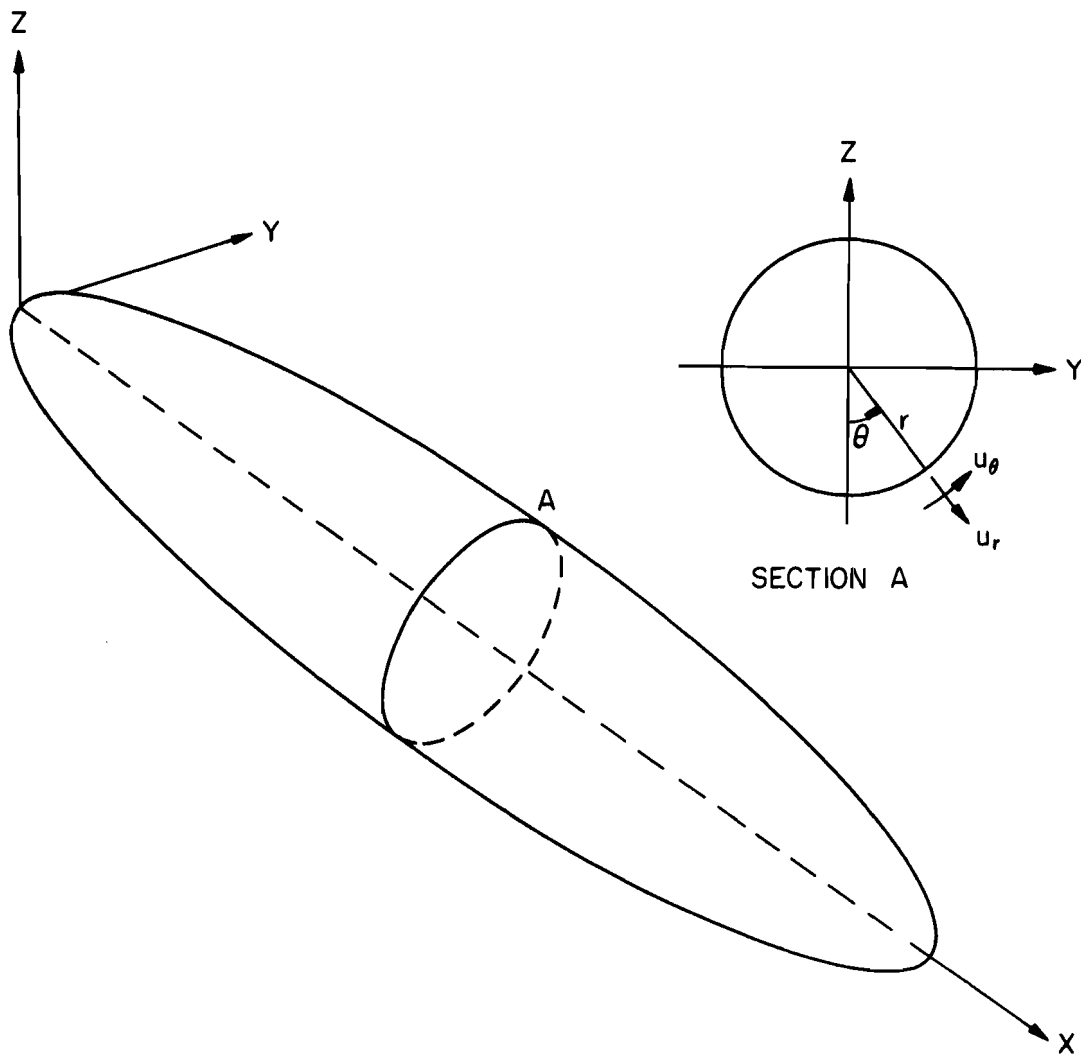


Figure (4.1). Illustration of the Fuselage Method

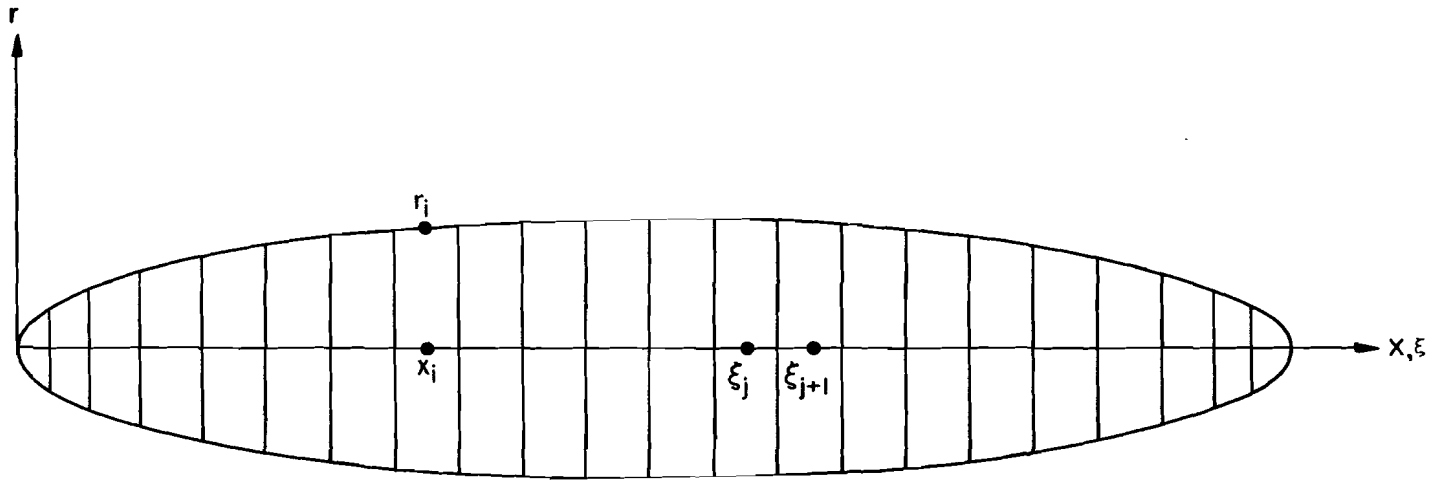


Figure (4.2). Division of the Fuselage into Streamwise Segments for the Modified Slender Body Solution

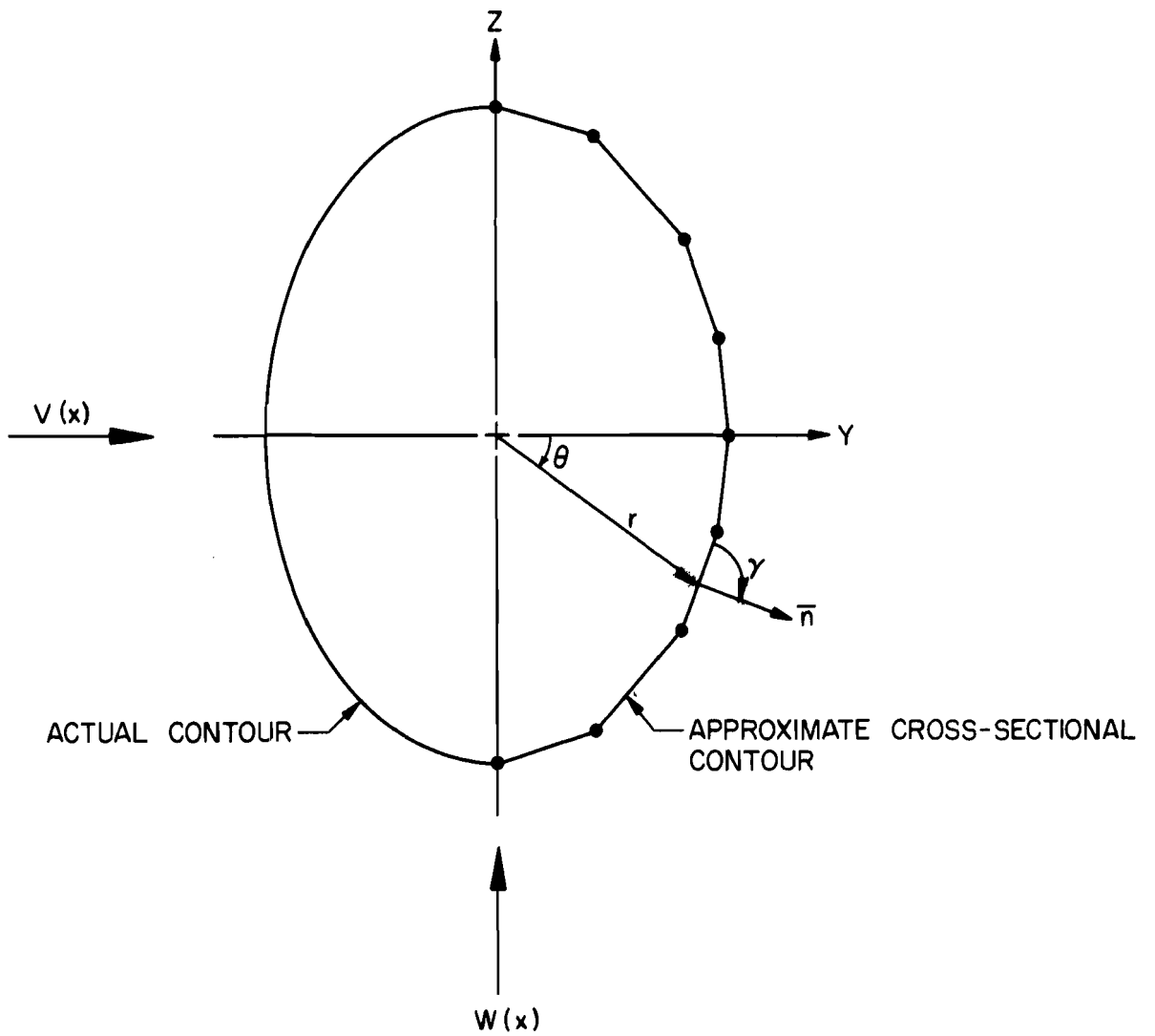


Figure (4.3). Division of Fuselage Cross-Sections into Circumferential Segments for the Modified Slender Body Solution

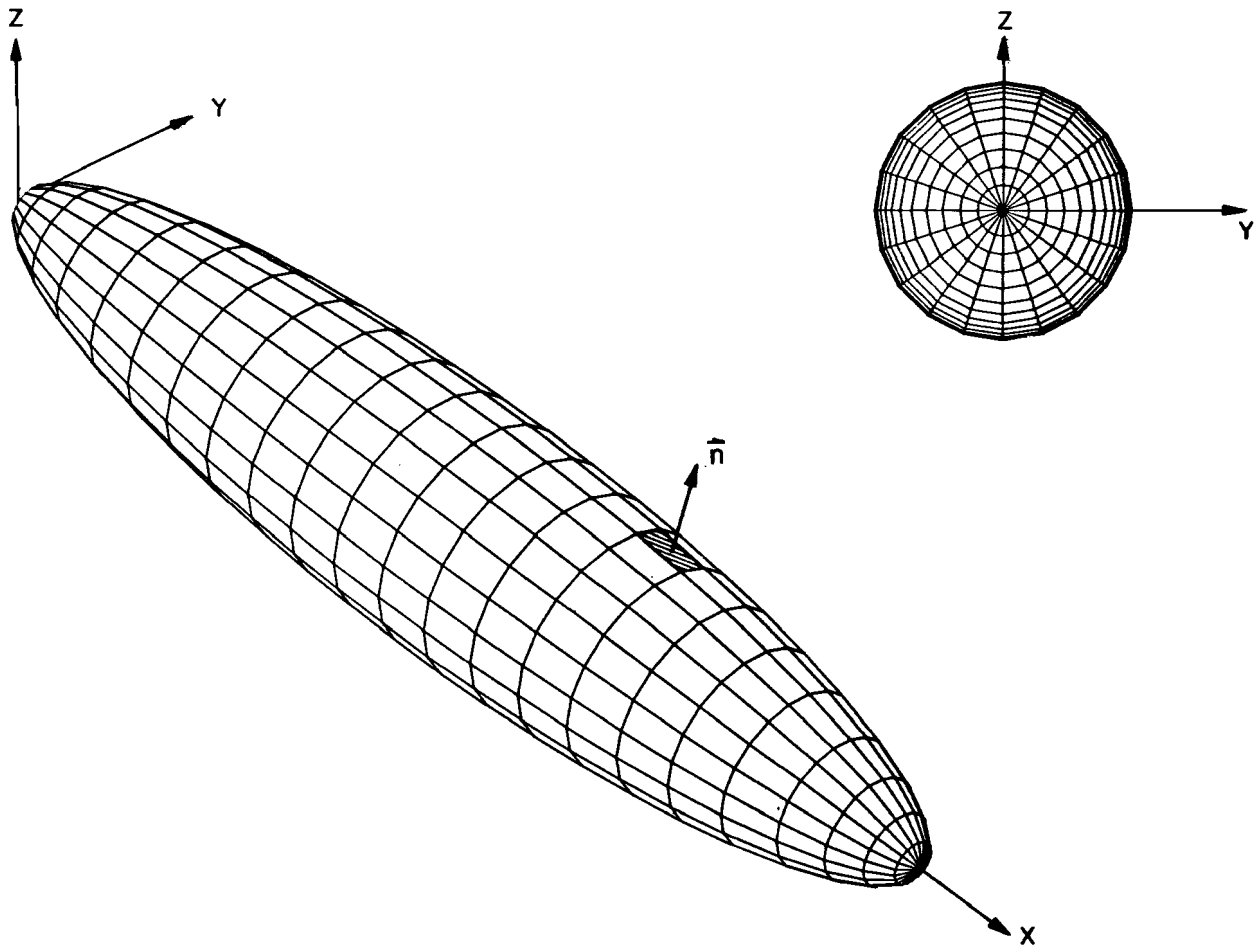


Figure (4.4). Representation of the Fuselage by a Lattice of Quadrilateral Elements for the Modified Slender Body Solution

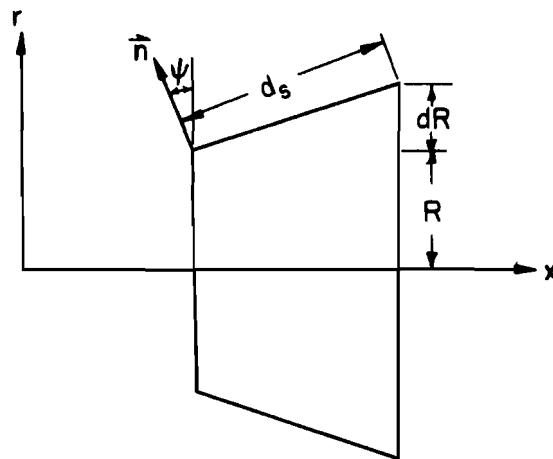


Figure (4.5). Definition of the Normal Vector on the Fuselage Surface

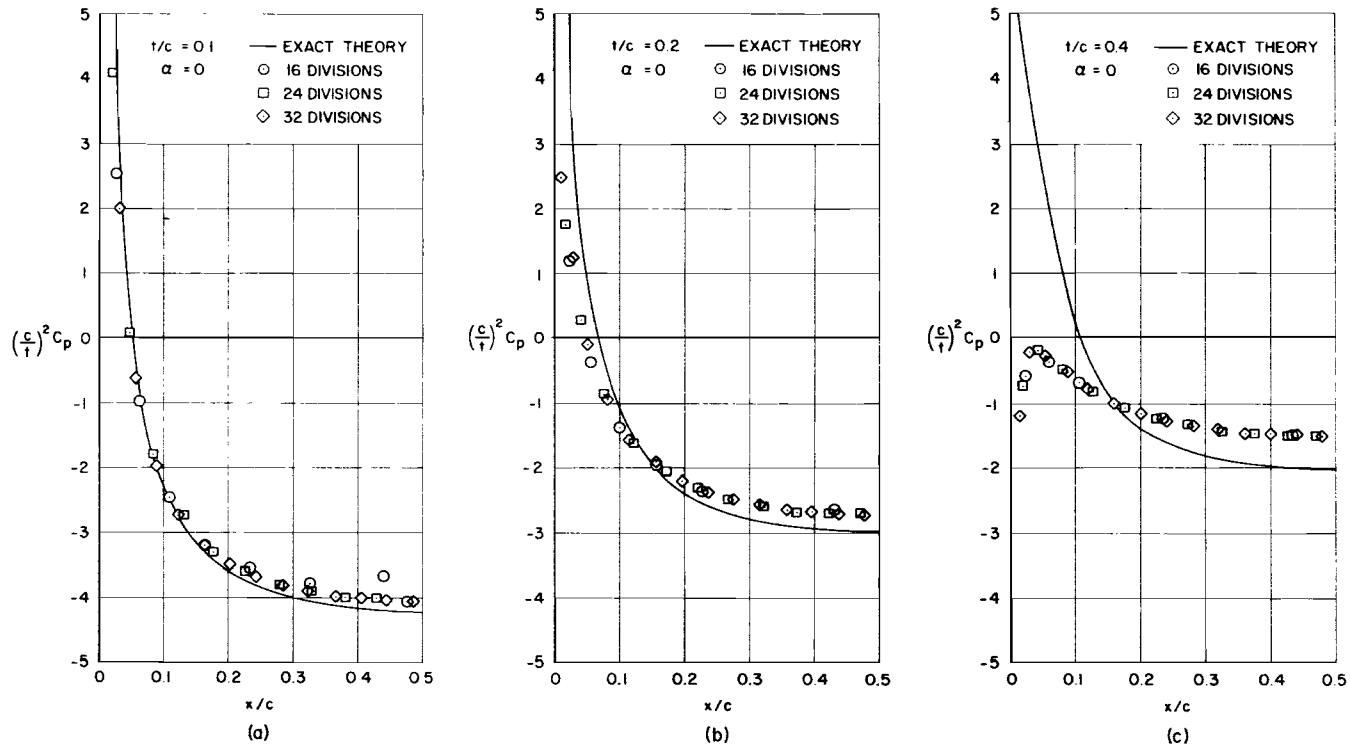


Figure (4.6). Pressure Distribution on Spheroids of Several Thickness Ratios at Zero Angle of Attack - Comparison Between Exact Theory and the Present Slender Body Method

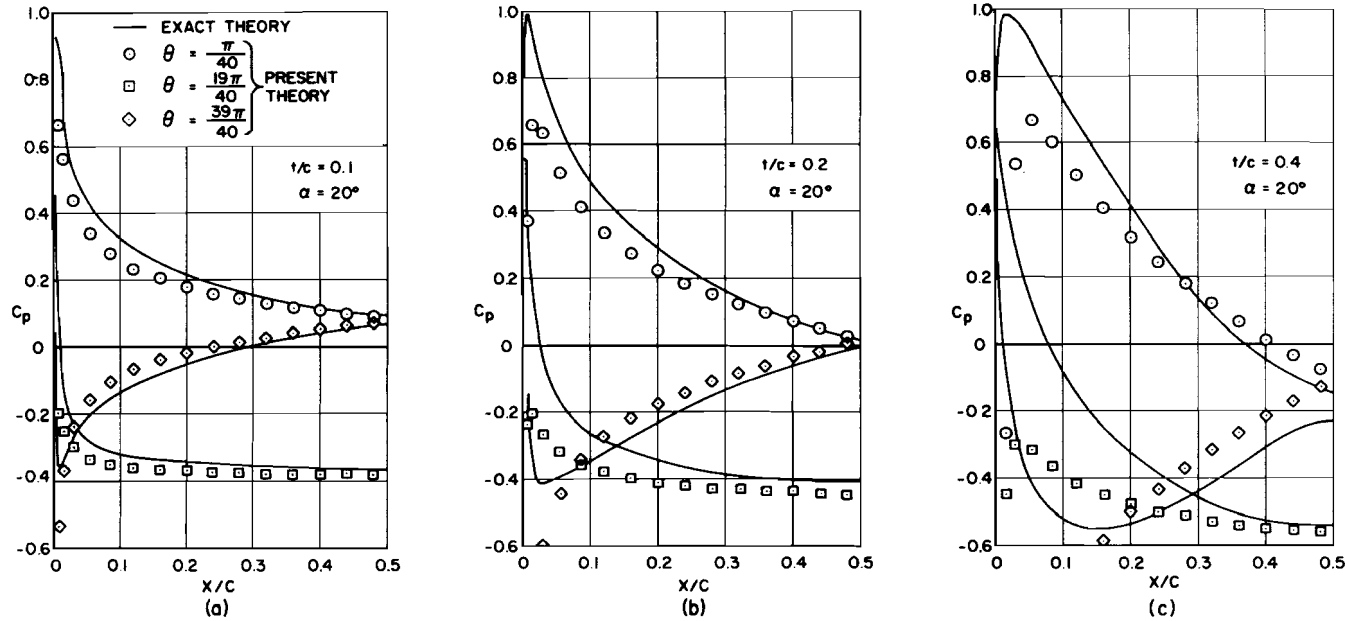


Figure (4.7). Pressure Distribution on Spheroids of Several Thickness Ratios at  $20^\circ$  Angle of Attack - Comparison Between Exact Theory and the Present Slender Body Method



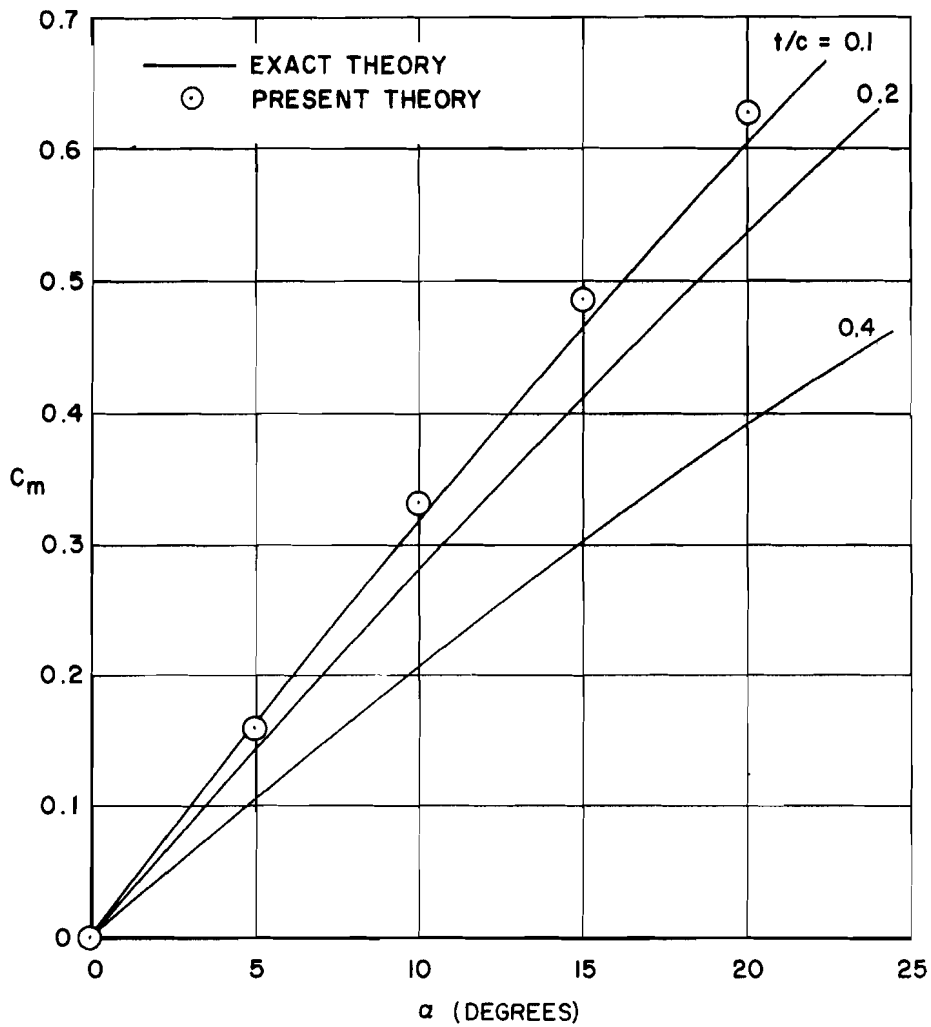


Figure (4.8). Pitching Moment on Spheroids of Several Thickness Ratios - Comparison Between Exact Theory and the Present Slender Body Method

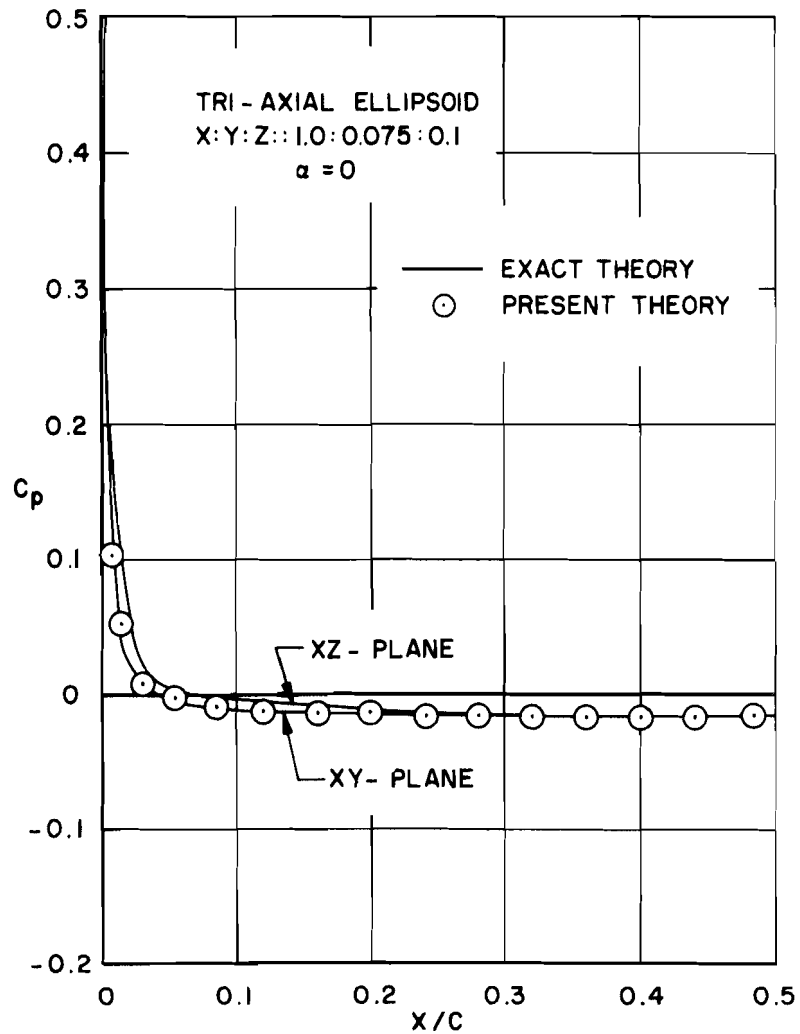


Figure (4.9). Pressure Distribution on a Tri-Axial Ellipsoid at Zero Angle of Attack - Comparison Between Exact Theory and the Present Slender Body Method

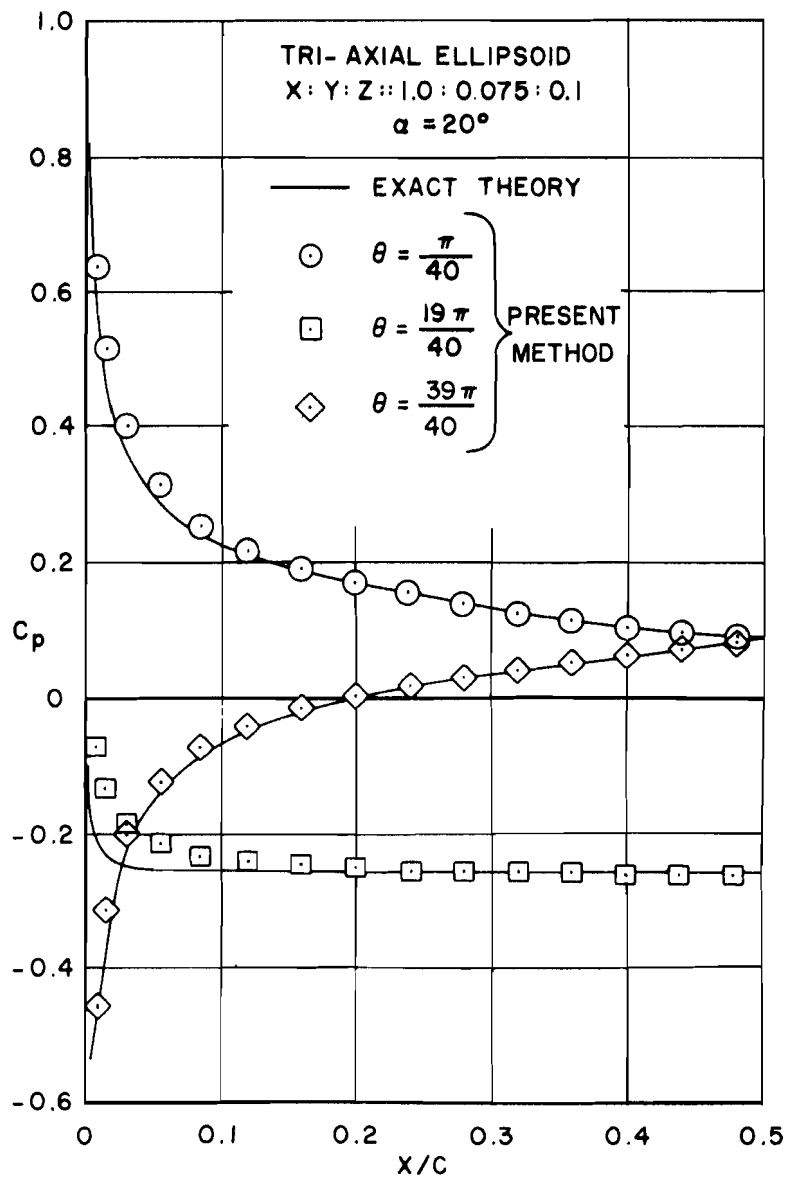


Figure (4.10). Pressure Distribution on a Tri-Axial Ellipsoid at  $20^\circ$  Angle of Attack - Comparison Between Exact Theory and the Present Slender Body Method

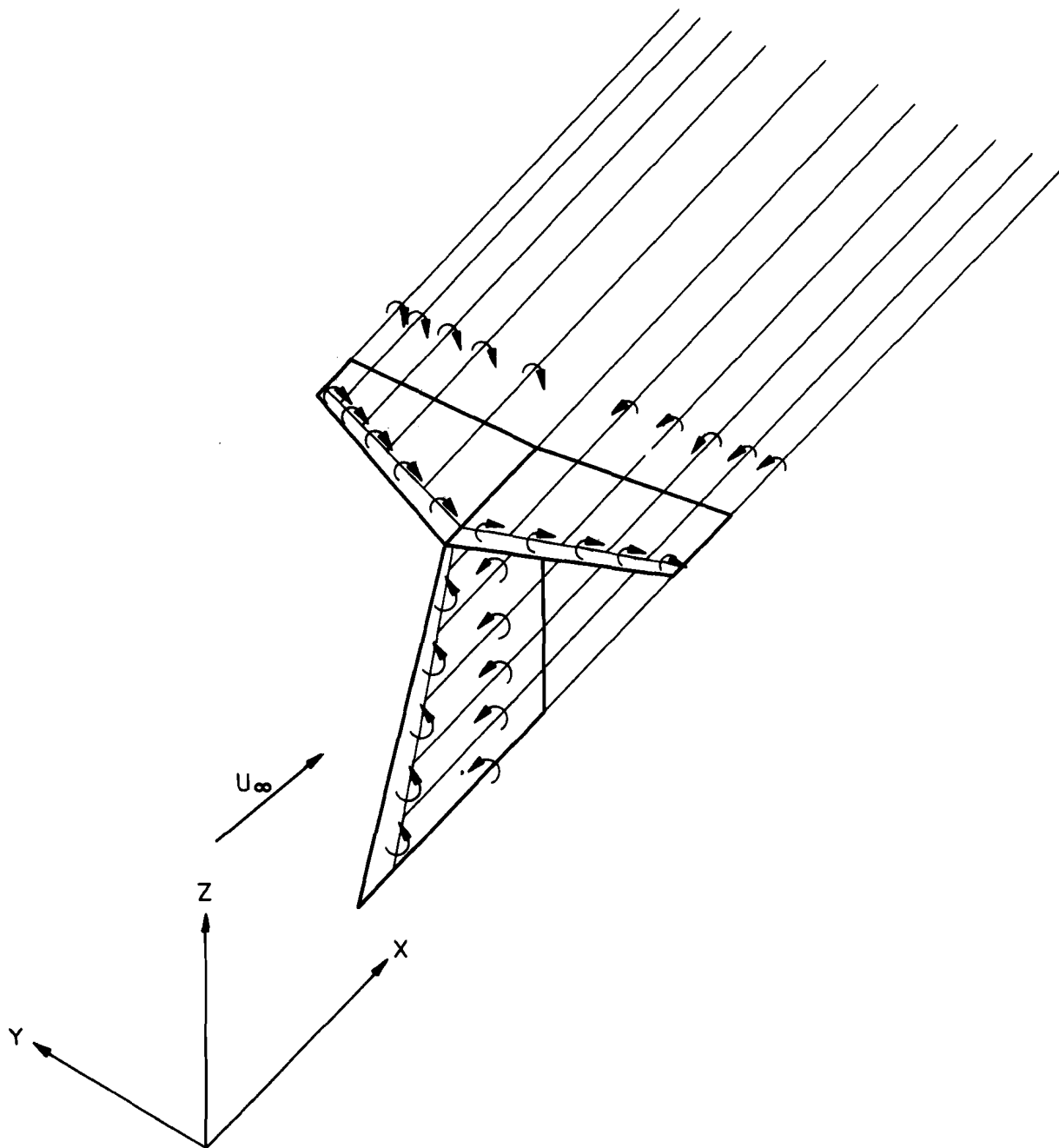


Figure (4.11). Illustration of a Typical STOL Empennage Arrangement

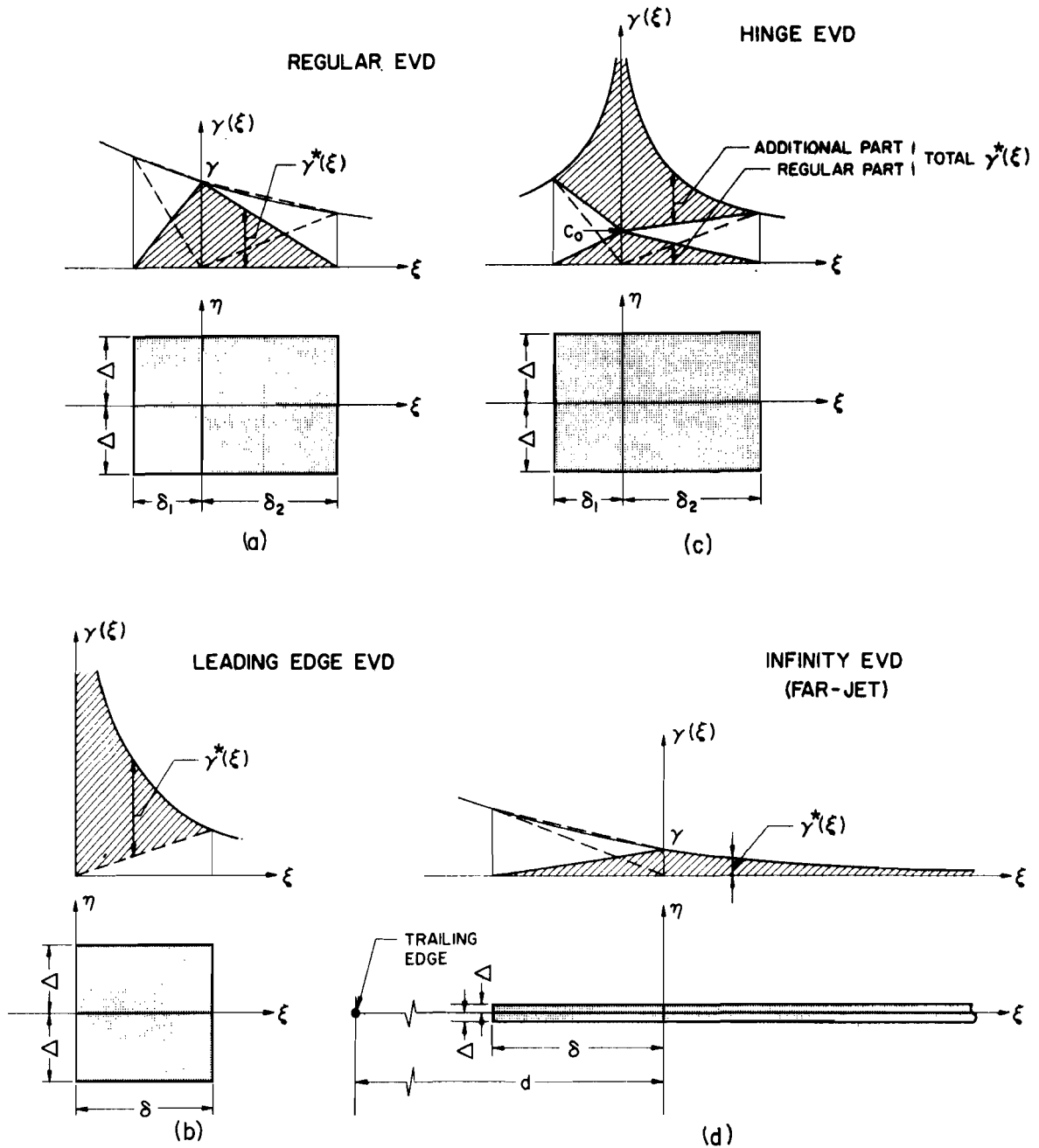


Figure (I.1). Illustration of EVD Types



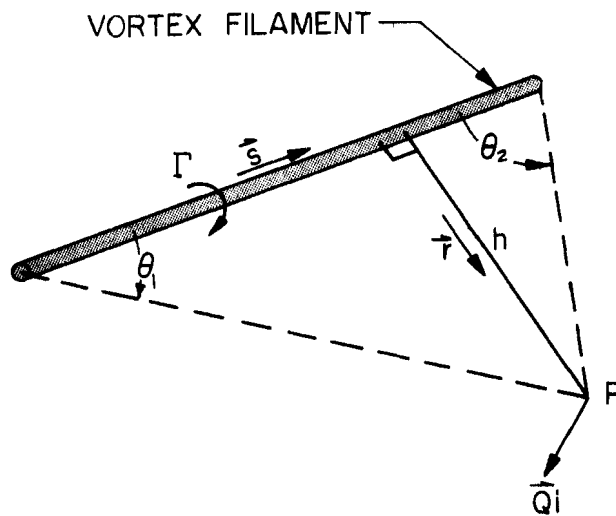


Figure (II.1). Illustration of the Biot-Savart Law for a Discrete Vortex Filament

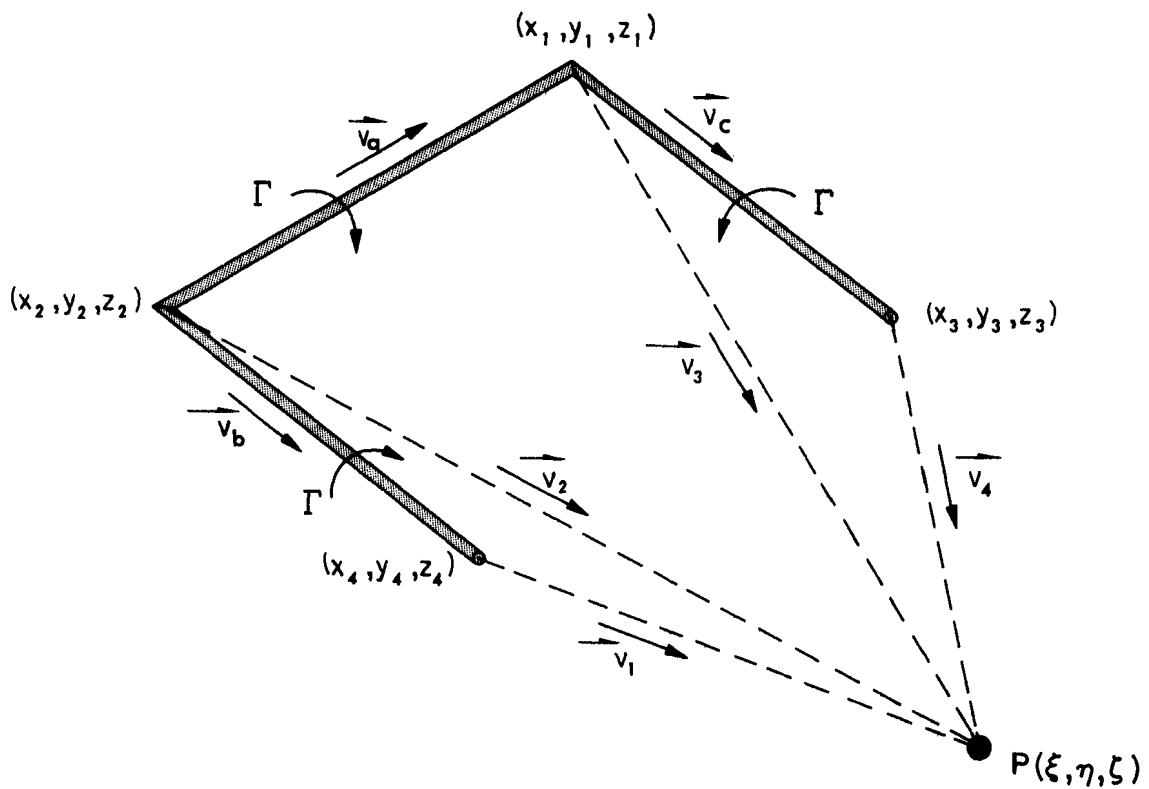


Figure (II.2). Illustration of the Evaluation of the Biot-Savart Law for a Discrete Horseshoe Vortex

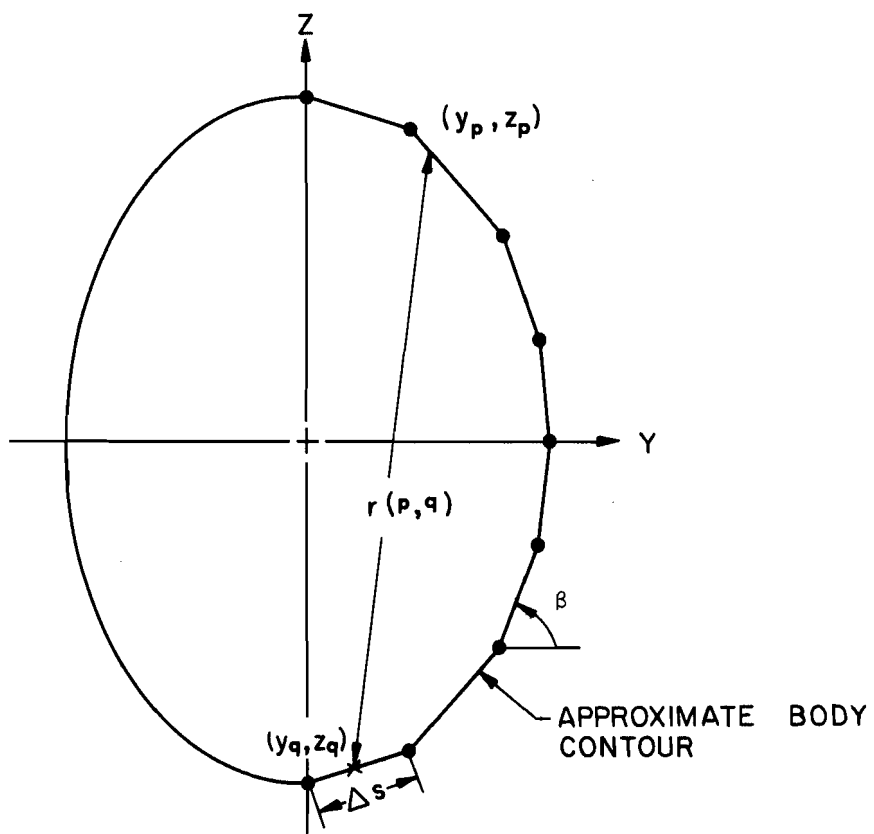


Figure (III.1). Illustration of the Application of the Neumann Solution to a Fuselage Cross-Section



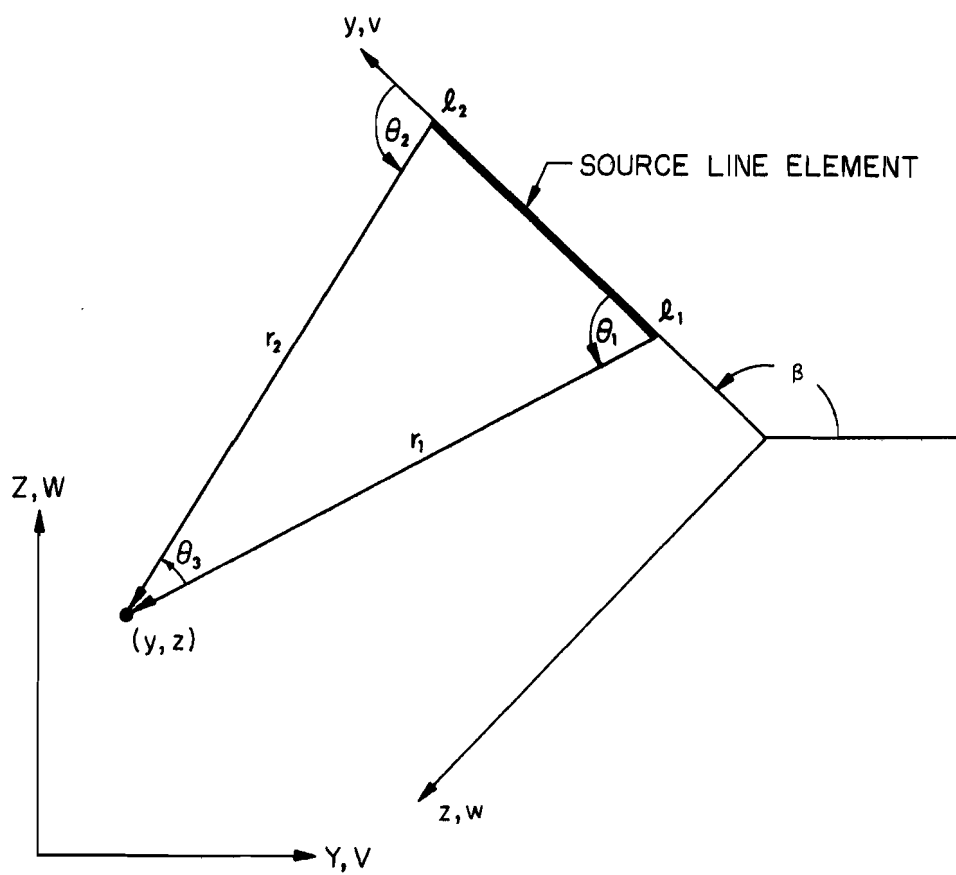


Figure (III.2). Illustration of the Calculation of the Velocity Induced by a Source Line Element



Unclassified  
Security Classification

**DOCUMENT CONTROL DATA - R&D**

*(Security classification of title, body of abstract and indexing annotation must be entered when the overall report is classified)*

<b>1. ORIGINATING ACTIVITY (Corporate author)</b> McDonnell Douglas Corporation Douglas Aircraft Company Long Beach, California 90846		<b>2a. REPORT SECURITY CLASSIFICATION</b> Unclassified	
		<b>2b. GROUP</b>	
<b>3. REPORT TITLE</b> METHODS FOR PREDICTING THE AERODYNAMIC AND STABILITY AND CONTROL CHARACTERISTICS OF STOL AIRCRAFT. VOL. I BASIC THEORETICAL METHODS			
<b>4. DESCRIPTIVE NOTES (Type of report and inclusive dates)</b> Final Technical Report			
<b>5. AUTHOR(S) (Last name, first name, initial)</b> Mark I. Goldhammer Michael L. Lopez Cheng-Chung Shen			
<b>6. REPORT DATE</b> December 1973		<b>7a. TOTAL NO. OF PAGES</b> 275	<b>7b. NO. OF REFS</b> 71
<b>8a. CONTRACT OR GRANT NO.</b> F33615-71-C-1861		<b>8a. ORIGINATOR'S REPORT NUMBER(S)</b> MDC J5965-01	
<b>b. PROJECT NO.</b> 643A		<b>8b. OTHER REPORT NO(S) (Any other numbers that may be assigned this report)</b> AFFDL-TR-73-146, Volume I	
<b>c.</b>			
<b>d.</b>			
<b>10. AVAILABILITY/LIMITATION NOTICES</b> Approved for public release; distribution unlimited			
<b>11. SUPPLEMENTARY NOTES</b>		<b>12. SPONSORING MILITARY ACTIVITY</b> Air Force Flight Dynamics Laboratory Wright-Patterson Air Force Base Ohio 45433	
<b>13. ABSTRACT</b> This is the first of three volumes of a report that describes methods for predicting the stability and control characteristics of STOL aircraft which utilize either the internally ducted jet flap, externally blown jet flap, or a mechanical flap with vectored propulsive thrust system. It is the intention that this methodology will provide design personnel with a capability to predict static and dynamic longitudinal and lateral-directional stability and control derivatives and coefficients during takeoff, approach, and landing phases of flight both in and out of ground effect.  For the three selected powered high lift systems, a common theoretical basis of the formulation of analytical engineering methods (Volume III) is presented. The theoretical methods developed and described herein include the following: <ul style="list-style-type: none"><li>o The Elementary Vortex Distribution (EVD) Jet-Wing Lifting Surface Theory</li><li>o The Ground Effect Method (an extension of the EVD method)</li><li>o The Jet-Wing Flow Field Method</li><li>o The Vectored Jet Flow Field Method</li><li>o The Modified Slender Body Fuselage Method</li><li>o The Empennage Method</li></ul> An extensive comparison of results obtained with these methods and those obtained with other theories and with experimental data is included. The computer program required for the solution of each method is described in Volume II.			

14. KEY WORDS	LINK A		LINK B		LINK C	
	ROLE	WT	ROLE	WT	ROLE	WT
AERODYNAMICS AERODYNAMIC STABILITY AND CONTROL BLOWING CIRCULATION CONTROL FINITE ELEMENT METHODS FLUID DYNAMICS HIGH LIFT SYSTEMS JET FLAP LIFTING SURFACE THEORY NUMERICAL ANALYSIS SHORT TAKEOFF AND LANDING AIRCRAFT SLENDER BODY THEORY VORTICITY WING THEORY						

**INSTRUCTIONS**

1. **ORIGINATING ACTIVITY:** Enter the name and address of the contractor, subcontractor, grantee, Department of Defense activity or other organization (*corporate author*) issuing the report.
- 2a. **REPORT SECURITY CLASSIFICATION:** Enter the overall security classification of the report. Indicate whether "Restricted Data" is included. Marking is to be in accordance with appropriate security regulations.
- 2b. **GROUP:** Automatic downgrading is specified in DoD Directive 5200.10 and Armed Forces Industrial Manual. Enter the group number. Also, when applicable, show that optional markings have been used for Group 3 and Group 4 as authorized.
3. **REPORT TITLE:** Enter the complete report title in all capital letters. Titles in all cases should be unclassified. If a meaningful title cannot be selected without classification, show title classification in all capitals in parenthesis immediately following the title.
4. **DESCRIPTIVE NOTES:** If appropriate, enter the type of report, e.g., interim, progress, summary, annual, or final. Give the inclusive dates when a specific reporting period is covered.
5. **AUTHOR(S):** Enter the name(s) of author(s) as shown on or in the report. Enter last name, first name, middle initial. If military, show rank and branch of service. The name of the principal author is an absolute minimum requirement.
6. **REPORT DATE:** Enter the date of the report as day, month, year; or month, year. If more than one date appears on the report, use date of publication.
- 7a. **TOTAL NUMBER OF PAGES:** The total page count should follow normal pagination procedures, i.e., enter the number of pages containing information.
- 7b. **NUMBER OF REFERENCES:** Enter the total number of references cited in the report.
- 8a. **CONTRACT OR GRANT NUMBER:** If appropriate, enter the applicable number of the contract or grant under which the report was written.
- 8b, 8c, & 8d. **PROJECT NUMBER:** Enter the appropriate military department identification, such as project number, subproject number, system numbers, task number, etc.
- 9a. **ORIGINATOR'S REPORT NUMBER(S):** Enter the official report number by which the document will be identified and controlled by the originating activity. This number must be unique to this report.
- 9b. **OTHER REPORT NUMBER(S):** If the report has been assigned any other report numbers (*either by the originator or by the sponsor*), also enter this number(s).
10. **AVAILABILITY/LIMITATION NOTICES:** Enter any limitations on further dissemination of the report, other than those

imposed by security classification, using standard statements such as:

- (1) "Qualified requesters may obtain copies of this report from DDC."
- (2) "Foreign announcement and dissemination of this report by DDC is not authorized."
- (3) "U. S. Government agencies may obtain copies of this report directly from DDC. Other qualified DDC users shall request through \_\_\_\_\_."
- (4) "U. S. military agencies may obtain copies of this report directly from DDC. Other qualified users shall request through \_\_\_\_\_."
- (5) "All distribution of this report is controlled. Qualified DDC users shall request through \_\_\_\_\_."

If the report has been furnished to the Office of Technical Services, Department of Commerce, for sale to the public, indicate this fact and enter the price, if known.

11. **SUPPLEMENTARY NOTES:** Use for additional explanatory notes.
12. **SPONSORING MILITARY ACTIVITY:** Enter the name of the departmental project office or laboratory sponsoring (*paying for*) the research and development. Include address.
13. **ABSTRACT:** Enter an abstract giving a brief and factual summary of the document indicative of the report, even though it may also appear elsewhere in the body of the technical report. If additional space is required, a continuation sheet shall be attached.

It is highly desirable that the abstract of classified reports be unclassified. Each paragraph of the abstract shall end with an indication of the military security classification of the information in the paragraph, represented as (TS), (S), (C), or (U).

There is no limitation on the length of the abstract. However, the suggested length is from 150 to 225 words.

14. **KEY WORDS:** Key words are technically meaningful terms or short phrases that characterize a report and may be used as index entries for cataloging the report. Key words must be selected so that no security classification is required. Identifiers, such as equipment model designation, trade name, military project code name, geographic location, may be used as key words but will be followed by an indication of technical context. The assignment of links, roles, and weights is optional.